Review

Studies on Quality of Joints and Phenomena Therein for Welded Vehicle Components Made of Aluminium Alloy – a Review

Bogdan Derbiszewski *, Andrzej Obraniak, Adam Rylski *, Krzysztof Siczek, Marek Wozniak

Posted Date: 25 March 2024

doi: 10.20944/preprints202403.1458.v1

Keywords: welding process; vehicle components; aluminium alloy

Review

Studies on Quality of Joints and Phenomena Therein for Welded Vehicle Components Made of Aluminium Alloy - A Review

Bogdan Derbiszewski [1,*], Andrzej Obraniak [2], Adam Rylski [3,*], Krzysztof Siczek [4] and Marek Wozniak [4]

[1] Polytechnic Faculty, Calisia University, 62-800 Kalisz, Poland; b.derbiszewski@uniwersytetkaliski.edu.pl
[2] Faculty of Process and Environmental Engineering, Lodz University of Technology, 90-924 Lodz, Poland; andrzej.obraniak@p.lod.pl
[3] Institute of Material Engineering, Lodz University of Technology, 90-924 Lodz, Poland; adam.rylski@p.lodz.pl
[4] Department of Vehicles and Fundamentals of Machine Design, Lodz University of Technology, 90-537 Lodz, Poland; KS: ks670907@p.lodz.pl; MW: marek.wozniak.1@p.lodz.pl
* Correspondence: b.derbiszewski@uniwersytetkaliski.edu.pl (B.D.); adam.rylski@p.lodz.pl (A.R.)

Abstract: To fulfil a need of limitation automotive emissions the reduction of vehicle weight is widely recommended and achieved in many ways, both by the construction of individual elements of the vehicle, and by the selection of light materials including Al alloys. Connecting these elements with each other and with elements made of iron alloys can be realized, inter alia, by welding or stir welding. However, the quality of the welds obtained varies widely and depends on many design, operational and environmental factors. The present study focused on a review of various welding technics used to joint both similar and dissimilar Al alloys utilized in automotive industry, the effect of various process parameters on welds quality, and phenomena appeared in such welds..

Keywords: welding process; vehicle components; aluminium alloy

1. Introduction

The necessity to limit emissions from vehicles [1–3] might be fulfilled inter alia via a reduction of their weight [4,5]. For example, the utilization of lighter and equally durable components for suspension elements and frames allowed accomplishing such an aim [6].

However, the vehicles' weight reduction achieved by changing their material composition is limited by the extent of material substitution and by material choice [5]. Although composite materials, such as carbon fiber reinforced plastics CFRPs [7,8] offer excellent mechanical properties for light-weighting, their production is more energy- and emissions-intensive than for conventional metals, and their recycling methods are limited. Therefore, the traditional mild steel and cast iron utilized in vehicle manufacturing can be partially replaced by high-strength steel HSS, magnesium alloys, wrought Al and cast Al [5]. For example, the B-pillar outer panel can also be made of high-strength 7075 alloy [9].

Many important structural components of the vehicle made from Al alloys are welded structures [10,11]. For the automobile body, Al alloys from the 5xxx and 6xxx groups are commonly used; however, welding problems occur [12,13]. Particularly, 6082 Al alloy can be applied to vehicle components [14].

The goal of present paper was to review various welding technics used to joint both similar and dissimilar l alloys utilized in automotive industry, the effect of various process parameters on welds quality, and phenomena in such welds. Additionally, several recommendations regarding the selection of the welding method for specific Al alloys' combinations have been formulated.

 doi:10.20944/preprints202403.1458.v1

If there are welded joints in a structural element, the strength of the element differs from the strength of the base material of this element. This difference is considered during design calculations using the so-called joint quality factor or joint efficiency factor or weld joint factor or strength reduction coefficient depending on the calculation method or code [15]. Joint quality factor values range from 0.0 to 1.0, depending on the material, type of weld and the level of accuracy of joint testing [16]. When there are two or more welds in a component, the worst-case weld is evaluated to determine the joint quality factor value. The joint efficiency can be expressed in term of the ultimate tensile strength (the ratio of the UTS of welded joint and that of base material – usually the softer one of dissimilar alloys) [17–19] or more seldom in terms of elongation (the ratio of the elongation of welded joints and that of base material – usually the softer one of dissimilar alloys) [18]

The review included considerations on the concept of weldability, technics for joining of vehicle components made of Al alloy including various welding types, such as conventional welding, friction stir welding FSW, resistance spot welding RSW, gas metal arc welding GMAW, cold metal transfer CMT welding, magnetic pulse welding MPW and collision welding and laser welding. Various Al alloys used for welding process and problems occurring during such a process were considered. Features of Al welded joints and phenomena occurred therein were widely discussed in the review.

2. Weldability

The welding process is closely related to the concept of weldability. The latter subjects to a wide range of definitions and interpretations considering various aspects of design, fabrication, fitness for service, and repair. It was reflected by definitions for weldability provided by both the American Welding Society and the ISO Standard 581:1980 [20]

In this review, as in [20] weldability was considered from the standpoint of materials' resistance or susceptibility to failure. From a fabrication standpoint, it characterized the ability to produce defect-free welded joints. Multiple weld defects generated during fabrication belonged to two groups:

one related to the welding process and procedures. This comprised lack of fusion, undercut, and slag inclusions avoidable by changes in process conditions.

one associated with the material. This comprised solidification cracks and hydrogen-induced cracks usually difficult to eliminate by changes in process conditions alone.

The weldability also characterized the behavior of welded structures after putting into service. The failures in such structures sometimes exhibited a time delay nature. Such failure modes included corrosion [21] fatigue [22–24] stress rupture (creep) [25–27] or complex combinations of these and other failure mechanisms [28] which could be unexpected and catastrophic.

3. Technics for Joining of Vehicle Components Made of Al Alloy

Joining of vehicle components made of Al alloys can be difficult, especially if components are made of the dissimilar Al alloys. Al alloys are difficult to weld due to their specific thermophysical properties and intricate physical metallurgy. Work-hardened alloys often exhibit strength loss in the Heat Affected Zone (HAZ). The strength of precipitation-hardened alloys is highly lowered in both HAZ and weld metal due to coarsening or full [29]. There are some technics allowing proper joining of such different components, especially adhesive bonding [30–33] pointwise mechanical fastening (by clinching or riveting, or with fasteners) [34,35], resistance spot welding RSW [36] electron beam welding EBW [37] cold metal transfer CMT welding [38], to name a few.

3.1. Various Kinds of Welding Process

3.1.1. Conventional Welding

Conventional welding of Al alloys allowed limiting technological or executive difficulties [39] No problems were reported when producing good-quality Al joints in conventional, less-efficient slag-free welding processes [40] Welding with a coated electrode did not provide acceptable weld quality, as porous structures with a tendency to crack occurred. Therefore, welding with coated

 doi:10.20944/preprints202403.1458.v1

electrodes is used rarely and only for irrelevant structural components [14]. The most popular non-slag welding processes used on the industrial scale are tungsten inert gas TIG and metal inert gas MIG methods [14,41]. Gas Tungsten-Arc Welding (GTAW) is also known as Tungsten Inert Gas (TIG) welding [42].

The TIG process of welding is characterized in that an electric arc appears between an infusible tungsten electrode and a bonded Al alloy in an inert gas shield. No additional material is needed, however, an extra binder material in the form of a wire can be introduced into the weld pool manually. Usually, a shielding gas in form of argon, helium, or Ar-He mixtures is fed via the nozzle of the welding torch to limit oxidation and nitrification of both the weld and the electrode.

The MIG welding process is characterized in that an electric arc exists between a fusible electrode and a bonded Al alloy under an inert gas shield. The electrode wire becomes the fusible electrode fed in an automatic and continuous way. The wire is selected according to technological guidelines for a specific welded Al alloy.

The pros and cons of both MIG and TIG processes [14] are presented in Table 1.

Table 1. Pros and cons of both MIG and TIG processes.

Welding process	Pros	Cons
MIG	- allowed welding several types of alloys in all positions, - high welding efficiency - higher from coated electrodes and TIG method, - relatively low cost of welding consumables, - high quality of welds, - allowed automation the method	- quality of produced welds affected by skills and experience of a welder, - high purchase costs of equipment and accessories, and - the necessity to use an additional binder
TIG	- allowed welding several types of alloys in all positions, - allowed welding thin metal sheets, - high quality of welds, - easy control and handling of the welding process, - lack of liquid metal splashing, - no needs to use an additional binder, - allowed automation the method applied without an additional binder.	- low welding speed and low efficiency, especially in case of thicker components, - quality of produced welds affected by skills of a welder, - impossible automation the method applied with an additional binder

However, despite the prevalence of advantages, welding of Al alloys with MIG and TIG processes still resulted in either poor functional properties of the joint or low relative efficiency [43,44]

3.1.2. Friction Stir Welding

Friction stir welding FSW utilized a non-consumable rotating cylindrical tool comprising a cylindrical threaded pin at one end, and a shoulder, at the other moves along the contacting surfaces of two rigidly butt-clamped plates placed on rigid backing support. At the same time, the shoulder is forced to the top surface of the workpiece. During the motion of such a tool along the butting surfaces, heat is generated from the frictional-energy dissipation at the shoulder/workpiece and, to a lesser extent, at the pin/work-piece contact surfaces. This enhanced temperature and caused softening of the material adjacent to such contacting surfaces. During the motion of the tool along the butting surfaces, thermally softened material in front of the tool was highly deformed, extruded around the tool to the region behind the tool and compacted/forged to form a joint/weld [45]. Due to tool rotation and forward translation, FSW is an inherently asymmetric process relative to the workpieces and material flow and temperature distribution during such a process are also asymmetric. For dissimilar Al alloys, the asymmetric character of the process is compounded by the discontinuity in material

 doi:10.20944/preprints202403.1458.v1

properties across the weld zone. Therefore, the placement of the alloys on either the advancing or retreating sides significantly influences the final weld properties [46]. The material around the tool joined due to both the stirring and the extrusion of the material. The shapes of final joint in FSW took forms of onion ring nuggets, zigzag-shapes, and void defect nuggets, which depend on welding conditions. The shape of final joint strongly affected its mechanical properties [47]. In comparison to the conventional welding methods, FSW needed much less energy and no cover gas or flux, and no filler metal, thus joining any Al alloy was independent of the compatibility of the composition being an issue in fusion welding [48].

FSW process is well recognized in literature [49–52] also in case of dissimilar alloys [53–55].

FSW process allows joining both similar Al alloys [56,57] and its dissimilar alloys [58,59]. FSW process is applied in the fabrication of Al alloy wheels and fuel tanks [60]. Friction stir lap welding FSLW joint, being a form of FSW, utilize plunging a rotational tool into two overlapped sheets and retracting it after passing a determined distance [61].

Parameters like tool geometry and joint configuration strongly affect the material flow and temperature evolution, and the same is reflected in the microstructure of joints. Due to the combination of frictional heat and mechanical intermixing of materials, typical micro-structural zones are evolved after FSW such as the stir zone SZ=nugget zone NZ, consist of fine and re-crystallized grains, (b) the thermo mechanically affected zone TMAZ, comprising of plastically deformed grains, and (c) the heat affected zone HAZ containing grains similar to base material (Figure 1). The fine grains structure of SZ was a result of severe plastic deformation caused by stirring action of the tool. The region next to SZ is less plastically deformed and is subjected to partial dynamical re-crystallization, and it is named TMAZ. However, no plastic deformation is seen in the HAZ region, and it only experiences a thermal effect [[62].

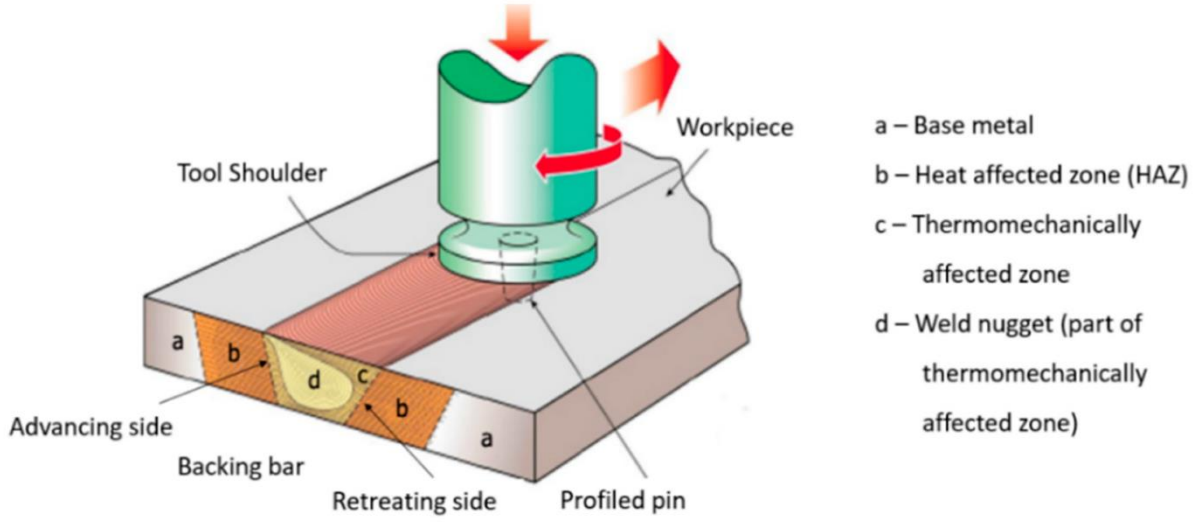

Figure 1. Weld zones in butt joint obtained from FSW process [63].

An FSW lap weld also comprises few zones [64]:

parent material PM - including the material portion positioned the farthest away from the center of the weld, without any deformation or change in mechanical and structural characteristics.

heat affected zone HAZ - including the material portion of the neighboring weld where the material undergoes the effects of heat causing a change in structure and mechanical properties.

This zone does not undergo plastic deformation.

thermoplastic deformation zone - including the material portion affected by the tool resulting in mechanical and heat reactions.

Al alloys can undergo intensive plastic deformation in this zone without the material recrystallizing. This zone covers the border between the non-crystallized material and the weld core.

 doi:10.20944/preprints202403.1458.v1

Weld core - including material portion undergoing full recrystallization. This zone is characterized by a small, axially distributed grain with the size of a few micrometers large (Al alloys). Through this zone, the FSW tool pin travels during the welding process.

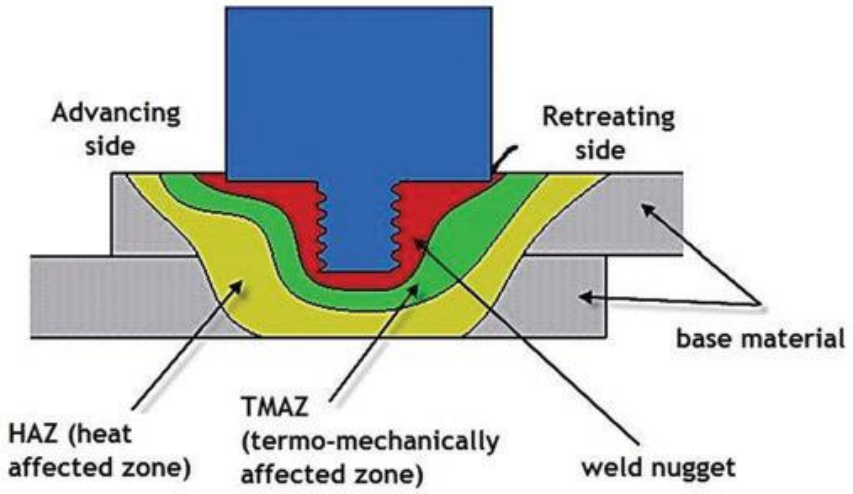

Figure 2. Weld zones in lap joint obtained from FSW process [64].

3.1.3. Resistance Spot Welding

Resistance spot welding RSW is a welding process that joint sheet metal pieces together by applying pressure and passing a large current through localized area while the sheets are fixed together. Resistance spot welding power supply type is divided into silicon-controlled rectifier SCR type and inverter DC type [65]. Kim et al. [36] reported that during resistance spot welding of the Al alloy sheet 5J32 for the car body the range of the optimal welding condition of the inverter type resistance spot welding was larger than that of the SCR type resistance welding. The nugget size obtained under inverter type resistance spot welding was larger than that of SCR-type of RSW in the same welding condition.

3.1.4. Gas Metal Arc Welding GMAW

Gas metal arc welding GMAW is an arc welding process using a metal wire as a combined electrode and filler metal in a plasma arc and inert shielding gas. GMAW provides high productivity and penetration, no need for flux, little spatter, and ability to weld in all positions. A typical weld bead in GMAW of Al alloys comprises three zones. At the beginning of the weld under a quasi-steady state a cold-weld is formed. The base metal is heated up from room temperature, electrode material starts to drop onto the welding coupon initiating the weld bead formation. The weld pool temperature, fluid flow, and weld bead shape vary continuously. At the middle of the weld, the welding process is at a quasi-steady state. Near its end, the arc termination prevents the energy and material transfer into the weld pool. The molten pool solidifies forming a crater-shaped weld end. The ripples are formed at the surface of the weld bead [66].

3.1.5. Cold Metal Transfer Welding

Cold metal transfer CMT welding is a modified MIG welding process based on short-circuiting transfer process differing from the classical MIG method by the type of mechanical droplet cutting method [67].

According to [[68] CMT welding process is an advanced variant of gas metal arc welding GMAW process with lowered heat input in which the welding wire is retracted during the short circuit providing sufficient time for the weld to cool before placing each drop.

CMT process allowed the controlling of material deposition and low thermal input by application of a dedicated wire feed system coupled with high-speed digital control [69].The control of the wire feed rate and the cycle arcing phase provided a proper realize of sufficient energy to melt

 doi:10.20944/preprints202403.1458.v1

both the base material and a globule of filler wire [70]. The CMT process was characterized mainly by:

the point of short circuit with low current corresponding to a low heat input, the short circuit occurrence in a stable controlled manner [31].

Kah et al. [71] described the short-circuiting transfer process, so-called "mechanically assisted droplet deposition", utilized in controlling short circuit by retracting the wire from short-circuiting.

Contrary to conventional MIG process, the droplet detachment mode of CMT process took place without any electromagnetic forces, what allowed the lower spatter [72].

Although there are some excellent reviews related various method of joining components made of Al alloys and the other material [38,73], several dissimilar welding technologies, based on either fusion welding or solid-state welding, are reviewed here, focusing on similar joining among Al alloys.

The retraction of the wire during the short-circuiting phase during the CMT welding prevented spatter generation and produced better weld bead aesthetics. The CMT welding showed more stability and the root produced showed a good finish, both on the surface and back of the joint than the MIG welding [74].

3.1.6. Collision Welding

According to [75] the firmly bonded metals, solid-state joining of similar as well as almost unweldable dissimilar metals (e.g., steel and Al alloys) can be achieved through high velocity forming, also referred to as collision welding. The advantage of such welding is the lowering of problems associated with a heat-affected zone HAZ, such as the formation of brittle intermetallic phases or cracking in fusion welding. The strength of collision welds can reach or even exceed that of the weakest parent material.

Known collision welding methods are [75]: explosive welding EXW (possible workpiece dimensions are in the order of meters), laser impact welding LIW (dimensions of the order of millimeters), and magnetic pulse welding MPW (dimensions of the order of centimeters). Bellmann et al [76] explained that collision welding was accompanied by the ejection of a metal jet, a cloud of particles (CoP), or both phenomena, respectively. The CoP formed during the collision of the joining components was compressed by the closing joining gap. At small collision angles, it reached temperatures allowing the melting of the joined surfaces. The formation of the CoP lowered with an enhancement of yield strength of the material and the escape of the CoP was limited by enhancing surface roughness. Both effects impeded welding with low-impact velocities. The weld formation was easier with smooth surfaces and under vacuum-like conditions. The temperature in the joining gap exceeded 5600 K under normal ambient pressure. Niessen et al. [77] stated that collision welding is a high-speed joining resulting from the plastic deformation of at least one of the joining components. During the process, the formation of a so-called jet and a cloud of particles appear and enable bond formation.

The collision kinetics affects both the cloud of particles (CoP) formation and its temperature, governing the bond mechanism and the achievable amount of welded area. The latter depends also on the initial collision angle, its progression, and the rolling movement.

The width of the weld interface can be enhanced by a smaller gradient of the collision angle when the weldable area of the welding window is achieved.

3.1.7. Magnetic Pulse Welding

Magnetic pulse welding MPW is based on the oblique collision between two joining partners (movable flyer and stationary target) at high relative velocities under a collision angle [78].

During MPW process the collision between flyer and target materials occurred under powerful Lorentz force produced by interrelating two counteracting magnetic fields [68]. The flyer is accelerated by an induced electromagnetic pressure generated by an electrical circuit comprising a charged capacitor bank and a coil actuator [78].

 doi:10.20944/preprints202403.1458.v1

Affected by a collision angle, a point of collision (PoC) moves along the colliding surfaces. When the dynamic elastic limit of the material is exceeded, material flow results from the plastic deformation of the contact surfaces and a stream of material is pushed ahead of the PoC [79,80]. This so-called jetting removes brittle oxide layers and surface contaminations from the surfaces, which are ejected either as a compact stream or as a dispersed cloud of particles (CoP) [81]. Depending on the collision conditions, the CoP either resulted from the dispersed material stream, the spalled surface contamination and oxide layers or both phenomena, whereas the cumulative jet can be partly or completely hidden by the CoP [76,81].

During such a process the hyper-plastic deformation needed for interfacial bonding is generated, because of the high strain rates related to high velocity impact between two metals. This high plastic deformation caused subsequently local heating and high strain-hardening in the welding interface [82]. Thus, increasing the local temperature causes to local fusion and the formation of a thin continuous layer at the interface of two metals [83], which is wavy in some cases.

MPW provides high bond strengths, no heat-affected zones and low electrical resistance, even between metals with differing thermomechanical and chemical properties][84,85].

According to [86],MPW process can be applied for several Al alloys including 1050, 2017, 3004, 5182, 5052, 6016, and 7075. Niessen et al. [77] studied the MPWed Al sheets (EN AW-1050A Hx4, yield strength: 99 MPa, tensile strength: 105 MPa) with an initial thickness of 2 mm for the target as well as the flyer. The thickness of the latter changed in the range of 1-2 mm. They found that during a single magnetic pulse welding process aluminum both fusion-like and solid-state welding can occur. The proper preparation of the flyer geometry affecting its rolling movement on top of the target during MPW can improve the weld interface formation.

3.1.8. Laser Welding

According to [87] or thicker weldments, penetration requires higher welding heat input. The high difference in temperature between the front and back of the weldment causes significant welding distortion. The laser mirror welding process utilizing the symmetrical double laser heat sources acting on the flat plate butt joint structure allows the deformation-free and high-efficiency welding of thick plates. The complex interactions of double keyholes and double-sided joint pools occurred during the welding process.

3.2. Problems during Welding Process

Welding process of Al alloys is accompanied by many problems including porosities, loss of alloying elements, bead geometry and softening of heat affected zone. Laser welding is widely used for Al alloys due to its advantages including low heat input, high welding speed (WS), formability, and high production rate [88].

The degradation of electrode life was the main barrier in application of the resistance spot welding RSW for Al vehicles [89–91]. The use of RSW cladding technique for different Al alloys allowed improving the sheet weldability, whilst maintaining the structural performance. This cladding combined a high conductive, electric stable Al alloy as covering sheet, with a high strength alloy as core sheet [92].

3.3. Al Alloys for Welding

Al alloys from the 5xxx and 6xxx groups are welded in TIG and MIG process, and the best parameters and ways of welding these alloys are still being sought [11–13,93].

According to [14] 6082 alloy can be welded with TIG and MIG processes. The MIG welding provided better effects than the TIG process regarding tensile strength and fatigue strength. TIG welding can be advantageous owing to obtained weld strength parameters but on an industrial scale, it created technological issues and relatively low WS. The most favorable effect of welding such Al alloy is obtained with MIG process using 4043-wire under the WS about 500 mm/min.

 doi:10.20944/preprints202403.1458.v1

According to [94] to achieve of the required end-use properties the components made of various Al alloys usually need heat treatment. The heat treatment processes are specified by the AMS2770 (Heat Treatment of Wrought Aluminium Alloy Parts) and AMS2771 (Heat Treatment of Aluminium Alloy Castings), detailing heat-treatment processes such as aging, annealing and solution heat treating in addition to parameters such as times, temperatures and quenchants.

Wrought Al alloys can be divided into two categories: non-heat treatable and heat treatable. Non-heat-treatable alloys, which include the 1xxx, 3xxx, 4xxx and 5xxx series alloys, derive their strength from solid solutioning and are further strengthened by strain hardening or, in limited cases, aging. Heat-treatable alloys include the 2xxx, 6xxx and 7xxx series alloys and are strengthened by solution heat treatment followed by precipitation hardening (aging) .

Various Al series possessed different chemical, physical and mechanical properties: 1000 series present high electric conductivity and lower mechanical strength, 2000 present high strength, 3000 series present high conductivity with better mechanical strength and formability, 4000 series have good corrosion resistance, 5000 and 6000 series good mechanical properties and formability, and the 7000 family is known as the ultra-high strength aluminium [92].

The automobile body structures are commonly made from Al alloys belonging to the following groups: 2XXX, 5XXX, 6XXX, and 7XXX. The general information regarding their composition, strength, and weldability is presented in Table 2 [14].

The 1100 Al alloy comprised almost 99% pure Al providing the very high malleability and corrosion resistance of the 1100-alloy sheets. This is used for heat insulators [95].

The 2xxx series comprises Al alloyed with Cu. The 2024-alloy is applied for pistons, break components, rotors, cylinders, wheels, and gears due to its high strength and fatigue resistance].[95].

The 3xxx series comprising Al alloyed with Mg provides high formability. The 3003-alloy exhibits high strength, good formability, workability, and drawing capabilities. It is applied for automotive piping, paneling, and power castings for hybrids and EV. The 3004-alloy shares similar characteristics as 3003-alloy and can be also applied for cowl grille panels and radiators. The 3105-alloy possesses high corrosion resistance, formability, and welding characteristics. It is applied in auto body sheet, for fenders, doors, and floor paneling [95].

The 4xxx series comprises Al alloyed with Si. The 4032-alloy is applied for pistons, compressor scrolls, and engine components. It exhibits high weldability and abrasion resistance [95].

The 5xxx series comprises Al alloyed with Mg thus it possesses the enhanced strength. The 5005-alloy is applied for body paneling, fuel tanks, steering plates, and piping. The 5052 alloy is used for fuel tanks, truck trailers, suspension plates, display paneling, bracketry, disk and drum breaks, and many other non-critical auto parts. The 5083-alloy is used in complex automotive components such as engine bases and body paneling. The 5182-alloy is applied for structural bracketry, doors, hoods, and front wing end plates. The 5251-alloy is applied for auto paneling [95].

The 6xxx series comprising Al alloyed with Mg and Si provides the best extrusion and casting capabilities, and ideal surface finishing character. The 6016 and 6022 alloys are applied for auto body covering, doors, trunks, roofs, fenders, and outer plates needing dent resistance. The 6061-alloy exhibits particularly very good surface finishing characteristics, corrosion resistance, and high strength. It is applied for cross members, brakes, wheels propeller shafts, truck and bus bodies, airbags, and receiver tanks. The 6082-alloy possessing very high impact resistance is used for load bearing framework. The 6181-alloy is applied for exterior body paneling [95].

The 7xxx comprising Al alloyed with Zn and Mg is immensely very powerful and possesses extremely high strength. The 7003-alloy is an extrusion one often used for welded shapes in manufacturing impact beams, seat sliders, bumper reinforcement, motorbike frames, and rims. The 7046-alloy possesses hollow extrusion capabilities and good welding character. It is applied similarly to 7003 [95].

Alloys from 2XXX and 7XXX groups exhibited the most favorable mechanical properties (extremely high ultimate). However, for technological reasons, the susceptibility to welding is best for materials from groups 5XXX and 6XXX [14].

Table 2. Al alloys applied in the automotive industry.

 doi:10.20944/preprints202403.1458.v1

Group of aluminium alloys	Main alloy components	Durability	Weldability
2XXX	Al – Cu	High	Low
5XXX	Al – Mg	Increased	High
6XXX	Al – Si – Mg	Increased	High
7XXX	Al – Zn	High	Low

Cast Al alloys cannot be work hardened, so they are used in either the as-cast or heat-treated conditions. Common heat treatments include homogenization, annealing, solution treatment, aging, and stress relief. Typical mechanical properties for commonly used casting alloys range from 138-345 MPa ultimate tensile strength and 103-276 MPa yield strength with up to 20% elongation [96]. The 7075 alloy possessed extremely limited weldability, which excluded the use of conventional welding methods [97].

Some Al alloys (i.e., 1000, 3000 and 4000 series) exhibited low mechanical performance, despite good electric and chemical properties, while the heat treatable Al-Mg-Si alloys (6000 series), presented process robustness issues, narrow welding lobe and/or short electrode life, despite good mechanical properties [92].

7000 series aluminum alloys are beneficial for automotive structures, allowing obtaining improved mechanical and safety properties. However, their proneness to hot cracking and welding embrittlement, to join 7000 series sheets the mechanical methods, such as self-piercing rivets are predestined [98].

3.3.1. Similar Al Alloys

CMT welding provided the efficient welding of similar alloys including 7075 alloy [99] and 6061 alloy [100]. Laser-CMT hybrid welding could join thin sheets made of 6061 alloy [101]. The Laser-CMT hybrid welding produced welded joints with better mechanical properties and aesthetics than the Laser welding and Laser-MIG hybrid welding. The post weld heat treatment PWHT improved the welded joints of 6061 alloys obtained using the CMT gas metal arc welding CMT GMAW via production of uniformly distributing the fine precipitates [102].The CMTW process can be applied to cladding of 6061 alloy [103], additive manufacturing, for example, of Al-6.3% Cu alloy [104] and repair welding including Al-Si-Mn alloy coating on a commercially pure Al plate [105].

3.3.2. Dissimilar Al Alloys

Luijendijk [106] reported that gas tungsten arc welding GTAW can be applied to dissimilar Al alloys of the series 5xxx and 6xxx including 5083 (AlMg4.5Mn)-O, 5754 (AlMg3)-H32, 6082 (AlMgSi1)-T6, 6060 (AlMgSi0.5)-T6, 6061 (AlMgSi1)-T4. Kaba et al. [107] reported that dissimilar 2024-T3 and 7075-T6 structural hardening Al alloys can be joined by the TIG twine electrode arc welding process.

Jweeg et al. [108] found that the processing of friction method was derived from the stir welding and provided fine grains. Two new methods including friction stir processing FSP and the reverse of rotation of stir processing RRSP were applied for joining 3 mm thick components made of dissimilar 5052 and 7075-T6 alloys. The FSW process included a one pass of the welded sample, the FSP engaged two passes of welding in the same rotational direction, and the RFSP engaged two passes of welding the first pass with a tool rotational speed (TRS) in a counter clockwise and the second in clockwise.

Dissimilar Al alloys can be joined using laser welding, nonvacuum electron beam NVEB welding, or gas tungsten arc welding GTAW, as the high electrical and thermal conductivity of Al excluded the use of mash-seam welding for such alloys [109–112].

Bamberg et al. [92] evaluated an increased weldability of an AW-6111 (core sheet) cladded with a 4040 (cover sheet) in RSW process, by establishing a proper welding lobe (affected by the nominal and maximum welding current levels and weld spot diameters). They also analyzed the electrode erosion behavior and the formed microstructure of joints. Compared to a pure 6111 Al sheet the cladded ones exhibited improved weldability characteristics and prolonged the electrode service life.

 doi:10.20944/preprints202403.1458.v1

Studying the CMT welding joints of components made of 5083-H111 and 6082-T651 alloys Gungor et al. [113] found that the micro-hardness of the welded joints was like characteristic hardness traverse across weldments [114], while hardness drops were slightly close to the base metal.

Hardness drops were maximum 18 % level. For 5083 similar alloy weld joint, microhardness values varied in range 77 - 92 HV0,2 and the hardness drops to their minimum values occurred in the weld zone. For 6082 similar alloy weld joint, microhardness varied in range 79 - 96 HV0,2, hardness enhanced in weld zone to around 96 HV0,2, while hardness decreased at the HAZ to 79 HV0,2. For 6082 base metal, hardness reached value of around 82 HV0,2. For 5083 and 6082 dissimilar alloy weld joint, microhardness varied in range 76 - 96 HV0,2. Microhardness in HAZ's of this joint were similar to that of 6082 similar alloy weld join and of 5083 and 6082 dissimilar alloy weld joint. Differently, weld zone of 5083 and 6082 dissimilar alloy weld joint exhibited a little higher hardness value. Microhardness rise in close HAZ of 6082 occurred due to the partially solution-treated zone where some of the precipitates were dissolved, causing some post-weld hardening, but those not dissolved were coarsened. Microhardness drops in precipitation hardened 6082 in far HAZ of 5083/6082 dissimilar alloy weld joint and of 6082 similar alloy weld one resulted from overaged zone where precipitate coarsening occurred [115].

The weld joints and base metal had adequate tensile strength values . Average yield and tensile strengths were 244 and 272.3 MPa for 5083 similar alloy weld joint, 216 and 230 MPa for 5083 and 6082 dissimilar alloy weld joint and 216.3 and 22.3 MPa for 6082 similar alloy weld one, respectively [113]. The CMT welding features were closer to FSW (higher WS and extremely low heat input) and had higher yield strength values than any other welding methods reported in literature.

5083 similar weld joint exhibited best fatigue performance parallel with porosity and yield stress values, then respectively 6082 similar weld joint, and 5083/6082 dissimilar weld one [113]. Elrefaey and Ross [[116] studied welding joints of components made of 5182-O and 6082-T4 alloy sheets obtained in CMT welding process. Such joints exhibited mechanical properties not worse than those for 5182/5182 and 6082/6082 joints. In the 5182 sheets, the HAZ exhibited microstructure comprising fine precipitates of second phase and coarsening of the Mg_2Al_3 precipitates in the Al matrix.

Boşneag et al. [117] experimentally studied the FSW process of three dissimilar alloys, with different properties including 2024, 6061 and 7075. They found that the rotation speed strongly affected the temperature of the process which can differ by up to 50 °C while the doubled value of rotation speed. The higher value for rotation speed lowered the needed vertical force. The roughness values enhanced with increasing the rotation speed and lowered with the progress of the welding process. The better profile of microhardness and the better mixing of metals in the joint appeared for higher values of the rotation speed.

Sharma and Upadhyay [118] studied the butt FSW process of dissimilar alloys 5086 and 7039. Single pass, dissimilar butt welds were obtained under optimized process parameters, threaded cylindrical tool, and 5086 plate on RS. They observed heterogeneous microstructure in the stir zone. The transition boundary comprised much more strengthening precipitates than regions rich in Zn or Mg.

Some variations of the collision welding are applicable also for dissimilar aluminum alloys. Pourabbas et al. [119] reported the use of the MPW for joining 4014/7075 alloys. Meng et al. [120] used the Vaporizing Foil Actuator Welding (VFAW) for joining 2024-T3/7075-T6 sheets.

4. Features of Al Welded Joints and Phenomena Occurred Therein

Most Al alloys are susceptible to liquation cracking during conventional fusion welding due to their wide partially melted zone PMZ, large solidification shrinkage, large thermal contraction, and residual intermetallic compounds [121–124]. If liquation cracking occurs during FSW of specific Al alloys, it must be considered to control and choose welding parameters should be controlled including tool dimension, backing material, cooling device, tool rotation speed, and peak temperature, to limit its incidence [125].

Cornacchia and Cecchel [126] studied the influence of various welding techniques including metal inert gas MIG, cold metal transfer CMT, and fiber laser-MIG hybrid, on the microstructural

 doi:10.20944/preprints202403.1458.v1

and mechanical properties of joints between extruded 6181/6082-T6. They reported the higher quality of CMT and fiber laser-MIG hybrid welding than traditional MIG.

During FSW process of alloys 2024 and 7010 the liquation or melted film formation other than liquation cracking occurred [127,128].

4.1. TIG and MIG Welding Methods

In case of TIG and MIG methods used for welding of components made of 6082 alloy, an enhancement in tensile strength and in the value of yield point in the weld area occurred. During tensile tests of samples made of welded parts made of such alloy, the cracking of such samples occurred outside of the weld area, while the exact location indicated the propagation of neck under tension in the HAZ area [14].

Wang et al. [129] studied the features of the various welded joint zone of 7003 alloy welded using 5356 welding wire by the TIG welding. They found that the heat-affected zone, occurring about 30 mm away from the centre of welding seam, was the softened one due to η'($MgZn_2$) coarsening. The corrosion resistance of TIG welded joint were, in order, Welded zone>Overaging zone>Base metal>Quenching zone. Continuous precipitates from grain in the quenching zone formed the continuous anode corrosion channel, which intensified stress corrosion cracking and exfoliation corrosion and thus lowered the corrosion resistance of the quenching zone. Discontinuous precipitates from grain in the over-aging zone and base metal increased corrosion resistance of those zones.

Alisibramulisi et al. [130] studied butt-welded joints of plates made of alloys 6060 and 7046 with two tempers T4 and T6 prior to welding. The joints were obtained during the pulsed MIG-welding process in one single pass using a stainless-steel backing and the filler wire 5183. The authors studied the subsequent effects of natural ageing NA and post-weld heat treatment PWHT on the joints' properties. Post-weld heat treatment PWHT or an alternative natural ageing NA significantly affected the resulting HAZ hardness distribution as well as cross-weld tensile properties for the alloys 6060 and 7046. Conversely, the initial temper condition was less important for the same properties. However, the initial temper condition influenced the resulting base material hardness and the elongation to fracture for the 6xxx alloy.

Haryadi and Kim [131] studied the effect of PWHT on FCG behavior and tensile properties of TIG butt welded 6013-T4 sheets. The T82 heat treatment was varied in three artificial aging times (soaking). They reported that the various aging in heat treatment T82 affected the mechanical properties of joints. The PWHT-T82 for 18 hours ageing gave the highest fatigue resistance, while the ageing 18 hours provided the highest tensile strength.

Hou et al. [132] studied the weldability of 5052 alloy sheet using MIG and an Al-Mg-In welding wire. They reported that the joint strength of Al5.4Mg0.13In welding wire was close to that of ER5356 welding wire. At the welding conditions of 90 A and 40 mm/min, the tensile strength of welded joint of Al5.4Mg0.13In welding wire and ER5356 welding wire reached 86.9 % and 86.1 % of the base metal's tensile strength, respectively. The spreading areas of Al5.4Mg0.13In welding wire were better than that of ER5356 welding wire, causing good wettability.

Shanavas and Raja Dhas [133] studied the mechanical properties of the joints obtained by the TIG welding and FSW processes with 5052- H32 alloy. They found that the joints fabricated by the FSW process exhibited better metallographic and mechanical properties than those fabricated by using the TIG welding process. The welding current and inert gas flow rate strongly affected the quality of the TIG welded joint. Such a quality was the best for a welding current of 180 A, inert gas flow rate of 11 lpm, WS of 100 mm/min, and an arc voltage of 20 V compared to other joints. Shetty et al. [134] reported that an appropriate selection of age hardening parameters comprising solutioning and artificial ageing with various elevated temperature - time conditioning with suitable welding parameters like current, voltage, WS, inert gas allowed fabricating sound joining of TIG welded 6061 and 5154 alloy.

Zhu et al. [135] studied an effect of post-weld treatment of the 5154 alloy by means of cleaning by Nd:YAG laser after welding with different cleaning speeds. They found that an Nd:YAG laser

 doi:10.20944/preprints202403.1458.v1

effectively removed the welding slag and eliminate the pores in the weld under a certain cleaning speed. For the cleaning speed in the range of 5.2-20.7 mm/s, laser cleaning eliminated the residual stress of the welded joint and improved the welding joint's strength.

Studying GTAW-obtained welded joints of dissimilar alloys of the series 5xxx and 6xxx including 5083-O, 5754-H32, 6082-T6, 6060-T6, 6061-T4 for plate thickness in range of 1.5-5 mm, Luijendijk [106] reported that the asymmetry of the welds appeared. The welding lowered the strength of the material in the HAZ in smaller extent for solution hardened and strain hardened alloys, than for precipitation hardened alloys. For the latter the post-welding strength was less reduced for the naturally aged condition than for the artificially aged case. The reduction in strength for the strain hardened alloys was independent of material thickness for its specified range.

Kaba et al. [107] reported that welding joints of dissimilar 2024-T3 and 7075-T6 structural hardening Al alloys obtained by the TIG twine electrode arc welding process providing a stable arc and a good bead appearance. The several zones: molten zone WZ, bonding zones LZ, heat-affected zones HAZ with various microstructures were generated. The HAZs were lower than those from the conventional TIG welding process. Precipitates of the type θ (Al_2Cu), S (Al_2CuMg) and η ($MgZn_2$), were formed in the HAZ of base metals 2024 and 7075, respectively. The microhardness was lower in the molten zone and higher in the HAZ of 7075 T6 alloy. An embrittlement of tensed samples was accompanied by a 44 % and 37 % drop in the tensile strength of 7075-T6 and 2024-T3 base metals, respectively. The use of GTAW process for various dissimilar combinations of 5182-H16, 5754-O, 6022-T4, and 6111-T4 provided various cracking resistance during welding. It was the highest for the 5182/5754 alloy pair, while combinations of 6022 with either 5754 or 5182 exhibited resulted in the lowest cracking resistance [136].

The Al 7xxx series alloys are weldable if an amount of the alloying additive of Cu is below 1 wt. %. The latter caused hot cracks in welds or heat affected zone HAZ due to melting the metal and mixing it with the filler metal during the welding process, using MIG or TIG processes [137]. Such methods are conducted with high linear energy influencing the relatively high degree of mixing of metals, thus enhancing the risk of hot cracks. The high-energy course of the process led to the formation of a dendritic structure in HAZ, significantly weakening the mechanical properties and corrosion resistance of these alloys [138].

The use of laser beam welding or hybrid laser/gas metal arc GMA welding was also limited for Al 7xxx series alloys. This was due to the high-power density of the integrated laser beam, compared to arc welding methods, enhancing the risk of hot cracks, and provoking intense metal evaporation generating many gas pores in turn [139]

Niu et al. [140] studied butt welded joints of components made of 2219-T87 alloys obtained by the double-pass tungsten inert gas arc welding process. They found that the two fusion zones FZs were almost the weakest regions in the joint, with microhardness values of 76 and 78 HV, respectively. Microhardness of the heat-affected zone HAZ raised along with enhancing distance from the fusion line except for a valley value at the distance of about 4.5 mm. The mean grain size of the two FZs was 74.4 and 79.2 μm, whereas 41.5, 44.9 and 43.4 μm for the two HAZs and base metal BM, respectively. The coarse whitish particles of FZs containing about 60.4% and 54.2 % Cu had a small strengthening effect, while the percentage was about 24.6% for the BM zone being close to that of HAZ. A high number of strengthening phases θ′ dispersed in the BM zone, whereas hardly any precipitates occurred in FZ and HAZ adjacent to FZ. So, the coarsening of grain size, lowering and segregation of alloying element content, and the precipitate evolution caused softening in FZ, while the precipitate evolution caused softening in HAZ.

Kwon and Weckman [141] studied welded joints of 1.2 thick sheets made of 5182 alloy obtained using plasma arc welding -TIG (PAW-TIG) double-sided process. They found that the structure of all joints mainly comprised tiny equiaxed crystals, and the proportion raised with enhancing of WS. In this process, the welding heat was concentrated, the cathode cleaning effect was high, and the welding seam was relatively big.

Nyrkova et al. [142] studied properties of welded joint of components made of alloy 2219 obtained by single-pass welding with a non-fusible electrode along and across the rolled product,

 doi:10.20944/preprints202403.1458.v1

and heat-treated to the state T62, in liquid amyl and its vapours at a temperature of 50 °C for 45 days. They reported that in the longitudinal direction welded joints exhibited yield strength varying in the range 301–317 MPa compared to that of the base metal in the range 295–297 MPa, strength limit in the range 409–415 MPa compared to that of the base metal in range 422–425 MPa, elongation in range 4.0–5.8 % and 17.6–19.1 %, respectively. In the transverse (P) direction such joints showed the yield strength varying in range 309–331 MPa compared to that of the base metal in range 304–307 MPa, the yield strength varying in range 392–414 MPa compared to that of the base metal in range 428–433 MPa, elongation in range (2.1–3.3) % and (12.6–15.0) %, respectively. The strength coefficient of welded joints in the longitudinal direction was 0.96, in the transverse 0.94. The joints in the above environment were resistant to corrosion cracking and intergranular corrosion, resistance against exfoliating corrosion was in grade 2. Aging in amyl and amyl vapours did not change the strength grades of the base metal samples and welded joints in both directions, while the plasticity parameters varied: the yield strength of the base metal enhanced by ~ (5–6) %, of welded joints lowered by ~ (6–7) %, the relative elongation of the base metal lowered ~ (5–16) %, of welded joints by about ~ 20 %. All samples were fractured in a viscous manner. After the exposure in amyl, the coefficient of the strength of welded joints in the longitudinal and transverse directions was equal to 0.91, after the influence of amyl vapors, it was 0.95 in the longitudinal direction and 0.96 in the transverse one.

According to Su et al. [143] the 5083 Al plates can be welded using 5356 alloy filler metals comprising various amounts of Sc and Zr. A great grain refinement occurred in the fusion zone FZ of welded joints after the additions of Sc and Zr. The filler metal modified with 0.2 wt.% Zr+0.1 wt.% Sc caused the smallest grain size with 29 μm, and the filler metal with 0.2 wt.% Sc+0.1 wt.% Zr additions caused the close grain size with 30 μm. The 0.2 wt.% Sc addition effectively modified the microstructure of filler metal and enhanced the mechanical properties. The grain size of the fusion zone for 5356 + 0.2 wt.% Sc+0.1 wt.% Zr filler metal was lowered by 75.8 % and the highest ultimate tensile strength UTS was enhanced by 15 % in comparison to that of the unmodified alloy joints. However, individual 0.2 wt.% Zr addition could not clearly modify the filler metal. The improvement of mechanical properties resulted from the occurrence of refined grains. According to Palanivel et al. [144] fusion welding joints of Al alloys can comprise various defects including hot cracking, porosity, slag inclusion, etc. which worsen the mechanical and metallurgical properties. These defects very seldom occur in the friction stir welded joints due to a lack of melting during the welding process. During the latter metals are joined in the solid state because of the heat generated by the friction and flow of metal by the stirring action.

Kumar and Sundarrajjan [145] optimized pulsed TIG welding parameters for butt joint of 2.14 mm-thick sheets made of 5456 alloy obtained using 5356 filler material. Before welding, the base metal sheets were pickled with a solution of NaOH and HNO_3, wire brushed, degreased in acetone, and finally preheated to 100 °C. After planishing the mechanical properties of joints enhanced by up to 15% due to internal stresses were relieved or redistributed in the weld region. The behavior of the welded joints at the optimum conditions including peak current of 80 A, base current of 40 A, the WS of 230 mm/min, and pulse frequency of 4 Hz resulted from the enhancement of an amount of Mg2Al3 precipitates formed in the Al matrix.

A proper selection of TIG welding parameters including current, torch speed, arc voltage, arc gap, electrode diameter, electrode tip angle, shielding gas and flux improve penetration as well as weld quality. The TIG welding disadvantage such as low weld penetration can be limited and TIG weld quality can be enhanced using various methods including ATIG (Activated Flux TIG), FBTIG (Flux Bounded TIG), PCTIG (Pulsed Current Tungsten Inert Gas) Welding. Particularly, the use of flux or fluxes and pulsed current method improved both the weld penetration and weld quality [146].

Chen et al [147] studied the effects of ultrasound on grain fragmentation in the TIG weld of pure Al. They found that the use of ultrasound can break the grain of the TIG weld of pure Al. The microstructure transformed from plane crystal, columnar crystal, and uniform equiaxed crystal into plane one, deformed columnar one, and nonuniform equiaxed one after the application of ultrasound. The ultrasonic amplitude and welding current highly affected grain fragmentation. The degree of fragmentation was first raised and then lowered with a raised in ultrasonic amplitude, and

 doi:10.20944/preprints202403.1458.v1

it raised with an enhancement in welding current. The higher intensity of acoustic nonlinearity increased the degree of grain fragmentation. The acoustic pressure in the weld pool exceeded the cavitation threshold, and cavitation bubbles appeared. The use of ultrasound practically unchanged the flow velocity in the weld pool. The high-pressure conditions under cavitation led to grain fragmentation in a pure Al TIG weld at an ultrasonic-assisted TIG welding process.

Gupta et al. [148] compared the TIG and MIG welding techniques applied for the 6062 alloy. They found that the impact strength of MIG joints exceeded that of the TIG joints. Despite, the hardness in weld metal region was lower than that of the BM. The hardness pattern in the MIG-based weld region exhibited higher values compared to these in the TIG-based one. In case of MIG the microstructure was exceptionally fine and equiaxed, exhibiting uniformly distributed grains with strengthening precipitates, while after the TIG welding the dendritic grain structures occurred. Due to fine grain structure the MIG-based joint exhibited better tensile and mechanical properties compared to those of the TIG-based one. The joint efficiency reached up to 40.5% in case of TIG, while up to 91.8% in case of MIG. Therefore, the MIG is the best suitable welding process to join 6062 alloy than the TIG welding.

Y. M. Zhang et al [149] studied a 6061-alloy joint obtained using a single power supply type double-sided double TIG welding process. The structure of such a joint was mainly equiaxed, with fewer columnar crystals, and the lower number of thermal cracks in the weld. Additionally, the pore size of such joints was lowered, and the distribution was diffused in comparison to the plasma arc welding with variable polarity.

Squillace et al [150] compared features of weld butt joints of 2024-T3 alloy obtained with TIG and FSW techniques. They noticed a general decay of mechanical properties of TIG joints, mainly due to elevated temperatures experienced by material. For FSW joint, lower process temperatures and high plastic deformations due to tool motion made a complex situation, because slightly lowered mechanical properties appeared in the nugget zone including flow arm zone and TMAZ, while in HAZ, due to starting heat treatment of alloy, a slight improvement of such properties appeared. In the nugget zone a light recovery of hardness relative to TMAZ occurred, due to the re-crystallization of an exceptionally very fine grain structure. In both kinds of joints, parent alloy exhibited a clear pitting tendency, while weld bead and HAZ showed passive behaviour. In case of FSW joint, such differences were less. The nobler behaviour occurred on the RS of the FSW bead compared to its AS.

Comparing the fatigue properties of 5052 alloy joints obtained by FSW and TIG techniques, Wang et al. [151] reported that the fatigue properties of FSW-based joints were better than those of the TIG-based ones.

Comparing microstructural and mechanical characteristics of welds of Al–4.5 Mg–0.26 Sc heat-treatable alloy obtained with TIG and FSW techniques, Cabello et al [152] found that hardening precipitates were more affected by the TIG than by the FSW process. This highly lowered mechanical properties of TIG welds.

Confronting the influence of welding processes on mechanical and metallurgical properties of welded Al–Mg–Sc alloy plates welded using FSW and TIG techniques, Zhao et al. [153] reported that the mechanical properties of the FSW-based joint were much better compared to those of the TIG-based one. The tensile strength and yield strength of the FSW-based joint were 19% and 31% higher than those of the TIG-based one, respectively. Due to the low welding temperature of the FSW process and the high thermal stability of Al_3(Sc, Zr) particles, the cold-working microstructures were well-preserved.

Comparing fatigue crack growth behaviour of square butt joints of 2219 alloy, obtained with the GTAW, EBW and FSW techniques, Malarvizhi and Balasubramanian [154] reported that the FSW joints exhibited superior fatigue crack growth resistance compared to EBW and GTAW joints. This was mainly provided by the formation of very fine grains.

Confronting the mechanical and metallurgical properties of Al-Mg-Mn-Sc-Zr alloy joints obtained with FSW and TIG techniques Zhen et al. [155] found that the strength of FSW and TIG joints lowered in comparison to that of the base metal but the strength of FSW ones was higher than that of the TIG ones. The loss of substructure strengthening and an insignificant loss of precipitation

 doi:10.20944/preprints202403.1458.v1

strengthening of Al_3(Sc, Zr) lowered the strength of the FSW joint. In case of the TIG welded joint, the lack of both the strain hardening and most precipitation strengthening effect of Al_3(Sc, Zr) particles contributed to its softening. Simultaneously, the grains in the nugget zone of FSW joints were finer than those in the molten zone of TIG joints.

Anjaneya Prasad et al. [156] studied 6061 alloy joints obtained by MIG and FSW techniques. The MIG welding process was realized with a WS of 110 mm/min. The FSW provided 10-100 times smaller grains than the MIG in the microstructure of the joints. The MIG produced a lower tensile strength than the FSW. The amount of heat input influenced the weld material hardness and the width of hardness resulted from shoulder diameter and heat input. The FSW enhanced the weld quality.

Jannet et al. [157] compared the mechanical properties of joints of 6061-T6/5083-O alloys obtained using FSW under four rotation speed (450, 560, 710 and 900 rpm) and Fusion Welding (MIG and TIG). They reported that PWHT process provided better tensile properties in all joints, however, the better tensile strength occurred for FSW joints. The latter exhibited the grain refinement with fine distribution of precipitates. The microhardness in HAZ and BM was lower than that in the weld region. The width of the HAZ of FSW joints was narrower than for Fusion Welded joints.

Sasidharanet al. [158] compared the tensile and microstructural properties of joints of AA2219 obtained with the DCSP (Direct current straight polarity) TIG and the FSW techniques. They found that the UTS of the DCSP TIG joint was of 257.5 MPa, while that of the FSW joint was of 287.9MPa, providing the WE of 58.5% and 65.4%, respectively. Percentage elongation for FSW was also higher than that of base metal. The FSW joints exhibited much fewer microporosities than DCSP TIG joints.

Kumar et al. [159] performed TIG, MIG and FSW processes for AA6061 alloy. FSW was realized under 60mm/min WS, 0.69 kJ/mm heat input, 635 rpm of TRS, 16mm tool shoulder diameter, 7mm pin diameter, 4.7mm pin length, and 20-degree tool tilt angle. The heat input in the case of the FSW was lower than that of TIG and MIG welding processes. In the FSW heat input was 38% lower than that for the TIG and 51.2% lower than that for the MIG. FSW joint efficiency was 19.4% higher than that for the TIG joints and 35.5% higher than that for the MIG joints. Compared to the TIG and the MIG, the FSW provided sound welds with higher joint efficiency and less heat input.

Navyashree and Sivaramakrishna [160] compared properties of plates made of 6082 alloy joined using TIG and FSW techniques. They found that the microstructure of the FSW joint differed from that of the TIG joint. The tensile strength and hardness of the FSW joint were better than those of the TIG joint. The FSW with a tool having a smooth pin provided a smooth surface finish. The HAZ of the FSW joint was well fused and free from nonmetallic defects.

Work-hardened (non-heat treatable) Al alloys including the 5xxx series exhibit much lower strength in the HAZ in the case of arc welding due to the annihilation of dislocations. In fusion welding of Al alloys, a wide HAZ is formed due to high heat conduction. However, in case of laser welding providing lower heat input and more concentrated energy, such a HAZ is narrower, and less strength loss is achieved therein [30].

Interestingly, the use of nanoparticles coated on base metals and coated on electrodes in fusion welding (GMAW and GTAW) provide joints with improved mechanical properties and microstructural formations by grain refinement [161].

Summarizing, the mechanical and metallurgical properties of welded joints are affected by welding process parameters. Fusion welding lowers mechanical properties due to softening in HAZ and weld metal [29]. FSW joints exhibited better mechanical and metallurgical properties in comparison to those of TIG and MIG joints, similarly to the [162]. According to [163] the MIG welding provides high WS and versatility. During MIG welding the porosity is the major problem affecting the weld strength. Also, residual tensile stress sometimes occurs affecting the mechanical properties of the welds. Due to faster cooling rates, sometimes, crack and deformation appear in MIG welded joints. Particularly changing values of welding current and WS can strongly affect the weld quality, its microstructure, hardness, tensile strength, and impact strength. Lower welding voltage and gas flow rate and higher WS and wire feed rate results maximum ultimate tensile strength of the weldment. During the MIG process weld metal can fail to fuse properly with the base metal under improper WS or welding angle. MIG welding is not suitable for vertical or overhead weld positions

 doi:10.20944/preprints202403.1458.v1

due to high heat input and fluidity of molten metal. During the welding of base metal, two zones including HAZ, and weld pool (Melted zone) appeared and a microstructure of them was strongly affected by input parameters. Especially the input current changed the grain size and structure of the HAZ by producing the heating effect.

The conventional MIG welding is characterized by an unstable arc, insufficient heat input and small penetration depth [5]. These problems can be resolved with the pulse-MIG welding technique based on pulsed current waveform allowing precise control of the metal transfer rate [164], applicable for 6061/A356 alloys joining or 5083 alloy joints [165].

The arc of MIG welding can be also stabilized using the plasma-MIG welding technique [166].

The microstructural and mechanical behaviour of the MIG weldments can be improved using alternating magnetic field and ultrasonic vibration. The metal transfer rate and stability of the Ultrasonic MIG welding are much better than that of conventional MIG one; [167,168].

The main TIG welding disadvantage such as a low weld penetration can be limited and TIG weld quality can be enhanced using various methods including ATIG (Activated Flux TIG), FBTIG (Flux Bounded TIG), PCTIG (Pulsed Current Tungsten Inert Gas) Welding. Particularly, the use of flux or fluxes and pulsed current method improved both the weld penetration and weld quality [146].

It can also be noted that the comparative studies focused on the use of various welding techniques for Al alloys of 5xxx series were conducted only by very few researchers.

4.2. Cold Metal Transfer CMT Welding Method

The Al alloys can be joined using low-energy welding methods, such as cold metal transfer CMT [38,169,170] being a modification of the GMA welding process, limiting the amount of heat input to the welding zone. The latter was due to metal transfer in a short arc using the reciprocating wire feeding RWF technology [171,172] During the CMT welding, temperature variations in welds and parent metals strongly affected material characteristics, residual stresses, and thus dimensional and shape accuracy of welded products [173]. Feng et al. [174] pointed that the CMT process is especially suitable for welding thin Al alloy sheets due to the low heat input and the slight deformation.

The welded joints of parts made of 7075 alloy using CMT method exhibited lack of spatter and cracks and extremely low porosity. The joints exhibited minimum micro-hardness in the weld zone WZ, and slight hardness weakening in HAZ compared to the base metal BM. The joint had mechanical property coefficients of 77 %, 60 % and 69 % for yield strength, ultimate tensile strength, and elongation, respectively. The CMT welding produced joints with mechanical characteristics better than the MIG and TIG processes and comparable to FSW and LBW processes [99].

During CMT welding thin sheets made of 6061 alloy using filler with the same composition as of base metal, the welded joints possessed a quasi-binary composition. The latter was less susceptible to solidification cracking, controlled fusion line, narrower heat affected zone HAZ and weakened intermetallic phase area. The welded joints revealed fine recrystallization. A uniform distribution of grains and their size in weld HAZ and base metal occurred [100].

Dutra et al. [175] studied welded joints obtained using two different wire electrodes 5183 and 5087. Weld using 5087 electrode exhibited higher mechanical performance during tensile tests. The micro-hardness was similar in both the WZ and HAZ. Welding joints obtained with both wire-electrodes showed the same toughness. The crack tip opening displacement toughness test showed that the applied combinations of base and feed material yield good cracking resistance characteristics. It was found a higher incidence of pores in the case of the 5183-wire electrode.

Shu et al. [176] studied the most vulnerable zones in three-pass cold metal transferring CMT welded joint. They found that the highest principal stress made the joint symmetric face overly sensitive to tensile cracks. The boundaries between the weld seam and the base plates were sensitive to cracks as to the equivalent von Mises stress was the highest when the first inter-pass cooling was finished. The third weld pass and the inter-pass remelted zones showed the low mechanical performances resulting from the coarse grain and coarse grain boundary, respectively.

During studies on CMT welding of parts made of AA7A52 alloy Shu et al. [177] found that the intergranular segregation, providing the coarse grain boundary between the weld passes, exhibited

 doi:10.20944/preprints202403.1458.v1

inferior mechanical performances. Tri-axial stress distribution in the fusion zone pointed to the tendency to tensile failure under service conditions. The softened zone was much wider inside the base plates than close to the flat surfaces. The strip-shaped quenched zone was narrower than the averaging zone internal plates. The control of heat input amount via a selection of the appropriate welding parameters provided welded joints of 7075 alloy without hot cracks [169].

One of the phenomena occurring in various Al welded joints is so called 'weld unzipping. Such joints under dynamic loading can fail by this mechanism characterized by the unstable crack growth along the heat affected zone/weld metal interface [178,179]

Gay et al.[180] stated that the fracture mechanics approaches allowed understanding weld unzipping. The failure along the weld lines was quantified via the difference between stable and unstable fracture . When a structure was subjected to certain load types, the propagation of a crack was driven by the stress field developing ahead of the crack tip . The stress and strain fields were characterized by the stress intensity factor KI, under elastic conditions or the J-integral JI or crack opening displacement under conditions of significant plasticity. Such parameters describe the mechanics of the crack affected by the applied load and the length of crack. The resistance of a particular material to fracture was the fracture toughness described by a single value of KI, or JI, at which fracture occurs in that material . However, in thin sections of tough metals, fracture was a clearly long-lasting process of deforming and tearing material ahead of the crack tip. This was characterized by a tearing resistance curve, being the function of the crack growth resistance (R) in a material against KI, or JI, known as a K-R or J-R curve, which captures the relationship between the crack tip stress and strain fields and the process of fracture for a particular metal. The balance between no fracture, stable fracture and unstable fracture was driven by the relative magnitudes of the stresses and strains ahead of the crack tip and the ability of the material to resist those stresses and strains . This was represented by a comparison of the stress intensity factor, or J-integral, for the cracked and loaded structure and the tearing resistance curve for the metal under consideration . No fracture occurred if the applied KI, or JI, was less than the $K_{material}$, or $J_{material}$, then the crack will not extend. Unstable fracture occurred when the applied KI, or JI, was higher than the $K_{material}$, or $J_{material}$, and the crack extended. Stable fracture was when the applied KI, or JI, was initially greater than the $K_{material}$, or $J_{material}$, and became less than the $K_{material}$, or $J_{material}$, as the crack extended then the crack arrested . It did not extend until the applied KI, or JI, was increased sufficiently for the material resistance to fracture to be overcome again.

Chinnasamy et al. [68] studied welded joints of components made of 2014-T6 alloys obtained by the pulsed CMT welding process. They reported that the defect-free weld was obtained under a constant WS of 450 mm/min, welding current of 110 A, and electrode feed rate of 5550 mm/min. The joint exhibited a maximum strength of 303 MPa, extending joint efficiency up to 67 %. It was mainly due to the welding wire pulsing and dip and retreat motion refining the dendritic grains in the weld metal and enhancing the strength of joints.

The CMT welding of 2A14 alloy in 3 mm thickness using ER2319 filler metal allowed obtaining joints with good quality under the welding current is 105 A and WS is 8 mm/s. The weld width and porosity gradually enhanced with the constant raising of welding heat input. The centre of the welded joint consists of many fine equiaxed dendrites, and the grey matrix is uniformly distributed accompanied by many dots and blocks as a white second phase, corresponding to the composition of the Al_2Cu phase. The microhardness of welded joints under various welding heat inputs was stable and exhibited a certain softening degree; the base material was the highest, followed by the heat-affected zone [181].

In case of 7475-T7351 alloy the CMT welds exhibited better mechanical properties as compared to those obtained with GMAW [182].

Tian et al. [183] reported that during CMT welding applied for aluminum alloy cladding fabrication, the enhancement of heat input caused the higher weld depth and contact angle, and lowered overlap length.

Summarizing, the lower volume of heat predestined the CMT welding for joining thin sheets and plates made of Al alloys [174,184] or from Al/steel [185].

 doi:10.20944/preprints202403.1458.v1

CMT technology is predestined not only for welding thin Al alloys, but also for welding of dissimilar metals such as Al alloy/steel and Al alloy/Mg alloy [185–188].

The use of CMT welding technique limits spatter, distortion of joints and requires limited clean up. CMT requires less current for the same amount of material deposition in comparison with conventional pulsed MIG welding [174].

In such a technique, the length of the arc can be monitored and can be controlled easily through mechanical means. Therefore, the stability of the arc is perfect, irrespective of the surface to be joined and during faster rate of joining, thereby making it possible to employ the technique of CMT welding in all position and for any application [185].

There are several types of recently developed types of CMT welding techniques namely CMT pulse advanced],[68] , CMT advanced, CMT + P, CMT Dynamic [189]. The conventional CMT, CMT pulse (CMT-P), CMT advanced (CMT-ADV) and CMT pulse advanced (CMT-PADV) are suitable process for depositing Al alloy due to the excellent performance in controlling porosity. Such depositing is applicable in modern additive manufacturing of Al alloys utilized also in the automotive industry [104,190].

According to [38] the Laser-CMT hybrid welding provides welds with better mechanical properties and aesthetics than the Laser welding and Laser-MIG hybrid welding.

4.3. Laser Welding

Bunaziv et al. [29] made an excellent review on laser beam and laser-arc hybrid welding of various Al alloys. They studied in detail solidification cracking, evaporation of alloying elements, porosity and keyhole stability, and weldability of such alloys.

Bergman et al. [191] noticed that the low absorption of laser radiation at a wavelength of 1064 nm and the high thermal conductivity hindered the effective laser welding of Al alloys including 5754 and 6016. According to Park and Rhee [192] in Al laser welding, the strength of weld is typically reduced by porosity, underfill, and magnesium loss. To overcome these problems, laser welded with filler wire is utilized.

Schempp et al. [193] noticed that refinement of the weld metal grain structure improved the mechanical properties of the weld and limited the susceptibility to solidification cracking of the weld metal. Using AlTi5B1 the refining by inoculation of the grain microstructure of laser beam LB and gas tungsten arc GTA Al welds, they limited the weld metal mean grain size, what by a transition from columnar to equiaxed grain structure columnar to equiaxed transition, CET occurred. The development of both grain size and shape was affected by the base metal (alloys 1050A, 5083 and 6082) and the welding process. The GTA welding process allowed a better refinement than in LB welds. The faster solidification of LB welds occurred than in GTA welds. Zhao and DebRoy [194] elaborated a numerical model for prediction of the keyhole geometry and the temperature profile, particularly the macro-porosity formation, during the laser welding of Al alloys. Based of knowledge that the weld metal with large pores when the welding mode changed from conduction to a keyhole mode or vice versa, the model allowed predicting the macro-porosity formation when the welding mode was caused by alteration in the process parameters.

Pastor et al. [195] investigated the porosity during the laser welding of Al alloys. They found that the macroporosity in the welds was caused by the instability of the keyhole. They explained that the too-quick collapse of the keyhole prevented the molten metal to flow into the center of the keyhole before the realization of solidification. The instability of the keyhole and the pore formation could be limited by controlling the laser beam defocusing and the WS. With respect to underfill, a recurrent defect occurred at the root of full-penetration welds.

Sheikhi et al. [196] studied the clear mechanism of the hot cracking phenomenon occurring during pulsed laser welding of 2024 alloy. The author explained that most forms of cracking were caused by the shrinkage strains occurring during the cooling down of the weld metal. The racing development was controlled by two opposing forces: the stresses generated by the shrinkage of the metal, and the surrounding rigidity of the base material. The shrinkage stresses are enhanced with the increase of the shrinking metal volume. The solidification rate affected the vulnerable zone length

 doi:10.20944/preprints202403.1458.v1

that controls the susceptibility to solidification cracking. A greater solidification rate caused a higher-volume change rate and a weakening vulnerable zone length enhancing the liquid flow rate. Therefore, for the removal of the solidification cracks, under the high solidification rate, a higher liquid flow rate or smaller vulnerable zone length was needed.

Yi et al. [197] studied the microstructure and texture of joints of plates made of 6016 and 5182 alloys obtained by the laser welding with wire under same welding process. They reported that the weld seams of 6016 and 5182 alloys comprised columnar dendrites and equiaxed dendrites and strong texture along the crystallographic direction <100> appeared in columnar dendrite area. Constitutional supercooling and heterogeneous nucleation affected together welded joints. As the heterogeneous nucleation strongly affected the 6016 alloy joint the ratio of the equiaxed dendrites in 6016 alloy was relatively high, the grain orientation randomly distributed, and the main texture of the columnar dendrites was the cube one (<100>{001}. While the heterogeneous nucleation slightly affected the 5182-alloy joint, the texture of the equiaxed dendrites distributed along <100> direction, the 5182-alloy joint mainly contained the columnar dendrites and the textures of the columnar dendrites were the fiber one <100>∥RD, the cube one (<100>{001}) and the Goss one (<100>{011}).

Sánchez-Amaya et al. [198] studied the effect of the laser power and the linear welding rate, on the sizes and properties of the butt weld beads made of the 5083-T0 and 6082-T6 alloys using a high-power diode laser. Maximum penetration values of 3 and 2.3 mm were obtained for 5083 and 6082, respectively. This was related to the thermal properties dependent on the total amount of alloying elements. The microstructure of the different beads was similar for both alloys and for all the studied conditions. The fusion zone had two zones, an external zone with a dendritic growth, and an inner part with fine precipitation of the second phases in a solid solution matrix of Al. In both alloys, the microhardness of the fusion zone was a little higher than that of the base metal surrounding the bead. The weld beads exhibited good corrosion resistance.

In the case of Al alloys 2xxx series, the one-sided laser welding heats the welding piece on one side, causing large deformation, sizeable residual stress, low penetration depth, and poor joint performance [87].

Zhu et al. [199] produced a joint of 2mm-thick components made of similar AA2219-O alloy in fiber laser welding, after which a combination of PWHT and electromagnetic (EM) pulse treatment was applied. This post-welded treatment provided joint efficiency exceeding 100%. Such a treatment lowered the occurrence of eutectic phases and promoted precipitation strengthening via dispersoids formation, i.e., G.P(II) zone and metastable θ" phase (Al2Cu). The joint hardness was higher than that in the BM. The tensile strength of 393 MPa after PWHT was reached, while that in BM was of 153 MPa, indicating its rise of 258%. After EM treatment, it further raised to 303%. The ductility (a decrease of area after tensile testing) lowered from 33% in the BM to 10% as-welded condition. Such ductility restored to 18% after PWHT, but down to 9–11% after EM treatment.

Wang et al. [200] obtained a joint of components made of 8 mm-thick similar alloy 5A06-H112 in fiber LBW. The WE reached up to 90%. Infinity-shaped oscillations (∞) with fiber LBW lowered porosity from 40% down to 2%. Simultaneously, weld elongation reached 90% of that in BM. The oscillations highly lowered penetration depth with a change from keyhole towards transition mode.

Peng et al. [201] produced a joint of components made of 35 mm-thick similar alloy 5A06 in fiber LBW under sub-atmospheric pressure. The WE at 10 Pa ambient pressure reached up to 90%, while at 1 atm up to 73%. The use of a sub-atmospheric pressure allowed enhancing mechanical properties of deep welds as a result of higher retained hardness in the fusion zone, lower porosity, lower evaporation of Mg, and more uniform grain distribution.

Braun [202] produced a butt joint of components made of similar 6013-T4/T6 alloy in the Nd:YAG LBW process with Al12Si wire and various atomized powders as filler material. The WE reached up to 75%. The welded joint was PWHTed which allowed enhancing WE up to 90%. No cracking appeared on the macro-level. In the as-welded condition for WM independently on tempering condition, similar hardness was obtained with softening (T6 for BM possessed 140 HV) except the weld obtained using AlSi12Mg5 powder. Hardness enhanced with the raising of Si with Mg content. Applied PWHT to the T6 condition restored low hardness in FZ but for WM low

 doi:10.20944/preprints202403.1458.v1

hardness persisted. Post-PWHT restoration in WM resulted from precipitation strengthening in α-Al dendrite cores comprising needle-shaped β" and Q' phases, aligned along <100> direction resulting from the Mg and Si enrichment from filler powder. The residual elements (Fe, Cu) harmful for mechanical properties appeared in the inter-dendritic area. The Al12Si was an optimum filler material compared to filler powders comprising Si with Zr, Mn, and Cr.

Zhang et al. [203] obtained a butt joint of 2 mm-thick components made of similar Al-Zn-Mg-Cu (0.23 wt.% Zr and 0.14 wt.% Er)-T6 alloy in fiber LBW. The welded joint was PWHTed (7–60 days) providing significant softening in WM and in HAZ closer to BM. The post PWHT WE reached up to 70%. Relatively small grains appeared near the fusion line, while the WM centre comprised equiaxed dendrites with higher grain sizes similar to BM. A strong segregation of alloying elements along grain boundaries appeared forming brittle T-phases comprising Al2Mg3Zn3. The matrix in WM exhibited a lack of Zn and Mg, inducing softening. A careful balance between heat input and response of alloying elements should be provided, which makes such alloys hard to weld.

Enz et al. [204] produced a T-joint of 2 mm-thick components made of dissimilar 7050/2023 alloys in the Fiber laser welding using 4047 wire. Helium as shielding gas allowed porosity suppression by lowering melt viscosity with improved degassing. The WE reached up to 90 % was achieved due to softening in welded zone and HAZ.

Viscusi et al. [205] obtained a T-joint of components made of dissimilar 3 mm-thick 6156/2.7 mm-thick 2139 alloys in Nd:YAG laser welding using 4047 wire. The WE reached even above 100 %. A little softening appeared in HAZ. The joint exhibited favourable strains distribution after welding in BM, not in softer HAZ.

Enz et al. [206] produced a butt joint of 2 mm-thick components made of dissimilar 7075-T6/5182-O alloys in Nd:YAG. LBW. A larger beam diameter (0.8 mm as focused) caused larger weld pool with improved degassing and low hydrogen (2 ppm). 7075-T6 alloy exhibited softening, while AA5182-O alloy possessed similar hardness in both WM and HAZ as BM. PWHT to T6 condition highly restored hardness similar to BM. The WE reached up to 118 %. Fracture appeared in BM of 5181 alloy, otherwise, fracture existed in the fusion zone resulting from discontinuities (undercut/underfills).

Bunaziv et al. [29] stated that the high thermal conductivity and reflectivity of Al alloys induce lower laser beam absorptivity with lower processing efficiency. Weld porosity, humping, and underfills often result from the low melting point and density promoting high liquidity with low surface tension. Porosity is the most persistent and it worsens mechanical properties. Laser beam welding (LBW) highly enhances productivity due to high penetration depths. Deep penetration keyhole mode may enhance productivity >10–20 times compared to conventional arc welding. However, welds are susceptible to cracking and porosity.

Bunaziv et al. [29] pointed out that both the process productivity and quality can be further improved using laser-arc hybrid welding (LAHW). Porosity can be minimized by optimizing process parameters, which is complex, especially for LAHW due to many adjustable parameters, sometimes interacting with each other and needing time to adjust. LAHW may be beneficial from the use of filler wire and wider process window through manipulation of heat inputs. Development of novel filler materials can provide enhanced strength and corrosion resistance. The use of novel technologies including laser beam oscillations, electromagnetic backing, shorter wavelength diode laser sources, grain refiners, and nanoparticles in filler wire may further improve the quality of welds. The use of a vacuum, although expensive can solve most processing problems highly enhancing productivity.

Summarizing, the laser welding technology are often used for joining Al alloys due to its adjustable heat input, high energy density, high accuracy, small deformation after welding, and small changes in structure, as was confirmed in [87].

The WE obtained using the laser welding process can exceed 100 %.

4.4. Laser-MIG Hybrid Welding

Laser-MIG hybrid welding links the advantages of both laser and MIG welding lowering residual stress and enhancing mechanical properties and efficiency. However, laser-MIG hybrid

 doi:10.20944/preprints202403.1458.v1

welding exhibited also cracks, porosity and coarse grains strongly affected the mechanical properties of welded joints ;[207–211].

Yan et al. [212] produced a defect-free joint of 8 mm-thick components made of similar 2A12 alloy (a Al-Cu-Mg alloy of 2xxx series, applied for truck wheels) in CO_2 laser-MIG hybrid welding using 2319 (Cu ~6 wt.%) wire, The joint efficiency reached up to 78 %. They observed the segregation of Cu/Si-rich precipitates on grain boundaries and in inter-dendritic areas causing intergranular fracture. The wire providing more Cu for the precipitates' formation allowed for obtaining higher strength. They suggested that the finer distribution of precipitates can be obtained by controlling welding parameters together with Cu-alloyed filler wire.

Ahn et al.; [213–215] obtained a butt joints of 3 mm-thick components made of similar 2024-T3 alloy in Fiber laser-MIG hybrid welding with different He–Ar shielding gas combinations and 4043 wire. The joint efficiency reached up to 86 %. They reported that He-rich shielding gas allowed obtaining wider welds with a lower undercut and underfill. HAZ softened up to 20 % as a result of the coarsening and dissolution of secondary phases under a low cooling rate. Weld metal strength was lowered by 30 % as a result of Mg evaporation and higher grain size. Some porosity and cracking appeared therein. The use of 4043 filler wire provided a little enhancement of the strength by lowering the crack sensitivity. The elongation with and without filler was of 24 %, 14.9 % for BM, and 3.7 % for weld, respectively. The next optimization of process parameters provided lowered crack sensitivity and higher stability through a combined application of a slightly defocused laser and lowering of both WS and heat input from the laser beam.

Yan et al. [216] produced a joint of components made of 4 mm-thick similar alloy 5083-H111 in Fiber laser-MIG hybrid welding using ER5356 wire. The joint efficiency reached up to 85 %. They observed lower softening in HAZ and WM compared to these of MIG. The HAZ width was 100 % narrower. Tensile strength was a little higher than that of MIG. Fatigue was improved but failure appeared as a result of porosity.

Similarly, Huang et al. [217] obtained a joint of components made of 10 mm-thick similar alloy 5083-H111 in Fiber laser-MIG hybrid welding using ER5356 wire. They also found softening in WM and HAZ. The applied laser setup provided uniformly dispersed Al6(Mn, Fe) secondary phases with a higher density of dislocations.

Leo et al. [218] produced a joint of components made of 3 mm-thick similar alloy 5754 in Fiber laser-MIG hybrid welding using ER5356 wire. The WE reached up 82%. The obtained weld was PWHTed at 35 °C for 50 min which allowed increasing of WE up to 98% close to BM with UTS of 244 MPa. It was due to eliminated softening by lowering segregation and restoration of the Mg solution strengthening mechanism.

Yan et al. [219] produced a joint of components made of 5 mm-thick components made of similar 6005-T5 alloy in Fiber laser-MIG welding using 5356 wire. The WE reached up to 74%. They found that the Fiber laser-MIG provided better results than MIG. The lowered joint efficiency resulted from the WM and HAZ softening (hardness lowered by 15%), porosity, larger grain size than BM, and losses of alloying elements (Mg, Mn) caused by the keyhole regime but lower than that obtained in MIG. LAHW provided a 100% narrower HAZ with lower decay in hardness compared to MIG.

Zhang et al. [220] obtained a butt joint of components made of 8 mm-thick components made of similar 6082-T6 alloy in Fiber laser-MIG welding using 5087 wire. They found equiaxed dendrites in the centre of WM which were twice smaller than those from pure MIG, 96 μm and 50 μm, respectively. Mg2Si phases re-precipitated due to a higher cooling rate during LBW. The strength lowered due to large pores in WM and coarsened precipitates to a size of 0.5–1.0 μm.

Yan et al. [221] produced butt joints of components made of 4 mm-thick components made of similar 6061-T6 alloy in Fiber laser-MIG welding using ER4043 wire. The WE reached up to 80%. They reported that LAHW using ER4043 filler wire provided higher weld strength resulting from smaller grain size with reprecipitation but lower fatigue due to microporosity compared to these in the case of using ER5356 filler wire.

Wang et al. [222] obtained a butt joint of components made of 3 mm-thick components made of similar 6061-T6 alloy in Fiber laser-TIG using ER5365 wire. The weld was PWHTed at 520 °C for 1 h

 doi:10.20944/preprints202403.1458.v1

which allowed reaching of the WE up to 87%. The weld high strength resulted from fine (nano-level) reprecipitation of β" phase with uniform distribution.

Hu and Richardson [223] produced a joint of 2 mm-thick components made of similar 7075-T6 alloy in Nd:YAG laser-MIG hybrid welding using 2319 wire. The weld joint was artificially aged at 120 °C for 24 h which provided a strength comparable to that of BM. The post-ageing WE reached up to 85 %. An intensive softening was obtained in an as-welded condition. Natural ageing (3 weeks) compared to 10-day artificial ageing only slightly improved the strength. Alloying elements were redistributed in dendritic structure along grain boundaries with depletion inside dendrite branches independently on PWHT type.

Ola and Doern [224] produced a joint of 6.3 mm-thick components made of similar 7075-T665 alloy in Yb:YAG laser-MIG hybrid welding using ER4043 wire. The laser-MIG provided much less HAZ cracking than the LBW using cold wire due to higher heat input inducing less tensile stresses on cooling. High cracking susceptibility in HAZ occurred. Post-welding natural ageing (5 weeks) restored hardness and provided WE of up to 85%.

Allen et al. [225] produced I-groove butt joints of 12.7 mm-thick components made of similar AA7xxx alloy in Fiber laser-MIG using 5556 wire. The WE reached up to 60%. LAHW provided level B quality with 0.3 % porosity resulted from cleaning parent material and application of low moisture shielding gas. The used filler wire provided very fine grains and enhanced mechanical properties. The tensile strength and elongation of the hybrid weld metal were a little lower than welds made by autogenous LBW. Weld metal was the least ductile zone resulting from the unfavourable microstructure comprising intensive micro-segregation and formation of inter-dendritic eutectic films.

According to [226] during hybrid laser-MIG welding of Al alloys, the intensity of evaporation of individual elements from the base metal and electrode wire, as well as the composition of the protective gas medium, highly influenced the passage of laser radiation to the metal welded. The use of Ar and high welding currents caused shielding of radiation and lowered the penetration depth. This effect can be limited using Ar/He mixtures or pure He to protect the weld pool, and the pulse modulation of laser radiation. Fir speeds in the range of 30-60 m/h, hybrid welding allows, compared to MIG, to enhance the WS of 6 mm thick metal by 80-160%, to lower the heat input into the welded metal by 30-60% times, and to highly lower the deformation of joints with a thickness of 4 mm. In hybrid welding of metal with a thickness of 6 mm or more using laser radiation with a power in range of 1-4 kW, the MIG method plays a leading role. Typical defects in hybrid welding of Al alloys including Al-Mg-Mn, Al-Cu-Mg and Al-Mg-Li have form of porosity and holes, which can be limited by the better protection of the weld pool and optimization of welding modes.

Hybrid Laser Beam Welding (HLBW) technology linking the advantages of laser welding with TIG was used for joining Al alloys. The use of Hybrid Laser Beam Welding enhanced the weld speed and improved weld penetration thus enhancing productivity and weld quality. The porosity formation is unavoidable in actual HLBW but controllable by adding a shielding gas unit, which is only accepted for required extremely high weld quality due to excessive costs. The HLBW of Al alloys exhibited high reflectivity which can be minimized by tilting the laser head to the needed degree of deviation but, this influences weld penetration [227].

4.5. The Laser -MIG Hybrid Welding Seems to be Particularly Useful for Some Al Alloys of 5xxx Series. Such a Technique Is Under Continuous Development Laser Mirror Imagewelding and Laser Impact Welding

During the laser mirror welding process, the symmetrical double laser heat sources act on the flat plate butt joint structure. The LMIW can realize the deformation-free and high-efficiency welding of thick plates. There are complex interactions of double keyholes and double-sided joint pools during the LMW process [7271].

Daehn and Lippold [220] explained that during LIW a focused laser beam ablated a sacrificial layer placed on the surface of a metal flyer foil. Rapid vaporization of such a layer generated a high-pressure plasma. By using a transparent overlay, the plasma was confined to further its pressure enhancement. The plasma produced shock waves and accelerated the flyer towards the target metal.

 doi:10.20944/preprints202403.1458.v1

Due to collision, jetting and interlocking of the foils appeared along a weld interface. The high-velocity gradients appeared amongst regions of the flyer foil upon laser incidence, affected by the spatial profiles of the laser beam and associated pressure pulse. The temporal profiles of the laser pulse and corresponding pressure load determined the nature of and time to impact during LIW.

Zhao et al. [239] studied the microstructure and mechanical properties of welding joints of components made of 5A06 alloy obtained using double-sided double-arc welding DSAW and laser-TIG LADSW double-sided welding joints. They found that the energy efficiency of LADSW exceeded that of DSAW. With the enhancement of laser power, the ratio of energy efficiency of LADSW to DSAW gradually raised. The tensile strength of the LADSW joints reached 365.1 MPa, and the elongation after breaking was of 9.0 %. The tensile strength and elongation at the break of DSAW joints were 327.8 MPa and of 5.5 %, respectively.

Qi et al. [88] studied the relationship between process parameters and weld bead formation for welded joints of components made of the 2219 alloy obtained using laser mirror welding. They reported that when the molten pool was formed, the stability of the keyhole was the worst, and the tensile performance was low. LMIWed joints are more uniform and symmetrical compared to those obtained with Laser double-sided asynchronous welding. The columnar crystals were formed at the interfaces of the two ends of the weld and the base metal. From the fusion line at the waist of the weld to the center of the weld, the size of the fine equiaxed dendrites gradually varied to coarse equiaxed ones. The tensile properties of LMIWed joints are affected by process parameters. Such properties first enhanced and then declined with an enhancement of the laser heat input. The LMIWed joint reached the highest tensile strength of 213 MPa under the laser power of 2.5 kW, and the WS of 2.0 m/min. Many pits appeared in the tensile joint fracture of a ductile nature. In addition, pore defects occurred in the tensile fracture morphology of the joints, induced by the instability of the keyhole during the welding process.

Summarizing the LMIW provides better joints' quality compared to those obtained using one-side laser welding [230,231].

Laser mirror welding is predestined to the flat plate butt structure. It provides high penetration depth, a small HAZ, good efficiency, small welding deformation, and slight post-welding residual stress. However, due to the unique structure of the flat butt joint, gravity affects the molten pool during welding impeding stability control of the latter, thus promoting defects such as welding pores, cracks, undercuts, etc. [7271].

Sadeh et al. [232] experimentally characterized spatial and temporal profiles of an Nd-YAG laser beam pressure pulse focusing on laser impact welding (LIW) simulation. LIW tests were conducted using standoff distances of 0.12, 0.26, 0.40, and 0.54 mm, as well as laser fluence values of 31.08 and 37.30 J/cm^2. Independently on the laser fluence value, sound welds were obtained only at standoff distances of 0.26 and 0.40 mm. The proper welds were obtained without spring-back in the central region. The strongest weld was obtained using a standoff distance of 0.26 mm and a laser fluence of 37.30 J/cm^2. In all tests, the failure appeared on the flyer (Al) side of the weld.

Wang and Gu [233] studied the effect of laser fluence on weld interface morphology during oblique LIW of 0.1 mm thick aluminum flyer foils to aluminum base foils of the 0.1 mm thickness. For similar metal couples (Al/Al), some uniform wavy structures occurred. The wavy morphology enhanced the direct contact area and facilitated interlocking between two metal surfaces providing strong bonding. The shock welding interface exhibited much higher hardness than the base metals. The tensed weldments exhibited limited shear strength after laser shock welding.

The laser-induced effects heavily depend on the laser spot size, laser wavelength, pulse duration, and the irradiated material [234].

Using the same laser pulse energy, laser impact generated ultrasounds or shock waves affected by the laser spot size, pulse duration, etc. Very good weld properties (for laser spot size of 6 mm and impact angle of 20 degrees) were obtained at laser fluences of 13.44, 14.15, and 14.85 J/cm^2 when they welded 0.05 mm thick sheets of aluminum and copper flyers to 0.1 mm thick sheets of aluminum base foils [235]. It was found that doubling and tripling the standoff distance between the foils raised the weld diameter by 50% and 83%, respectively.

 doi:10.20944/preprints202403.1458.v1

Summarizing, the laser shock welding is a process predestined for producing metallurgical bonds between both similar and dissimilar metal pairs.

4.6. Electron Beam Welding

Cam et al. [236] studied welded joints of plates made of different Al alloys: 2024, 5005, and 6061 obtained via electron beam EB welding for plate thickness of 5 mm except 3 mm for alloy 5005, to found the local microstructure–property relationships that would satisfy the service requirements for an electron beam welded Al alloy component with weld zone strength undermatching. Autogenous electron beam EB welding allowed obtaining defect-free welds of alloys 5005, 2024, and 6061. However, a low level of porosity occurred in most cases, which was acceptable for Al alloy weldments. An extremely low level of porosity was obtained in all EB welds owing to surface cleaning before welding and the vacuum environment of the EB welding process.

The Mg loss appeared in the fusion zone of all the joints during welding. No distinct heat-affected zone HAZ existed in the alloy 5005 joint, although a clear hardness minimum appeared in the HAZ region. For the alloy 6061 joint indicated an overaged HAZ region occurred. In the alloy 2024 joint, a narrow HAZ region with particle coarsening (overaged region) also existed. The fusion zone of the alloy 2024 joint exhibited columnar dendritic grain formation with uniformly dispersed particles, whereas the fusion zones of alloys 5005 and 6061 showed a dendritic solidification microstructure with isolated particles along the grain boundaries, as well as within the grains [236].

The EB welded joints possessed minimum hardness in the fusion zones (strength undermatching) due to loss of strengthening elements and/or phases (dissolution). Although the hardness minimum was in the HAZ region of the alloy 5005 joint, the hardness lowering in the fusion zone was not as significant as those in the other two joints. The coarsening of strengthening phases lowered the hardness in the HAZ regions . After transverse tensile test of autogenous EB welded joints, their strength slightly lowered and losses in ductility occurred for alloys 2024 and 6061, owing to strain concentration in the narrow, lower strength fusion zone (~2 mm in width), although the alloy 5005 joint had a relatively high ductility level, compared to the respective baseplate [236].

The fusion zone of the alloy 5005 joint, and both the fusion zone and HAZ of the alloy 6061 joint showed higher fracture toughness than that of the base material, and thus displayed higher resistance to stable crack growth. The fusion zone of the alloy 2024 joint showed similar or slightly lower fracture toughness values than those of the respective baseplate, whereas the HAZ region showed the lowest R curve behaviour [236].

Kim et al. [19] studied EB joint of 4.5 mm thick AA6061-T6 plates obtained at a traveling speed of 1200 mm/min, under the beam current of 35 mA and accelerating voltage of 60 kV in a vacuum of 10^{-3} Pa. They found that relative to the rolling directions of the tested specimens, the tensile strengths exhibited no difference between the longitudinal and transverse welds. The tensile fracture of the transverse welded specimens appeared in the base material zone far from the weld. The ductile fractured zone comprised only dimples with a micro-void coalescence. The joint efficiency of a longitudinal welded joint was of 85%, while that of a transverse welded joint was of 74%. The hardness distributions of the weld centerline for a square butt- welded zone were in the range of 61 to 70 VHN, whereas those for the heat affected zone were in the range of 75 to 87 VHN. It resulted from the welding heat cycle and the use of AWS 4047 filler material (Al-10%Si). The filler addition caused a higher hardness compared to the fusion welding joint due to the shear stresses induced by the tool motion, leading to a fine-grain structure.

Fujii et al. formation in [237] explained the mechanism of bubble generation during welding 2219 Al alloy using Electron beam (EB) welding and gas tungsten arc (GTA) welding in both terrestrial and microgravity environments. While hydrogen is the main source of the porosity in Al alloys, the bubbles are formed via a reaction between the molten Al and Al_2O_3 forming Al_2O. The pores are formed only in a vacuum, as during electron beam welding. The pores are distributed only in the upper part, while the pores due to hydrogen are widely distributed in the upper half. The pores are formed due to a chemical reaction at the highest temperature, and not due to the lowered solute species. The number of pores highly lowered under microgravity during EB welding, but it enhanced

 doi:10.20944/preprints202403.1458.v1

for GTA welding using a shielding gas containing hydrogen. The number of pores raised with the enhanced thickness of the oxide film.

Elseddig et al. [238] studied the effects of beam current, sweep size, WS, and focus position on the ultimate tensile strength (UTS) when welding AA1350 aluminum alloy with electron beam. They predicted the optimal arrangements of the welding parameters focused on the maximizing UTS of the weld joint.

According to [239] Electron beam welding (EBW) is advantageous compared to the other traditional fusion welding methods due to its high-energy density, deep penetration, large depth-to-width ratio and very small HAZ. The authors, using Taguchi method with grey relational analysis, optimized EB welded joint of 2219 alloy, from the yield strength, hardness, and bead geometry.

Using EBW Sobih et al. [240] obtained an acceptable joint of 2219 alloy. They reported that the EB cosmetic pass enables eliminating the undesired surface undercutting of the weld bead. The small beam diameter provided a distinguished weld zone with a full penetration depth and small bead width (3.51 mm). While the high heating and cooling rate during electron beam welding induced a small HAZ, an ultimate tensile strength of 295 MPa related to WE of 62% was obtained.

4.7. Resistance Spot Welding RSW

Al alloys possessing high electrical and thermal conductivity need higher current (2.5 to 3 times), and shorter weld time than steel. The resistance spot welding RSW of Al alloys required consistency of uniform pressure and current. During Al RSW welding the deterioration of electrodes may occur due to non-uniformity of pressure and current. Electrode erosion can also occur causing the formation of undersized welds avoidable by using proper surface coatings and treatments on electrodes [241].

Al easily reacts with oxygen in the atmosphere forming surface oxide films of high resistivity and corrosion protection ability, thus preventing forming of weld nugget in RSW [149].

Auhl and Patrick et al. [242] reported that breaking down of oxide film and proper weld nugget formation usually needed high electrode pressure. Additionally, the surface cleaned with chemicals allowed obtaining thinnest oxide layer elongating the electrode life [242–246].

The use of hybrid processes, such as the combination of ultrasonic waves or magnetic excitation can improve the weld nugget quality of RSW welded Al alloys. These allowed obtaining defect-free joints with good mechanical properties [247,248]. Resistance welding should be utilized for components made of alloy 7178 [249].

Resistance to general corrosion of the copper-free wrought 7xxx alloys is good, approaching that of the wrought 3xxx, 5xxx, and 6xxx alloys. The copper-containing alloys of the 7xx.x series, such as 7049, 7050, 7075, and 7178, have lower resistance to general corrosion than those of the same series that do not contain copper. All 7xxx alloys are more resistant to general corrosion than 2xxx alloys but less resistant than wrought alloys of other groups [250].

Fracchia et al. [251] studied welded joints of two sheets made of the 5454-alloy obtained with a resistance welding process. After a mechanical processing of lamination, they observed the presence of the defect. They reported the good mechanical properties of the joints while in the defect the oxide inclusions occurred. The authors noted that the mechanical properties of welded joints of Al and its alloys can be worsened due to gas porosity, oxide inclusions and oxide filming, solidification (hot) cracking or hot tearing, reduced strength in the weld and HAZ, lack of fusion, reduced corrosion resistance and reduced electrical resistance.

Matokhnyuk et al. [252] studied fatigue behaviour of welded joints of 40 mm plates made of 2219 alloy obtained using resistance butt welding and argon-arc welding, under symmetric and pulsating loading cycle. They found that at stresses exceeding the endurance limit, the fracture of specimens was of a multi-site nature and began from their surface. At stresses close to the endurance limit, the fatigue crack in the specimens fractured at a lower number of loading cycles and initiated from their surfaces and at longer lives, from subsurface fracture initiation sites. Under zero-to-tension loading cycles and the same heat treatment conditions, the endurance limit value of specimens made by resistance butt welding was close to that of specimens without weld and significantly exceeded

 doi:10.20944/preprints202403.1458.v1

that of specimens with argon-arc weld. For both types of welding, the fatigue cracks propagated via pores in the weld or in the heat-affected zone.

Bamberg et al. [92] reported that the cladding of various Al alloys is commonly used to improve the sheet weldability, simultaneously maintaining the structural performance. Such a cladding utilizes the combination of a high conductive, electric stable aluminium alloy as a covering sheet, with a high strength alloy as a core sheet. They evaluated the improved weldability of an AW-6111 (core sheet) cladded with an AW-4040 (cover sheet), affected by a proper welding lobe, the electrode erosion behavior, and the formed microstructure. Compared with a pure AW-6111 aluminum sheet the cladded sheets exhibited weldability characteristics and enhanced electrode service life.

Bamberg et al. [98] realized the RSW of AW-7075 free of welding discontinuities providing proper weld lobe, electrode cap durability and better microstructure characteristics. The welding was conducted using upslope welding current, CuAg0.1 electrode caps and higher electrode force. This lowered the temperature at the contact surface, limiting electrode erosion and a tendency for Cu–Al alloying. The quality of the welding and mechanical properties was high.

Summarizing, the cladding of various aluminium alloys is beneficial due to providing the better the sheet weldability, whilst maintaining the structural performance. According to [253] the high contact resistance caused by the oxide layer on the surface of Al alloys, and the required high welding current during RSW of Al alloys caused rapid electrode tip wear and inconsistency in weld quality. The cleaning of the oxide layer, sliding of a few microns between sheets, increasing the electrode force, and using a low-current pre-heating highly lowered the contact resistance and increased joint quality.

4.8. Friction Welding

Ochi et al. [254] studied the effect of heat input on performance of friction welded joints of 5056 alloy. The heat input for welding solid materials was classified into six categories, viz. friction heat input and deformation input during friction stage, upset stage and total stage. The authors found that the deformation heat input during the upset stage affected the joint performance, and the sound joints were obtained with the deformation heat input over 100 J/s. The sound joints were obtained with upset burn-off length over 2 mm.

Studying welding joints of dissimilar 5052 and 7075-T6 alloys obtained by FSW, FSP and RFSP, Jweeg et al. [109] found that the tensile strength for samples of FSP and RFSP were higher than that of FSW for all the TRSs of welding. The micro hardness values for all samples at the stir zone exceeded that of base metal of 7075-T6 and was lower than base metal of 5052, the hardness of FSP and RFSP for speed range of 710-1500 rpm was about 50 % higher than that of the metal of base for 7075.

Interestingly, the FSW is predestined for heat exchanges applied in the automotive industry, where porous cast components are often used. Such a process is also recommended for cast or extruded battery trays. 4.8.1. Friction stir welding

The main advantages of FSW, being a substantial phase operation are extremely very low distortion, absence of alloy related to deformation and high fabrication durability. Such a process is applicable for the fabrication of various joint types including butt, tap, T, spot, and fillet joints further weld hollow parts like a tank, tube, pipes, and stocks with different thicknesses. It is also utilized for welding tapered hollow sections and parts of three-dimensional shapes [255].

According to Patil et al. [256] the quality of the FSW of dissimilar Al alloys combinations was strongly affected by welding parameters including the BM placement, the TRS and WS. The placement of the BM drives material flow, while rotational and WSs affect heat input on both sides of the joint during welding. The welding parameters affected also the mechanical properties including the hardness and the joint strength. Some studies related to the effect of the placement of BM (i.e., a particular material is placed on the AS or the RS) on the material flow and the resulting microstructure in the SZ and the mechanical properties of the weld. The other authors investigated the influence of tool geometry including shoulder diameter to pin diameter ratio and pin profile (cylindrical, conical, polygonal) on the microstructure and mechanical features of the weld.

 doi:10.20944/preprints202403.1458.v1

4.8.1.1. Positioning of Alloy

The placement of the alloy strongly affected material stirring and mixing. Particularly, it can determine the final microstructure of joints made between Al alloys with significantly different mechanical properties [257,258]. The higher hot-strength material should be placed on the advancing side to enhance mechanical properties of the dissimilar joint [259–261]. Local weld temperatures were highest on the AS where the highest shear rates appeared.

Welded joints of components made: the first of 2024-T351/5083-H112 alloys and the second of 7075-T651/2024-T351 alloys (Table 3) studied by Niu et al. [262] contained 2024 and 7075 alloys placed on the AS while 5083 and 2024 alloys placed on the RS, respectively.

Studying an 2024/7075 joint Niu et al. [263] found that the top section of the SZ was composed of the BM of RS, whereas the middle and bottom sections of the BM of AS. Studying FSWed joints of 7075-T651/2024-T351 alloys (Table 3),) Hasan et al. [264] found that materials fixed location on the AS and RS of weld influenced the quality of joint, which was better in case when the softer base material was positioned on AS.

The proper FSWed joints of 7075-T6/2024-T3 alloys studied by Ge et al. [61] were obtained the 7075 and 2024 sheets were placed as upper sheet RS and lower sheet AS, respectively.

Studying FSWed joints of components made of 7075-T651/5083-H111 alloys (Table 3) Kalemba-Rec et al. [265] reported that at higher TRSs and in the configuration with 5083 on the AS and 7075 on the RS was accompanied with occurrence of porosity, voids, or wormholes in the stir zone. The highest tensile strength defect-free joint was obtained with 5083 on the advancing side, 7075 on the retreating side, a TRS of 280 rpm, and the Triflute pin. Then the WE reached above 100%. However, the effect of alloy location on the WE was rather small.

The proper FSWed joints of 2024-T4/7075-T6 alloys, studied by Safarbali et al. [266] were obtained when 2024 alloy was placed on AS while 7075 alloy was placed on RS of joint.

During studies of FSWed joints of plates of dissimilar 6351-T6/5083-H111 alloys Palanivel et al. [267] placed 6351 alloy on the AS and 5083 alloy on the RS. They observed that the tool shoulder increased the material transport at the top surface, from the RS to the AS, pushing it downward within the tool pin diameter.

During studies on FSWed joints of components made of dissimilar alloys 2017A-T451 and 7075-T651 Hamilton et al. [268] found that the 7075-alloy exhibited longer positron lifetimes than the 2017A alloy. The positron lifetime profiles across the weld comprised many local maxima and minima on the AS and RS, corresponding to the hardness behavior. Weld temperatures on the advancing side were greater compared to those on the retreating side promoting more precipitation on the AS away from the weld center. This behavior related to the higher positron lifetime on the advancing side compared to the retreating side, at the same distances from the weld center.

Studying FSWed joints of dissimilar 5052/Al-Mg_2Si alloys (Table 3), Huang et al. [269] utilized 5052 alloy on RS and Al-Mg_2Si one on AS. They observed that on the top of the RS and at the bottom of the AS, the weld nugget WN comprised no banded structure. Contrary, on the top of the AS and at the bottom of the RS, and at the center of the WN, a banded structure occurred. Such a band structure partly covering weld width extended from the AS toward the RS. A rich Al-Mg_2Si layer was formed at the weld top surface also of the RS. The interface between the 5052 alloy and the rich Al-Mg_2Si region at the bottom of the RS appeared as transitional layer with a thickness of 50 μm. The interface began from the RS at the top surface due to the materials on the RS were not driven to the AS. With enhancing distance from the top surface, the interface was located on the AS due to the materials on the RS were dragged to the AS.

Studying FSWed joints of components made of dissimilar 2024/6061 alloys (Table 3) Moradi et al. [270] found that the fraction of precipitates in the stirred zone of the retreating side exceeded that of the advancing side. The extent of continuous dynamic recrystallization in the thermo-mechanically affected zone TMAZ of the advancing side was less than that of the retreating side and the recrystallized grains seldom occurred on the advancing side. The initial texture components became asymmetric after FSW process. The overall texture intensity was weaker on the advancing side and stronger on the retreating side than that in the starting materials. The discontinuous static

 doi:10.20944/preprints202403.1458.v1

recrystallization and/or meta-dynamic recrystallization occurred on the advancing side. The microhardness profile on the advancing side was almost identical, while it comprised three distinguishable regions on the retreating side.

The FSWed joints of 6061-T6/6351-T6 alloys (Table 3) studied by Prasanth and Raj [271] were obtained for the cases where each of dissimilar 6061-T6 and 6351-T6 alloys was placed separately on the AS and the on the RS of joints.

Studying double-sided FSWed joints of components made of dissimilar 6082-T6/7075-T6 alloys (Table 3), Azeez and Akinlabi [178] reported that little abnormalities at the retreating side were caused by the pre-heating of the plates during the initial welding process.

In case of single-sided FSWed joints of components made of the same alloys Azeez and Akinlabi [272] reported that some microstructure imperfection occurred at the weld nugget when 6082 Al plates were clamped on the RS to the backing plate. However, deviation in the positioning of the Al plates prevented the fabrication of good bonding and quality welds despite the material flow and mixing occurrence.

The proper FSWed joints of rolled plates made of dissimilar 6061-T651/5A06-H112 alloys (Table 3), studied by Peng et al. [273] were obtained when 6061 alloy was placed on AS while 5A06 alloy was placed on RS of joint.

The correct FSWed joints of dissimilar 6101-T6/6351 alloys (Table 3), studied by Das and Toppo [274] were obtained when 6101 alloy was placed on AS while 6351 alloy was placed on RS of joint.

The proper FSWed joints of dissimilar 2024-T3/6063-T6 alloys (Table 3), studied by Sarsilmaz [275] were obtained when 2024 alloy was placed on AS while 6063 alloy was placed on RS of joint.

Studying FSWed joints of components made of dissimilar 2219-T87/2195-T8 alloys (Table 3), No et al. [276] found that the best joining properties were obtained for conditions including 600 rpm and 180-240 mm/min when the 2219-T8 alloy was on the RS.

During studies on FSWed joints of components made of dissimilar wrought 2017A/ cast AlSi9Mg alloys (Table 3), Kopyscianski et al. [277] reported that the AlSi9Mg alloy on the AS dominated the weld center. The local maximum on the AS was on the nugget side with a high density of the bands of the 2017A alloy.

The proper FSWed joints of dissimilar 5083-H12/6061-T6 alloys studied by Ghaffarpour et al. [278] were obtained when 6061 alloy was placed on AS while 5083 alloy was placed on RS of joints. The FSW joints possessed a much higher quality and improved mechanical properties than those obtained with TIG welding.

Studying the UFSWed joints of dissimilar alloys 6061 and 7075 Bijanrostrami et al. [279] placed 6061 alloy on the AS and 7075 alloy on the RS on top of a steel backing plate. The FSWed joints of dissimilar Al 6082-T6/5083-H111 alloys (Table 3), studied by Kasman et al. [280] were obtained when 6082 alloy was positioned on AS while 5083 alloy was positioned on RS of joints. The small cavity- and tunnel-type defects occurred at the nugget zone and were located on the advancing side of the pin. These defects lowered the strength and elongation of the weld joint.

The FSWed joints of the 6 mm thick sheets made of dissimilar 5083-H111/6351-T6 alloys (Table 3), studied by Palanivel et al. [[144] were obtained when 6351-T6 alloy was placed on AS, while 5083-H111 alloy was placed on TS of joint. Similarly, during studies presented in [183,187] 6351 alloy was placed on AS, while 5083-H111 alloy was placed on the RS of joint. The grain size within the friction stir processed (FSPed) region was much smaller than in the parent material due to the higher temperature and extensive plastic deformation. The grain size in the TMAZ clearly differed from that in the FSPed region.

FSWed joints of dissimilar 5052-H32/6061-T6 alloys (Table 3), studied by Doley and Kore [281] were obtained when 5052 alloy was placed on RS while 6061 alloy was placed on AS of the joints. The microhardness values of the dissimilar welds were lower at heat-affected zones HAZ on both the sides of weld line, whereas the lowest one occurred at HAZ of 5052 alloy.

During studies on the effect of shoulder diameter to pin diameter ratio on microstructure and mechanical properties of FSWed joints of dissimilar 2024-T6/7075-T6 alloys (Table 3), Saravanan et al. [282] placed 2024-T6 alloy on the AS, and 7075-T6 on the RS. They reported that the joints

 doi:10.20944/preprints202403.1458.v1

fabricated with the ratios of 2 and 2.5 fractured in heat-affected zone HAZ region of the advancing side, and joints fabricated with the ratios of 3, 3.5, and 4 fractured at stir zone SZ. For all the D/d ratios, minimum hardness was seen at HAZ region in the advancing side and was maximum in the SZ and again decreases at HAZ in the retreating side.

Studying FSWed joints of sheets made of dissimilar Al-Mg-Si/Al-Zn-Mg alloys (Table 3), Yan et al. [283] and [284]found that for the Al-Zn-Mg alloy positioned at the advancing side AS, the joints exhibited better fatigue properties caused by the bridging effect of the big secondary phase particles. For the Al-Zn-Mg alloy placed at the AS, there was limited movement of the Al-Mg-Si alloy material to the AS due to its easier flow. For the Al-Mg-Si placed at the RS, there was no RS material Al-Zn-Mg flow to AS due to the high resistance to flow of such a material.

The proper FSWed joints of dissimilar 2024-T3/6061-T6 alloys (Table 3), studied by Zapata et al. [285] were obtained when 2024 alloy was placed on AS while 6061 alloy was positioned on RS of joints.

Studying FSWed joints of the dissimilar UFGed 1050/ 6061-T6 alloys (Table 3), Sun et al. [286] reported that sound welds were performed at the wide revolutionary pitches from 0.5 to 1.25 mm/min, only when the 6061-T6 alloy was put on the AS. Otherwise, welds comprised the large defects formed in the softened 1050 Al side RS.

The proper FSWed joints of dissimilar 2024-T3/2198-T3 alloys (Table 3), studied by Texier et al. [287] were obtained when 2024-T3 and 2198-T3 sheets were on RS and AS of joints, respectively.

The correct FSWed joints of dissimilar 6061/7050 alloys (Table 3), studied by Rodriguez et al. [288] and [289] were obtained when 7050 alloy was positioned on AS while 6061 alloy was positioned on RS of joints.

The proper lap FSWed joints of dissimilar 6111-T4/5023-T4 alloys (Table 3), studied by Yoon et al. [47]. Two different joints, one with 6111 as the top plate RS and the other with 5023 as the top plate, were used.

Studying FSWed joints of the dissimilar 6061/5086 alloys (Table 3), Ilangovan et al. [290] placed 6061 alloy on the AS and 5086 alloy on the RS. They found that the AS of the thermo-mechanically affected zone AS-TMAZ was the softest region in the microhardness plot for both pin profiles including straight cylindrical STC one, threaded cylindrical THC one and tapered cylindrical TAC one. It was due to the dissolution of precipitates in the AS-TMAZ region because of the heating and cooling cycles prevailing during welding. Under tensile loading the strain localization occurred in such a region causing the failure therein. Only slight hardness variations appeared at the RS.

During studies on butt FSWed joints of components made of dissimilar 2050/6061 alloys (Table 3), Reza-E-Rabby et al. [291] found that joint quality, process parameters and welding temperature depended on material orientation in FSW. Defect-free welded joints with effective material transportation in the weld nugget zone were formed for 2050 on the advancing side. In the latter case, the tool was also less loaded by in-plane reaction force.

The proper FSWed joints of dissimilar 5083-O/6082-T6 alloys (Table 3), studied by Donatus et al. [292] were obtained when 5083 alloy was positioned on AS while 6082 alloy was positioned on RS of joints.

Studying FSWed joints of components made of dissimilar cast Al–Si alloys A319/A413 (Table 3), Karam et al. [293] obtained sound joints between the A319 and A413 plates, when A413 alloy was placed on AS while A319 alloy was placed on RS of joints. Each tensed welded specimen was fractured outside the welded regions at the A413 base metal placed on the AS.

The proper butt FSWed joints of dissimilar 7075-O/6061-O and 7075-T6/6061-T6 alloys (Table 3), studied by Ipekoglu and Cam [294] were obtained when 6061 alloy was placed on AS while 7075 alloy was positioned on RS of joints.

Studying the FSWed joints of dissimilar 6061-T6/ 7075-T6 alloys (Table 3), Cole et al. [295] reported that quality of welds was sensitive to alloy placement, tool offset, and tool–workpiece interface temperature. Under tensile loading, the welds failed in the heat-affected zone of 6061 on the AS of the weld. Weld tool offsets into the retreating side 7075 enhanced the tensile strength of the joint. The weld AS was hotter than the RS at both the tool shoulder and pin. There was a 20 °C

 doi:10.20944/preprints202403.1458.v1

enhancement in advancing-side shoulder interface temperature when offsetting from −2 to +2 mm, while a lesser enhancement appeared at the pin interface (~3 °C). The strongest welds (−2 mm offset) corresponded to the lowest temperatures on the AS.

During studies on lap FSWed joints of 5 mm thick sheets made of dissimilar 2024-T3/7075-T6 alloys (Table 3), Song et al. [296] found that the WS and joint combination affected the hook geometry which in return affected the lap shear strength. In all 2024/7075 joints, voids occurred, and the joints fractured from the tip of hook on AS along the SZ/TMAZ interface during lap shear test inducing tensile fracture mode. In 7075/2024 joints, the hook-on RS horizontally extended a long distance into the bottom stir zone at higher WSs. 7075/2024 joints exhibited greater failure load than 2024/7075 joints at lower WSs while the opposite trend occurred at higher WSs.

The proper FSWed joints of dissimilar 6061-T6/5083 alloys (Table 3), studied by Jannet and Mathews [297] were obtained when 6061 alloy was placed on the AS while 5083 alloy was placed on the RS of joints.

The correct FSWed joints of dissimilar 5083-H111/ 6351-T6 alloys (Table 3), Palanivel et al. [298] and [299] obtained when 6351 alloy was placed on the AS while 5083 alloy was placed on the RS of joint.

During studies on butt FSWed joints of plates made of dissimilar 2014-T6/ 6061-T6 alloys (Table 3), Jonckheere et al. [300] found that the alloys placement or tool lateral shift affected the welds hardness as they influence the precipitate radius and volume fraction. The 2014 alloy was successively placed on the RS and on the AS. More 2014 occurred in nugget zone if tool was shifted towards 2014 alloy on the AS.

Similarly, Jonckheere et al. [301] reported that material flow and joint quality, regardless of material placement, were affected by the welding conditions and their influences on heat input and weld nugget temperatures. If the 2014 alloy is placed on the AS of the weld, an abrupt transition between the weld nugget and the 6061-alloy appeared leading to premature fracture in tension.

The FSWed joints of the dissimilar A356/6061-T6 alloys (Table 3), studied by Ghosh et al. [302] and [303] were obtained when 6061 alloy was placed on the AS while A356 alloy was placed on the RS of joints. According to [302] low hardness of A356 alloy appeared at retreating side. The increment of hardness at AS was correlated to the higher strength of 6061 with respect to A356 alloy. It was due to a composite microstructure where both the alloys contributed appeared near weld line. As reported in [303] during welding, in front of tool, material got plasticized and transported from the RS to the AS.

During studies on FSWed joints of dissimilar Al alloys Koilraj et al. [304] found that the microstructures of the weld TMAZ on the AS exhibited highly deformed grains, with a clearly discernible SZ/TMAZ and TMAZ/HAZ boundaries. On the RS these boundaries were diffused, especially the latter. On the AS, there was a significant drop in hardness from the 2219 base material to the weld nugget boundary. On the RS, only slight drop in hardness appeared from the 5083-base material to the weld nugget boundary.

Studying the FSWed dissimilar cast and wrought 6061 alloy (Table 3), Dinaharan et al. [305] reported that the material location strongly affected the material flow behavior. The material in the advancing side occupied the major portion of the weld zone under enhanced TRS. The joint exhibited maximum tensile strength when cast Al alloy was positioned on the advancing side.

During studies on FSWed joints of dissimilar 5083-H111/6351-T6 alloys (Table 3), Palanivel et al. [306] reported that the transportation of plasticized material from AS to RS was uniform from top to bottom of the joint when straight pin profile tool was utilized.

The proper FSWed joints of dissimilar 5052-H34/5023-T4 alloys (Table 3), studied by Song et al. [127] were obtained when 5052 alloy was placed on the AS while 5053 alloy was placed on the RS of joints.

Studying FSWed joints for dissimilar 5052/A5J32 alloy sheets (Table 3), Kim et al. [307] obtained defect-free welds under all welding conditions with fixing the A5J32 alloy on the retreating side. However, for fixing the 5052 alloy on the retreating side, some welding defects occurred at the joint under certain welding conditions with a weakened heat input. Placing the high-strengthened Al alloy

 doi:10.20944/preprints202403.1458.v1

on the AS led to excessive agglomerations and defects due to limited material flow. Therefore, placing such a kind of Al alloy should be at the RS to limit the resistance to material flow.

The proper FSWed butt joints of dissimilar 7050-T7451/ 2024-T351 alloys (Table 3), studied by Prime et al. [308] were obtained when 2024 alloy was placed on the AS while 7050 was placed on the RS of joints.

Gérard and Ehrström [259] suggested that the material with the higher solidus temperature should be on the AS to improve joint quality and to eliminate internal defects/porosity.

During studies on the butt FSWed joints of dissimilar 2024-T351/ 6056-T4 alloys (Table 3), Amancio-Filho et al. [260] placed the 2024-T351 alloy on the AS as the stronger one from the alloys joined.

In case of FSWed joints of wrought 6061/ Al and A356 Al alloys (Table 3), Lee et al. [261] found that the joint properties are strongly affected by the alloy on the RS. The mechanical properties of the stir zone were greater when 6061 Al alloys were fixed at the retreating side. The WE was of 80% for similar A356 joint, and for the cases of dissimilar alloys of 83% for A356 on AS, and of 87% for A356 on the RS, respectively.

Liu et al. [57] studied the relations between welding parameters and tensile properties of the FSWed joints of components made of the 2017-T351 alloy (Table 3). The voids-less joints fractured near or at the interface between the weld nugget and the thermo-mechanically affected zone TMAZ on the advancing side.

Studying the FSWed joints of components made of 1050-H24 alloy (Table 3), Liu et al. [309] found that the location of the maximum strain gradually moved to the RS from the AS of the joint. Therefore, the fracture location of the joint gradually changed to the RS from AS of the joint as the WS gradually increased.

The FSWed joints of dissimilar cast AlSi9Mg (hypoeutectic silumin)/ 2017A alloys (Table 3), studied by Mroczka [310] were obtained when 2017A alloy was positioned on AS while AlSi9Mg alloy was positioned on RS of joints. During the process, the welding line was offset toward the advancing side, and an additional heat source was applied from the root side. Studying FSWed joints of components made of 2017A alloy (Table 3) Mroczka et al. [311] found that microhardness exhibited a tendency to grow on the advancing side of the joint.

The FSWed joints of dissimilar 7003/7046 alloys (Table 3), studied by Yang et al. [312] were obtained when 7003 alloy was placed on AS while 7046 alloy was placed on RS of joints. The hardness was much higher on the RS than that on the AS, and the average hardness difference between the two sides was about 30HV. After artificial ageing, the hardness enhanced significantly, while the hardness difference rose to about 50HV for the two sides.

Kasman and Ozan [313] studied butt FSWed joints of 6013 Al plates (Table 3) obtained via pin offset technique. The highest tensile strength equal to 206 MPa was obtained under 1.5 mm pin offset towards the advancing side and 500 min−1 TRS.

Zhao et al. [314] studied the influence of exchanging AS and RS side material on microstructure, mechanical properties, and electrochemical corrosion resistance for FSWed joints of components made of dissimilar 6013-T4/7003 alloys (Table 3). The joint with the 6013-T4 placed at the AS was called the A6R7 joint. Accordingly, the A7R6 referred to the joint with the Al7003 placed at the AS. The authors reported that various joint cross-sections appeared when exchanging AS and RS materials. The material on the AS was more deformed during the welding process. When the Al6013 was positioned on the AS, the plastic flow of the weld was enough. Independently on the AS or RS, the Al6013-T4 side was the weak region for both tensile strength and hardness.

For, lap FSW process when the rotation speed was low, and the WS was high, void-type defects appeared on the AS or center of the nugget [315].

Studying FSWed joints of 6061-T6 alloy (Table 3), Juarez et al. [316] reported that the surface fracture surfaces of tensile specimens, for the welding without heat treatment BMW and solubilized heat treatment and partial aging before welding HTBW cases, most of the fractures occurred on the AS of the tool and in the heat-affected zone. Fracture appeared on the unaffected material zone UFM and RS for the solubilized heat treatment and aging after welding HTAW case.

 doi:10.20944/preprints202403.1458.v1

Godhani et al. [317] obtained proper butt joints of dissimilar 6061-T6/ 7075-T6 alloys (Table 3) when 6061 alloy was placed on the AS, while 7075 on the RS of the joint.

Investigating FSWed joints of components made of dissimilar 5052/ and 6061 alloys obtained with various pin-eccentric stir tools (the pin eccentricities of 0, 0.4, and 0.8 mm, respectively), Chen et al. [318] found that sound joints were obtained for the 6061 alloy on the AS.

Zhang et al. [319] studied the FSWed joints of 5 mm thick 7075AA7075-T651/2024 and AA2024-T351 similar and dissimilar alloys obtained using tool with cylindrical taper threaded pin, shoulder diameter of 15 mm, pin diameter 3.76 mm on the insertion side and of 6.66 mm on the shoulder side, pin length of 5 mm under TRS of 600, 950, 1300 and 1650 rpm, WS of 100 mm/min, tilt angle of 2.5 degrees. They found that the width of the TMAZ on the RS is greater than that of the AS.

Material flow under specific welding conditions was the common thread among the authors, with material placement close, but distinguishably secondary. Various configurations of FSW joints of various Al alloys were presented by Patel et al. [256].

Table 3. Configurations of FSW joints of various Al alloys.

Refs.	Configuration	Alloy Combinations	Thick (mm)	Alloy Positioning	
				AS	RS
262	Butt	2024-T351/5083-H112	6.35	2024	5083
262	Butt	7075-T651/2024-T351	6.35	7075	2024
264	Butt	7075-T651/2024-T351	6	Both	Both
265	Butt	7075-T651/5083-H111	6	Both	Both
265	Butt	5052/$AlMg_2Si$	8	Al-Mg_2Si	5052
270	Butt	2024-T351 /6061-T6	6	2024	6061
271	Butt	6061-T6/6351T6	6.35	Both	Both
272,328	Butt	6082-T6/7075-T6	10	7075	6082
273	Butt	6061-T651and 5A06-H112	5	6061	5A06
274	Butt	6101-T6/6351-T6	12	6101	6351
275	Butt	2024-T3/6063-T6	8	2024	6063
276	Butt	2219-T87/2195-T8	7.2	Both	Both
277	Butt	2017A-T451/cast AlSi9Mg	6	2017A	AlSi9Mg
280	Butt	5083-H111/6082-T6	5	6082NR	5083NR
144	Butt	5083-H111/6351-T6	6	6351	5083
144	Butt	5083-H111/6351	6	6351	5083
282	Butt	2024-T6/7075-T6	5	2024	7075
283,284	Butt	Al-Mg-Si/Al-Zn-Mg	15	Both	Both
286	Butt	UFG 1050/6061-T6	2	Both	Both
287	Butt	2024-T3/2198-T3	3.18	2198	2024
288,289	Butt	6061-T6/7050-T7451	5	7050	6061
290	Butt	5086-O/6061-T6	6	6061	5086
291	Butt	2050-T4/6061-T651	20	Both	Both
292	Butt	5083-O/6082-T6	NR(~7)	5083	6082
293	Butt	A319/A413 cast	10	A413	A319
294	Butt	7075-O/6061-O 7075-T6/6061-T6	3.17	6061	7075
295	Butt	6061-T6/7075-T6	4.6	Both	Both
297	Butt	5083-O/6061-T6	6	6061	5083
302,303	Butt	A356/6061-T6	3	6061	A356
304	Butt	2219-T87/5083-H321	6	2219	5083
305	Butt	6061 cast/6061 rolled	6	Both	Both

 doi:10.20944/preprints202403.1458.v1

306	Butt	6351-T6/5083-H111	6	6351	5083
127	Butt	5052-H34/5023-T4	~1.5	5052	5023
307	Butt	5052-H34/5023-T4	1.5 & 1.6	Both	Both
308	Butt	7050-T7451/2024-T351	25.4	2024	7050
260	Butt	2024-T351/6056-T4	4	2024	6056
261	Butt	cast A 356/6061	4	Both	Both
57	Butt	2017-T351	5	Both	Both
309	Butt	1050-H24	5	Both	Both
310	Butt	2017A-T451/AlSi9Mg	6	2017A	AlSi9Mg
311	Butt	2017A	6	Both	Both
312	Butt	7003-T4/7046-T4	3	7003	7046
314	Butt	6013-T4/7003	2.8	Both	Both
313	Butt	6013-T6	5	Both	Both
316	Butt	6061-T6	9.5	Both	Both
317	Butt	6061-T6/7075-T6	6	6061	7075
279	Underwater Butt	6061-T6/7075-T6	5	6061	7075
46,268, 326	Butt NA Butt	2017A-T451/ 7075-T651	6	Both	Both
298,299	NA Butt	6351-T6/5083-H111	6	6351	5083
300,301	NA Butt	2014-T6/6061-T6	4.7	Both	Both
278	NA	5083-H12/6061-T6	1.5	6061	5083
285	NA	2024-T3/6061-T6	4.8	2024	6061
281	NA	5052/6061	1, 1.5	6061	5052
266	NA	2024-T4/7075-T6	4	2024	7075
267	NA	6351-T6/5083-H111	6	6351	5083
315	Lap	6111-T4/5023-T4	1	Both	Both
296	Lap	2024-T3/7075-T6	5	Both	Both
47	Lap	6111-T4/5023-T4	1	Both	Both
61	Lap	7075-T6/2024-T3 7075-upper; 2024-lower	3	2024	7075

It can be notice that the material position (AS/RS) plays significant role in FSW process, particularly in the case of dissimilar Al alloys. The placement of harder material in the AS, for both butt and to a lesser extent lap configuration, provides better joints' quality. It is in agreement with observations from [320].

4.8.1.2. Tool Rotation and Welding Speeds

The tool rotation speed influenced the intensity of plastic deformation and thus material mixing. Kalemba-Rec et al. [265] found that material mixing was proportional to the tool rotation speed for a dissimilar 7075-5083 joint. Under high tool rotation speeds numerous imperfections including poor surface (flash), voids, porosity, tunneling or formation of wormholes occurred due to the excessive heat input [322,323] Low WSs enhanced heat input and are often accompanied by defects such as tunneling [297,302,321,324,325].

Obtaining defect-free joint with a good metallurgical bond and mechanical properties needs the selection of the appropriate/optimized combination of tool rotation and WS, particularly for combinations of dissimilar Al alloys [271,276,278,279,281,285,286,293,297,298,302–304]. Welded joints of components made: the first of 2024-T351/ 5083-H112 alloys and the second of 7075-T651/ 2024-T351 alloys (Table 4), studied by Niu et al. [262] were obtained under TRS of 600 rpm and WS of 150 mm/min, respectively.

 doi:10.20944/preprints202403.1458.v1

The proper FSWed joints of 7075-T651/2024-T351 alloys (Table 4), studied by Hasan et al. [264] were obtained under TRS of 900 rpm and WS of 150 mm/min.

Ge et al. [61] studied how EST affects the shear failure load of lap joints. Shear fracture mode occurred in lap joints obtained with a small (3-mm) pin at all WSs. The higher TRS, lower WS, and bigger plunge depth improve the diffusion bonding strength of lap joint. The lap shear failure load decreased with the increase of WS, due to worsened diffusion bonding induced by lower heat input. The highest lap shear failure load with a small pin was obtained at WS of 60 mm/min.

Studying FSWed joints of components made of 7075-T651/ 5083-H111 alloys (Table 4), Kalemba-Rec et al. [265] reported that at higher TRSs and in the configuration with 5083 on the advancing side and 7075 on the retreating side was accompanied with occurrence of porosity, voids, or wormholes in the stir zone. The highest tensile strength defect-free joint was obtained for a TRS of 280 rpm. The higher TRS at a constant traverse speed caused the lower joint efficiency.

Saeidi [324] found that an enhancement in TRS from 450 to 800 rpm, at a selected WS (30, 41.5, or 50 mm/min) initially lowered and then enhanced the joint efficiency.

The proper FSWed joints of 2024-T4/ 7075-T6 alloys (Table 4), studied by Safarbali et al. [266] were obtained under TRS of 1140 rpm, and WS of 32 mm/min.

Palanivel et al. [267] conducted studies on FSWed joints of components made of dissimilar 6351-T6/ 5083-H111 alloys (Table 4) focusing on optimization of, inter alia, TRS and WS. The WE reached up to 78.7% for the full impeller shoulder tool, WS of 60 mm/min and TRS of 1000 rpm.

For study on FSWed sheets made of dissimilar alloys 2017A-T451 and 7075-T651 Hamilton et al. [326] obtained qualitied welds using a tool positioned with the tool tilt angle of 1.5 deg. The TRS and WS were 355 rpm and 112 mm/min, respectively, and the applied force during processing was of 32.8 kN.

Gupta et al. [327] conducted studies on FSWed joints of components made of dissimilar 5083-O and 6063-T6 alloys focusing on optimization of tool geometry, TRS, and WS. The multi-optimal set of weld properties comprising tensile strength, average hardness at weld nugget zone, the set of process parameters and average grain size at weld nugget zone was obtained for 900 rpm of TRS, 60 mm/min of WS. The WE reached up to 76.4%.

Huang et al. [269] quoted that for Al metal matrix composites MMCs, the material flow depended on the rotation speed and the reinforcing phases. The welding of Al-Mg/ Al-Mg_2Si alloys (Table 4) also depended on the hard and brittle intermetallic compounds of the primary Mg_2Si phases in Al-Mg_2Si alloys.

The proper FSWed joints of dissimilar 2024/6061 alloys (Table 4), studied by Moradi et al. [270] were obtained under a TRS of 800 rpm and WS of 31.5 mm/min.

The FSWed joints of dissimilar 6351-T6/ 6061-T6 alloys (Table 4), studied by Prasanth and Raj [271] were obtained under TRS values of 600, 900, and 1200 rpm, and WS values of 30, 60, and 90 mm/min. The highest WE was obtained for TRS of 900 rpm, WS of 60 mm/min and axial force of 6 kN.

The proper FSWed joints of dissimilar 6082-T6/ 7075-T6 alloys (Table 4), studied by Azeez et al. [272,328] were obtained under TRS values of 950, and 1000 rpm, and WS values of 80 and 100 mm/min.

Peng et al. [273] studied FSWed joints of rolled plates made of dissimilar 6061-T651 and 5A06-H112 alloys (Table 4), obtained for various rotation speeds and transverse speeds. With the increase of rotation speed, more heat was generated during FSW. The increasing of heat input could enlarge the size of HAZ and reduce the slant angle of HAZ and thus lead the fracture angle to decrease and cause the dimples change from inclined ones to normal ones.

Studying FSWed joints of plates made of dissimilar 6101-T6/ 6351-T6 alloys (Table 4), Das and Toppo [274] found that with an enhancement of the TRS the impact strength behavior pointed to a high change in mechanical properties. The impact test samples exhibited a ductile fibrous fracture.

Investigating FSWed joints of components made of dissimilar 2024-T3/6063-T6 alloys (Table 4), Sarsilmaz [275] found that micro-structural and mechanical properties were strongly affected by variations in welding parameters within the chosen range of welding conditions. Under lower

 doi:10.20944/preprints202403.1458.v1

rotational and higher traverse speed in all welding conditions, the Wohler curves exhibited maximum fatigue strength.

Studying FSWed joints of components made of dissimilar 2219-T87/2195-T8 alloys (Table 4), No et al. [276] found that the WS only slightly affected the properties of the joint, but the latter strongly depended on the TRS.

Kopyscianski et al. [277] obtained high weld quality for the process parameters including WS equal to 112 mm/min, TRS equal to 355 rpm and vertical force equal to 32.8 kN (Table 4).

The proper FSWed joints of 5083-H12/ 6061-T6 alloys (Table 4), studied by Ghaffarpour et al. [278] were obtained under TRS values in the range of 700–2500 rpm, and WS values in the range of 25–400 mm/min.

Studying the underwater FSWed joints of dissimilar 6061/7075 alloys (Table 4), Bijanrostami et al. [279] found that the maximum tensile strength of 237.3 MPa and elongation of 41.2% were reached under a TRS 1853 rpm and a traverse speed of 50 mm/min. Thus, the WE reached up to 76.5%.

Studying the effect of the TRS to WS ratio (υ ratio) on the strength of the FSWed joints of dissimilar 6082-T6/5083-H111 alloys (Table 4), Kasman et al. [280] found that nugget zone profile containing onion rings of the shape depended on the value of the TRS and WS. These speeds varied also the effect of a constant υ ratio on the profile and structure of the nugget zone. At a lower TRS and WS lower UTS values occurred.

Studying FSWed joints of dissimilar 5083-H111/6351-T6 alloys (Table 4), Palanivel et al. [144] reported that a low WS and a high TRS enhanced the frictional heat because of the enhanced residing time of tool. TRS caused stirring and mixing of the material about the rotating pin, which in turn enhanced the temperature of the metal. Thus, the TRS strongly affected the WS. A low TRS providing a low heat input led to a lack of stirring and yielded defects. Contrary, during FSW, the enhancement in the TRS caused an increase in the heat input. More heat input destroyed the regular flow of plasticized material, and an enhanced TRS induced the excessive release of stirred materials to the upper surface, which left voids in the weld zone. The lowest and highest WS produced defects due to the increased frictional heat and insufficient frictional heat generated, respectively. The FSW at higher WSs caused a short exposure time in the weld area with insufficient heat and poor plastic flow of the metal and produced defects in the joints. Higher WSs causing low heat inputs provided faster cooling rates of the welded joint and hence yields defects.

The proper FSWed joints of 6 thick dissimilar alloys 6351/ and 5083-H111 alloys (Table 4), studied by Palanivel et al. [281] were obtained under TRS of 950 rpm, WS of 1.0 5mm/s and axial force 10kN.

Studying FSWed joints of components made of 5052-H32/6061-T6 blanks (Table 4), Doley and Kore [282] found that for all thicknesses, weld produced at 63 mm/min speed exhibited more ductility compared to that produced at 98 mm/min.

Saravanan et al. [283] reported that the maximum tensile strength of 356 MPa appeared with the D/d ratio of 3, TRS of 1200 rpm, WS of 12 mm/min, and axial load of 8 kN (Table 4).

Yan et al. [283,284] obtained proper FSWed joints of sheets made of dissimilar Al-Mg-Si/Al-Zn-Mg alloys (Table 4) under TRS equal to 800 rpm and WS equal to 180 mm/min.

Studying FSWed joints of components made of dissimilar 2024-T3/6061-T6 alloys (Table 4), Zapata et al. [285] found that the enhancement of the TRS decreased the magnitude of the longitudinal residual stresses. This was due to the rise of heat input and the weakening of thermal mismatch between the different zones of the weld. The effect of the WS on the residual stress was small in comparison to the effect of the TRS, generating only a small rise in the profile of the retreating side when it was enhanced.

Studying butt FSWed joints of 2 mm thick plates including the one rolled from ultrafine-grained UFGed 1050 alloy and the one made of the 6061-T6 alloy (Table 4), Sun et al. [193] found that at various WSs, two fracture modes occurred for the tensed specimens depending on their revolutionary pitches. The FSWed joints were obtained under TRS of 800 rpm and WS values of 400, 600, 800, and 1000 mm/min.

 doi:10.20944/preprints202403.1458.v1

From a second source of information, studying the butt FSWed joints of the ultrafine grained UFGed 1050 Al plates with a thickness of 2 mm with the 2 mm thick 6061-T6 alloy plates (Table 4), Sun et al. [286] reported that after welding process under a revolutionary pitch varying in range from 0.5 to 1.25 mm/rev, in the joint stir zone, the initial nano-sized lamellar structure of the UFGed 1050 Al alloy plate changed into an equiaxial grain structure with a greater average grain size as a result of the dynamic recrystallization and subsequent grain growth. An equiaxial grain structure with a lower grain size simultaneously appeared in the 6061 alloy plates, together with coarsening of the precipitates.

The proper FSWed joints of 2024-T6/ 6061-T6 alloys (Table 4), studied by Sun et al. [329] were obtained under TRS of 1000 rpm, and the WS of 500 mm/min.

During studies on butt FSWed joints of components made of dissimilar 6061 and 7050 alloys Rodriguez et al. [289] found in joints microstructure occurred distinct lamellar bands and various degrees of intermixing affected by TRS. The joints consistently fractured on the 6061-alloy side. Two modes of failure existed, one through the stir zone and the other through the heat-affected zone. The inadequate material intermixing produced at low TRSs induced low mechanical strength and failure through the stir zone. The failure through the heat-affected zone at high TRSs occurred due to the material softening. Studying FSWed joints of components made of dissimilar 6061 to 7050 high strength Al alloys Rodriguez et al. [288] found that the cyclic strain hardening and the number of cycles to failure enhanced with increasing the TRS.

The proper butt FSWed joints of dissimilar 6061/7050 alloys (Table 4), studied by Rodriguez et al. [288] and [289] were obtained under TRS values of 270, 340, 310 rpm, and WS of 114 mm/min.

The lap FSWed joints of plates made of dissimilar 6111-T4/ 5023-T4 alloys (Table 4), studied by Yoon et al. [47] were obtained with a revolutionary pitch of 0.067 mm/rev, with an onion ring nugget with a rotation speed of 1500 rpm and a WS of 100 mm/min, and a revolutionary pitch of 0.7 mm/rev, with a void-defect nugget with a TRS of 1000 rpm and a WS of 700 mm/min.

Ilangovan et al. [290] reported that all three pin profiles yielded the surface defect free joints with TRS of 1100 rpm and WS of 22 mm/min (Table 4), as then the heat generation was almost the same for those tool pin profiles.

During studies on butt FSWed joints of components made of dissimilar 2050/ 6061 alloys (Table 4). Reza-E-Rabby et al. [291] found that quality welds can be produced at low rotational and travel speed. Flats could not produce defect free welds at the highest WS.

The proper FSWed joints of dissimilar 5083-O and 6082-T6 alloys (Table 4), studied by Donatus et al. [292] were obtained under TRS of 400 rpm, and WS of 400 mm/min.

The FSWed joints of dissimilar cast Al–Si alloys A319, A413 (Table 4), studied by Karam et al. [293] were obtained under rotational values of 630, 800, 1000 rpm, and WS values of 20, 40, 63 mm/min. The average size of the Si particles and of α-Al grains enhanced with a rise of the TRS and/or lowering of the WS. At the center of stirred zone, the Si particles were more uniformly distributed at low welding or high TRSs than in the case at higher welding or lower TRSs. The average hardness of the welded regions enhanced with the rise of the WS and/or lowering the TRS.

The butt FSWed joints of dissimilar 7075-O/6061-O and 7075-T6/6061-T6 alloys (Table 4), studied by Ipekoglu and Cam [294] where obtained under TRS values of 1000 and 1500 rpm, and WS values of 150 and 400 mm/min. The enhancing rotational rate raised the amount of the RS base material BM in the DXZ microstructure.

Cole et al. [295] found that the highest joint strength was achieved at 700 rev/min spindle speed and 100 mm/min weld speed with 7075-T6 on the retreating side (Table 4). The highest value of weld interface temperatures was obtained for the low tool travel speed value equal to 100 mm/mm.

During studies on lap FSWed joints of 5 mm-thick sheets made of dissimilar 2024-T3/ 7075-T6 alloys (Table 4), Song et al. [296] found that the hook deflects significantly upwards into the stir zone SZ at lower WSs in both combinations. The WS and joint combination affected the hook geometry which in return affected the lap shear strength. In both joint combinations, the lap shear strength raised with the enhancement of WS. 7075/2024 joints exhibited greater failure load than 2024/7075 joints at lower WSs while the opposite trend occurred at higher WSs. In case of 2024/7075 joints the

 doi:10.20944/preprints202403.1458.v1

WE varied in the range of 15-39% dependent on the WS in the range of 30-300 mm/min. The WE reached up to 57% under the WS of 150 mm/min for the case of 7075/2024 joint.

The proper FSWed joints of dissimilar 6061-T6/5083-0 alloys (Table 4), studied by Jannet and Mathews [297] were obtained under TRS values of 600, 750, 900, and WS of 60 mm/min.

The FSWed joints of 5083-H111 and 6351-T6 alloys studied by Palanivel et al. [298] were obtained under TRS of 950 rpm, and for three values of WS including 36, 63, and 90 mm/min. The WS of 63 mm/min provided the best quality of welds.

The butt FSWed joints of dissimilar 2014-T6 and the 6061-T6 alloys studied by Jonckheere et al. [300] were obtained under TRS values of 500, 1500 rpm, and WS of 90 mm/min. Welds obtained under a TRS of 500 rpm containing more 2014 alloy in their stirred zone or in contact with the tool shoulder were cooler and presented a narrower softened zone. Welds obtained under a TRS of 1500 rpm exhibited no effect of the tool shift or the alloys placement on their hardness profile.

Palantivel et al. [299] reported that the joints exhibited better tensile strength using straight square pin profiled tool with TRS of 950 rpm, WS of 63 mm/min and axial force of 14.7 kN (Table 4). The axial force acting on the tool most contributed on the UTS, and it was followed by tool pin profile, WS and TRS, for the range considered. The WE can reach up to 88.6%.

Studying FSWed joints of components made of dissimilar A356/ 6061 alloys (Table 4), Ghosh et al. [302] reported that with an increase in WS, matrix grain size became finer, without incessant limiting of Si-rich particles' size affected by interaction time between tool and substrate. The maximum joint efficiency of 116 % with respect to that of 6061 alloy occurred at an intermediate tool-traversing speed, providing fine matrix grain size and a small size of Si-rich particles.

The lap FSWed joints of 7075-T6/ 2198-T351 alloys (Table 4), studied by Velotti et al. [330] were obtained under a TRS of 830 rpm, and a WS of 40 mm/min. The WE was quite low in comparison to that obtainable the butt FSWed joints of the same alloys' pair.

Studying FSWed joints of plates made of dissimilar 2219-T87/ 5083-H321 alloys (Table 4), Koilraj et al. [304] found WS strongly affected the joint soundness. The welds were obtained under TRS values in range of 400-800 rpm, and WS in range of 15-60 mm/min. The WE reached up to about 90%.

Investigating the FSWed dissimilar cast and wrought 6061 alloy (Table 4), Dinaharan et al. reported [305] that the material location prior to welding and TRS strongly affected the material flow behavior. The material in the advancing side occupied the major portion of the weld zone under enhanced TRS. The joint exhibited maximum tensile strength when cast Al alloy was positioned on the advancing side at all TRSs.

Studying of FSWed joints of components made of dissimilar 5083-H111/ 6351-T6 alloys (Table 4), Palanivel et al. [306] reported that the TRS and pin profile influenced the joint strength because of varying material flow, loss of cold work in the HAZ of 5083 side, dissolution and over aging of precipitates of 6351 side and formation of macroscopic defects in the weld zone. They found that an increase in TRS (from 600 to 1300 rpm) at a constant traverse speed of 60 mm/s, for various pin geometry, initially enhanced and then lowered weld effectiveness. The weld fabricated using TRS of 950 rpm and straight square pin profile reached its efficiency up to 88.6%.

Sivachidambaram et al. [341] reported three various relations between TRS and joint efficiency for various WSs (40, 60, and 80 mm/min). The FSWed joints of dissimilar 5052-H34/ 5023-T4 alloys (Table 4), studied by Song et al. [127] were obtained under TRS of 1500 rpm, and WS values in range of 100-700 mm/min.

Ghosh et al. [303] reported that tool rotation and traversing speed significantly affected the microstructure of welds. Welding at low TRS and WS caused the generation of fine grain size of 6061 alloy near the interface, limited residual thermal stress, lowered the extent of recovery–recrystallization, enhanced defect density, promoted the finer distribution of Si-rich particles and increased consolidation of transported material at the back of the tool to eliminate discontinuities within weld nugget. The welds fabricated at the lowest tool rotational and traversing speed exhibited the best mechanical properties. The 80 mm/min tool-traversing speed was optimal to achieve joint efficiency of ~116% with respect to that of 6061 Al alloy.

 doi:10.20944/preprints202403.1458.v1

The FSWed joints of dissimilar 5052/ A5J32 alloys (Table 4), studied by Kim et al. [307] were obtained under TRS values of 1000, and 1500rpm, and WS values of 100, 200, 300, and 400 mm/min. In the case where A5J32 was fixed on the RS, the highest strength of the welded joints appeared under conditions of 1000 rpm and 300 mm/min. The WE reached up to about 94 %.

The proper FSWed butt joints of 7050-T7451/ 2024-T351 alloys (Table 4), studied by Prime et al. [308] were obtained under WS of 50.8 mm/min.

The correct FSWed joints of dissimilar 5182-O, 5754-O, and 6022-T4 alloys (Table 4), studied by Miles et al. [332] were obtained under rotation speed values in range of 500 to 1500 rpm, and WS values in range of 130 to 400 mm/min.

The proper butt FSWed joints of 6061-Al as itself, and of dissimilar 6061-T6/ 2024-T3 alloys (Table 4), studied by Ouyang and Kovacevic [333] were obtained under TRS values in range of 151-914 rpm, and WS values in range of 57-330 mm/min.

The butt FSWed joints of dissimilar 2024-T351/ 6056-T4 alloys (Table 4), studied by Amancio-Filho et al. [260] were obtained under TRS values in range of 500 to 1200 rpm and the WS values in range of 150 to 400 mm/min. Sound joints were obtained at TRS equal to 800 rpm and WS of 150 mm/min.

The proper FSWed joints of cast A356/wrought 6061 alloys (Table 4), studied by Lee et al. [261] were obtained under TRS of 1600 rpm, and WS values in range of 87 to 267 mm/min.

The correct FSWed joints of dissimilar 7003/7046 alloys (Table 4), studied by Yang et al. [312] were obtained under TRS of 2000 rpm and WS of 400 mm/min.

Mastenaiah et al. [321] reported that defect free joints were produced with TRS 400 to 2000 rpm, tool offset position from -2mm to +2mm at WS of 30 mm/min (Table 4) The joints produced with TRS in the range of 400-800 rpm, WS in the range of 30-390 mm/min and tool offset position from -2 mm to +1 mm also resulted in sound joints. The WE reached up to 97 %. Only welds obtained at the lowest TRS and highest WS and tool offset towards 219 alloy side exhibited defects. The extent of intermixing was affected by the TRS and WS. Intimate mixing of dissimilar alloys appeared at higher TRSs and lower WSs. The dissimilar joints FSWed under the conditions of high heat input (TRS varying from 400 to 2000 rpm) and lowest WS of 30 mm/min contained extensive intermixing in the nugget zone.

Studying the FSWed joints of rolled sheets made of dissimilar 2024/ 5056 alloys, Ivanov et al. [334] found that the proper joints were obtained using lower linear WSs and high tool rotation speeds.

Investigating butt FSWed joints of components made of alloy 6063 and 5083 obtained for various TRSs in the range of 600-1200 rpm, 4 kN axial load and WS of 40 mm/min (Table 4) Kumar et al. [335] reported that the joints of higher tensile strength, lower flexural strength and lower impact strength with maximum hardness were fabricated at the TRS of 1000 rpm with a cylindrical profile. The flexural strength and impact strength lowered whereas the tensile strength and hardness enhanced with the rise of the tool's TRS.

Studying FSWed joints of 2618-T87/ 5086-H321 alloys (Table 4), Sasikala et al. [336] reported that the obtaining of the sound joints was affected, inter alia, by WS. The WE reached up to 90%.

Investigating the FSWed joints of components made of 2014-T6 alloy (Table 4), Aydin et al. [337] found that the hardness in the softened weld region lowered with a decrease in the WS. Independently of the TRSs, the best tensile and fatigue properties of the joints occurred under the WS of 80 mm/min. The WE varied in the range of 93-97 %

Studying the FSWed joints of components made of 3003-H12 alloy (Table 4), Aydin et al. [338] found that the tensile weld strength enhanced with an increase in the WS or a decrease in the rotation speed. The tensile fractures of the joints were in base metal under welding parameter combinations of 1070 rpm and 40 mm/min or 2140 rpm and 224 mm/min. All other joints failed at heat affected zone. The yield and ultimate tensile strengths of the joints lowered almost linearly with an enhancement of TRS at a constant WS, while such strengths of the joints enhanced almost linearly with a rise of WS at a constant TRS. The elongation values of FSW joints were smaller at higher TRS or lower WS.

Investigating the single-sided butt FSWed joints of 3 mm thick 3003-O non-heat-treatable Al alloy (Table 4), Aydin et al. [339] reported that the welding parameters strongly affected the fatigue

 doi:10.20944/preprints202403.1458.v1

behaviours of the 3003-O FS welds. The fatigue life of FS welds obtained under the WS of 40 mm/min at various rotating speeds were about 2 – 3 times longer compared to those of FS welds with the WSs of 80 mm/min and 112 mm/min at various TRSs at a fixed stress amplitude under the stress ratio R = −1. At a much lower WS and a higher TRS, the fatigue life of the joints was increased due to the enhanced amount of heat supplied to the weld per unit length.

Studying the FSWed joints of 4 mm thick plates made of 2024 alloy (Table 4) without post-process heat treatment Weglowski et al. [340] reported that the weldability of Al alloys used for FSW process was good and provided good quality of welded joints for a wide range of welding parameters. The kind of tool had no effect on joint properties at the same welding parameters.

Nejad et al. [341] studied the structure and mechanical properties of FSWed joints of plates made of 2024-T4 alloy (Table 4) with cylindrical outer and concave end surface shoulder and varied depth. Joints were obtained for two different tool designs including a threaded one and an unfeatured one. Obtaining a defect-free weld structure with both probe tools needed well different rotation and traverse speeds. TRS of 500 rpm, WS of 55 mm/min and plunge depth of 2.7 mm for threaded tool, and TRS of 1300 rpm, WS of 115 mm/min and plunge depth of 2.9 mm for unthreaded tool allowed obtaining the finest grain in stir zone, the best visual quality and smoothness, the highest tensile strength, elongation, and micro-hardness.

Studying the FSWed joints of 6 mm thick plates made of 2024-T351 alloy (Table 4), Milčić et al. [342] obtained the compounds without errors and with an acceptable flat surface under the constant TRS of 750 rpm, and the WS varied in range from 73 to 150 mm / min. The relation between the TRS and WS directly affected the fracture toughness and energy necessary for the initiation and propagation of the crack in the joint. The weld joint obtained under 750/116 rpm/(mm/min) exhibited better properties and microstructure than the joints obtained under conditions of 750/73 and 750/150 rpm/(mm/min), respectively. The WE of 97% was achieved under rotation speed of 750 rpm and WS of 116 mm/min.

Investigating the FSWed joints of 8 mm-thick plates made of 2014-T6 alloy (Table 4), Lin et al. [343]reported that the weld tensile strength was affected by welding parameters. The maximum ultimate tensile strength of 360 MPa equal to 78 % appeared at a TRS of 400 rpm and WS of 100 mm/min.

Studying the FSWed joints of components made of 2014 alloy (Table 4), Sinhmar and Dwivedi [17] reported that after welding process realized at TRS of 931 rpm and WS of 41 mm/min, the mechanical performance of 2014 lowered. Simultaneously the corrosion resistance of the weld joint was higher than that of the base metal.

Investigating the FSWed joints of components made of the 2014-T6 alloy (Table 4) Ugender et al. [344] reported that the defect-free welds were obtained at a TRS of 900 rpm, taper cylindrical tool pin profile and traverse speed of 40 mm/min, respectively.

Studying the FSWed joints of components made of the 2017-T351 alloy (Table 4), Liu et al. [57] found that the tensile properties and fracture locations of the joints strongly depended on the welding process parameters. Under the optimum revolutionary pitch of 0.07 mm/rev corresponding to the TRS of 1500 rpm and the WS of 100 mm/min, the maximum ultimate strength of the joints corresponded to 82% of that of the base material.

Investigating the FSWed joints of components made of 1050-H24 alloy (Table 4), Liu et al. [309] reported that a softened region located at the weld and heat affected zones appeared in the joints. The degree of softening and tensile properties of the joints depended strongly on WS and TRS. The optimum FSW parameters were affected both by the tensile properties and the welding parameters. They were obtained for WS of 200 mm/min and the TRS of 1000 rpm.

The FSWed joints of cast AlSi9Mg/ 2017A alloys (Table 4), studied by Mroczka [310] were obtained under TRS of 560 rpm, and WS of 1120 mm/min. The FSWed joints of 2017A alloy (Table 4), studied by Mroczka et al. [311] were obtained under TRS of 355 rpm, and WS of 280 mm/min. Studying the FSWed joints of sheets made of 2017A alloy Mroczka et al. [345] found that a higher TRS (900 rpm then 355 rpm) the properties of the joint lowered. Cracks along grain boundaries and

 doi:10.20944/preprints202403.1458.v1

separation of grains at welds occurred at higher TRSs. They were due to the grain boundaries within joint nugget lost cohesion during the welding process at the high rate.

Takhakh and Abdullah [346],compared fatigue properties of welded joints of plates made of 3003-H14 alloy (Table 4) obtained by FSW (at TRS of 1500 rpm and WS of 80 mm/min) and TIG welding. They found that the fatigue properties of FSW joints were slightly lower than the base metal and higher than these of TIG welding.

Studying the FSWed joints of components made of 3003-alloy (Table 4), Chekalil et al. [347] reported that the joint mechanical properties were affected in the order by the TRS, feed rate and tool tilt angle. The best mechanical properties of a welded joint were obtained under the TRS of 1423.9 rpm, feed rate of 400 mm/min and tool tilt angle of 1.28.

Investigating the butt FSWed joints of plates made of 3003-H24 alloy (Table 4), Kasman and Ozan [348] reported that at a WS of 50 mm/min, tunnel-type defects with large size appeared in joints welded with the TRS of 500 and 1000 rpm. The tunnel-type defects also occurred under WS of 80 mm/min and TRS of 500 and 800 rpm. However, cavity-type defects occurred at both WSs. All welded joints fractured between the base metal and the heat-affected zone, except for the joints welded under WS of 50 mm/min WS, and TRS of 500 and 1000 rpm. The highest ultimate tensile strength among all the welded joints equal to 128 MPa was obtained under WS of 50 mm/min and TRS of 800 rpm. The welded joints were fractured in a ductile manner except the joint produced under WS of 50 mm/min and TRS of 500 rpm.

Studying the butt FSWed joints of 6013 Al plates (Table 4) obtained via pin offset technique Kasman and Ozan [313] found that the highest tensile strength equal to 206 MPa was obtained under 1.5 mm pin offset towards the advancing side and 500 min^{-1} TRS, leading to the ratio of tensile strength of the joint to the ultimate tensile strength of the base metal (joint efficiency) equal to 74 %.

Kasman and Yenier [322] reported that a defect-free joint was obtained under TRS of 1000 rpm, WS of 80 mm/min, and a 22-mm tool shoulder diameter (Table 4). The UTS lowered with enhancement of WSWS or TRSTRS. The WE for 5754 alloy lowered with an enhancement in WS, however, can exceed 100% for some weld cases. As for 7075 alloy, the efficiency varied in the range of 23.3-41.9 %.

Xu [349] studied FSWed joints of 5 mm thick plates made of 3003-H17 alloy (Table 4) under WS of 1500 and 3000 mm/min and a constant TRS. They found that the UTS of weld joint lowered with an enhancement in the WS from 1500 mm/min to 3000 mm/min at a constant TRS of 2000 rpm and shoulder plunge depth of 0.2 mm. The WE reached 87 % at WS of 1500 mm/min.

Studying the FSWed joints made of 3003 alloy (Table 4), Goyal et al. [350] reported that the best UTS was obtained for the process parameters including a WS of 74.64 mm/min, a TRS of 971.77 rpm and a tool tilt angle of 1.52, respectively.

Janeczek et al. [351] studied the effect of the shape of a tool and welding parameters on the quality of FSWed joints of components made of alloy 3004 (AlMn1Mg1) (Table 4). Various butt joints were made with a cylindrical and tapered threaded tool with a TRS of 475 rpm. The other joints were obtained with TRS of 475 rpm and WS of 300 mm/min with the use of a cylindrical threaded pin. Most of the specimens were properly joined for TRS of 475 rpm. In the joints obtained under WS of 300 mm/min, the material was not stirred properly. The best joint quality appeared for a TRS of 475 rpm and various WS values between 150 and 475 mm/min. The WE widely varied in the range of 61.9-87.6%, however the individual cases of below 27% were also noticed.

Studying butt FSWed joints of components made of dissimilar 7020-T651/ 5083-H111 alloys (Table 4), Torzewski et al. [352] found that the FSWed samples obtained under TRS of 800 rpm and WS of 200 mm/min exhibited the best strength properties: UTS = 303 MPa, YS = 157 MPa, and A = 11.6 %. All joints obtained at WS of 100 mm/min reached the efficiency of 95%.

Choi et al. [353] studied spot FSWed joints of sheets made of 5454 alloy (Table 4) with the different thicknesses of 1.4 and 1.0 mm obtained under the TRS in the range from 500 to 2500 rpm, and plunging to the depth of 1.8 mm under a constant tool plunge speed of 100 mm/min. The rotating tool was maintained at the plunge depth during the dwell time ranging from 0 to 7 sec. The pull-out

 doi:10.20944/preprints202403.1458.v1

speed of the rotating tool was 100 mm/min. The enhancement of TRS changed the macrostructure of the friction-stir-spot-welded zone, especially the geometry of the welding interface.

Studying the FSWed joints of components made of 1100 alloy (Table 4), Selvarajan and Balasubramanian [354] reported that a maximum tensile strength of 105 MPa, hardness value of 67 HV, and minimum corrosion rate of $0.69*10^{-4}$ in the stir zone region was obtained under the optimized parameters of 893 rpm TRS, 100 mm/min WS, 6.5 kN axial force, shoulder diameter of 14.8 mm, pin diameter of 4.9 mm, and tool material hardness of 45.4 HRC.

Dong et al. [355] studied microstructure and mechanical properties of welded joints of components made of dissimilar 7003-T4/ 6060-T4 alloys (Table 4), obtained by underwater friction stir weld UFSW. They reported that sound and defect-free joints were obtained in the UFSW process, however, tunnel defects appeared with a high WS of 240 mm/min. With the enhancement of the WS, more η and η′ phases remained because of the lower heat input.

Sheikhi and dos Santos [356] studied the effect of welding parameters and welding tools on the weld quality and mechanical properties of FSWed joints of tailor welded blanks TWBs made of 6181-T4 alloy in a thickness combination 1 to 2 mm as-produced (Table 4). Changing the WS had the biggest effect on the measured temperature and the heat input.

Zhou et al. [357] studied FSWed joints of 6061-T6 alloy sheet obtained under the TRS of 11,000 rpm, and the WS varying from 200 mm/min to 500 mm/min. The sound joints were obtained under the travel speed of 300 mm/min. Due to the stirring effect of high TRS, the proportion of low angle boundaries in all zones was lower than that of the traditional FSW, while the average grain size was like traditional FSW. The WE reached up to 87.2%. Generally, for lap FSW process when the rotation speed was high and the WS was low, the weld nugget occurred on an onion ring shape, and when the rotation speed was low, and the WS was high, void-type defects appeared on the AS or center of the nugget [315].

The FSWed joints of 6061-T6 alloy (Table 4), studied by Juarez et al. [316] were obtained at constant TRS of 1000 rpm, WS of 90 mm/min, penetration speed of 9 mm/min, and holding time of 10 seconds. The last parameters allowed lowering the defects of welding.

Godhani et al. [317] obtained FSWed joints of dissimilar 6061/7075 alloys (Table 4) under the WS of 31.5 mm/s, TRS of 765 rpm, and tool tilt angle of 2° forward. Various FSW process parameters for FSW joints of various Al alloys were presented by Patel et al. [256].

Studying FSWed 5 mm- thick plates made of 5086-O/ and 6061-T6 alloys, Aval et al. [358] reported that the enhanced TRS and lowered WS provided weaker welds and coarser grain size in the weld nugget.

Investigating the butt FSWed plates of 2219-T62 alloy, Xu et al.[359] found that with the enhanced TRS, the longitudinal residual stress lowered on the top surface, but raised on the bottom surface.

Studying the FSWed joints of 5 mm- thick 7075AA7075-T651 and 2024AA2024-T351 similar and dissimilar alloys, Zhang et al. [319] found that enhancing the TRS caused the widened TMAZ on the AS and RS. The mixing degree in the joints is remarkably affected by the TRS. Low TRS limited material mixing, while the typical onion ring of mixing pattern appeared at the high TRS. Compared to the base materials, significant grain refinement (average grain size: 1.7 μm) appeared at a TRS of 600 rpm. The enhanced TRS caused grain coarsening. The nugget zone of all the joints is dominated by a simple shear texture and varied with the TRS.

Sivachidambaram et al. [341] studied butt FSWed joint of 6mm- thick components made of dissimilar 5383/7075 alloys using tool with shoulder diameter of 24 mm, square pin with diameter of 8 mm and length of 5.7 mm under TRS in the range of 700-900 rpm, weld speed in the range of 40-80 mm/min, tilt angle of 0 degree, and the axial load of 10 kN. They found that varying WS affected yield stress and the lower WS caused maximum yield stress. The TRS of 700 rpm and WS of 40 mm/min provided very high tensile strength and hardness.

The influence of TRS on mechanical properties and thus on joint efficiency is not clear due to it is strongly affected by other parameters, e.g., traverse speed and the type of materials joined. The optimization of welds' quality very often considers the effect of both TRS and WS.

 doi:10.20944/preprints202403.1458.v1

Table 4. FSW process parameters for FSW joints of various Al alloys.

Refs	Alloy Combinations	Thick	Rotation Speed	Welding Speed	Plunge depth	Tool tilt angle	Downward force
		[mm]	[rpm]	[mm/min]	[mm]	[°]	[kN]
262	2024-T351/5083-H112	6.35	600	150			
262	7075-T651/2024-T351	6.35	600	150			
264	7075-T651/2024-T351	6	900	150			
61	7075-T6/2024-T3 Lap joint: 7075-upper; 2024-lower	3	600	30, 60, 90, 120	0.2	2.5	
265	7075-T651/5083-H111	6	280,355, 450, 560	140			26.4
266	2024-T4/7075-T6	4	1140	32			
267	6351-T6/5083-H111	6	800,1000 1200	45, 60, 75			
46,265 326	2017A-T451/7075-T651	6	355	112		1.5	32.8
327	5083-O/6063-T6	6	900	60			
269	5052and$AlMg_2Si$	8	1000	80		2.5	
270	2024-T351/6061-T6	6	800	31.5		2	
271	6061-T6/6351-T6	6.35	600,900, 1200	30, 60, 90			
272,328	6082-T6/7075-T6	10	950, 1000	80, 100			
273	6061-T651/5A06-H112	5	600, 900, 1200	100, 150	4.7	2	
274	6101-T6/6351-T6	12	900,1100, 1300	16			
275	2024-T3/6063-T6	8	900,1120 1400	125, 160, 200		2.5	
276	2219-T87/2195-T8	7.2	400, 600, 800	120, 180, 240, 300			
277	2017A-T451/cast AlSi9Mg	6	355	112			
278	5083-H12/6061-T6	1.5	700,1800 2500	25, 30, 212.5, 400			
279	6061-T6/7075-T6	5	1000, 1375, 1750, 2125, 2500	50, 125, 200, 275, 350	0.2	3	
280	5083-H111/6082-T6	5	400,500, 630, 800	40, 50, 63, 80		2	
144	5083-H111/6351-T6	6	800-1200	45-85		1	15
281	5052/6061	1, 1.5	1500	63, 98			
282	2024-T6/	5	1200	12			8

 doi:10.20944/preprints202403.1458.v1

	7075-T6						
283,284	Al-Mg-Si/Al-Zn-Mg	15	800	180	0.2	2.5	
285	2024-T3/6061-T6	4.8	500, 650, 840	45, 65		2	
286	UFG 1050/6061-T6	2	800	400, 600, 800, 1000		3	8
329	2024-T6/ 6061-T6	4	1000	500		2.5	
288,289	6061-T6/7050-T7451	5	270, 340, 310	114			
47	6111-T4/5023-T4 Lap joint	1	1500 1000	100 700			
290	5086-O/6061-T6	6	1100	22		1	12
291	2050-T4/6061-T651	20	150, 300, 300	101, 203, 406			
292	5083-O/6082-T6	NR(~7)	400	400			
293	A319/ A413 cast	10	630, 800, 1000	20, 40, 63	1	3	
294	7075-O/6061-O 7075-T6/6061-T6	3.17	1000 1500	150 400			
295	6061-T6/7075-T6	4.6	700-1450	100			
296	2024-T3/7075-T6 Lap joint	5	1500	50, 150, 225, 300	0.2	2.5	
297	5083-O/6061-T6	6	600, 750, 900	20, 40			
298	6351-T6/5083-H111	6	950	36, 63, 90			
300	2014-T6/6061-T6	4.7	500, 1500	90			
299	6351-T6/5083-H111	6	600-1300	36-90			9.8, 12.25, 14.7, 17.18, 19.6
302	A356/6061-T6	3	1000	70-240		3	
330	2198-T351/7075-T6 Lap joint	3 & 1.9	830	40		2	
304	2219-T87/5083-H321	6	400-800	15-60			
305	6061 cast/6061 rolled	6	800,1000 1200, 1400	50			8
306	6351-T6/5083-H111	6	600, 950, 1300	60		0	8
127	5052-H34/5023-T4	~1.5	1500	100-700		3	
303	A356/6061-T6	3	1000, 1400	80, 240			
307	5052-H34/5023-T4	1.5 & 1.6	1000, 1500	100, 200, 300, 400		3	
308	7050-T7451/2024-T351	25.4	NA	50.8			

 doi:10.20944/preprints202403.1458.v1

332	5182-O/5754-O 5182-O/6022-T4 5754-O/6022-T4	~2	500, 1000, 1500	130, 240, 400			
333	6061-T6/2024-T3	12.7	151-914	57-330			
260	2024-T351/6056-T4	4	500-1200	150-400			
261	cast A 356/wrought 6061	4	1600	78-267		3	
312	7003-T4/7046-T4	3	2000	400	0.3	2.5	
321	2219-T6/5083-H116	5	400, 800, 1200, 1600, 2000	30, 210, 390, 570, 750			
335	6063/5083	6	600,800, 1000	40			4
336	2618-T87/5086-H321	6	450,600, 750, 850	15, 35, 50, 65			
337	2014-T6	3	1070, 1520, 2140	40, 80, 112			
338	3003-H12	3	1070, 1520, 2140	40, 80, 112, 160, 224			
339	3003-O	3	1070, 1520, 2140	40, 80, 112			
340	2024-T4	4	350	210			
341	2024-T4	3	300-1300	40-145	2.7, 2.9	6	
342	2024-T351	6	750	73, 116, 150			
343	2014-T6	8	300-800	50-300			
17	2014	NA	931	41			
344	2014-T6	5	900	40		2.5	5
57	2017-T351	5	1500	25-600		3	
309	1050-H24	5	600-2000	100-800		3	
310	2017A-T451 /AlSi9Mg	6	560	1120		1.5	
311	2017A	6	355, 900	280		1.5	
346	3003-H14	3	1500	80			
347	3003	2	1000, 1500, 2000	200, 300, 400			
348	3003-H24	3	500,800, 1000	50, 80			
313	6013-T6	5	500, 630, 800	50			
322	5754-H111/7075-T651	5	1000, 1250	80, 100, 125			
349	3003-H17	5	2000	1500, 3000	0.2		
350	3003	5	663,800, 1000, 1200, 1336	20, 40, 70, 100, 120		0.65, 1, 1.5, 2, 2.35	
351	3004	5	95-600	115-925			
352	5083-H111/7020-T651	5	400,800, 1200	100, 200, 300			
353	5454-O	1, 1.4	500-2500	100			

 doi:10.20944/preprints202403.1458.v1

354	AA1100	5	562,700, 800,900, 1037	40.54, 75, 100, 125, 159.5			3.62, 5, 6, 7, 8.38
355	7003-T4/6060-T4	4.5	1000	40, 120, 240			
315	6111-T4/5023-T4	1	1000, 1250, 1500	100, 300, 500, 700			
356	6181-T4	1, 2	1300, 1600, 2000	800, 1000, 1125, 1500		1.5, 3	4.5, 5.5
357	6061-T6	1	11000	200-500	0.05		
316	6061-T6	9.5	1000	90			
317	6061-T6/7075-T6	6	765	31.5		2	

4.8.1.3. Tool Geometry

Zhou et al. [357] reported that the geometry of the shoulder and the pin profile strongly affected heat generation and material flow during welding process. The high shoulder size governed a heat input. The common shoulder profiles included the flat, the concave and the convex. The pin features such as a spiral or a groove improved frictional behavior and material flow in joint. Threads guided material flow around the pin in a rotational and a translation direction [264,265,290,360]. The polygonal pin profiles provided pulses in the flow during material stirring and mixing, causing material adhering to the pin [361–364].This pulsating effect highly impeded material flow in joints between dissimilar Al alloys. Thus, the cylindrical or a conical pin profile with various features provided for good material flow leading to obtain sound joints between the dissimilar Al alloys.

Hasan et al. [261] studied effect of welding tool pin flute radius during the FSW process of dissimilar 7075-T651/2024-T351 alloys (Table 5) on the weld quality. Five pin tools with various flute radii (0, 2, 3, 6, and ∞ mm) were investigated. They found that the flute radius affects the material flow pattern and weld quality. The strongest joint was obtained for the flute radius equal to the pin radius. The joint efficiency reached up to 94.3%.

Ge et al. [61] studied how EST affects the shear failure load of lap joints. Shear fracture mode occurred in lap joints obtained with a small (3 mm) pin at all WSs. The tensile fracture mode appeared for the lap joints obtained with greater (4 mm or 5 mm) pin. Studying FSWed joints of components made of alloys 7075-T651 and 5083-H111 Kalemba-Rec et al. [265] reported that the use of the Triflute pin provided greater tensile strength and WE.

Palanivel et al. [267] studied the effect of shoulder profiles on the 5083-6351 combination properties (Table 5). They utilized three different shoulder features including the partial impeller, the full impeller, and the flat grove. The full impeller shoulder tool provided the optimum mechanical strength due to the increased material flow in joint. The pin profile strongly influences material stirring and mixing. Cylindrical or conical pin profiles without threads provided a smaller surface to the material. Such pin profiles with the threaded and flat features enhanced the contact area.

For study on FSWed sheets made of dissimilar 2017A-T451/7075-T651 alloys (Table 5), Hamilton et al. [326] obtained qualitied welds using a tool made of HS6-5-2 high speed steel with a scrolled shoulder with a 24 diameter. The pin diameter tapered linearly from 6 mm at the shoulder to 4.5 mm at the tip with an overall height of 5.7 mm. The pin was also threaded.

Gupta et al. [327] conducted studies on FSWed joints of components made of dissimilar 5083-O/ 6063-T6 alloys (Table 5) focusing on optimization of tool geometry, TRS, and WS. The multi-optimal set of weld properties comprising tensile strength, average hardness at weld nugget zone and average grain size at weld nugget zone was obtained for 18 mm of shoulder diameter and 5 mm of pin diameter.

The proper FSWed joints of Al-Mg2Si/Mg_2Si5052 alloys studied by Huang et al. [269] were obtained using an H13 steel-made pin tool comprising a concave 18-mm-diameter shoulder and a conical pin (the end and root diameter are 4 and 6 mm, respectively) with a pin length of 5.7 mm.

The correct FSWed joints of dissimilar 2024/ 6061 alloys (Table 5), studied by Moradi et al. [270] were obtained using AISI H13 hot work steel tool possessing a conical geometry with 18 mm shoulder

 doi:10.20944/preprints202403.1458.v1

diameter, a 4° conical cavity, a square frustum probe measuring 3.5–7 mm in diameter, and 5.9 mm in length.

The proper FSWed joints of dissimilar 6351-T6/ 6061-T6 alloys (Table 5), studied by Prasanth and Raj [271] were obtained using cylindrical tool having a scroll with 0.75 mm taper at the tip of the pin, and it has 16 mm probe diameter, 14 mm shoulder diameter, 5 mm pin length and of 4 mm pin diameter, made of molybdenum M42 with HRC 63.

The correct FSWed joints of dissimilar 6061-T651/ 5A06-H112 alloys (Table 5), studied by Peng et al. [273] were obtained using tool with cylindrical shoulder diameter of 16 mm, and conical pin with diameter varying from 5 to 4.2 mm, and the length of 4.6 mm.

The proper FSWed joints of dissimilar 2024-T3/ 6063-T6 alloys (Table 5), investigated by Sarsilmaz [275] were obtained using D5 steel tool with conical triangular pin profile quenched-tempered to 60 HRC.

The sound FSWed joints of dissimilar 2219-T87/ 2195-T8 alloys (Table 5), studied by No et al. [276] were obtained using the tool made of austenitized H13, with a spiral shape and a shoulder diameter of 16 mm.

The proper FSWed joints of dissimilar wrought 2017A/ cast AlSi9Mg alloys (Table 5), studied by Kopyscianski et al. [277] were obtained using a modified Whorl-type tool made of HS6-5-2 high speed steel with a 24 mm diameter and scrolled shoulder. The threaded pin diameter tapered linearly from 6 mm at the shoulder to 4.5 mm at the tip with an overall height of 5.7 mm.

The correct FSWed joints of 5083-H12/ 6061-T6 alloys (Table 5), studied by Ghaffarpour et al. [278] were obtained using tool with shoulder diameter in range 10–14 mm, and pin diameter in range 2–4 mm. The FSWed joints of studied by Bijanrostami et al. [279] were obtained using tool made from 2344 steel heat-treated to obtain hardness by 52 HRC, and comprised the shoulder with diameter of 15 mm, and a threaded conic pin with conic angle of 5°, the length of 4.7 mm, and a diameter of 5 mm.

Studying the FSWed joints of dissimilar 6082-T6/ 5083-H111 alloys (Table 5), Kasman et al. [280] found that the pin shape significantly affected the tensile properties and microstructure of weld joints. The strengths of the weld joint obtained with the pentagonal-shaped pin were lower than those with triangular-shaped pin. The pin shape influenced each nugget zone profile containing onion rings.

Palanivel et al. [144] obtained proper FSWed joints of the 6-mm-thick sheets made of dissimilar 5083-H111/ 6351-T6 alloys (Table 5) using the straight square tool pin with a shoulder diameter of 18 mm, a pin diameter of 6 mm and a pin length of 5.6 mm.

The proper FSWed joints of 6 mm-thick components made of dissimilar alloys 6351/ and 5083-H111 alloys (Table 5), studied by Palanivel et al. [281] were obtained using five tool pin profiles including straight cylinder, threaded cylinder, square, tapered square, and tapered octagon without draft. The ratio of shoulder diameter and pin diameter was of 3. The tool material was HCHCr steel oil hardened to obtain a hardness of 60–62 HRC. The joint obtained using a tapered square pin profiled tool provided the least tensile strength. Using straight cylinder, threaded cylindrical, tapered square and tapered octagon pin profiled tools such a strength varied insignificantly. It resulted from the difference in dynamic orbit created by the eccentricity of the rotating tool during the FSW process.

Studying FSWed joints of components made of the dissimilar 2024-T6/ 7075-T6 alloys (Table 5), Saravanan et al. [283] found that the joint fabricated under D/d ratio equal to 3 showed better mechanical properties in comparison to other joints.

Yan et al. [284,285] obtained proper FSWed joints of sheets made of dissimilar Al-Mg-Si/Al-Zn-Mg alloys (Table 5) using tool with shoulder diameter of 35 mm, and pin with diameters of the pin root and pin bottom equal to 20 and 12 mm, respectively, while pin length was of 14.5 mm.

The correct FSWed joints of dissimilar 2024-T3/ 6061-T6 alloys (Table 5), studied by Zapata et al. [286] were obtained using a tool consisted of a 20 mm diameter concave shoulder with a 4 mm diameter tapered threated pin.

 doi:10.20944/preprints202403.1458.v1

The proper butt FSWed joints of UFGed 1050/ 6061-T6 alloys (Table 5), studied by Sun et al. [287] were obtained using the rotating tools made of tool steel, containing a concave-shaped shoulder with a diameter of 12 mm and a threaded pin with a diameter of 4 mm and a length of 1.8 mm.

Sun et al. [329] studied the influence of various shapes of tool pin including conical thread, deep groove thread, and conical cam thread on the plastic flow of 2024-T6/6061-T6 alloys (Table 5) during FSW process. They found that the metal in the weld nugget zone WNZ came from the base metal of the advancing side, the thread was the driving force of the downward movement of the FSW plastic metal. The deep groove thread tool pin strongly drove the metal downward. The conical cam thread tool pin provided the strongest stirring of materials and the best metal fluidity. Welds were obtained using tool with shoulder with concentric circles and diameter of 18 mm, and pin with diameter varied from 7 to 5 mm and length of 3.7 mm.

The proper FSWed joints of dissimilar 6061/7050 high strength Al alloys (Table 5), studied by Rodriguez et al. [288] and [289] were obtained using a tool consisted of a cylindrical threaded pin and a shoulder having a diameter of 10 mm and of 18 mm respectively.

The sound lap FSWed joints of plates made of dissimilar 6111-T4/5023-T4 alloys studied by Yoon et al. [40] were obtained using a tool with a shoulder diameter of 8 mm, and a threaded pin with diameter of 3 mm, and length of 1.45 mm. During studies on FSWed components made of the heat treatable 6061 and non-heat treatable 5086 alloys (Table 5), Ilagovan et al. [290] found that the use of threaded tool pin profile provided better flow of materials between two alloys and the generation of defect-free stir zone. It also allowed obtaining higher hardness values of 83 HV in the stir zone and higher tensile strength of 169 MPa compared to those of the other two pin profiles.

During studies on butt FSWed joints of components made of dissimilar 2050/6061 alloys (Table 5), Reza-E-Rabby et al. [291] found that joint quality, process parameters and welding temperature depended on pin features. Pin with thread flats allowed production of quality welds in some cases.

The proper FSWed joints of dissimilar 5083-O/ 6082-T6 alloys (Table 5), studied by Donatus et al. [292] were using the tool with a diameter to length ratio was 1 : 0.8 with a 25 mm diameter scroll shoulder applicable at a tilt angle of 0°.

The correct FSWed joints of dissimilar cast Al–Si alloys A319/A413 (Table 5), studied by Karam et al. [293] were obtained using tool with shoulder diameter of 26 mm, and conical threaded pin with diameters varying from 10 to 6 mm, and length of 9 mm.

The proper butt FSWed joints of dissimilar 7075-O/6061-O and 7075-T6/6061-T6 alloys (Table 5), studied by Ipekoglu and Cam [294] where obtained using tool with a concave shoulder diameter of 15 mm, and a M4 threaded cylindrical pin with diameter of 4 and length of 3 mm.

The correct FSWed joints of dissimilar 6061-T6/7075-T6 alloys (Table 5), studied by Cole et al. [295] were obtained using a tool with a 4.4 ° concave shoulder with diameter of 15 mm, and a threaded, conical tapered pin with three flats with diameter varying from 7.0 mm to 5.2 mm, and the pin length of 4.7 mm.

The proper lap FSWed joints of dissimilar 2024-T3/7075-T6 alloys (Table 5), studied by Song et al [296] were obtained using a tool with a 15 mm diameter concave shoulder and a 6 mm long threaded taper cylindrical pin with the top and bottom diameter of 4 mm and 6 mm, respectively.

The sound butt FSWed joints of dissimilar 2014-T6/ 6061-T6 alloys (Table 5), studied by Jonckheere et al. [300] were obtained using tool with a 15 mm diameter scrolled shoulder and threaded pin with three flats with a diameter of 5 mm and length of 4.4 mm.

Palantivel et al. [299] for welding utilized tools with shoulder to work piece interference surface with 3 concentric circular equally spaced slots of 2 mm in depth on all tools. The tools utilized also five pin configurations including straight square, tapered square, straight hexagon, straight octagon, and tapered octagon without draft. The most helpful was straight square pin profiled tool.

The proper FSWed joints of dissimilar A356/6061 alloys (Table 5), studied by Ghosh et al. [302] were obtained using a tool made of high-speed steel with concave shoulder diameter of 15 mm, and cylindrical pin with diameter of 5 mm and length of 2.6 mm.

 doi:10.20944/preprints202403.1458.v1

The correct FSWed lap joints of 7075-T6/2198-T351 alloys (Table 5), studied by Velotti et al. [330] were obtained using tool with shoulder diameter of 15.5 mm, and conical pin with maximum diameter of 4 mm and length of 3.1 mm.

Studying FSWed joints of plates made of dissimilar 2219-T87/5083-H321 alloys (Table 5), Koilray et al. [304] found the ratio between tool shoulder diameter and pin diameter the most dominated the joint soundness while pin geometry also strongly influenced it. Welds were obtained using tools with a pin with length of 5.7 mm and diameter of 6 mm. The ratio between tool shoulder diameter and pin diameter took values 1.5, 2, 2.5, 3 increasing with TRS and WS.

The proper FSWed joints of dissimilar cast and wrought 6061 alloy (Table 5), investigated by Dinaharan et al. [305] were obtained using a tool with a shoulder diameter of 19.2 mm, and a hexagonal pin profile with diameter of 6 mm and length of 5.8 mm.

Studying of FSWed joints of components made of dissimilar 5083-H111/6351-T6 alloys (Table 5), Palanivel et al. [306] reported that the TRS and pin profile influenced the joint strength because of varying material flow, loss of cold work in the HAZ of 5083 side, dissolution and over aging of precipitates of 6351 side and formation of macroscopic defects in the weld zone. Weld were obtained using tool with flat shoulder diameter of 18 mm, and pins with diameter of 6 mm, length of 5.7 mm, and various profiles including straight square, straight hexagon, straight octagon, tapered square, and tapered octagon. Square pins produced highly intense pulses which long last compared to those for hexagon and octagon pins causing severe and random layer-by-layer material movement.

The proper FSWed joints of dissimilar 5052-H34/5023-T4 alloys (Table 5), studied by Song et al. [127] were produced using a left-handed threaded tool with shoulder diameter of 12 mm, and a pin with diameter of 3.8 mm, and length of 1.45 mm.

The correct FSWed joints of dissimilar A356/6061 alloys (Table 5), studied by Ghosh et al. [303] were obtained using a tool with concave shoulder diameter of ~15 mm, and a cylindrical pin with diameter of ~5 mm, and length of ~2.6 mm.

The proper FSWed joints of dissimilar 5052 and A5J32 alloys (Table 5), studied by Kim et al. [307] were produced using a tool with shoulder diameter of 8 mm, and the threaded cylindrical pin with diameter of 3 mm and length of 1.45 mm.

The correct FSWed butt joints of 7050-T7451/2024-T351 alloys studied by Prime et al. [308] were obtained using tool with threaded pin.

The sound FSWed joints of dissimilar 5182-O, 5754-O, and 6022-T4 alloys (Table 5), studied by Miles et al. [332] were produced using tool with a concave shoulder with diameter of 10.2 mm, and the cylindrical threaded pin with diameter of 3.18 mm, and length of 1.95 mm.

The proper butt FSWed joints of 6061-Al as itself, and of dissimilar 6061-T6/2024-T3 alloys (Table 5), studied by Ouyang and Kovacevic [333] were obtained using tool with threaded pin.

The sound butt FSWed joints of dissimilar 2024-T351/ 6056-T4 alloys (Table 5), investigating by Amancio-Filho et al. [260] were produced using tool with 5 mm diameter threaded cylindrical pin and 15 mm concave shoulder.

The correct FSWed joints of cast A356/wrought 6061 alloys (Table 5), studied by Lee et al. [261] were obtained using tool with screw-like pin.

The proper FSWed joints of the 2017-T351 alloy studied by Liu et al. [57] and the FSWed joints of 1050 - H24 alloy (Table 5), studied by Liu et al. [309] were produced using tool with shoulder diameter of 15 mm, and pin with diameter of 5 mm and length 4.7 mm.

The correct FSWed joints of cast AlSi9Mg/ 2017A alloys (Table 5), studied by Mroczka and these [310] were of 2017A alloy studied by Mroczka et al. [311] were obtained using tool with shoulder diameter of 22 mm, and cylindrical threaded pin with diameter of 8 mm.

The various FSWed joints of a 6061-T6 alloy (Table 5), studied by Zhou et al. [357] were obtained using tools with three configurations of pin including a quadrangular prism, quadrangular frustum pyramid, and frustum one. When the shape of the pin was a quadrangular frustum pyramid, sound joints are obtained.mm.

 doi:10.20944/preprints202403.1458.v1

Studying butt FSWed joints of components made of 6063/5083 alloys (Table 5), Kumar and Kumar [335] reported that the joints of higher tensile strength, lower flexural strength and lower impact strength with maximum hardness were fabricated at the tool with a cylindrical profile.

Sheikhi and dos Santos [356] studied the effect of welding parameters and welding tools on the weld quality and mechanical properties of FSWed joints of tailor welded blanks TWBs made of 6181-T4 alloy (Table 5) in a thickness combination 1 to 2 mm. The peak temperature during welding slightly increased with increasing pin diameter. The effect of shoulder type on such peak temperature was negligible .

Studying FSWed joints of 2618-T87/ 5086-H321 alloys (Table 5), Sasikala et al. [336] reported that the obtaining of the sound joints was affected by the fraction of tool contact area to pin diameter, and to a lower extent by pin shape.

Investigating the FSWed of 4 mm thick plates made of alloy 2024 Weglowski et al. [340] reported that the joints welded with the different tools and under various conditions exhibited a characteristic shape of a nugget zone, heat-affected zone and thermo-mechanically affected zone. The kind of tool had no effect on joint properties at the same welding parameters. The WE was of 91.1% for the Triflat tool with the flat bottom pin, while it was of 95,7% for the Triflute tool with the round bottom pin.

Nejad et al. [341] studied the structure and mechanical properties of FSWed joints of plates made of 2024-T4 alloy (Table 5) with cylindrical outer and concave end surface shoulder and varied depth. Joints were obtained for two different tool designs including a threaded one and an unfeatured one. Obtaining a defect-free weld structure with both probe tools needed well different rotation and traverse speeds. Despite increasing the elongation and strength properties of joints obtained with the threaded tool, they exhibited elevated average hardness and less uniform properties over various welding zones in comparison to the joints prepared by unfeatured tool.

Studying the FSWed joints of components made of the 2014-T6 alloy (Table 5), Ugender et al. [344] reported that the defect-free welds were obtained using taper cylindrical tool pin profile. The joints fabricated at a taper cylindrical tool profile with a 3 mm radius of curvature exhibited better mechanical properties compared to the straight cylindrical tool profile. The WE was of 69.5% for the taper cylindrical tool, while it was of 63.4% for the straight cylindrical one.

Burek et al. [365] studied tool wear effect on the quality of lap FSWed joints of Al7075-T6 alloy sheets for two thicknesses (Table 5). They explained that due to the small diameter of the pin and the great forces occurring in the process, this element was most susceptible to tool wear. The welding process caused the tool to undergo friction wear, resulting in lowered tool dive depth in the jointed material. After creating 200m of joints, the strength of the joints lowered and the changes in the stirring conditions in the material became more intensive. The degradation of the tool led to lowering the characteristic sizes of the thermoplastic zone strongly affecting the joint strength.

The FSWed joints of 3003 alloy (Table 5), studied by Chekalil et al. [347] were obtained using tool with flat shoulder with diameter of 19.5 mm, and conical pin with diameter varying from 6.8 to 5 mm, and length of 1.7 mm. The FSWed joints of 3003-H17 alloy studied by Xu [349] were obtained using tool with shoulder diameter of 16 mm, and conical threated pin with maximal diameter of 6 mm, length of 4.7 mm, and taper angle of 2.5°. Similar joints studied by Goyal et al. [350] were obtained using tool with concave shoulder with diameter of 18 mm, and square pin with diameter of 6 mm, and length of 4.75 mm.

Janeczek et al. [351] studied the effect of the shape of a tool and welding parameters on the quality of FSWed joints of components made of 3004 alloy (Table 5).Various butt joints were made with a self-developed tool with cylindrical threated and tapered threaded pin. They found that the material outflow for the joints made with the cylindrical threaded pin was higher than that for the joints made with the tapered threaded pin. However, voids-like defects appeared in the joints made with the tapered threaded tool. The use of the cylindrical tool provided higher for about 37% mechanical properties compared with those for the tapered threaded joint.

Studying the FSWed joints of components made of 1100 alloy (Table 5), Selvarajan and Balasubramanian [354] found that optimized parameters of welding process comprised shoulder diameter of 14.8 mm and, pin diameter of 4.9 mm, and tool material hardness of 45.4 HRC .

 doi:10.20944/preprints202403.1458.v1

The proper FSWed joints of 6061-T6 alloy (Table 5), studied by Juarez et al. [316] were obtained using tool with flat shoulder diameter of 25.4 mm, composite pin with a hexagonal shank with a maximum diameter of 8 mm and a length of 9 mm and a cylindrical collar with a diameter of 11 mm and a height of 3 mm made of H13 steel.

Khan et al. [366] studied the influence of tool pin offset and tool plunge depth on the formation of defects such as tunnel (tunneling defect) and kissing bond (KB) in 4.75 mm thick FSWed plates made of AA5083-H116 and AA6063-T6 alloys. The joints were obtained using tool made of Tungsten carbide, with tapered conical pin, shoulder diameter of 20 mm, pin length of 4.4 mm under TRS of 450 rpm, WS of 100 mm/min, tilt angle of 2 degrees, tool offset in range of 0.5-1.5 mm (AS to RS) and plunge depth of 0.3/0.4 mm. They found that the tunneling defects appeared at all offset (including zero offset) values towards stronger material (AS). The cross-section of the tunnel varied with the amount of offset. KBs appeared at the interface for all pin offset values except 0.5 mm towards softer material and high plunge depth causing the poor mechanical properties. Therefore, both plunge depth and tool pin offset strongly affected the weld quality. The plunge depth provided heat generation and the control over forging action and welding thrust. Tool pin offset distributed the heat and mixed the joined alloys.

Table 5. Tools parameters used for FSW process for joining various Al alloys.

Refs.	Alloy Combinations	Thick (mm)	Tool profile (-)		Shoulder diameter	Pin diameter/ length/ taper angle	Tool material hardness
			Shoulder	Pin	[mm]	[mm]/ [mm]/ [°]	[HRC]
264	7075-T651/2024-T351	6	concave	conical threaded and with flute radius (0, 2, 3, 6, and ∞mm))	18	6/5.7	AISI H13
61	7075-T6/ 2024-T3 Lap joint: 7075-upper; 2024-lower	3	concentric-circles-flute	tapered	13.5	6/3,4,5/16.7	
265	7075-T651/5083-H111	6	spiral (convex scrolled)	triflute, tapered with a thread	24	10/5.8; 10 (6 on tip)/5.8	HS 6-5-2
267	6351-T6/ 5083-H111	6	partial impeller, full impeller, flat grove	cylindrical or conical with and without threads			
46 268,, 326	2017A-T451/7075-T651	6	scrolled	tapered threaded	24	6-4.5/5.7	HS 6-5-2
327	5083-O/6063-T6	6			18	5	
269	5052/Al-Mg_2Si	8	concave	conical	18	6-4/5.7	H13 steel

 doi:10.20944/preprints202403.1458.v1

270	2024-T351/6061-T6	6	conical with 4° cavity	square frustum	18	7-3.5/5.9	H13 steel
271	6061-T6/ 6351-T6	6.35	cylindrical scrolled	cylindrical	14	4/5	molybdenum M42/ HRC 63
273	6061-T651/5A06-H112	5	cylindrical	conical	16	5-4.2/4.6	
275	2024-T3/ 6063-T6	8		conical triangular			D5 steel/60
276	2219-T87/2195-T8	7.2	spiral		16		H13 steel
277	2017A-T451/cast AlSi9Mg	6	scrolled	tapered threaded	24	6-4.5/5.7	HS 6-5-2
278	5083-H12/ 6061-T6	1.5			10-14	2-4	
279	6061-T6/ 7075-T6	5		conic threated	15	5/4.7/5°	2344 steel/52
280	5083-H111/6082-T6	5		triangular, pentagonal	20	5-6	DIN EN 1.7131 steel
144	5083-H111/6351-T6	6		straight square	18	6/5.6	
282	2024-T6/ 7075-T6	5	flat	smooth cylindrical	15-16	3-8/4.7	high carbon steel
283 284	Al-Mg-Si/Al-Zn-Mg	15			35	20-12/14.5	
285	2024-T3/ 6061-T6	4.8	concaved	tapered threaded	20	4	
286	UFG 1050/6061-T6	2	concave	thread	12	4/1.8	steel
329	2024-T6/ 6061-T6	4	concentric circles	conical thread, deep groove thread, conical cam thread	18	7-5/3.7	
288289	6061-T6/7050-T7451	5		cylindrical threaded	18	10	
47	6111-T4/ 5023-T4 Lap joint	1		threaded	8	3/1.45	
290	5086-O/ 6061-T6	6		straight cylindrical, threaded cylindrical,	18	6-5/5.7	steel HSS

 doi:10.20944/preprints202403.1458.v1

				tapered cylindrical			
291	2050-T4/ 6061-T651	20	single scroll	conical threaded	25.4	15.9/12.7/ 8°	steel H13
292	5083-O/ 6082-T6	NR(~7)	scroll	triflute	25	8/6.4	
293	A319/A413 cast	10		conical threated	26	10-6/9	steel H13
294	7075-O/ 6061-O 7075-T6/ 6061-T6	3.17	concave	cylindrical threaded	15	4/3	steel H13/52
295	6061-T6/ 7075-T6	4.6	concave	conical threaded	15	7-5.2/4.7	steel H13
296	2024-T3/ 7075-T6 Lap joint	5	concave	cylindrical threaded	15	6-4/6	steel H13/52
300	2014-T6/ 6061-T6	4.7	scrolled	cylindrical threaded	15	5/4.4	
299	6351-T6/ 5083-H111	6	with concentric circular slots	straight square, tapered square, straight hexagon, straight octagon, tapered octagon without draft	18	6/5.6	high carbon high chromium steel
302	A356/6061-T6	3	concave	cylindrical	15	5/2.6	high speed steel
330	2198-T351/7075-T6 Lap joint	3 and 1.9	flat	conical	15.5	max 4/3.1	
304	2219-T87/5083-H321	6		straight cylinder, tapered cylinder, cylindrical threaded tapered threaded	9, 12, 15, 18	6/5.7	Steel H13/50-55 VHN
305	6061 cast/6061 rolled	6	with concentric circular slots	hexagonal	19.2	6/5.8	HCHCr steel/ 62
306	6351-T6/5083-H111	6	flat	straight square, straight hexagon, straight octagon, tapered square, tapered octagon	18	6/5.7	High carbon high chromium steel/63 HRC
127	5052-H34/ 5023-T4	~1.5		cylindrical threaded	12	3.8/1.45	

 doi:10.20944/preprints202403.1458.v1

303	A356/6061-T6	3		cylindrical	15	5/2.6	HSS steel
307	5052-H34/ 5023-T4	1.5 & 1.6		cylindrical threaded	8	3/1.45	
308	7050-T7451/2024-T351	25.4		threaded			
332	5182-O/ 5754-O 5182-O/ 6022-T4 5754-O/ 6022-T4	~2	concave	cylindrical threaded	10.2	3.18/1.95	H13 steel
333	6061-T6/ 2024-T3	12.7		threaded			
260	2024-T351/6056-T4	4	concave	cylindrical threaded	15	5	
261	cast A356/ wrought 6061	4		screw-like			
57	2017-T351	5			15	6/4.7	
309	1050-H24	5			15	6/4.7	
26	2017A-T451/AlSi9Mg	6		cylindrical threaded	22	8	
311	2017A	6			25	8	
357	6061-T6	1	flat	quadrangular prism, quadrangular frustum pyramid, frustum	7	2-1.5/0.9	
335	6063/5083	6		Straight cylindrical	20	5/5	steel HSS
356	6181-T4	1, 2	concave, scroll	cylindrical and threaded	13	5, 6.5, 7	
336	2618-T87/5086-H321	6		Straight cylinder, tapered cylinder, cylindrical threaded tapered threaded	24, 30, 33, 36	12/5.7	steel H13
340	2024-T4	4		triflute with round bottom pin, triflat with round bottom pin, triflute with flat bottom pin,			high speed steel SW7M

 doi:10.20944/preprints202403.1458.v1

				triflat with flat bottom pin			
341	2024-T4	3	cylindrical, concave	tapered unthreaded, tapered threaded	20	6/3	
344	2014-T6	5		straight cylindrical, tapered cylindrical	18	6/4.8	stainless steel
365	7075-T6	1, 0.8	concave	cylindrical threaded	10	4/1.2	Schilling 10S4ZGO/54-56
347	3003	2	flat	conical	19.5	6.8-5/1.7	X210Cr12 steel
349	3003-H17	5		conical threated	16	6/4.7/2.5°	
350	3003	5	concave	square	18	6/4.75	steel H13/45
351	3004	5	flat	cylindrical threated tapered threated	21	10/4.5/10°	
354	1100	5			7.86, 12, 15, 18, 22.13	2.6, 4, 5, 6, 7.37	high carbon steel 33, 40, 45, 50, 56 HRC
316	6061-T6	9.5	flat	composite (cylindrical shaft and cylindrical	25.4	11/9(3)	H13 steel
317	6061-T67075-T6	6	flat	cylindrical	21	6/6	

Summarizing, it can be notice that the pin length should be a little less than the plate thickness for butt joints arrangement to prevent the tool damaging or the backing plate of FSW machine used for FSW process. Additionally, the tool pin profile and diameter, shoulder shape and diameter, TRS and WS the most highly affect FSW process, particularly in case of dissimilar aluminium alloys. It is in agreement with observations from [320].

4.8.1.4. Microstructure Evolution

The typical microstructure of a FSW joint comprised three zones including HAZ, TMAZ and SZ [367,368] The shapes of such zones were affected by the thermal and mechanical deformation induced by the tool during the welding process. The SZ exhibited fine-grain microstructures due to extensive grain refinement, while the TMAZ exhibited an elongated grain structure [369,370] The welding parameters affected the microstructure evolution, due to the higher influence of the material movement or flow in joints between dissimilar Al alloys compared to joints between the same Al alloys. The appropriate selection of all process parameters provided an intensive material mixing on both sides AS and RS of the joint and thus a sound weld. The electron backscatter diffraction EBSD - based orientation maps for the 5083-2024 joint [371] revealed tilted and elongated grains in the TMAZ and refined grains d in the SZ resulting from dynamic recrystallization. Grain boundary orientations also varied in all three zones. The SZ comprised a higher amount of large (>10°) angular grain

 doi:10.20944/preprints202403.1458.v1

boundaries, while more of low (2–10°) angular grain boundaries appeared in HAZ. The SZ also exhibited a more intense texture compared to other zones.

Studying the FSWed joints of 7075-T651 and 2024-T351 alloys Hasan et al. [130] found the difference in materials flow and mixing relating to the tool pin design. The grain size and shape of onion rings appearing in nugget zone were affected by material placement and tool pin geometry. The mixing stir zone became more homogeneous when the flute radius reached that of the tool pin. Three different sub-layers appeared in the weld nugget, two of them were close to each base welding material, and the other was a mix of both materials. The non-recrystallized heat-affected zone HAZ and thermo-mechanically affected zone TMAZ were similar in chemical composition to their corresponding base materials.

Ge et al. [61] reported that four typical zones including base material BM, heat-affected zone HAZ, thermo-mechanically affected zone TMAZ, and stir zone SZ appeared in the lap weld cross-section. Stir zone SZs presented a bowl-like shape due to the tool geometry effect and comprised nonuniform grain size along the joint thickness due to the differences in material flow and temperature during the welding process. The dynamic recrystallization also occurred therein caused by the strong stirring of the tool and the elevated temperature effect. The material concentrated zone MCZ was also formed under the material plastic flow towards the tool zone during welding process. Simultaneously, the lath-like microstructure of the BM transformed into fine equiaxed grains. TMAZ comprised severely deformed and elongated grains induced by strong plastic deformation of SZ during FSW. The grains of 2024 alloys appeared in the upper sheet near the lap interface due to the laminar material flow. Also, the microcracks can occur on the tip of the cold lap on RS and gradually fade away in SZ.

Studying FSWed joints of components made of alloys 7075-T651 and 5083-H111 Kalemba-Rec et al. [265] found that the weld centres comprised fine, equiaxed grains resulting from dynamic recrystallization. For a particular TRS, no differences in grain refinement appeared. The insufficient heat input had a neglected effect on grain size changes. However, the microstructure consisted of regions in the form of bands differing in grain size and in chemical composition. The bands came from both base alloys: one formed by the 7075 alloy and the other by the 5083 alloy. The dominant region of the stir zone comprised elements from the alloy from the advancing side. Studying the post-weld heat treated dissimilar FSWed 7075 and 2024 joints Safarbali et al. [266] reported that fracture existed at the interface between thermo-mechanical affected zone TMAZ and heat affected zone HAZ on the retreating side 7075 of as-welded joint, while by applying post-weld heat treatment fracture was shifted towards the stir zone SZ of the welded joint. In post-weld heat treated joints, fracture surface was inter-granular, while in as-weld joint, fracture surface was mostly trans-granular. This was due to dissolution and coarsening of precipitates within grains in post-weld heat treated joints.

Studying FSWed sheets made of dissimilar alloys 2017A-T451 and 7075-T651 Hamilton et al. [326] reported that because of the flow of surface material into the welded sheet thickness, the weld nugget comprised alternating layers of 7075 and 2017A. Such layers exhibited distinctive precipitate distributions because of their unique temperature histories affected by the material's initial position. Supersaturated surface material flew into the process zone and formed a core comprising GP zones re-precipitating upon cooling. Mid-plane and bottom-plane material flew toward the sheet surface and embraced the surface material core. Within such region, the weld temperatures exceeded the equilibrium θ phase in 2017A, lowering the hardness, and simultaneously dissolved the equilibrium η/T phase in the 7075, causing re-precipitation of GP zones upon cooling and a hardness recovery.

During studies on FSWed joints of components made of dissimilar alloys 2017A-T451 and 7075-T651 Hamilton et al. [170] reported that the microstructures comprised many dislocations due to remnants from the extrusion process and post-solution treatment stretching. The 7075 base alloy contained a much higher number of second phase particles due to the T6 temper than the 2017A alloy, being in the T4 temper. The dislocation density and the average grain size in both base alloys extruded and stretched under similar conditions were similar. The microstructure of weld nuggets was composed of interleaving bands of material from each alloy. The material from one side predominated on the other side of the nugget. On the RS of the nugget of the AS 2017A – RS 7075

 doi:10.20944/preprints202403.1458.v1

weld the number of second-phase particles in 7075 was much higher than that in 2017A, while the density of residual dislocations between the two alloys was comparable. In the TMAZ and HAZ changes in the type and/or concentration of secondary phase particles can appear, particularly distinct in the 2017A alloy placed on the advancing side during welding.

Studying FSWed joints of components made of Al-Mg_2Si alloy and 5052 Al alloy Huang et al. [269] identified three distinct zones in FSW joint: the base material zone BMZ, the transitional zone, and the weld nugget WN. The primary Mg_2Si phases comprised coarse equiaxed crystals for Al-Mg_2Si alloys in the BMZ. The WN was a mixture of rich Al-Mg_2Si and rich 5052 alloy forming a banded structure. In the WN, the equiaxed crystals varied into polygonal particles with lowered sizes in the rich Al-Mg_2Si zone. In addition to the white-rich Mg phase appearing in the rich 5052 zone near the interface, the 5052 alloy was unchanged.

Studying FSWed joints of components made of dissimilar 2024 and 6061 alloys Moradi et al. [270] found grain refinement in the stirred zone via continuous and discontinuous recrystallization. The fraction of precipitates in the stirred zone of the retreating side exceeded that of the advancing side. The extent of continuous dynamic recrystallization in the TMAZ of the advancing side was less than that of the retreating side and the recrystallized grains seldom occurred on the advancing side. The initial texture components became asymmetric after FSW process. The overall texture intensity was weaker on the advancing side and stronger on the retreating side than that in the starting materials. The discontinuous static recrystallization and/or meta-dynamic recrystallization occurred on the advancing side.

Studying double-sided FSWed joints of components made of 6082-T6 and 7075-T6 dissimilar alloys Azeez and Akinlabi [272] reported that the microstructure deviated from the conventional trend. The weld nugget exhibited no onion ring with a long flow arm. The worm hole defect occurred at the heat affected region of the 6082-T6 alloy. Little abnormalities at the retreating side were caused by the pre-heating of the plates during the initial welding process.

Studying single-sided FSWed joints of components made of dissimilar 6082-T6 and 7075-T6 alloys Azeez et al. [328] reported that the equiaxed grain structures resulted from the dynamic recrystallization mechanism at the weld nugget. Some microstructure imperfection occurred at the weld nugget when 6082 Al plates were clamped on the retreating side to the backing plate. However, deviation in the positioning of the Al plates prevented the fabrication of good bonding and quality welds despite the material flow and mixing occurrence.

Studying FSWed joints of dissimilar alloy 6061-T651 and 5A06-H112 Peng et al. [273] noticed that the grain structure evolution in the stir zone was dominated by continuous dynamic recrystallization. The grain size in the HAZ and TMAZ was refined. Fractures in all tensile specimens were of ductile nature due to the presence of dimples. The enhancement of heat input enlarged the size of HAZ and lowered the slant angle of HAZ leading the fracture angle to decrease and changing the dimples from inclined ones to normal ones. Shear stress formed shallow and inclined dimples, whilst equiaxed and normal dimples resulted from normal stress.

The FSWed joints of dissimilar alloys 2024-T3 and 6063-T6 studied by Sarsilmaz [275] comprised several weld zones including BM, SZ, TMAZ, and HAZ formed in close relation to plastic flow and frictional heat generation during the welding process. Such joints were sound without any micro cracks, micro voids, and unbounded regions in the welded interface. There were different morphologies of the micro-structure at interface zone of joint. All welds exhibited the formation of the elliptical onion structure in the weld center. The SZ also included onion rings where the tool pin contacted the welded parts. Onion ring patterns exhibited lamellar-like structures of stacked two materials. Under low values of traverse speed and high TRS, when higher frictional heat was generated, generated weld nugget was wider than under other parameters. The higher temperature and severe forging deformation resulted in grains smaller than those of the base metal. The SZ had a fine equiaxed grain structure. Under low values of TRS and WS, the clear vase-like boundary line appeared between TMAZ and SZ due to high deformation and frictional heat between the weldment and the tool pin.

 doi:10.20944/preprints202403.1458.v1

Studying FSWed joints of components made of 2219-T87 and 2195-T8 dissimilar alloys No et al. [276] found that the microstructure of the weld joint underwent dynamic recrystallization because of high deformation and frictional heat. During studies on FSWed joints of components made of dissimilar Al alloys: wrought 2017A and cast AlSi9Mg Kopyscianski [277] reported that the weld microstructure comprised alternating bands of the welded alloys. The AlSi9Mg alloy on the advancing side dominated the weld center. The grain size within the bands was close in both alloys. The nugget side comprised a high density of the bands of the 2017A alloy.

Studying Fessed joints of the 6061-7075 alloy Bijanrostami et al. [279] found that under high heat input conditions including high rotation and low WSs, large grains and smaller dislocation densities appeared in the SZ. Contrarily, under low heat input conditions, various defects developed. Studying the effect of the TRS to the WS ratio (υ ratio) on the strength of the FSWed joints of dissimilar alloys 6082-T6 and 5083-H111 Kasman et al. [280] found that the small cavity- and tunnel-type defects occurred at the nugget zone, profile of which contained various onion rings. According to Palanivel et al. [281] the FSW joints can comprise defects such as pinhole, tunnel defect, piping defects, kissing bonds, cracks, etc. caused by the improper flow of metal and insufficient consolidation of the metal in the weld zone. Studying FSWed joints of components made of 5052- H32 to 6061-T6 blanks Doley and Kore [282] found that the dynamic recrystallization and finer grain size with uniform mixing appeared at the center of SZ. Intermetallic compounds were also formed during welding. Studying FSWed joints of components made of the dissimilar 2024-T6 and 7075-T6 alloys Saravanan et al. [283] found that the joint fabricated under D/d ratio equal to 3 provided the fine recrystallized structure of SZ, and the grain size smaller than the base material grain size due to smaller shoulder diameter. Studying FSWed joints of sheets made of dissimilar Al-Mg-Si/Al-Zn-Mg alloys Yan et al [284] found that different joint cross-sections were obtained for different sheet configurations. Coarser β' phases occurred at the heat affected zone HAZ of the AlMgSi alloy side.

Yan et al.[284] reported that for the Al–Zn–Mg AS joints, the precipitated phases were the AlFeMnSi or AlMnCrSi phases and the β′ phase owned sizes of about 0.5–0.8 μm. For the Al–Mg–Si AS joints, similar precipitated phases occurred with smaller β′ phase owning sizes of about 0.3–0.5 μm. The quantity of the β′ phase on the Al–Mg–Si AS joint was more than that on the Al–Zn–Mg AS joints. The secondary phase particle at the joint fracture region was characterized by submicron β′ phase. For the Al–Zn–Mg AS joint the β′ phases were more dispersed, which was beneficial to the bridging effect. The FSWed joints of dissimilar alloys 2024-T3 and 6061-T6 studied by Zapata et al. [285] exhibited various regions including the TMAZ and HAZ with similar shapes, locations, and sizes in all the samples. All the sample cross-sections presented a ring flux pattern in the nugget region indicating the vertical movement of the material.

Studying butt FSWed joints of 2 mm thick plates including the one rolled from ultrafine-grained UFGed 1050 Al alloy and the one made of the 6061-T6 alloy Sun et al. [286] found that in the stir zone, the initial nano-sized lamellar structure of the UFGed 1050 Al alloy plate took the form of an equiaxial-grain one with a larger average grain size caused by the dynamic recrystallization and subsequent grain growth. Simultaneously, an equiaxial-grain structure with a significantly smaller grain size occurred in the 6061 alloy plates, together with coarsening of the precipitates.

Studying FSWed joints of 2024-T6 alloy Sun et al. [329] found that the metal in the weld nugget zone WNZ came from the base metal of the advancing side, when the thread was the driving force of the downward movement of the FSW plastic metal. All joints formed a particularly good union, with an onion ring pattern appearing in cross-section. The minimum grain size of the WNZ obtained with the conical cam thread stirring head was 7~12 μm. FSW usually allows elimination of porosity, small distortion, and so on [372,373]. During studies on butt FSWed joints of components made of dissimilar 6061 to 7050 alloys Rodriguez et al. [289] found in joints microstructure occurred distinct lamellar bands and various degrees of intermixing affected by TRS .

Studying lap FSWed joints of plates made of dissimilar alloys 6111-T4 and 5023-T4 Yoon et al. [47] found that the threaded probe well correlated to the onion ring structure formed as soon as it touched the probe. The remnant of original interface between the top and bottom plates after the

 doi:10.20944/preprints202403.1458.v1

welding process and asymmetrical flow around rotating tool well correlated to the formation of void defects under low heat input conditions.

During studies on FSWed components of the heat treatable 6061 and non-heat treatable 5086 alloys Ilagovan et al. [290] found that the use of threaded tool pin profile provided better flow of materials between two alloys and the generation of defect-free stir zone. Such tool provided formation of finer and uniformly distributed precipitates, circular onion rings and smaller grain compared to the tapered pin profiled tool. During studies on butt FSWed joints of components made of dissimilar alloys 2050 and 6061 Reza-E-Rabby et al. [291] found that the stir zone comprised bands of mixed and unmixed material with the degree of material intermixing increasing with the enhancement of TRS. Under monotonic tensile loading, welds failed via the heat-affected zone on the 6061-alloy side of the weld. For the low TRS, failure appeared in the stir zone due to poor material intermixing.

Studying the anodizing behavior of FSWed joints of dissimilar 5083-O and 6082-T6 alloys in 4M H_2SO_4 solution Donatus et al. [292] found that the 5083-O rich zones were more oxidized during anodizing compared with the 6082-T6 rich zones. The nugget and the thermo-mechanically affected regions of the individual basic alloys exhibited a decrease in porous anodic oxide thicknesses. Sputtering deposition of pure Al on the weld, prior to anodizing, lowered the variations in the oxide thicknesses across the weld. Such a method prevented the boundary dissolution related to the activity of the Mg_2Si phase often occurred after anodizing the dissimilar weld of the alloys. Studying FSWed joints of plates made of dissimilar cast Al–Si alloys A319 and A413 Karam et al. [293] found that the joints comprised the Si particles and of α-Al grains. At the center of stirred zone, the Si particles could be more uniformly distributed than in the other zones.

Studying the butt FSWed joints of dissimilar 7075-O/6061-O and 7075-T6/6061-T6 alloys studied by Ipekoglu and Cam [294] found that the as-welded 1500/400 O joint exhibited no welding defect except its root region, while some weld defects appeared in such a joint after post-weld heat treatment PWHT. The joint areas of the dissimilar T6 joints obtained in both the as-welded and post-weld heat-treated conditions exhibited no weld defects. The dynamically recrystallized zones DXZs of all the as-welded joints both in the O and T6 temper conditions comprised a layered (banded) structure formed due to the mixing of two BMs, known as the intercalation of BMs. Microstructure of the DXZs was dominated by the alloy located on the AS. The typical orientation of the grains in the TMAZ was strongly affected by the material flow resulting from the action of the stirring tool. PWHT had only a slight effect on the shape of the grains in the TMAZ. PWHT also caused the formation of abnormal grain growth AGG, both in O and T6 joints. The AGG formation occurred all over the cross-section, in the O joints, whereas in the shoulder regions in the T6 joints.

Studying the lap FSWed joints of dissimilar 2024-T3 and 7075-T6 alloys Song et al. [296] found that welded joints comprised four typical zones including base metal BM, HAZ, TMAZ and SZ. The grain structure in the HAZ of the upper 2024 sheet was like that of BM. In TMAZ microstructure comprised severely deformed and elongated grains resulting from drastic plastic deformation of SZ during FSW. In SZ, the microstructure included dynamically recrystallized fine equiaxed grains resulting from the drastic deformation induced by sufficient stirring during welding. Grains in the upper SZ were coarser than those in the bottom SZ due to the former had more time to grow up provided by the higher temperature compared to those in bottom SZ. During studies on FSWed joints of components made of dissimilar 5083-H111 and 6351-T6 alloys Palanivel et al. [298,306] reported that the weld zone comprised three types of microstructures, namely unmixed region, mechanically mixed region, and mixed flow region. Studying FSWed joints of components made of dissimilar A356 and 6061 alloys Ghosh et al. [302] reported that microstructure of WN had uniform dispersion of Si-rich particles, fine grain size of 6061 alloy, and disappearance of the second phase within 6061 alloy.

Studying the FSWed lap joints of 7075-T6 and 2198-T351 studied by Velotti et al. [330] noticed that the hook defect comprising an S-shaped separation line between the two materials joined, typical for such joining technique in this specific configuration was not fully avoidable, as the stirring action caused by tool motion cannot completely mix two materials initially stacked. Such a defect caused a preferential path for the crack growth and propagation and for the localized corrosion phenomenon,

 doi:10.20944/preprints202403.1458.v1

affecting the joint behavior. The kissing bonds resulted from inadequate material mixing and stirring occurred in the core of the nugget zone and in the radii between skin and stringer. Both the alloys exhibited microstructure with round shaped equiaxed grains. The average grain size for the 2198 was about the 30% of the one of the 7075.

Investigating FSWed joints of plates made of dissimilar Al–Cu alloy 2219-T87 and Al–Mg alloy 5083-H321 Koilray et al. [304] found the material placed on the advancing side dominated the nugget region. Welds comprised base material zone BM, stir zone or weld nugget SZ, thermo-mechanically affected zone TMAZ, and heat-affected zone HAZ. BM contained many undissolved second-phase intermetallic particles. The second-phase particles in alloy 2219 comprised Al_2Cu (θ) eutectic particles, while alloy 5083 included iron/manganese aluminides. Compared to alloy 2219, alloy 5083 comprised fewer and finer second-phase particles. The TMAZ on the advancing side exhibited highly deformed grains, with discernible SZ/TMAZ and TMAZ/HAZ boundaries. However, on the retreating side, these interfaces were diffused, especially the latter. In the HAZ, on either side of the weld nugget, the grain structure exhibited no noticeable changes compared to the respective base materials.

Studying the FSWed dissimilar cast and wrought 6061 alloy Dinaharan et al. [305] found that the microstructure of the dissimilar joints comprised four zones including base metal, HAZ, TMAZ and weld zone. The weld zone covered an unmixed region and a mechanically mixed one. The unmixed region consisted of the microstructure of cast and wrought 6061 alloy. The mechanically mixed region occurred near the zigzag line containing the microstructure of both Al alloys. Some degree of penetration of one alloy into the other occurred. The plasticized dissimilar alloys were mechanically coupled in the mechanically mixed region. Both the materials after dynamic recrystallization during FSW exhibited finer grain structure than before FSW.

Studying FSWed joints of components made of dissimilar alloys 5052-H34 and 5023-T4 Song et al. [127] noticed that in the same manner as constitutional liquation, at high heating rate, the main liquation-inducing precipitates were not dissolved in the matrix and reacted with Al to form the partially melted zone PMZ, after which liquation cracking occurred where strain was applied to the PMZ. Solid solution treated 5023 alloy comprised in the matrix many precipitates including Mg_2Si, Al_6CuMg_4, and $Al_6(CuFe)$. Al_6CuMg_4 formed a stable phase at room temperature and reacted with the Al matrix at around 470°C. The main liquation-inducing precipitate was Al_6CuMg_4 forming the PMZ (constitutional liquation) at around 480 °C during the FSW process.

Studying FSWed joints of components made of dissimilar A356 and 6061 alloys, Ghosh et al. [303] reported that the structure of joints exhibited recovery-recrystallization in the stirring zone and breaking of a coarse eutectic network of Al–Si. Dispersion of fine Si rich particles, refinement of 6061 grain size, low residual stress level and high defect density within weld nugget allowed increasing bond strength. Lowering the tool rotational and traversing speed enhanced the domination of such phenomena.

Studying the FSWed joints of dissimilar 5052/A5J32 alloys, Kim et al. [307] reported that the weld nugget was formed according to the arrangement of the materials. The softened material moving from the AS toward the RS caused the formation of an empty region with the shape of the tool pin. The material on the RS filled most of the upper half of the empty region. When the A5J32 alloy was fixed on the RS, a high amount of the base material on the retreating side A5J32 was stirred toward the advancing side 5052, as the rigid material A5J32 was easily pushed out from the soft material 5052 and the two base materials were stirred in a zigzag shape. When the 5052 alloy was fixed on the RS, the flow of 5052 (retreating side) was limited by the more rigid material on the advancing side A5J32. The softened A5J32 accumulated unnaturally. Under conditions with a lower heat input, such as at 1000 rpm and 400 mm/min, some welding defects occurred. Under opposite conditions, defect-free welds were obtained.

Studying the FSWed butt joints of 7050-T7451/ 2024-T351 alloys, Prime et al. [308] noticed that the stirred zone, i.e., the weld nugget or dynamically recrystallized zone comprised fine equiaxed grains. The nugget exhibited the onion ring structure. On both sides of the stir zone, there are TMAZs comprising highly deformed grains from the stirring action. The TMAZ was more uniform on the

 doi:10.20944/preprints202403.1458.v1

advancing side and more diffuse on the retreating side. The heat-affected zones extended out of the TMAZs on both sides.

Miles et al. [332] reported the occurrence of failures in the heat-affected zone HAZ of the 6022 or in the weld nugget itself for the welded joints of components made of the dissimilar 5182/6022 and 5754/6022 alloys. The 5182/5754 alloy pair studied was softening-free, as such alloys were in the annealed condition, while the softening occurred in the 6022 side of the 5182/6022 and 5754/6022 alloy pairs.

Ouyang and Kovacevic [333] studied material flow and microstructural evolution for welded joints of components the one made of 6061alloy as itself and the second of dissimilar alloys 6061-T6 and 2024-T3 both of 12.7 mm in thickness obtained via FSW under different welding conditions. They found that plastic deformation, flow, and mechanical mixing of the material were characterized by asymmetry characteristics at both sides of the same and dissimilar welds. The microstructure in dissimilar 6061 /2024 alloys welds highly differed from that in case of a 6061 alloy to itself. Vortex-like structures with the concentric flow lines characteristic for a weld of 6061 alloy to itself, and alternative lamellae with various alloy constituents for a weld of 6061 and 2024 alloy, resulted from the stirring by the threaded tool, in situ extrusion, and traverse motion along the welding direction. The nugget zone of dissimilar 6061-Al/2024-Al welds comprised the mechanically mixed region with the dispersed particles of different alloy constituents, the stirring-induced plastic flow region with alternative vortex-like lamellae of the two Al-alloys, and the unmixed region with fine equiaxed grains of the 6061 alloy. Within these regions, the material withstood an extremely high degree of plastic deformation due to the occurrence of dynamic recovery or recrystallization of the microstructure. The degree of material mixing, the thickness of the deformed Al-alloy lamellae, and the material flow patterns were affected by the related positions in the nugget zone and the processing parameters.

Studying the butt FSWed joints of dissimilar 2024-T351/ 6056-T4 alloys, Amancio-Filho et al. [260] reported that the welds comprised four various regions including base material BM, heat affected zone HAZ, thermo-mechanically affected zone TMAZ and stir zone. The BM of 2024-T351 alloy microstructure exhibited elongated grains in the rolling direction. This BM contained copper-rich particles being second phase θ-$CuAl_2$. The BM of 6056-T4 alloy also revealed the microstructure with grains oriented in the rolling direction. This BM comprised two kinds of particles: the ones rich in Mg and Si, identified as the intermetallic β-Mg_2Si and the others rich in Mn and Fe. The stirred zone of joint exhibited a lamellar material flow pattern due to material mechanical mixing. The SZ revealed a dynamically recrystallized microstructure with refined grains. The thermo-mechanically heat-affected zone of the alloy 6056-T4 possessed annealed structure. Change in grain orientation started in the transition between TMAZ/stir zones. The grains were rotated by tool action and by reaching approximately 90° tilting, some degree of recrystallisation occurred, represented by a lowered grain size. Lee et al. [261] found that the microstructures of dissimilar formed A356/6061 joint exhibited the mixed structures of two materials. The stir zone exhibited the onion ring pattern look-like a lamellar structure. The microstructure of the SZ comprised the material fixed at the retreating side.

Studying the FSWed joints of components made of 7003/7046 dissimilar alloys Yang et al. [312] observed an obvious "S"-shaped dividing line in the weld nugget area of the 7003/7046 dissimilar alloy FSW joint. Both sides of the S line comprised fine equiaxed grains, with a size of about 5 μm; the grain size in the heat-affected zone and the heat-affected zone was higher than that in the nugget zone, and the structure in the heat-affected zone comprised recrystallized grains and recovered grains. The coarsening of subgrains lowered the grain size of the heat-affected zone on the 7003 side, and the grain size of the heat-affected zone on the 7046 side was coarsened.

Investigating FSWed joints of dissimilar 2219-5083 alloys Mastenaiah et al. [321] found that the nugget zone revealed the mixing pattern highly affected by the tool offset, the tool rotation speed and the tool traverse speed. Intimate mixing of dissimilar alloys occurred at higher tool rotation speeds and lower tool traverse speeds.

 doi:10.20944/preprints202403.1458.v1

Studying the FSWed joints of dissimilar 2618-T87/ 5086-H321 alloys, Sasikala et al. [336] reported that the nugget region was dominated by material on the forward-moving side. The weld contained four microstructural zones: BM, SZ, TMAZ, and HAZ. Both BMs contained particles of second-phase intermetallic. Iron/manganese aluminides appeared in alloy 5086's second-phase particles, while eutectic Al_2Cu particles were in alloy 2618. Particles in the alloy's second phase 5086 were smaller and finer than those in alloy 2618. The grain structure of the weld nugget was like that in the HAZ. The SZ/TMAZ and TMAZ/HAZ boundaries were clearly distinguishable on the forward-moving side of the TMAZ. Dispersion of them was higher on the RS.

Studying the single-sided butt FSWed joints of 3003-O alloys Aydin et al. [339] reported that the welds comprised four zones: BM, HAZ, TMAZ and SZ. The BM microstructure revealed the elongated grains resulting from the rolling operations. The stirred zone revealed a fine-grained equiaxial dynamic recrystallized microstructure. The grain size in the SZ was smaller than that of BM. An enhancement in rotation speed and lowering WS lowered the grain size in the SZ due to the higher heat input for dynamically recrystallized microstructure. The TMAZ microstructure exhibited a highly deformed structure near the SZ zone due to less heat and deformation appearing in TMAZ compared to those in the SZ. After the TMAZ appeared the HAZ exposed only to a thermal cycle, but the plastic deformation therein was insufficient to modify the initial grain structure. The transition zones from the stirred zone to TMAZ of the joints also occurred. On the AS a distinct boundary between the SZ and the TMAZ appeared while the boundary between the SZ and the TMAZ on the RS was unclear . The region with Al_2O_3 particles, stretching from the top to bottom across the whole section of all 3003-O weld zones at the RS contained the 'kissing bond' defects.

Aydin et al. [337] found that BM microstructure comprised the elongated grains resulting from the rolling operations. In the weld centre the NZ occurred, which revealed dynamically recrystallized grains. On the AS, microstructure varied rapidly due to the higher speed of plastic material than on the RS, and a distinct boundary between the NZ and TMAZ occurred. On the RS, microstructures from the NZ to TMAZ varied more smoothly. In the TMAZ the grain structure was deformed but no recrystallization occurred. The microstructure in the HAZ affected by the heat but not by deformation, was like that of BM; the grains were slightly overgrown due to the exposure to welding heat.

Studying the FSWed of 4 mm thick plates made of alloy 2024 Weglowski et al. [340] reported that the joints exhibited a characteristic shape of a nugget zone, heat-affected zone and thermo-mechanically affected zone.

Studying the FSWed joints of 2024-T4 alloy Nejad et al. [341] reported that the best welds features including the finest grain in stir zone, the best visual quality and smoothness, were obtained with rotation speed of 500 rpm, traverse speed of 55 mm/min, plunge depth of 2.7 mm and by threaded tool, and with rotation speed of 1300 rpm, traverse speed of 115 mm/min, plunge depth of 2.9 mm and by unthreaded tool. Unthreaded tool provided more uniform structure from the point of view of smoothness. The WE widely varied in range from 35.6% to 95.7%.

Investigating FSWed joints of 8 mm thick plates made of 2014-T6 Al alloy Lin et al. [343] found that the different regions of the joint exhibited different microstructure variation affected by different thermomechanical actions therein.

Liu et al. [374] reported that defects including void, unbonded interface and incomplete refilling appeared when using 7075 alloy as the upper sheet. No defects occurred when using 6061 alloy as the upper sheet. With enhancement of the sleeve plunge depth, better material mixing appeared between the upper and lower sheets.

Studying FSWed joints of components made of 2017A alloy Mroczka et al. [311] reported that the weld nugget exhibited an average grain size of 5 μm, moderate density of dislocations as well as the presence of nanometric precipitates located mostly in grains interiors. The weld nugget presented ductile fracture with brittle precipitates in the lower part.

Investigating FSWed joints of components made of a cast AlSi9Mg and 2017A alloy Mroczka [310] found that welds comprised defects, despite greater plasticity of the material occurring due to the raising of temperature. The constituent stable phases within the cast alloy exhibited considerable

 doi:10.20944/preprints202403.1458.v1

fragmentation to various degrees. The material above the weld nugget was unmixed and comprised non-welding micro-defects. A metastable state of the 2017A alloy occurred within the weld nugget zone due to the natural ageing.

Studying butt FSWed joints of 6013 Al plates obtained via pin offset technique Kasman and Ozan [313] found kissing bonds in welds, originating from the broken oxide layers, and formed particularly in the stir zone. The microstructure of joints comprised phases belonging to Mg_2Si, $Al_4Cu_2Mg_8Si_7$ and Al(MnFe)Si.

Kasman and Yenier [322] reported that the microstructure of the two BMs comprised elongated grains in the rolling direction. The nugget zone included the fine equiaxed grains formed by the occurrence of dynamic recrystallization. The structure of grains in the TMAZ was deformed, elongated, and oriented to the rotation of the pin. The size and orientation of grains of the TMAZ differed from that on the NZ. Compared to the TMAZ structure, that of HAZ comprised grains overgrown and was like that of the BM.

Investigating butt FSWed joints of components made of dissimilar 7020-T651 and 5083-H111 alloys Torzewski et al. [352] found various shapes of the stir zone and defects caused by excess and insufficient heat input.

Studying spot FSWed joints of sheets made of 5454 alloys Choi et al. [353] found that the enhancement of tool rotation speed changed the macrostructure of the friction-stir-spot-welded zone, especially the geometry of the welding interface. However, the change in the dwell time at the plunge depth of the tool only slightly affected the microstructure of the welds.

Dong et al. [355] reported that SZ comprised fine and equiaxed grains due to dynamic recrystallization. With the enhanced cooling rate, microstructure of the UFSW joint is finer than that of air-cooling FSW, and the area of HAZ and TMAZ in the UFSW joint becomes smaller. The precipitation evolution was strongly affected by the processing parameters of UFSW. In the 1000-120 sample, fine precipitates exist in HAZ, TMAZ and SZ

Zhou et al. [357] reported that the pattern of the weld cross section was a “flat T” and no obvious “S curve” occurred in nugget zone NZ. Heat affected zone HAZ and thermo-mechanically affected zone TMAZ were also narrow. The nugget zone NZ comprised the grains finer than those in other zones. A clear band line appeared between the nugget zone NZ and thermo-mechanically affected zone TMAZ located between NZ and the heat affected zone HAZ. There was no clear dividing line between HAZ and the base-metal BM. No obvious “S curve” appeared in all joints.

Tra et al. [375] reported that in case of FSW process the fatigue crack propagation FCP rates depended to the propagating location, the test temperature, and the PWHT conditions.

Studying FSWed joints of sheets made of 6013-T6 alloy Kafali and Ay [389] reported that the microstructure of the welding zone comprised four subzones including a base material, heat affected zone HAZ, thermo-mechanical affected zone TMAZ and weld nugget. The parent material and the weld region contained homogenous distributions of the fine and coarse Mg_2Si particles. A dynamically recrystallized grain structure appearing in the weld nugget exhibited a smaller grain size compared to the BM. Such dynamically recrystallized grains were equiaxed contrary to the elongated grains in the rolled BM. Fine equiaxed grains in the FSW region occurred due to dynamic recrystallization due to plastic deformation during the welding process.

Investigating the butt FSWed joints of sheets made of the dissimilar 2014-T3/5059-H11 Al alloys Saleh [377] found that a structure of fine grain occurred in the nugget zone due to recrystallization.

Studying the FSWed joints of components made of 2219-T87/2219-T62 alloys Venkateswarlu et al. [378] found that the microstructure of the 2219-T62 welds exhibited coarse grains formation in the thermo-mechanically affected zone and heat-affected zone.

For FSWed joints of Al alloy 2014-T651 Kollapuri [379] reported that HAZ comprised large grain size compared to the nugget zone.

Studying FSWed joints of components made of 3003 alloy with different initial microstructures Tan et al. [380] reported that the size of recrystallized grains and the number of second-phase particles in the weld nugget zone WNZ lowered with a decrease in welding ambient temperature. At the same

 doi:10.20944/preprints202403.1458.v1

welding condition, both the size of recrystallized grains and the volume fraction of (Fe,Mn)Al_6 particles in the hot bands were below those in the annealed hot bands.

Studying the FSWed joints of plates made of 7204-T4 alloys Deng et al. [381] reported that the average grain size AGS and recrystallization fraction of nugget zone NZ reached 4.7 μm and 81.9 % in as-welded AW treatment, 4.8 μm and 82.4% under the post-weld artificial aging AA treatment, 5.9 μm and 86.5% under the heat treatment of solid solution followed by artificial aging SAA, respectively. The grain structure of NZ was slightly influenced by AA treatment, and the AGS and recrystallization fraction of NZ enhanced by 25.5% and 5.6% under SAA treatment.

Zhao et al. [314] studied the influence of exchanging advancing AS and retreating RS side material on microstructure, mechanical properties, and electrochemical corrosion resistance FSWed joints of components made of dissimilar 6013-T4 and 7003 alloys. The joint with the 6013-T4 placed at the advancing side AS was called the A6R7 joint. Accordingly, the A7R6 referred to the joint with the 7003-alloy placed at the AS. The authors reported that various joint cross-sections appeared when exchanging AS and RS materials. The material on the AS was more deformed during the welding process. When the 6013 alloy was positioned on the AS, the plastic flow of the weld was more sufficient.

Studying FSWed joints of components made of dissimilar 2024-T3 and 2198-T3 alloys Texier et al. [287] found banded macrostructures with heterogeneous mechanical properties in the shoulder-affected region. They were accompanied by pronounced textures regions. The banded macrostructures appeared in the nugget region.

For FSWed joints of 6061-T6 alloy Juarez et al. [316] noticed four characteristic zones of friction welding including agitation zone (stir zone), TMAZ, HAZ and unaffected material UFM. The fracture surfaces of tension specimens revealed the micro-voids present in the fracture zones for the three cases BMW, HTBW and HTAW. The fracture surface of the base material presented micro-holes of 6-8 μm in diameter. For the case of BMW and HTBW, the diameter of the micro-holes was greater compared to the base material at 8-10 and 10-12 μm, respectively. It was due to the reduction and separation of nucleation sites, allowing them to grow at a larger size. For HTAW case, the micro-holes had small and shallow sizes, due to the occurrence of numerous nucleation sites causing the merge of micro-holes, limiting growth at a larger size. Solubilized and partial ageing heat treatments of 6061-T6 alloy initiated the formation and distribution of the precipitates in the material. The predominant precipitates for the BMW and HTBW cases were Al-Mg and Al-Si, respectively; while for the HTAW case, it was Fe-Mg_2Si.

Unfried-Silgado et al. [382] studied the influence of shoulder geometry of tool (flat and featured by concentric circles and by spirals) on microstructure and mechanical properties of FSWed joints of AA1100 alloy obtained using a milling machine revolutionary under pitch value (R) constant of 0.1 mm/rev. They reported that the featured shoulder tools strongly affected the thermal cycles, generating a plasticized wide region and the biggest grain size in the stir zone when compared with the flat shoulder tool. The featured shoulder tools induced thermal cycles in the regions out of the stir zone less severe than flat shoulders. The surface area of tested tools was 27% and 11% lower in flat shoulders than in featured shoulders, respectively.

Studying butt FSWed joints of dissimilar alloys 6061-T6/7075-T6 Godhani et al. [317] noticed that the size of the grains varies in the different joint zones including nugget zone NZ, thermo-mechanically affected zone TMAZ, heat-affected zone HAZ, and base metal BM. Size of the grain deciding the strength was affected by amount of heat input, mixing of the materials, and the rate of cooling. The high grain density of 7075 induced the strength of 7075 was higher than of 6061. The grain density in the nugget zone is the highest, and hence the welded specimen has higher strength compared to the base metals. The failure can occur from the advancing side of joint as the density of grain was less compared to other locations.

Aval et al. [358] studied the effect of tool on the mechanical properties and microstructural behaviour of FSWed 5 mm-thick plates made of 5086-O and 6061-T6 alloys. They found that the tool with a concave shoulder and a conical probe with three grooves provided higher heat input and temperatures promoting more homogeneous stir zones than the tools with flat shoulders and

 doi:10.20944/preprints202403.1458.v1

threadless or threaded cylindrical probes. The grain sizes of the SZ on the 6061 side were finer than those on the 5086 side, and lowering the weld pitch, i.e., a ratio of WS/TRS induced coarser grain structures in the SZ. The material in the weld nugget zone was a mixture of the two alloys, with closer to Mg content in 6061 region.

Studying the FSWed joints of components made of 5052 and 6061 alloys obtained with various pin-eccentric stir tools, Wang et al. [383] found that the welding heat input caused both the coarsening of strengthening precipitates and dynamic recrystallization and softening of the nugget zone (NZ). The use of pin eccentricity promoted the material flow in the NZ and the higher area of the "onion ring". The average grain size and fraction of recrystallized grain in the NZ lowered with the enhancement of the pin eccentricity.

Guo et al. [384] studied FSWed joint of components made of dissimilar 6061/7075 alloys. They found that the material mixing was much better for 6061 alloy on the AS and multiple vortexes centers formed vertically in the nugget center. The onion ring comprised three distinct sub-layers: 6061 alloy sub-layer, 7075 alloy one, and mixed sub-layer of the two alloys. The thicknesses of these onion ring sub-layers were in range 30–100 μm. Both AA6061 and AA7075 alloys were dynamically recrystallized. The grain size highly lowered with the enhancement of WS. The grain size of 7075 alloy sub-layer was much lower than that of AA6061 sub-layer in the same weld. The fractured surfaces of tensile tested specimens exhibited many equiaxed dimples with various size. Shallower dimples occurred in the fractured surface of the joints obtained under lower heat input. Second phase particles comprising incoherent β-Mg2Si and various Al–Fe–Si intermetallics effectively provided nucleation sites for microvoids during fracture process.

Sato et al. [385] investigated the mechanical and microstructural behavior of FS welded joints of 2024/7075 alloys. They found that the amount of heat generation highly influenced the material movement around the pin. The high heat input caused onion ring patterns in the SZ, while low heat input clearly divided the SZ into 2024 and 7075 regions.

Da Silva et al. [386] investigated FSWed joints between components made of dissimilar 2024/7075 alloys. The maximum WE was of about 96% and the welded specimens were fractured in HAZ of RS.

The 3 mm thick plates made of dissimilar 7075/5083 alloys, studied by Dewangan et al. [387], were FSWed using tool made of H13 steel, under TRS of 1400 rpm and WS of 20 mm/min and 45 mm/min, obtaining grain size in range 6-10 μm.

The 2.5 mm thick plates made of 2219/7475 alloys, studied by Khan et al [388], were FSWed using tool made of High Carbon Steel and possessing cylindrical threaded pin, under rotating speed of 900 rpm and WS of 100 mm/min, obtaining grain size below 6 μm.

Abidi et al. [389] studied T-FSW joint of 2 mm thick 7075/2024 alloys with 7075 placed as stringer and 2024 as skin obtained using tool made of High chromium high carbon steel with shoulder diameter in range of 12-16 mm, tapered cylindrical pin with length of 1.9 mm and diameter of 1.8 mm on the insertion side and of 5.6 mm on the shoulder side, under TRS in the range of 560-900 rpm, WS range of 40-63 mm/min and tilt angle of 2 degrees. They found that the TMAZ zone underwent induced plastic deformation caused by lesser heat input. This led to partial recrystallization forming coarse grains.

4.8.1.5. Mechanical Properties Hardness

The hardness of the FSW joint was strongly associated with the joint strength and its deformation behavior. The hardness distributions exhibited a high asymmetry along the cross-section of dissimilar material joints due to the various microstructural zones SZ, TMAZ, HAZ resulting from the thermo-mechanical history during welding. As the maximum temperature occurred at the SZ, precipitates or strengthening particles dissolved partially or completely lowering hardness in SZ. The lowest hardness values appeared in the HAZ due to the coarsening of precipitates or over-ageing. Thus, failures occurred most in the HAZ zone or site. The hardness values in SZ were higher than those in the BM (exhibiting sometimes low strength values) due to the combined influence of grain refinement

 doi:10.20944/preprints202403.1458.v1

and the effect of both BMs in the SZ. However, various initial conditions of heat-treatable alloy combinations could make such hardness distribution completely different [256].

Studying FSWed joints of components made: the first of 2024-T351/5083-H112 alloys and the second of 7075-T651/2024-T351 alloys, Niu et al. [262] characterized joints hardening by the ratio of HVf/HVw, where HVf and HVw were the microhardness of the fractured and the as-welded joints, respectively. This ratio was higher than one in the SZ, TMAZ and HAZ, which related to the strain-hardening behavior of the joints. The hardness distribution in the dissimilar material joints was strongly affected by strain hardening and the fracture origin.

For the FSWed joints of 7075-T651/2024-T351 alloys, Hasan et al. [130] found that the distribution of weld hardness determines the tensile strength of welding joint. The weld hardness drops at the HAZ of softer material. Maximum reduction in weld hardness at the heat-affected zone was achieved using the pin tool with a flute of radius equal to that of the pin.

Ge et al. [61] reported that 7075 BM exhibited higher hardness compared to 2024 BM value. The SZ of 7075 upper sheet possessed much higher microhardness than HAZ or TMAZ of 2024 lower sheet.

Kalemba-Rec et al. [265] reported that for the AS 7075 - RS 5083 welds obtained using the Triflute pin, the profiles for all TRSs were close, however, under TRS of 560 rpm, an abrupt hardness drop in the SZ occurred due to the presence of voids in the weld area. For the AS 5083- RS 7075 configuration, the hardness profiles were different. Under a TRS of 280 rpm, the hardness profile was like that for the AS 7075-RS 5083 configuration. For other speeds, the hardness in the stir zone lowered to 80 HV characteristic of the base 5083 alloy bands appearing in SZ. For both configurations, the maximum hardness in the stir zone was of 150 HV remaining constant from the weld center up to approaching the 7075 alloy. Regardless of the alloy configuration, on the 5083-alloy side, the hardness was about 80 HV remaining constant transverse the weld. On the 7075-alloy side, the hardness lowered from 150 HV to 120 HV and then enhanced to 160 HV (characteristic half of a W-shape). Hardness profiles for the case of the threaded taper tool were like those for the Triflute pin, but values of hardness were higher. The maximum hardness in the weld center can reach a value of 180 HV for the AS 7075-RS 5083 joints, while for the AS 5083–RS 7075 configuration, it was about 160 HV.

Investigating FSWed joints of components made of Al-Mg_2Si/5052 alloys, Huang et al. [265] reported that the hardness gradually enhanced from the BMZ of the 5052 to the welded joint to the Al- Mg_2Si BMZ.

Studying FSWed joints of components made of dissimilar 2024/6061 alloys, Moradi et al. [270] found that the microhardness profile on the advancing side was almost identical, while it comprised three distinguishable regions on the retreating side.

Investigating double-sided FSWed joints of components made of 6082-T6/7075-T6 alloys, Azeez and Akinlabi [272] reported irregular profiling in the Vickers hardness distribution, contrary to the conventional 'W'-shape trend, due to the difference in the chemical composition of alloys and the rate of precipitation. The microhardness evolution deviated from the conventional trend.

Studying FSWed joints of dissimilar 6061-T651/5A06-H112 alloys, Peng et al. [273] reported that the nano-hardness for each zone varied according to relation BM > NZ > HAZ for the 6061 side, indicating that the mechanical properties of 6061 were weakened after FSW. On the 5A06 side, the change of mechanical properties for each zone was small after FSW. The nano-hardness in NZ and TMAZ was slightly higher compared to that in BM. The mechanical properties of 6061 were more vulnerable to heat input than those of 5A06.

Investigating FSWed joints of components made of 2219-T87 and 2195-T8 alloys, No et al. [276] found that the microhardness in the upper part of stirring part exhibited even distribution. In the middle- and lower-part hardness on AS with 2195 alloy was clearly higher compared to that on RS of joint. Hardness increased with enhancing TRS and WS.

During studies on the effect of shoulder diameter to pin diameter ratio on microstructure and mechanical properties of FSWed joints of dissimilar alloys 2024-T6 and 7075-T6 Saravanan et al. [282] placed 2024-T6 alloy on the AS, and 7075-T6 on the RS. They reported that the joints fabricated with the ratios of 2 and 2.5 fractured in heat-affected zone HAZ region of the advancing side, and joints

 doi:10.20944/preprints202403.1458.v1

fabricated with the ratios of 3, 3.5, and 4 fractured at stir zone SZ. For all the D/d ratios, minimum hardness was seen at HAZ region in the advancing side and was maximum in the SZ and again decreases at HAZ in the retreating side.

Studying butt FSWed joints of ultrafine-grained UFGed 1050/6061-T6 alloys, Sun et al. [286] reported that the base metal of both the UFGed 1050 and 6061-T6 alloys exhibited the highest microhardness value. For both materials from the BM to HAZ microhardness lowered gradually. For the 6061-T6 alloy, such a decrease was due to the intensive solid solution of precipitates and the simultaneous occurrence of coarsening of particles resulting from the weld thermal cycles. The stir zone also comprised some regions with a high hardness value like that of the base metal, due to the significantly refined grain size. For the UFG 1050 alloy, the hardness was lowered due to the grain growth and the dislocation density.

Investigating FSWed joints of components made of dissimilar 2024-T3/ 2198-T3 alloys Texier et al. [287] found significant differences appearing between hardness and local tensile properties.

During studies on butt FSWed joints of components made of dissimilar 6061/7050 alloys, Rodriguez et al. [289] found that due to the distinct mechanical properties of the two alloys, a consistent asymmetric microhardness distribution profile appeared across the weld nugget, independently of TRS.

Ghosh et al. [302] found that the microhardness profile was related to welded joint microstructure. Low hardness of A356 alloy appeared at RS. Enhancement in hardness near the weld line occurred due to the composite microstructure affected by both alloys. Further increment at AS appeared due to the higher strength of 6061alloy with respect to A356 alloy.

Studying FSWed joints of plates made of dissimilar 2219-T87/ 5083-H321 alloys, Koilray et al. [304] found the lowest hardness in the weldment occurred in the heat-affected zone on alloy of 5083 side.

Kim et al. [307] reported that the 5052 and A5J32 base materials had hardness values of 72 HV and 78 HV, respectively. The hardness in the welded zone of A5052 were lower compared to that of the base metal 5052 due to the dissolution of the second phase particles and annealing during the welding progress. When 5052 was fixed on the RS, the hardness in the vicinity of the shoulder exceeded that of the base metal 5052. The flow of the softened 5052 on RS was restricted by the material on the advancing side A5J32, causing the concentration of work hardening. The hardness values in the welded zone of A5J52 exceeded that of the base metal A5J52_78HV, due to the interaction of the recrystallized fine-grain microstructure and agglomeration of the precipitates. When 5052 was fixed on the RS, excessive agglomeration occurred in a narrow region, due to the restricted flow, and higher hardness occurred compared with the other region. Therefore, the hardness of A5J32 in the welded zone significantly exceeded that for the A5J32 Al alloy fixed on RS.

Studying FSWed joints of sheets made of 6013-T6 alloy, Kafali and Ay [376] reported that the average hardness of the base material reached 130 HV while for the weld nugget it was 100 HV. The average hardness in the TMAZ was lower than in the weld nugget .

During studies on butt FSWed joints of plates made of dissimilar 2014-T6/ 6061-T6 alloys Jonkheere et al. [300] found that the welds' hardness profile were affected by the proportion of each alloy included in the stirred zone, due to the difference between the softening temperatures of both alloys. The 6061 alloy's HAZ was the weak link in all dissimilar welds. The alloys placement or tool lateral shift affected the welds hardness as they influence the precipitate radius and volume fraction.

Investigating butt Fessed joints of sheets made of the dissimilar 2014-T3/5059-H11 alloys, Saleh [377] found that the TMAZs and HAZs of 2014-alloy possessed the lowest hardness values. The hardness lowered through the weld zone compared to both base metals .

Studying FSWed joints of components made of 2014-T6 alloy Aydin et al. [337] found that the hardness in the softened weld region lowered with a decrease in the WS.

Investigating FSWed of 4 mm-thick plates made of 2024 alloy, Weglowski et al. [340] reported that the hardness profile of welds had a characteristic run, typical for FSWed joints.

 doi:10.20944/preprints202403.1458.v1

Studying FSWed joints of 6 mm thick plates made of alloys 2024-T351 Milčić et al. [342] reported that the distribution and allocation of microhardness were affected by the level of temperature and plastic deformation being highest under the tool shoulder and around the pin.

Investigating FSWed joints of plates made of 2024-T4 alloy Nejad et al. [341] reported that joints obtained with the threaded tool exhibited elevated average hardness over various welding zones in comparison to the joints prepared by unfeatured tool.

Investigating FSWed joints of components made of 2219-T87/2219-T62 alloys, Venkateswarlu et al. [378] found that the hardness distribution in the stir zone differed significantly for two different heat-treatment material conditions 2219-T62 against 2219-T82.

Studying stress corrosion cracking SCC of FSWed joints of 2014-T651 alloy, Kollapuri [379] reported that at 70 % yield, stress induced was lower and so the material failure was determined by its hardness.

Investigating FSWed joints of 8 mm-thick plates made of 2014-T6 alloy Lin et al. [343] found that the different regions of the joint exhibited different microhardness distribution affected by different thermomechanical actions therein.

During studies on FSWed joints of components made of dissimilar alloys 2017A-T451 and 7075-T651 Hamilton et al. [270] found that the positron lifetime profiles across the weld comprised many local maxima and minima on the advancing and retreating sides, corresponding to the hardness behavior. Such variations in positron lifetime and hardness away from the weld center were due to the temperature distribution in these areas relative to the critical temperatures for secondary phase nucleation and/or dissolution in the two alloys.

Studying FSWed sheets made of dissimilar alloys 2017A-T451 and 7075-T651 Hamilton et al. [326] reported that during the flow of surface material into the welded sheet thickness, mid-plane and bottom-plane material flew toward the sheet surface and embraced the surface material core. Within such region, the weld temperatures exceeded the equilibrium θ phase in 2017A, lowering the hardness, and simultaneously dissolved the equilibrium η/T phase in the 7075, causing re-precipitation of GP zones upon cooling and a hardness recovery.

Investigating FSWed sheets of dissimilar 2017A-T451/ 7075-T651 alloys, Hamilton et al. [46] found that near the weld center, process temperatures allowed the fully dissolving of the equilibrium η phase in 7075 and the partially dissolving of the equilibrium S phase in 2017A. Upon cooling hardness recovered for both alloys. Due to the more complete dissolution of the equilibrium phase in 7075, the hardness recovery skewed toward the AS or the RS of the weld of the 7075 workpiece.

During studies on FSWed joints of components made of dissimilar wrought 2017A and cast AlSi9Mg alloys Kopyscianski [277] reported that the hardness of the base materials was 80 HV1 and 136HV1 for the AlSi9Mg and 2017A alloys, respectively. The local maximum on the advancing side was on the nugget side with a high density of the bands of the 2017A alloy.

Studying FSWed joints of components made of 2017A alloy Mroczka et al. [311] reported that microhardness in the cross-section of the joints only slightly varied; however, after the artificial ageing process hardness enhanced. The variation in hardness of the joint after the ageing process pointed out post-process partial supersaturation in the material and higher precipitation hardening of the joint. For the FSWed joints of components made of a cast AlSi9Mg and 2017A alloys Mroczka [310] reported that the hardness distribution within the weld nugget zone revealed a low strengthening of both cast and wrought alloys. A metastable state of the 2017A alloy occurred, although, the alloy hardness enhanced within the weld nugget zone due to the natural ageing. The hardness of the heat-affected zone in such an alloy slightly changed also due to the natural ageing.

Investigating the stud joints of 2017 alloy obtained by the friction welding process Morikawa et al. [390] reported that at the weld interface it was formed a stair zone with a hardness close to that of base metals, while the heat-affected zone of the bar and the plate was softened.

Studying FSWed joints of 2024-T6 alloy Sun et al. [329] reported that with the conical cam thread stirring head the obtained hardness was lowest at the junction of the heat-affected zone HAZ and the thermo-mechanically affected zone TMAZ. The hardness obtained with the conical cam thread at that point exceeded that of other stirring heads.

 doi:10.20944/preprints202403.1458.v1

Investigating the FSWed joints of components made of 7003-7046 dissimilar alloys Yang et al. [312] found that the hardness was much higher on the retreating side 7046 alloy side than that on the advancing side 7003 Al-alloy side, and the average hardness difference between the two sides was about 30HV. After artificial ageing, the hardness enhanced significantly, while the hardness difference rose to about 50HV for the two sides.

During studies butt FSWed joints of components made of dissimilar 7075-O/6061-O and 7075-T6/6061-T6 alloys Ipekoglu and Cam [294] found that a hardness enhanced in the joint area for the joints produced in the O-temper condition, whereas a hardness loss occurred in the joint area of the joints formed in the T6-temper condition.

Studying FSWed joints of components made of dissimilar cast Al–Si alloys A319 and A413, Karam et al. [293] reported that the average hardness of the welded regions enhanced with the rise of the WS and/or lowering the TRS.

Investigating the FSWed joints of components made of dissimilar 6013-T4 and 7003 alloys Zhao et al. [314] found that independently on the AS or RS, the 6013-T4 side was the weak region for the hardness. The fracture position coincided with the minimum hardness position.

During studies on FSWed components of the heat treatable 6061 and non-heat treatable 5086 alloys Ilagovan et al. [290] found that the use of threaded tool pin profile allowed obtaining higher hardness values of 83 HV in the stir zone compared to those of the other two pin profiles. The enhanced hardness resulted from the formation of fine grains and intermetallics in the stir zone.

Yoon et al. [315] found that when the soft material was on the top, the softening material and the deformed surface height resulted from friction heat generation by the rotating shoulder. The more influencing deformed surface height was lowered with the enhancement of revolutionary pitch. When the soft material was at the bottom, the movement of the un-bonded line and hooking appeared resulting from the vertical flow of the rotating tool pin. The more influencing un-bonded line appeared along the interface between two materials deformed toward the hard material.

Studying spot FSWed joints of sheets made of 5454 alloys, Choi et al. [353] reported that in all cases, the average hardness in the friction-stir-spot-welded zone exceeded that of the base metal zone.

Investigating FSWed joints of components made of 5052-H32 to 6061 T6 blanks, Doley and Kore [281] reported that microhardness values of the dissimilar welds were lower at heat-affected zones HAZ on both the sides of weld line, whereas the lowest one occurred at HAZ of 5052.

Studying the FSWed joints of components made of AA1100 alloy Selvarajan and Balasubramanian [354] reported that hardness value of 67 HV in the stir zone region was showed by the FSW joints obtained under the optimized welding parameters and tool material hardness of 45.4 HRC.

For butt FSWed joints of components made of 6063/ 5083 alloys, Kumar and Kumar [335] reported that the joints with maximum hardness were fabricated at the TRS of 1000 rpm with a cylindrical profile. The hardness enhanced with the rise of the TRS.

Studying FSWed joints of 6061-T6 alloy Juarez et al. [316] reported that the micro-hardness at the stir zone was of 85 HV for the base material welded BMW, 109 HV for the material with heat treatment before welding HTBW, and 134 HV for the material with heat treatment after welding HTAW. For the case of HTAW, the micro-hardness exhibited the lowest dispersion of values between 124 HV and 148 HV along the four characteristic zones. The hardness of the BMW case was much lower compared to the base material due to the ageing of the material and the thickening of the precipitates resulting from the mechanical work and heat generation during welding. The hardness for the HTAW case exceeded that of the base material due to a uniform distribution of precipitates in the zone of agitation inside the welded zone, combined with a smaller size of precipitates.

Dixit [391] studied the effect of different pin profiles including straight cylindrical, triangular, and square on microhardness of butt FSWed joints of 4 mm thick strips made of AA1200 alloy. The joints were obtained with the help of high carbon high chromium alloy tool of various pin profiles under two different TRSs. The hardness of the stir zone varied with position and ranged from 30 HV to 40 HV and was higher than that of the parent metal equal to 32 HV. It was due to grain refinement affecting material strengthening and since the grain size in the friction stir zone was much finer than

 doi:10.20944/preprints202403.1458.v1

that of parent metal thus enhancing the hardness of FSZ. Also, the small particles of intermetallic compounds also increased the hardness.

Attah et al. [392] studied the influence of AISI H13 steel-tapered tool on the FSWed joints of components made of dissimilar 7075-T651 and 1200-H19 alloys. They found that the hardness values were of 50 and 175 HV for AA1200- H19 and 7075-T651, respectively, under three WSs including 30, 60 and 90 mm/min, at a constant TRS of 1500 rpm, a tool tilt angle of 2°. The hardness enhanced with the WS from 81.99 to 98.5 HV as the speed raised from 30 to 60 mm/min and lowered to 77 HV at 90 mm/min. The hardness at 1500 rpm and 60 mm/min enhanced from 70.22 to 98.58 HV with increasing the tilt angle from 1- 2°, a further increase from 2–3° lowered the hardness to 66 HV.

Studying FSWed 5 mm thick plates made of dissimilar 5086-O/6061-T6 alloys Aval et al [358] found that the hardness profile on 6061 side quickly lowered. Such hardness variation was smoother for samples FSWed by the tool with a concave shoulder and a conical probe.

Investigating FSWed joints of components made of dissimilar 7075/ 5083 alloys, Dewangan et al. [387] reported that the hardness of weld region reached value 116 HV.

Studying FSWed joints of components made of dissimilar 6061/ 7075 alloys Guo et al. [384] found that all joints failed in HAZ on the 6061 side where hardness minima was located regardless of the relative materials position or the welding process parameters.

Studying the FSWed joints of 5 mm thick 7075-T651/ 2024-T351 similar and dissimilar alloys Zhang et al. [319] found that the hardness enhanced and then lowered from the top to the bottom along the welding center thickness direction. The tensile fracture locations coincide with that of minimum hardness values at various TRSs.

Tensile strength and residual stresses

The joint strength raised with the rotation speed due to the increased material mixing effect [267,297,299,306] tool rotation speed increased plastic deformation and WS governed the thermal cycle, residual stresses, and rate of production. The selection of the appropriate combination of such speeds strongly affected weld quality or joint strength.

Studying the butt FSWed plates of 2219-T62 alloy, Xu et al. [359] found that the residual stresses on the top surface reached about 171 MPa, while only 243 MPa for the weld with tunnel defect and had the conventional “M” profile with tensile stress peaks in the HAZ zone. Those on the bottom surface exhibited the inverted “V” profile with tensile stress peaks of 99.4 MPa in the weld centre.

Bijanrostami et al. [279] studied the 6061-7075 joint and found that maximum joint strength was reached under a combination of moderate rotation and low WS. However, the maximum joint strength of an A356-6061 joint was reached under low rotation and WS by Ghosh et al. [302,303]. The fine grain size, fine distribution of Si particles and lower residual stresses in the SZ appeared under low rotation and WSs. Together with rotation and WSs, the effect of tool geometry like the pin profile or features [264,267,290,291,306] pin shapes [280,299] and shoulder diameter to pin diameter ratio [282,304] influenced joint strength. The pin profile or feature governed material flow and mixing at the joint interface, the pin shape influenced SZ size and material movement, while the shoulder-to-pin diameter ratio affected frictional heat generation between the tool and the BM. The conical threaded pin was the best configuration for the 6061–5086 joint, as it provided uniformly distributed precipitates and the generation of the onion rings resulted from appropriate material mixing in the SZ, as reported by Ilangovan et al. [290] The tensile strength of the dissimilar FSWed Al joints depended on the microstructure evolution during FSW, which in turn was influenced by the heat input controlled by the welding parameters.

Studying FSWed joints of components made: the first of 2024-T351/ 5083-H112 alloys and the second of 7075-T651/ 2024-T351 alloys, Niu et al. [262] reported that the tensile strength and elongation of FSWed joints were much deteriorated in comparison to the weaker BM, especially for 2024-T351/ 5083-H112 joint.

Investigating the FSWed joints of 7075-T651 and 2024-T351 alloys Hasan et al. [130] found that placing the softer 2024 alloy on the AS slightly enhanced the tensile properties of welding joints. The introduction of pin tool flute/flat improved the ultimate tensile strength and elongation of welds regardless of the fixed location of base materials. Using a truncated threaded pin tool with a flute of

 doi:10.20944/preprints202403.1458.v1

radius equal to that of the pin the tensile strength of weld reached the maximum value of 424 MPa, which represents an efficiency of about 94.3% with respect to the softer material.

Ge et al. [61] studied how EST affects the shear failure load of lap joints. Shear and tensile fracture modes can occur. Mode I was the shear fracture mode, in which the failure occurred along the original lap interface of two sheets. This mode occurred in lap joints when the mixing of materials between the upper and lower sheets hardly occurred and the nature of the joining mechanism at the interface was close to diffusion bonding. It was combined with the alclad layer owning low strength.

The tensile fracture mode exhibited two different fracture paths [54]:

Mode II - wherein the crack initiated from the tip of the cold lap defect CLD, propagated upward along the SZ/TMAZ interface, and finally fractured at the top surface of upper sheet,

Mode III - wherein the crack initiated from the tip of the hook defect HD, propagated downward along the HAZ/TMAZ interface, and fractured at the bottom surface of lower sheet. Such two different fracture modes are strongly affected by the size and orientation of the HD or CLD. The cracks occurring in the HD and the CLD of the lap joint continued their propagation upwards or downwards when the lap joint underwent tensile stress during the tensile test.

Studying FSWed joints of components made of 7075-T651/ 5083-H111 alloys, Kalemba-Rec et al. [265] reported that defect-free joint of the highest tensile strength 371 MPa was obtained with 5083 alloy on the AS, 7075 alloy on the RS, a TRS of 280 rpm, and the Triflute pin.

Investigating FSWed joints of components made of Al-Mg_2Si alloy and 5052 alloy Huang et al. [269] reported that the UTS and elongation of the welded joint were greater than those of the base material of the Al-Mg_2Si, whereas they were lower than those of the 5052-base alloy. The WE exceeded 100% relative to the softer material and reached 61% relative to the 5052 alloy. The particle-matrix interfacial debonding fracture mechanism occurred.

Studying FSWed joints of dissimilar 6061-T651/ 5A06-H112 alloys, Peng et al. [273] noticed that after welding, the yield strength of 6061 lowered by 50% to about 115 MPa and the ultimate tensile strength decreased from 277 MPa to about 190 MPa mainly due to the unstable work hardened state of rolled 6061 was destroyed by elevated temperature generated in FSW. The WE reached 68.5% relative to 6061 alloy, and decreased from 70% to 68% with increased the ratio of rotation speed and WS from 4 to 12 r/mm.

Studying FSWed joints of dissimilar 2024-T3/ 6063-T6 alloys, Sarsilmaz [275] found that under TRS of 900 rpm and WS of 200 mm/min the highest tensile strength of 348 MPa was obtained which was 74% of the tensile strength of the 2024 base metal. An enhancement in tensile strength was 45% higher than the base tensile strength of 6063. All tensile failures occurred at HAZ location always at the 6063 side.

Investigating FSWed joints of components made of 2219-T87/ 2195-T8 dissimilar alloys No et al. [276] found lack of correlation between tensile strength and WS, however, tensile strength increased with enhancing TRS, up to 800 rpm.

During studies on FSWed joints of components made of dissimilar wrought 2017A/cast AlSi9Mg alloys Kopyscianski et al. [277] reported that the tensile strength was of 132 MPa, while the elongation was below 1 %.

Studying FSWed joints of dissimilar 6082-T6/ 5083-H111 alloys, Kasman et al. [280] obtained the highest tensile strength for the weld joint obtained using a triangular-shaped pin and the UTS was of 198.48 MPa. At a lower TRS and WS for each tool pin shape, lower UTS values appeared. The UTS enhanced with increasing the TRS and the WS, while keeping their υ ratio constant for the triangular-shaped pin. The WE varied from 55% to 68% depending on both presence of defects in the weld joint and the strength of the base material.

Saravanan et al. [282] reported that the tensile strength enhanced with increasing in shoulder diameter to pin diameter ratio up to 3 and then lowered by further enhancement in the ratio. The maximum tensile strength was of 356 MPa at the ratio of 3, while the lowest one of 316 MPa at the ratio 4. The WE varied from 76 % to 86 %, depending on the mentioned ratio.

 doi:10.20944/preprints202403.1458.v1

Studying FSWed joints of sheets made of dissimilar Al-Mg-Si/Al-Zn-Mg alloys Yan et al. [283] found that the tensile strengths of the dissimilar Al-Mg-Si/Al-Zn-Mg joints using both configurations exceeded that of the Al-Mg-Si FSW joint.

According to Sun et al. [286] FSWed joints produced at the revolutionary pitches of 1.25 and 1 mm/rev, exhibited both the tensile strength and elongation lower than those obtained at the smaller revolutionary pitches. Due to the insufficient mixing of the two materials in the stir zone and a couple of micro-defects at the 6061-T6 alloy zone the strength of the joints was lowered. Decreasing the revolutionary pitch to 0.75 or 0.5 mm/rev enhanced the heat input, intensifying the plastic deformation and the mixing of the two materials in the stir zone. This resulted in a more homogenous microstructure of the stir zone increasing the tensile strength and elongation increased to about 110 MPa and 13 % for the case of 0.75 mm/rev and 110 MPa and 22.5 % for the case of 0.5 mm/rev. The largest joint efficiency was 55 % with respect to the UFG 1050 Al base metal. Remarkably high heat input in the joints produced at 0.5 mm/rev caused grain growth of both materials causing again a small decrease of the tensile strength compensated by a much-enhanced elongation.

During studies on butt FSWed joints of components made of dissimilar 6061/ 7050 alloys, Rodriguez et al. [289] found that under monotonic tensile loading, the joint strength enhanced with the rise in the TRS. The WE reached up to 62 %.

During studies on FSWed components of the heat treatable 6061 and non-heat treatable 5086 alloys Ilagovan et al. [290] found that the use of threaded tool pin profile allowed obtaining higher tensile strength of 169 MPa compared to those of the other two pin profiles. The lowered size of weaker regions, such as TMAZ and HAZ ones, caused higher tensile properties. The WE varied from 50.4 % to 67.6 %.

Studying FSWed joints of components made of dissimilar cast Al–Si alloys A319 and A413 Karam et al. [293] found that the welded joints exhibited better tensile properties than the base alloys. The A413 base alloy exhibited lower ultimate tensile and yield strengths when compared with A319 base alloy, thus under tensile the welded specimens fractured at A413 alloy side.

During studies butt FSWed joints of components made of dissimilar 7075-O/6061-O and 7075-T6/6061-T6 alloys Ipekoglu and Cam [294] found that the strength values of all the O-joint specimens were close to those of the 6061-O BM, and all the specimens failed within the 6061 BM side away from the joint area. This was due to the shielding effect provided by the strength overmatching resulting from the grain refinement or precipitation of strengthening particles in this zone during FSW process of Al alloys in the O-temper condition, i.e., softened state. The WE in case of initial O state was about 100 %. After PWHT (T6 treatment) the highest WE of about 93 % for the 1000/150-PWHT specimens, and of 87.5 % in case of 1500/400-PWHT specimens. In case of initial T6 state the highest WE was of about 80 % for the 1000/150 specimens, and of 67.8 % for the 1500/400 ones. After PWHT the WE was of 89.1 % for 1000/150-PWHT specimens and of 90.8 % for the 1500/400-PWHT ones.

During studies on butt FSWed joints of 4.76mm thick sheets made of dissimilar 6061-T6 and 7075-T6 alloys Cole et al. [295] found that weld tool offsets into the retreating side 7075 enhanced the tensile strength of the dissimilar joint. Such an enhancement was facilitated by lower average weld temperatures with the enhanced amount of 7075 stirred into the nugget. The WE enhanced with a lowered amount of power input to the weld, where the subsequent WE was highly affected by the alloy most sensitive to heat input and weld temperature.

Ghosh et al. [302] found that tensile properties of welding nuggets WN were highly dependent on its microstructure. Kim et al. [307] reported that the tensile strength exhibited similar values, regardless of the arrangement of the materials. The welding defects occurring under welding conditions with a lower heat input did not affect the tensile properties. When A5J32 was fixed on the retreating side, the highest strength of the welded joints equal to 224.1 MPa appeared under conditions of 1000 rpm and 300 mm/min.

Prime et al. [308] studied FSWed butt joints of components made of 7050-T7451/ 2024-T351 alloys. They found that the stresses in the test specimen removed from the parent welded plate reached values up to 32 MPa and had the “M” profile with tensile stress peaks in the heat-affected zone outside the weld. The peak residual stress values were below 20% of the material yield strength.

 doi:10.20944/preprints202403.1458.v1

Such low stresses were achievable only by solid state welding with less distortions, while for fusion welding, such a low value was hardly possible. The fatigue behaviour is strongly affected by these low values of residual stresses. The peak tensile residual stresses appeared in the HAZ on both sides due to local frictional heating at the tool material interface. Tensile residual stress resulted from that the hotter material was forced by the other material during welding.

Studying the butt FSWed joints of dissimilar 2024-T351/ 6056-T4 alloys, Amancio-Filho [260] reported that the tensile strength of the weld joint was up to 90% of the 6056-T4 alloy. Fracture occurred in the thermo-mechanically heat-affected zone of the alloy 6056-T4, where annealed structure led to lowered microhardness. The drop in tensile strength and the associated increase of strain appeared in the regions of microhardness drop. The obtained joint efficiency in terms of the UTS was of 55.8% for 2024-T351 alloy and of 71.4% for 6056-T4 alloy. However, the joint efficiency in terms of elongation at the rupture was poor (9-14%).

Ivanov et al. [334] studied FSWed joints of rolled sheets made of 2024/ 5056 alloys obtained for various thicknesses. For weld joints with tensile strength not less than 0.9, the welding process parameters were complexly affected by the tensile strength of the base metal.

Investigating butt FSWed joints of components made of 6063/ 5083 alloys, Kumar and Kumar [335] reported that the joints of higher tensile strength were fabricated at the TRS of 1000 rpm with a cylindrical profile. The tensile strength enhanced with the rise of the TRS. The WE varied from 32.3% to 43%, when TRS enhanced from 600 to 1000 rpm.

Studying of FSWed joints of components made of dissimilar 5083-H111/6351-T6 alloys, Palanivel et al. [306] reported that the TRS and pin profile influenced the joint tensile strength because of varying material flow, loss of cold work in the HAZ of 5083 side, dissolution and over aging of precipitates of 6351 side and formation of macroscopic defects in the weld zone.

Investigating the FSWed dissimilar cast and wrought 6061 alloy Dinaharan et al. [305] found that the joint exhibited maximum tensile strength when cast Al alloy was positioned on the advancing side at all TRSs. Studying FSWed joints of components made of Al- Mg_2Si alloy and 5052 alloy Huang et al. [289] found that the UTS end elongation of the welded joint were greater than those of the base material of the Al- Mg_2Si, whereas they were lower than those of the 5052-base alloy.

Saleh [380] studied the microstructure and mechanical properties of butt FSWed joints of sheets made of the dissimilar 2014-T3/ 5059-H11 alloys obtained by bonding the two materials perpendicular to their rolling directions. They found that the ultimate tensile strength values of the dissimilar joint varied in range from 54% to 66% of those of the base metal.

Sasikala et al. [336] studied the effect of rotational and cross-sectional speeds, geometry, and the tool-to-pin-diameter ratio on the tensile strength of the FSWed joints of plates made of dissimilar 2618-T87/ 5086-H321 alloys. Heat affected zones with tensile failures appeared on the alloy 5086 side of the weldment.

Lin et al. [343] studied FSWed joints of 8 mm thick plates made of 2014-T6 alloy. They found that the weld tensile strength was affected by welding parameters. The maximum ultimate tensile strength of 360 MPa equal to 78% that of base metal appeared at a rotating speed of 400 rev min^{-1} and WS of 100 mm min^{-1}. The different regions of the joint exhibited different tensile strengths dependent on the microstructure variation and microhardness distribution affected by different thermomechanical actions therein.

Morikawa et al. [390] studied the strength of the stud joints of 2017 alloy obtained by the friction welding process. They reported that the tensile strength of joints enhanced with pressure and friction time, and the highest tensile strength reached 275 MPa (63.1 % joint efficiency for the bar base metal). The fatigue strength of joints enhanced under their high tensile strength.

Studying the FSWed joints of 2024-T6 alloy Sun et al. [329] found that the tensile strength for all joints was more than 80% of the BM, and the maximum tensile strength of the joint welded with the conical cam thread tool pin reached 364.27 MPa, which was 86.73% of the base metal BM. The elongation after break reached14.95 %. All joints were tensile fractured by plastic fracture.

Investigating the FSWed joints of 3003 alloy Chekalil et al. [347] found that the tensile properties of joints remained good. The tensile strength of the weld joint was up to 75% of that of the base metal.

 doi:10.20944/preprints202403.1458.v1

Kasman and Ozan [348] studied the influence of welding process on the structural properties of the butt FSWed joints of plates made of 3003-H24 alloy. They found that the highest ultimate tensile strength among all the welded joints equal to 128 MPa was obtained under 50 mm/min WS and 800 rpm TRS. The WE was remarkably close to 100%. The size of the defects was affected by the tensile properties of welded joints.

Aydin et al. [338] studied the effect of welding parameters (rotation speed and WS) on the mechanical properties of FSWed joints of components made of 3003-H12 alloy joints. The tensile weld strength enhanced with an increase in the WS or a decrease in the rotation speed. The tensile fractures of the joints were in base metal under welding parameter combinations of 1070 rpm and 40 mm/min or 2140 rpm and 224 mm/min. The ultimate tensile strengths of the joints lowered linearly with an enhancement of rotation speed at a constant WS, while such strength of the joints enhanced almost linearly with a rise of WS at a constant rotation speed.

Goyal et al. [350] studied the effect of welding parameters on the UTS of FSWed joints made of 3003 alloy. The best UTS equal to 127.2 MPa was obtained for the process parameters including a WS of 74.64 mm/min, a TRS of 971.77 rpm and a tool tilt angle of 1.52, respectively. The WE reached up to 89.4%.

Deng et al. [381] studied the effect of post-weld heat treatment on the microstructure and mechanical properties of the FSWed joints of plates made of 7204-T4 alloys. They reported that the ultimate tensile strength UTS of the FSW joints were 296.6, 318.2, 357.4 MPa under the heat treatments of AW, AA, and SAA, respectively .

Yang et al. [312] studied the influence of post-weld artificial ageing on microstructure and mechanical properties of FSWed joints of components made of 7003-7046 dissimilar alloys. They found that after artificial ageing, the tensile strength enhanced slightly, and the elongation was slightly changed for the joint. The WE slightly exceeded 100% in both cases of natural and artificial ageing.

Kasman and Ozan [313] studied butt FSWed joints of 6013 Al plates obtained via pin offset technique. They found that the highest tensile strength equal to 206 MPa was obtained under 1.5 mm pin offset towards the advancing side and 500 min^{-1} TRS, leading to the ratio of tensile strength of the joint to the ultimate tensile strength of the base metal (joint efficiency) equal to 74 %.

Zhao et al. [314] studied the FSWed joints of components made of dissimilar 6013-T4/7003 alloys. The joint with the 6013-T4 placed at the advancing side AS was called the A6R7 joint. Accordingly, the A7R6 referred to the joint with the 7003 placed at the AS. The authors reported that independently on the AS or RS, the 6013-T4 side was the weak region for tensile strength. The WE for joint A6R7 was of about 93%, while that for the joint A7R6 was of 87 %.

Studying FSWed joints of sheets made of dissimilar Al-Mg-Si/Al-Zn-Mg alloys Yan et al. [283] found that the tensile strengths of the dissimilar Al-Mg-Si/Al-Zn-Mg joints using both configurations exceeded that of the Al-Mg-Si FSW joint.

Liu et al. [309] studied mechanical properties of FSWed joints of components made of 1050 - H24 alloy. They reported that the maximum tensile strength of the joints was equivalent to 80% of that of the base material. Under deviation of the welding parameters from the optimum values, the tensile properties of the joints deteriorated, and the fracture locations of the joints varied.

Studying butt FSWed joints of the ultrafine grained UFGed 1050 alloy plates with a thickness of 2 mm with the 2 mm-thick 6061-T6 alloy plates Sun et al. [286] found that the maximum tensile strength reached about 110 MPa. The WE reached up to about 55%.

Investigating FSWed joints of 1100 alloy Selvarajan and Balasubramanian [354] reported that a maximum tensile strength of 105 MPa was showed by the FSW joints obtained under the optimized welding parameters. The WE reached up to 95.4%.

Studying the underwater FSWed joints of dissimilar 6061/7075 alloys Bijanrostami et al. [279] found that the maximum tensile strength of 237.3 MPa and elongation of 41.2% were reached under a TRS 1853 rpm and a traverse speed of 50 mm/min. In comparison with the optimum condition, greater heat inputs induced lowered joint strength and the higher elongations for the joints.

 doi:10.20944/preprints202403.1458.v1

Investigating welded joints of components made of dissimilar 7003-T4/6060-T4 alloys obtained by underwater friction stir weld UFSW Dong et al. [355] reported that the ultimate tensile strength of the joints reached up to 185 MPa. The strength increased due to the microstructure modification caused by water cooling. The WE was of 90.4 % and was higher compared to the case of the classic FSW process.

Jassim and Al-Subar [393] studied FSSWed joints of 3mm thick sheets made of 1100 alloy by overlapping the edges of sheet as lap joint. The joint tensile strength enhanced with raising the TRS and the maximum value of tensile strength equal to 233 MPa, twice higher than the one of base metal, occurred at a TRS of 2000 rpm. The WE varied in the range of 74.5-141 %.

Studying the FSWed joints of components made of 1100 alloy Senapati and Bhoi [394] reported that the UTS of the welded specimen enhanced by 20% compared to that of the parent material due to the uniform dispersion of silicon particles present within the base material. Studying the butt FSWed joints of 3 mm thick strips made of 1200 alloys Joseph et al. [395] found that the ultimate tensile strength of the welded region lowered due to insufficient mixing of the material or due to heat evolved during friction stir welding. The lower feed rate provided a joint with higher tensile strength due to better mixing of the material.

Investigating the FSWed joints of components made of dissimilar 7075-T651 and 1200-H19 alloys Attah et al. [392] found that the UTS enhanced from 126.04 to 151.54 MPa with an increase in the WS from 30–60 mm/min and lowered to 128.37 MPa at 90 mm/min. The UTS increased from 123.32 to 151.54 MPa as tilt angle increased from 1–2° and lowered to 122.2 MPa as tilt angle enhanced to 3°.

For FSWed joints of 6061-T6 alloy Juarez et al. [316] reported that the tensile strength for the BMW case was close to that in joints obtained by fusion welding. For the HTBW case, the tensile strength was enhanced by 10% compared to that obtained in BMW. For the HTAW case, an efficiency of 96% of tensile strength compared to that of the base material was observed.

Studying FSWed joints of dissimilar 7075-T651 and 1200-H19 alloys Attah et al. [392] found the impact energy enhanced from 12.9 to 21.4 J with an increase in the WS from 30 to 60 mm/min and lowered to 5.4 J at 90 mm/min. The UTS enhanced from 126.04 to 151.54 MPa with an increase in the WS from 30–60 mm/min and lowered to 128.37 MPa. The UTS increased from 123.32 to 151.54 MPa as tilt angle increased from 1–2° and lowered to 122.2 MPa as tilt angle enhanced to 3°. Under the tilt angle of 2°, rotational and traverse speeds of 1500 rpm and 60 mm/min, respectively, the highest impact energy of 21.4 J was obtained.

Investigating butt FSWed joint between dissimilar 6061-T6/7075-T6 alloys, Godhani et al. [317] found that during the tensile tests of specimen the fracture took place from the HAZ of the 6061 side under all investigated welding conditions. The breakage in the cup-and-cone form pointed to the ductile nature of the failure. The WE reached up to 61.4%.

Sato et al. [396] applied FSW to a 1.5 mm thick pieces made of accumulative roll-bonded (ARBed) 1100 alloy with ultrafine grained microstructure and high hardness. Transversely to the rolling direction an elongated ultrafine grained microstructure occurred. These pancake-shaped ultrafine grains with some dislocations and sub-boundaries therein, typically resulted from the ARB process, were surrounded by high angle boundaries with misorientations above 15°. The mean thickness and length of the pancake-shaped grains were 260 and 450 nm, respectively. The initial material hardness was of 30 HV, while after ARB it raised to about 85 HV, due to the grain refinement. The FSWed joints were obtained under rotation speed of 500 rpm, WS of 12 mm/s using the tool with a shoulder diameter of 9 mm, a pin diameter of 3 mm, a pin length of 1 mm and pin threaded. The welding direction was identical to the rolling direction (RD) of the ARB process. The tool-to-workpiece angle was 3° from the vertical axis in the weld. The authors found that FSW suppressed high lowering of hardness in the ARBed material, however the SZ and the TMAZ exhibited small lowering of hardness due to dynamic recrystallization and recovery. The FSW prevented softening in an ARBed Al alloy 1100 with an equivalent strain of 4.8 in the as-ARBed condition.

Studying FSWed 5 mm thick plates made of 5086-O and 6061-T6 alloys, Aval et al.],[358] , in the case of 5086/6061 joint obtained the weld UTS varying in the range of 219-240 MPa and the weld

 doi:10.20944/preprints202403.1458.v1

elongation of 17%/23%, while WE varied in the range of 87-95%. In the case of 6061/5086 joint the weld UTS varied in the range of 228-248 MPa, while WE varied in the range of 90- 98%.

For the FSWed joints of components made of dissimilar 5052/6061 alloys obtained with various pin-eccentric stir tools reported [318] found that all tensioned joints failed in the NZ, and the joint obtained by the 0.8 mm-pin-eccentric stir tool exhibited the highest tensile strength of 196 MPa due to the raised grain-boundary and dislocation strengthening. The WE reached up to 86%.

Investigating FSWed joints of components made of dissimilar 7075/5083 alloys, Dewangan et al. [387] reported that the UTS of weld region reached value of 237.4 MPa and WE was of 80%.

Studying FSWed joints of sheets made of 2219 and 7475 alloys, Khan et al. [388] reported that the UTS of weld region reached value of 267.2 MPa, elongation was of 5%, and the WE was of 57%-92%.

For FSWed joints of components made of dissimilar 6061/7075 alloys, Guo et al. [384] found that the UTS of joints enhanced with the lowering heat input. The highest UTS was of 245 MPa.Summarizing, it can be noticed that most studies carried out on FSW were focused on BM in the as-rolled condition for 2xxx-5xxx, 2xxx-6xxx, 2xxx-7xxx, 5xxx-6xxx, 5xxx-7xxx Al series. Some studies considered the effect of base material placement of welded joints features and it remains inconclusive. Base material placement is an issue for the cases of high differences in mechanical properties of the BMs as in the 6xxx-7xxx and the 5xxx-7xxx combinations. Some studies concerned welding parameters optimization studies, particularly the effect of tool offset on welds quality. The further studies are necessary including these using microstructure characterization to better recognize the material flow in the SZ.

During FSW process the residual stresses are very low, much low compared to those of the fusion processes.

The higher mechanical properties mainly resulted from the fine grains in the stir zone of FSWed joints.

The FSWed weld (joint) efficiency can widely vary in range of 57-98%, and even exceed 100% relative to the softer material.

4.8.1.6. Reinforcement of Weldment

The mechanical properties and microstructure of the FSWed joints can be enhanced by grain refinement via the micro- and nano- sized solid particles reinforcement [397].

Various nanoparticles can be incorporated in FSW of Al alloys [397–402].

Vimalraj et al. [403] stated that varying TRS, WS, number of passes and direction of travelling tool affected the joint fabrication. They found that the size, type, and quantity of reinforcing nanoparticles (SiC and TiC) beneficially influenced the formation of microstructure and joint properties.

Moradi et al. [404] studied the effect of weld pass number on micro-structural, natural ageing and mechanical performance of SiC-incorporated FSW of Al alloys. They found smaller size of grains at nugget zone for two passes than that for single pass due to smaller initial grain size and more homogenized and finer distribution of SiC particles. However, the repeated thermal cycle and high hot deformation highly limited the precipitation hardening effect, thus highly lowering hardness.

SiC particles with size between 20-60 nm are the most often used as the reinforcing particles [320].

4.8.2. Friction Stir Spot Welding

Friction stir spot welding FSSW is a kind of the friction stir welding FSW process. It provides a spot, lap-weld without bulk melting of joined materials. The tensile shear strength of the FSSW welded joints is affected by the pin height, tool rotation and welding time [405] The FSSW process of Al alloys provides significant energy and cost savings) compared to electric resistance spot welding [406] The FSSW process for Al alloys (Table 6) is more beneficial over other welding processes such as RSW, MIG-Spot, and mechanical joining techniques [407]. The FSSW is relatively cheap due to

 doi:10.20944/preprints202403.1458.v1

improved energy efficiency and a virtual lack of a consumable. That is, FSSW requires no water, no compressed air, nor complex electrical transforming equipment [408].

Jassim and Al-Subar [393] studied FSSWed joints of 3mm thick sheets made of AA1100 alloy (Table 6) by overlapping the edges of sheet as lap joint. The process was done using a drilling machine instead of milling machine under TRS varied in range of 760-2000 rpm with manual and automatic compression. Hardness enhanced at the center zone of welded joint which was 1.45-2.85-fold higher than the hardness of base metal. The optimum TRS was of 1065 rpm. The joint tensile strength enhanced with raising the TRS and the maximum value of tensile strength equal to 233 MPa, twice higher than the one of base metal, occurred at a TRS of 2000 rpm. The depth of tool penetration was in the range of 3.25 to 6 mm depending on the load and heat.

Senapati and Bhoi [394] studied the FSWed joints of components made of 1100 alloy (Table 6) obtained using a square pin tool. They reported that the temperature on the advancing side AS of the weld was about 20-25 °C higher than its retreating side RS. The UTS of the welded specimen enhanced by 20% compared to that of the parent material due to the uniform dispersion of silicon particles present within the base material. The finely arranged equiaxed grains appeared in the nugget region of the weld. The formation of alumina Al_2O_3 took place in the weld nugget due to high heat generation and exposure to atmospheric oxygen during welding. Residual stress possessed an M-shaped distribution. The samples joined at low travel speed and high TRS exhibited compressive residual stress in the joint region. Contrary, the residual stress of the material lying below the tool shoulder was tensile one. The residual stress in the AS possessed a higher magnitude than the RS of the weld specimen.

Joseph et al.[395] studied the effect of the spindle speed and feed rate on the micro-hardness, yield strength and ultimate tensile strength of butt FSWed joints of 3 mm thick strips made of 1200 alloys (Table 6) obtained using H13 tool steel 56 HRC tool with two different pin profiles. The cylindrical with groove and tapered pin profiles were used to fabricate the joints under three various TRSs and three various feed rates. Both two different sets of tools used provided satisfactory

According to Praveen and Yarlagadda [409] pulse gas metal arc welding GMAW-P is one of the ways for welding joint various Al alloys as it achieves lowered heat input in the weld. The hardness increased in the welded area. The yield strength and ultimate tensile strength of the welded region lowered due to insufficient mixing of the material or due to heat evolved during friction stir welding. The 750-rpm spindle speed provided the best weld results. The lower feed rate provided a joint with higher tensile strength due to better mixing of the material. The tapered tool provided better weld than the cylindrical one.

Levise et al. [410] studied the effect of the process parameters on the mechanical properties of the FSSWed joints of components made of dissimilar 2024/7075 alloys (Table 6). They found that the tensile shear force enhanced to the maximum with the changes in the TRS. The optimal tensile shear force and hardness equal to 4.18 kN and 134 HV, respectively, were obtained for the tool plunge depth of 3.3 mm, TRS of 2000 rpm and tool dwell time 40 s.

Kulekci et al. [405] studied the effect of welding pin height, TRS and WS on tensile shear strength of FSSWed joints of components made of 5005 alloy (Table 6). They found that pin height was the major factor affecting the tensile shear strength of FSSW joints, whereas TRS and WS were the second-ranking factors. The enhancement of tool plunge depth raised the weld tensile shear strength of FSSW joints. The maximum tensile shear strength of 122.16 MPa was obtained for 2.60 mm pin height, 1500 rpm tool rotation and 10 s welding time. However, the minimum tensile shear strength of 58.92 MPa was obtained for 2.20 mm pin height, 1500 min^{-1} tool rotation and 10 s welding time. The WE widely varied in the range of 54.5-111%.

Borah et al. [411] studied FSSWed joints made of 6063 series of 1 mm thickness (Table 6). A process for double spot friction stir welding DSFSW and double spot zigzag friction stir welding DSZFSW providing welded joint higher strength was considered. They compared various mechanical properties of the joints with these of single-spot friction stir welding, obtained using three different probe shape tools at three different spindle speeds. They found that at low WSs, the tensile-shear strength of the welding specimen was higher. The DSFSW joints, welded by a triangular probe

 doi:10.20944/preprints202403.1458.v1

tool exhibited higher tensile strength compared to that of a single spot and DSZFSW joint. Under high spindle speed, the hardness value of the welding specimen lowered while the grain size enhanced.

Suresh et al. [412] reported that in FSSW, a rotating hardly-wearing tool is pressed with a high force against upper surface of two overlapping sheets. The simultaneous effect of frictional heat and the applied pressure provides bonding the components metallurgically without melting. The tool is drawn out of the welded piece after a dwell time.

Welded joints of 6061-T6 alloy (Table 6),, studied by Suresh et al. [412], were obtained by swept friction stir spot welding. Al_2O_3 nanoparticles were added into the guide hole for improving the weld characteristics. The percentage of reinforcement was varied by changing the guide hole diameter in range 1.5 – 3.0 mm. Using the non-dominated sorting teaching learning-based optimization algorithm the optimum welding parameters included guide hole diameter of 2.8 mm, TRS of 1387 rpm and WS of 17mm/min.

Table 6. FSSW process parameters applied for joints of various Al alloys.

Refs	Joint	Thickness	Rotational speed	Welding speed	Welding time	Plunge depth	Tool
		[mm]	[rpm]	[mm/min]	[s]	[mm]	
405	EN AW 5005	1.5	1500/2000		5/10		Cylindrical Shoulder diameter 10/shoulder length 50/ Cylindrical Pin diameter 4mm/Pin height 2.2/2.6 mm/ AISI 1050 steel 52 HRC
407	EN AW 5005	1.5	1500/2000		5/10		Cylindrical Shoulder diameter 10/shoulder length 50/ Cylindrical Pin diameter 4mm/Pin height 2.2/2.6 mm/ AISI 1050 steel 52 HRC
393	1100	3	760/1065/1445/ 2000		40-64/28-40/23-57/32-40		Cylindrical shoulder diameter 10/shoulder length 55/tapered pin min diameter 3, pin length 2/5/ tilt angle 10/ HSS material
394	1100	5	1100-1500	20-60		0.1-0.5	cylindrical shoulder diameter of 21 mm/square pin width 7 mm/ pin length of 4.5 mm / tool steel
395	1200	3					Cylindrical pin with groove, and tapered pin/ H13-Tool Steel 56 HRC
410	2024 up/7075 bottom	5	1500/2000/2500	20/40/60		3/3.3/3.6	Cylindrical shoulder diameter 16 mm/ shoulder length 50 mm/ cylindrical pin

 doi:10.20944/preprints202403.1458.v1

					diameter 4 mm/ pin length 2.5 mm
411	6063	1	1220/660/380		Cylindrical shoulder diameter 12 mm/pin length 1.7 mm/ Pin Circular/Square/Triangular
412	6061-T6	2	1200/1400/1600/1800	10/15/20/25	Cylindrical Shoulder Diameter 12/ Threaded Pin Diameter M5/ Pin Length 2.85/ H13 tool steel

Summarizing, it can be noticed that FSSW can be applied for similar Al alloys with thickness up to 5 mm, although joining of dissimilar 2024/7075 alloys is also possible. The FSSWed joint strength is highly affected by pin height, TRS, WS and welding time. The joints strength was higher compared to that of that of the parent material. Suresh et al. [412] reported that the FSSW provided the weld with no contamination, blowholes, porosity, and cracks.

4.9. Gas Metal Arc Welding GMAW

Zhu et al. [413] studied butt welded joints of 5 mm-thick plates made of 7003-T5 alloys obtained by gas metal arc welding GMAW method focusing on the effect of stress concentration introduced by weld reinforcement on fatigue strength. They found that the fatigue strength of 7003-T5 alloy butt joints with the weld reinforcement reached values of 50 MPa, which was 45% of that for the joints without the weld reinforcement. The fatigue source and propagation differed for the specimens with and without the welder due to the stress concentration at the weld root. The stress concentration with a factor of 1.7 strongly affected the fatigue strength, but slightly the tensile strength.

Sangduang et al. [414] studied welded joints alloys 5154 obtained by GMAW. They noted that the weld porosity defect often occurred in the Al alloys welding affecting mechanical properties. The best condition for the finest weld bead was at the current 200 A with the travel speed 75 cm/min.

According to Praveen and Yarlagadda [409] reported that fabricators of Al alloys utilize the pulse gas metal arc welding GMAW-P technology allowing reduction in the heat input to the base material of joined parts. It operates mainly in one drop per pulse providing the stable arc, and producing lesser distortions and fumes. Such a technology operates with a big diameter electrode wire for wider application ranges limiting wire feeding problems in welding equipment and porosity incidence due to a lower surface area to volume ratio. GMAW-P provides improved deposition character such as better wetting is useful for overcoming viscosity at the joint in comparison to conventional GMAW. GMAW-P technology is well suited for joining of extruded parts, as they are more tolerant to fit up and can weld varying thickness sections 319.

Ramaswamy et al. [415] valuated tensile properties of single V butt joints of thin sheets made of 6061-T6 alloy obtained by four variants of the GMAW process (constant current, pulsed current, cold metal transfer, and pulsed cold metal transfer) under optimized conditions. They found that the hardness in the weld metal, i.e., 79 HV for the pulsed cold metal transfer PCMT joints was 14% higher than that of the continuous current GMAW joints. The PCMT-welded joint exhibited also the highest tensile strength of 227 MPa being 16% higher than the continuous current GMAW joints. The fracture surface of the tensile specimens was highly dominated by the dimples with tearing ridges due to high joint plastic deformation before failure independently of the welding process. The PCMT joints exhibited superior tensile properties with controlled segregation of phases compared to the other variants of the GMAW process due to the pulsing effect associated with the retraction of the wire.

 doi:10.20944/preprints202403.1458.v1

Mercan et al. [416] studied different alloys 5754 and 6013 joined by GMAW method under various welding parameters. While the welded samples were bent 180°, the cracks, and fractures occurred on the fusion line boundary due to unsuitable welding parameters. The highest toughness value occurred in the HAZ of 5754 alloy. The toughness values in the HAZ of 6013 alloy on the joints and weld metal were nearly the same. The maximum hardness value was in the HAZ of 6013 alloy, followed by that of the weld metal and that of the HAZ of 5754 alloy. The structures of all the weld metals were dendritic.

Kaushal and Sharma [417] studied the effect of GMAW parameters including the welding current, voltage and gas flow rate on mechanical properties including tensile strength, hardness, microstructure, and microhardness of 6mm thick alloy 6061 plates. As Al alloys exhibit large microstructural changes after welding the welding current should be controlled as its too-high values result in high heat input and weakening of the weld profile.

Çevik [418] studied 3 mm-thick 7075-T651 alloys joined using different welding currents via the GTAW method. They reported that the grain size of the weld center rose due to heat input occurring with the enhancement of the welding current. Micro cracks (hot cracking) appeared in the roots of welding seams. The enhancement in the welding current affected the hardness distribution of the weld zone. The impact strength of the welded sample was negatively affected by the grain coarsening and micro-cracks in the welds.

Gierth et al. [190] studied the wire arc additive manufacturing of AlMg5Mn alloy by using the gas metal arc welding GMAW process. The temperature–time-regimes affected the resulting microstructure, weld seam irregularities, and the mechanical properties of additively manufactured Al parts. Therefore, multilayer walls were built layer-wise using the cold metal transfer CMT process including conventional CMT, CMT advanced, and CMT pulse advanced arc modes.

Jin et al. [419] compared the difference in pulse base currents (ΔIb) and the difference in the pulse peak currents (ΔIp) for welded joints of 6061-T6 alloys obtained using the double pulse gas metal arc welding DPGMAW. They found that changing ΔIp caused welding defects or even welding failure. The welding stability after changing ΔIb was much better than that after changing ΔIp. The individual fish-scale width of the weld joint remained unchanged when ΔIb was at various values. The average absorbed work, tensile strength, yield strength, and elongation of the weld joints obtained by various ΔibΔIb values reached 31.1%, 60.2%, 52.9% and 37.9% of the base metal, respectively.

Gas metal arc welding (GMAW) needs trivial bevel preparation, raising costs [420]. Kim et al.][421] studied multi-pass deposition with GMAW, noticing that it is time-consuming both with the single wire and with the twin wire method. The use of relatively high heat input leads to severe distortions highly limiting the productivity and weld quality obtained with such a method. Gas metal arc welding GMAW is used for the same alloys with thickness up to 5 mm, although joining dissimilar alloys 5754 and 6013 is also possible. The developed type of GMAW, namely double pulse gas metal arc welding DPGMAW was noticed.

4.10. Magnetic Pulse Welding MPW

Magnetic pulse welding is more widely used to join Al alloys with steel [75,422–425] Ti alloys [426] or Mg alloys [427]. However, some application for joining only Al alloys were also found.

According to Zhang et al. [428] magnetic pulse welding can be used for both linear welding and tubular welding of 6061-T6 components. Linear seam MPW was performed under 4-8 kJ discharge energy with 210 kA peak current for 6061-T6 plates of 0.5 mm thickness. The standoff distance between the flyer plate and the stationary plate was 4.5 mm and the overlap was 12.7 mm. The tubular MPW joint specimen was obtained by 45 kJ discharge energy, with 860 kA peak current. The outer and inner diameters for the 6061-T6 tube were 50.8 and 47.5 mm, respectively. The 6061-T6 rod had an outer diameter of 40.89 mm and an inner one of 25.4 mm. The standoff distance was 3.30 mm, and the overlap was set as 19.05 mm. The microstructure of MPWed joints of 6061-T6 exhibited almost one order of magnitude grain refinement in the welded interface in comparison to base metals . The large crystallographic misorientations between these grains also appeared. It resulted from the local

 doi:10.20944/preprints202403.1458.v1

high-strain rate deformation near the faying interfaces during high-velocity impact. The interface was formed by true solid-state bonding. Intensive spalling appeared away from the welded region after the tubular MPW process. In such a spalled region the strain gradient and extensive plastic deformation occurred. The local deformation in the bulk matrix appeared away from the impacting surface due to the progression of alternating compression and tension deformation waves.

During studies on the welded joints of components made of dissimilar alloys 4014 and 7075 using magnetic pulse welding MPW Pourabbas et al. [119] found that depending on collision angle and discharge energy the formation of three various welding interfaces with wavy, molten wavy and porous morphologies occurred. The hardness of the welding interface with the molten layer was much greater compared to that of the base metals because of the grain refinement phenomenon resulting from the rapid melting and solidification during MPW process. The formation of porous welding interface resulted from gas entrapment and the base metal vaporization. The sample welded under the collision angle of 6° and discharge energy of 7.35 kJ showed the highest rupture force about 13.8 kN among all samples due to the wavy welding interface of this sample providing an adequate bonding between two metals. The lower rupture force of the samples welded with higher collision angle and/or discharge energy was due to microcracks caused by huge plastic deformation.

Pereira et al. [429] reported that the continuous joining along the complete perimeter of the 6083-T6 tube to rod was provided under the optimal welding parameters combination including: 2 kJ of discharge energy, 1 mm of stand-off distance and an impact angle above 15°, which corresponds to 6-turn coil positioned on the tube centre. The obtained joint exhibited a mechanical resistance like the base material. No modifications of the grain size or precipitates appeared at the joint interface. It can be noticed, that MPW process can be applied for components made of both similar and dissimilar Al alloys and for both linear and tubular welds.

Okagawa and Aizawa [430] proposed a parallel MPW arrangement leading to seam welds between 1 mm thick Al sheets. They experimentally investigated the seam weld shearing strength affected by the kinetic energy of the sheets before the collision and magnetic pressure after the collision.

Raoelison et al. [431] simulated the MPW process assuming a linear flyer velocity distribution with a mean value of 600 m/s for Al workpieces. The simulation model developed allowed predicting of thermomechanical material flow in the form of particle jetting.

It seems, that MPW can be potentially used for pairs of some both similar and dissimilar Al alloys.

4.11. Vaporizing Foil Actuator Welding VFAW

The vaporizing foil actuator VFA can be used for impact welding of Al flyer sheets to high-strength steel and magnesium plates [432]. In VFAW, a sudden capacitor-discharge produces a very high current via a thin conducting foil, vaporizing it almost instantaneously. This generates a very high-pressure plasma accelerating the flyer plate towards the target plate [317]. Vivek et al. [433] elaborated on the so-called vaporizing foil actuator welding VFAW; same dimensions as in magnetic pulse welding MPW.

Hahn et al. [434] compared magnetic pulse welding and vaporizing foil actuator welding against each other in the form of lap joints of 1 mm thick sheets made of 5005A alloy under identical conditions including charging energies of the pulse generator, specimen geometry, initial distances between the flyer and target plate. Impact velocities obtained from rapidly vaporizing Al foils were up to three times greater than those of purely electromagnetically accelerated flyer plates. No magnetic pulse welds were achieved, while each vaporizing foil process provided a strong weld in that failure always occurred in the joining partners instead of in the weld seam during tensile tests.

Meng et al. [120] studied the microstructure of welded joints of sheets made of 2024-T3 and 7075-T6 alloys obtained by vaporizing foil actuator welding VFAW. They stated that dynamic preform solved the poor formability problem of the target material. But with a standoff sheet inserting in the flyer and target, the joints exhibited higher weld strength, compared to that with flyer preformed method. The microstructure of the circular weld area of the joint exhibited a wave interface with a

 doi:10.20944/preprints202403.1458.v1

thin melt layer formed at the center and edge parts. The crystal grains near the bonding interface were elongated and refined. Therefore, the weld joining was facilitated through plastic forming and melting.

Kapil [435,436] elaborated a type of solid-state impact welding technique VFAW utilizing the high pressures from the rapid vaporization of a foil actuator to drive a flyer sheet at extremely high speeds to cause a high-speed impact with a target sheet leading to formation of a solid-state joint. The process provides a joint devoid of any HAZ and thus allows joining of various material.

Kapil [435] studied the effect of natural aging and application of heat treatments on material weldability, mechanical properties of the joints, and weld interface characteristics of spot welds of 6111-T4 similar alloys. Such alloys were naturally aged at room temperature for a period of 6 months and welded to itself as-received AR and under a combination of different heat treatments using VFAW. It was found that aging and different heat treatment cycles had little to no effect on the weldability and all samples exhibited repeated button pullout BP-type failure. The joint failure was governed by thinning and tearing of the region around the bond and affected by the mechanical properties of the BM. The strength of the welds was close to that of the parent metal. The PFHT cycle provided the highest strength values while samples paint-baked had the highest energy absorption and ductility. The welded samples were significantly hardened compared to BM zone due to the severe plastic deformation upon the high-speed impact and cold working during the preforming operations before welding. Microhardness had constant values through the weld region. Impact-induced strain hardening had maximum effect in AR-AR samples and the least effect in PFHT-PFHT samples. Samples welded as-received and samples paint baked after being welded as-received had similar widespread re-solidified molten zones along the wavy interface, while the PFHT-PFHT and PFHT-PFHT PB samples had very narrow and localized zones. Such re-solidified molten zones were softened, however, appeared in the weld interior, and have a lower effect on joint performance. It can be noticed, that VFAW process can be applied for components made of both similar and dissimilar Al alloys.

Nassiri and Kinsey [437] simulated VFAW for 2 mm thick flyer and 3 mm thick base Al plates using the arbitrary Lagrangian–Eulerian (ALE) and the Smoothed particle hydrodynamics (SPH) methods. In both methods, they assumed an initial constant flyer velocity and impact angle. They found that the SPH method properly simulated material jetting, but was less accurate than the ALE one.

Groche et al. [438] experimented with process window acquisition in HVIW. They used 2 mm thick Al workpieces and achieved total normal impact velocities of up to 262 m/s. When the collision point velocity exceeded the sound speed in Al, jetting did not occur giving no bonding.

Hansen et al. [439] studied VFAWed joints of components of 0.96 mm thick 6061-T6 alloy and 0.76 mm thick 5052 alloy in lap and spot-like configurations, at a variety of impact velocities. They found that welds failed in coach-peel outside the joint interface. The 5052 hardened within 100 μm of the interface. The 6061-T6 softened a little within 50 μm of the interface.

Hansen et al. [440] reported that VFAs can be used to consistently launch AA2024 sheet metal flyers on the order of 0.5 mm thick to velocities between 300 and 1000 m/s within distances from 0.25 to 3 mm. The velocity can be controlled by jointly or separately varying the VFA thickness and the input energy. A faster current source provided higher pre-vaporization energy deposition, Ed, but the relationship between the ratio Ed/Evap and the vaporization pressure was linear regardless of foil thickness. Thicker foils needed more input energy to vaporize, better pressure confinement in the setup, and a higher acceleration distance. The temporal development of pressure from thinner foils was beneficial for the VFA welding setup with a shorter acceleration distance and the same workpiece velocity. The flyer sheet launch and flight were planar across the active area of the foil, with a < 0.5 μs delay in the center as compared to the edges. The delay lowered with the enhancement of the Ed/Evap ratio. The lag in the center can be compensated with the use of the foil actuator with no end effect.

 doi:10.20944/preprints202403.1458.v1

Meng et al. [441] found that VFAW was a feasible method to weld 2024/7075 alloys. Strengths of the welds made with standoff sheets were higher than those of the ones made with preformed target sheet. The dynamic preforming was one solution for forming materials with poor formability.

It seems that VFAW is still under development, however it can provide better results in case of Al alloys than MPW.

It can be noticed that TIG and MIG processes are suitable for fusion welding most of the wrought grades in the 1XXX, 3XXX,5XXX, and 6XXX series; particularly the 5XXX alloys exhibit excellent weldability. TIG and MIG processes are also well-suited for medium-strength 7XXX series alloys. The fusion welding for high-strength alloys, such as 7010, 7050, whereas majority of the 2XXX alloys is not advised due to being prone to liquefaction and solidification. The FSW process is well-suited for producing sound welds in Al alloys. This process is also advised for heat-treatable alloys prone to hot cracking. The FSW is also well-suited for Al-steel combination [320]. The laser welding is applicable for Al-Al joints [29,207,208], and also for dissimilar joints of some steel types (stainless one, low carbon one) and Al alloys such as 1050, 5052, 5083, 6016, 6061, 6082, 6111, and 7075. Resistance spot welding is also well-situated for both Al-Al joints [253] and Al-steel joints [241].

The mechanical properties associated with FSW joints are generally better than those obtained with arc welding. Although the strength properties of welds obtained using FSW are comparable to or even lower than those obtained by laser welding or the MIG process, the fatigue performance of FSW joints is better than those produced by laser welding or the MIG process. Additionally, mismatch tolerance, low weld-to-weld variability, and very rare weld defects made the FSW process superior to competitive processes.

5. Summary

Joining of various components made of various Al alloys, both casting and wrought used in automotive industry is a complex problem. The components used in electrical vehicles can be joined by conventional adhesive bonding, weld-bonding and self-piercing riveting, friction stir spot welding, ultrasonic spot welding, laser braze-welding and cold metal transfer welding [442].

Joining of Al castings is difficult due to their often appearing porosity, poor surface quality, a tendency toward hot cracking, and low ductility [443].

The Al castings from various processes possess various gas content, surface finish, and mechanical properties, causing their various joinability by fusion welding and mechanical joining [443].

Various grades of Al castings exhibit various cracking susceptibility, and various joint porosity issues. The Al-Si alloys are less sensitive to solidification cracking during welding, while Al-Cu, Al-Mg, Al-Mg-Si, Al-Zn-Mg, alloys are more sensitive to it. The higher solidification/freezing range the higher is susceptibility to hot cracking, and the higher fraction of eutectic phase in the microstructure and a eutectic phase with sufficient wettability the lower is susceptibility to hot cracking. The same grade of castings obtained from different casting processes can differ in their gas content and joinability. Castings made by high-quality High-Pressure Die Casting (HPDC), squeeze casting, and semi-solid metal SSM casting possess a much lower gas content [443].

The Al castings can be joined via friction stir welding, laser welding, arc welding, electron beam welding, laser arc hybrid welding, self-piercing riveting, clinching, flow drill screw, etc. The mentioned and the other welding technics are also used for joining both similar and dissimilar Al wrought alloys applied in automotive industry; however, it can be noticed, that friction stir welding process is the most often used. Additionally, the other forms of FSW process are being developed, for example FSSW one.

Particularly, successful FSWed joining of Al alloys was obtained between, inter alia, 6061/7050 [289], 6061/7075 [384], 6082/2024 [444], 2024/7075 [445,446], 5083/6351 [205], 2219/5083 [203], 6082/7075 [447], 6061/5086 [190], 2219/7039 [448].

Also, the laser welding is very often used techniques for various Al alloys in automotive industry, however classical MIG and TIG methods are also often met in practice. They can be linked,

 doi:10.20944/preprints202403.1458.v1

as in the case of the laser-MIG hybrid welding or plasma-MIG welding providing even better weld quality.

The use of laser welding and FSW to joint various Al alloys can provide obtaining WE close to or even exceeding 100%.

Underwater friction stir weld (UFSW) can provide the higher WE compared to the classic FSW process [355].

The mechanical properties and microstructure of the FSWed joints can be improved by grain refinement via the micro- and nano- sized solid particles, for example SiC or TiC, reinforcement [397].

Commonly used fusion welding techniques like RSW, leads to inhomogeneous material microstructure distribution and the presence of a HAZ, lowering the mechanical and fatigue properties of the produced joints, as described in [449].

Solid-state welding techniques like FSW, impact welding, UW, etc. can replace conventional fusion welding techniques and mechanical fastening processes mentioned in [412]. Age-hardening Al alloys widely used in automotive industry exhibited high specific strength, good formability, and corrosion resistance [16]. Ageing of components after their welding using various welding processes can be a good practice in case of some Al alloys, for example 6061-T4 one, as it improves significantly weld strength, however, it depend on the joint type and joined materials and also on filler metal [450].

Age-hardening Al alloys (for example of the 6xxx series) commonly used in automotive industry are usually in T4 temper exhibiting lower strengths. The strength of such alloys is enhanced by cold working and the heat treatment cycles. The paint baking PB cycle precipitation hardens the material to a T6 temper and post form heat treatment PFHT overages the material sacrificing ductility for increased strength. The PB treatment of parts painted and cured in an oven at temperatures of 180°C allows simultaneous cures the paint and strengthens the alloy [451].

Natural aging of the 6xxx series Al alloys change their mechanical properties [452]. Prolonged natural aging of Al alloys in T4 temper enhances yield strength, however, lowers formability and affects bending and hemming properties. The heat treatable 6xxx series Al alloys are naturally aged by clustering and GP-zone formation worsening the age-hardenability during the PB cycle [453].

However, the precipitation strengthening effect strongly depends on the welding heat input. To improve the performance of joints welded by conventional fusion welding exhibited a large welding softening range and severe softening degree lowering the joint performance. To improve the latter many effective methods, including low-heat-input welding methods, externally assisted cooling techniques and post-weld treatment techniques were adopted. However, the joint performance remains lower compared to that of the base metal but can be further improved. The PWHT for dissimilar age-hardening Al alloys is a challenge due to that various base metals need various optimal treatment processes. Therefore, it is necessary to conduct further studies in such areas [16].

The important problem during welding of components made of Al alloys is the gas content therein. Friction stir welding (FSW) is less sensitive than other welding techniques as to the gas content of the Al cast components. However, FSW is only suitable for simple smooth welding lines, welded components should be clamped rigidly, and a backing plate is needed for poorly stiff components. The Al castings for fusion welding need to have a low gas content like hydrogen one. The air pockets and hydrogen contents in cast Al components induce porosity in the weld bead. Due to the large weld pool and lower welding speed, arc welding processes are less sensitive to gas content, and then the parameters for degassing are very important. Electron beam welding is the least sensitive fusion welding process to gas content due to the degassing effect of vacuum, although the size of the welded components is limited. Due to the outgassing, high heating and cooling rates, and complex weld fluid flow, laser welding is the most sensitive to gas content, and for this reason, Al castings for laser welding need a very low gas content to avoid a high porosity in the welded joints. Hybrid welding, with a combination of laser beam welding and TIG or MIG welding, can be beneficial to the welding of Al castings [443].

Electron beam welding, using a multiple-process technique or hybrid laser welding can configure the molten baths to facilitate degassing and limit inhomogeneous porosity in the joint area. With such processes joints with low porosity can be achieved [443].

 doi:10.20944/preprints202403.1458.v1

Mechanical joining methods, such as SPR and clinching, are not as sensitive to gas content as fusion welding processes, but the Al castings should be ductile enough to limit severe cracks generation during the joining process. Sometimes, heat treatment of the Al castings increase their ductility. Using process optimization can limit the number and severity of the cracks generated [443].

As to fusion welding and FSW of Al castings, if the casting is suitable for heat treatment, then heat treatment after welding or a combination of pre- and post-welding heat treatments more efficiently improves joint mechanical properties than heat treatment before welding. The heat treatment made before welding process can give no improvement effect on mechanical properties of the joint. For mechanical joining processes such as SPR and clinching, because sufficient ductility is required from the Al castings to avoid severe cracking, heat treatments to improve ductility will need to be conducted before the joining [443].

A still unsolved problem is the hot cracking of welded components made of Al alloys, particularly casting ones. Hot cracking susceptibility is affected by alloying content, grain structures, solidification rate, constrains, etc. During fusion welding the hot cracking can be limited using proper filler wires, adding grain refining elements, reducing welding speed, methods to limit residual stress or solidification rate, etc. To diminish the occurrence of such cracking, excess material restraint should be avoided. For crack-sensitive alloys, careful selection and control of process parameters, together with the use of an appropriate filler wire, provide high quality of welds. The welded Al alloys should have a weld-metal composition away from the peak of the crack sensitivity curve. Dual beam laser welding, electron beam welding, and laser arc hybrid welding are beneficial for reducing solidification cracks [443].

The other unsolved problem met during welding of components made of Al alloys is porosity causing loss of mechanical strength, creep, fatigue, and corrosion failures [443].

The porosity is formed during fusion welding of Al castings due to:

- the absorption and subsequent entrapment of the ambient gases during welding;
- the existing gas content in the base material;
- the entrapment of gas bubbles due to the imperfect collapse of the keyhole during keyhole welding [443].

Mainly hydrogen causes porosity and is contented therein, due to its significantly different solubility in liquid and solid Al. Cleaning the surface of parts before welding lowers the source of hydrogen and the resulting porosity. The optimized welding parameters limits the joint porosity of Al castings, but the most efficient way is to improve the casting process to reduce the gas content of cast parts. The following methods limit the welding porosity of Al casting: laser arc hybrid welding, dual beam laser welding, electron beam welding, beam oscillation, electromagnetic field degassing, etc. Increasing the size of the weld pool and reducing the solidification rate gives more time for the gas bubbles to move out of the weld pool, which is beneficial for reducing weld porosity [443].

Author Contributions: "Conceptualization, A.R. and B.D.; Methodology, K.S.; Software, M.W.; Validation, A.O., B.D. and A.R.; Formal Analysis, M.W.; Investigation, A.R.; Resources, K.S.; Data Curation, A.R.; Writing – Original Draft Preparation, K.S.; Writing – Review & Editing, A.O.; Visualization, M.W.; Supervision, A.R.; Project Administration, B.D.; Funding Acquisition, B.D.".

Funding: No funding.

Conflicts of Interest: Authors declare no conflict of interest.

References

1. **Dzikuc, M., Adamczyk, J. and Piwowar, A.** Problems associated with the emissions limitations from road transport in the Lubuskie Province (Poland). Atmospheric Environment. 2017, Vol. 160, pp. 1-8.
2. **Lyu, P., Wang, P.(S.), Liu, Y., Wang, Y.** Review of the studies on emission evaluation approaches for operating vehicles. Journal of Traffic and Transportation Engineering (English Edition). 2021, Vol. 8, 4, pp. 493-509.
3. **Angnunavuri, P.N., Kuranchie, F.A., Attiogbe, F., Nerquaye-Tetteh, E.N.** The potential of integrating vehicular emissions policy into Ghana's transport policy for sustainable urban mobility. SN Appl. Sci. 2019, Vol. 1, 1201.

4. **Correia, G.N., Batista, T.P., Marques, S.S. and Silva, C.M**. How car material life-cycle emissions are considered in environmental rating methodologies? Suggestion of expedite models and discussion. Renewable and Sustainable Energy Reviews. 2014, Vol. 38, pp. 20-35.
5. **Serrenho, A.C., Norman, J.B. and Allwood, J.M.** The impact of reducing car weight on global emissions: the future fleet in Great Britain. Philos Trans A Math Phys Eng Sci. 2017, Vol. 375, 2095, p. 20160364.
6. Neuer Audi Space Frame mit hohen Anteilen an Aluminium und CKF/New Audi Space Frame with increased content of aluminium and CFK. Audi. 2015, Aluminiumkarosserien/Aluminium car bodies, Vol. 3.
7. **Anwar, Miftahul & Diharjo, Kuncoro.** Application of Carbon Fiber-Based Composite for Electric Vehicle. Advanced Materials Research. 2014, Vol. 896, pp. 574-577.
8. A review of carbon fiber materials in automotive industry. **Ahmad, H., Markina, A.A., Porotnikov, M.V. and Ahmad, F.** 2020. Vol. 971, p. 032011.
9. **Harrison, N.R. and Luckey, S.G.** Hot Stamping of a B-Pillar Outer from High Strength Aluminum Sheet AA7075. SAE International Journal of Materials and Manufacturing. 2014, Vol. 7, pp. 567-573.
10. **Kutsuna, M., Kitamura, S., Shibata, K., Sakamoto, H. and Tsushima, K.** Improvement of the joint performance in laser welding of aluminium alloys. Welding in the World. 2006, Vol. 50, 1-2, pp. 22-27.
11. **AlShaer, A.W., Li, L. and Mistry, A.** Effect of filler wire properties on porosity formation in laser welding of AC-170PX aluminium alloy for light-weight automotive component manufacture. Proceedings of the Institution of Mechanical Engineers, Part B: Journal of Engineering Manufacture. 2015, Vol. 231, 6, pp. 1-13.
12. **Arun, N., Cijo, M. and Joby, J.** Influence of Gas Tungsten Arc welding parameters in Aluminium 5083 alloy. Inter. J. Eng. Sci. Inno. Technol. 2013, Vol. 2, 5, pp. 269-277.
13. **Kumar, A. and Sundarrajan, S.** Optimization of pulsed TIG welding process parameters on mechanical properties of AA 5456 Aluminum alloy weldments. Materials & Design. 2009, Vol. 30, 4, pp. 1288-1297.
14. **Szczucka-Lasota, B., Wegrzyn, T. and Jur, A.** Aluminum alloy welding in automotive industry. Transport Problems. 2020, Vol. 15, 3, pp. 67-78.
15. Red-Bag. Joint quality factor (joint efficiency coefficient). PCC User Manual version 4.4.x. Calculation. [Online] 10 January 2024. https://redbag.com/pcc/doc/calculations/jointqualityfactor.html]
16. **Cheng, J., Song, G., Zhang, X., Liu, C., Liu, L.** Review of Techniques for Improvement of Softening Behavior of Age-Hardening Aluminum Alloy Welded Joints. Materials. 2021, Vol, 14, p. 5804.
17. **Torzewski, J., Łazińska, M., Grzelak, K., Szachogłuchowicz, I. and Mierzyński, J.** Microstructure and Mechanical Properties of Dissimilar Friction Stir Welded Joint AA7020/AA5083 with Different Joining Parameters. Materials. 2022, Vol. 15, 5, p. 1910.
18. Fracture Toughness Behaviour of FSW Joints on Aluminium Alloys. **von Strombeck, A., dos Santos, J.F., Torster, F., Laureano, P., Kogak, M. Threadhill P.L. (Ed.):** First International Symposium on Friction Stir Welding - Proceedings, June 14-16, 1999, in Thousands Oaks, CA, USA. Cambridge, UK: The Welding Institute Ltd, 1999. CD-ROM;
19. Experimental Investigation on Tensile Test Properties of EB Welded Joints of Aluminum 6061-T6 Alloy for Plate-type Fuel Assembly Fabrication. **Kim, S.S., Kang, D.H., Jeong, Y.J., Park, J.M.** Transactions of the Korean Nuclear Society Spring Meeting Jeju, Korea, May 23-24, 2019]
20. **Lippold, J.C.** Welding Metallurgy and Weldability. s.l. : John Wiley & Sons, Inc., 2015.
21. **Wojdat, T., Kustroń, P., Jaśkiewicz, K. and Pabian, J.** Study of Corrosion, Structural, and Mechanical Properties of EN AW-6082 and EN AW-7075 Welded Joints. Materials. 2021, Vol. 14, 16, p. 4349.
22. **Lee, J., Park, S.-Y. and Choi, B.-H.** Evaluation of Fatigue Characteristics of Aluminum Alloys and Mechanical Components Using Extreme Value Statistics and C-Specimens. Metals. 2021, Vol. 11, p. 1915.
23. **Li, H., Gao, J. and Li, Q.** Fatigue of Friction Stir Welded Aluminum Alloy Joints: A Review. Appl. Sci. 2018, Vol. 8, p. 2626.
24. Bahaideen, Farhad & Saleem, Ahmed & Hussain, Khaleed & mohd ripin, Zaidi & Ripin, & Ahmad, Zainal & Samad, Zahurin & Badarulzaman, Nur Azam. Fatigue Behaviour of Aluminum Alloy at Elevated Temperature. Modern Applied Science. 2009, Vol. 3, 4, pp. 52-61.
25. **Azadi, M. and Aroo, H.** Creep properties and failure mechanisms of aluminum alloy and aluminum matrix silicon oxide nano-composite under working conditions in engine pistons. Mater. Res. Express. 2019, Vol. 6, p. 115020.
26. **Chen, P. Fan, X., Yang, Q., Zhang, Z., Jia, Z. and Liu, Q**. Creep behavior and microstructural evolution of 8030 aluminum alloys compressed at intermediate temperature. Journal of Materials Research and Technology. 2021, Vol. 12, pp. 1755-1761.
27. **Li, Z. & Fu, Xue-Song & Chang, Z.-L & Zhou, Wen & Chen, Guo-Qing.** Creep behavior and forecast of welded joint for 2219T87 aluminum alloy at room temperature. Zhongguo Youse Jinshu Xuebao/Chinese Journal of Nonferrous Metals. 2014, Vol. 24, 9, pp. 2235-2242.
28. **Fourmeau, M., Børvik, T., Benallal, A., Hopperstad, O.S.** Anisotropic failure modes of high-strength aluminium alloy under various stress states. International Journal of Plasticity. 2013, Vol. 48, pp. 34-53.

29. **Bunaziv, I., Akselsen, O.M., Ren, X., Nyhus, B., Eriksson, M.** Laser Beam and Laser-Arc Hybrid Welding of Aluminium Alloys. Metals. 2021, Vol. 11, p. 1150.
30. **Petrie, E.M.** Adhesive Bonding of Aluminum Alloys. Metal Finishing. 2007, Vol. 105, 9, pp. 49-56.
31. **Li, Y.D., Zhao, P.Z., Feng, Y.J., Cao, H.L.** Influence of anodic oxide film structure on adhesive bonding performance of 5754 aluminum alloy. Transactions of Nonferrous Metals Society of China. 2019, Vol. 29, 9, pp. 1836-1841.
32. **Lathabai, S.** 20 - Joining of aluminium and its alloys. [book auth.] R. (Ed.) Lumley. Metals and Surface Engineering, Fundamentals of Aluminium Metallurgy. s.l. : Woodhead Publishing, 2011, pp. 607-654.
33. **He, X.** A review of finite element analysis of adhesively bonded joints. Int. J. Adhes. Adhes. 2011, Vol. 31, 4, pp. 248-264.
34. **Barnes, T.A. and Pashby, I.R.** 99. Joining techniques for aluminium spaceframes used in automobiles: Part II—Adhesive bonding and mechanical fasteners. J. Mater. Process. Technol. 2000, Vol. 99, 1-3, pp. 72-79.
35. **Groche, P., Wohletz, S., Brenneis, M., Pabst, C. and Resch, F.** Joining by forming - A review on joint mechanisms, applications and future trends. J. Mater. Process. Technol. 2014, Vol. 214, 10, pp. 1972-1994.
36. **Kim, D.C., Park, H.J., Hwang, I.S. and Kang, M.J.** Resistance spot welding of aluminum alloy sheet 5J32 using SCR type and inverter type power supplies. Archives of Materials Science and Engineering. 2009, Vol. 38, 1, pp. 55-60.
37. **Sun, Z. and Karppi, R.** The application of electron beam welding for the joining of dissimilar metals: An overview. J. Mater. Process. Technol. 1996, Vol. 59, 3, pp. 257-267.
38. **Selvi, S., Vishvaksenan, A. and Rajasekar, E.** Cold metal transfer (CMT) technology - An overview. Defence Technology. 2018, Vol. 14, 1, pp. 28-44.
39. **Lakshman Singh, Rajeshwar Singh, Naveen Kumar Singh, Davinder Singh, Pargat Singh.** An Evaluation of TIG Welding Parametric Influence on Tensile Strength of 5083 Aluminum Alloy. International Journal of Mechanical, Industrial Science and Engineering. 2013, Vol. 7, 11, pp. 795-798.
40. **Yao Liu, Wenjing Wang, Jijia Xie, Shouguang Sun, Liang Wang, Ye Qian, Yuan Meng, Yujie Wei.** Microstructure and mechanical properties of aluminum 5083 weldments by gas tungsten arc and gas metal arc welding. Materials Science Engineering: A. 2012, Vol. 549, pp. 7-13.
41. **Wadelton, F.** Aluminum 7005-6061 custom frames. Bicycle fabrication. [Online] www.frankthewelder.com.
42. How To Advice and Tips for Welders of All Experience Levels. [Online] 10 January 2024. https://www.weldinghandbook.com/types-of-welding/\
43. **Haboudou, A., Peyre, P., Vannes, A.B. and Peix, G.** Reduction of porosity content generated during Nd:YAG laser welding of A356 and AA5083 aluminium alloys. Material Science and Engineering. 2003, Vol. 363, 1-2, pp. 40-52.
44. **Peng, Z., Yang, S., Wang, Z. and Gao, Z.** Fatigue Property and Small Crack Propagation Mechanism of MIG Welding Joint of 6005A-T6 Aluminum Alloy. Materials. 2022, Vol. 15, p. 4698.
45. **Grujicic, M., Arakere, G., Pandurangan, B., Hariharan, A., Yen, C.-F. and Cheeseman, B.A.** Development of a Robust and Cost-Effective Friction Stir Welding Process for Use in Advanced Military Vehicles. J. of Materi Eng and Perform. 2011, Vol. 20, pp. 11-23.
46. **Hamilton, C., Dymek, S., Kopyściański, M., Węglowska, A. and Pietras,** A. Numerically Based Phase Transformation Maps for Dissimilar Aluminum Alloys Joined by Friction Stir-Welding. Metals. 2018, Vol. 8, p. 324.
47. **Yoon, T.-J., Yun, J.-G. and Kang, C.-Y.** Formation mechanism of typical onion ring structures and void defects in friction stir lap welded dissimilar aluminum alloys. Mater. Des. 2016, Vol. 90, pp. 568–578.
48. **Mishra, R.S. and Ma, Z.Y.** Friction stir welding and processing. Materials Science and Engineering: R: Reports. 2005, Vol. 50, 1-2, pp. 1-78.
49. **Mishra, R. and Komarasamy, M.** Friction Stir Welding of High Strength 7XXX Aluminum Alloys. 1. Waltham : Butterworth-Heinemann, 2016. ISBN 978-0-12-809465-5.
50. **Mishra, R. and Sidhar, H.** Friction Stir Welding of 2XXX Aluminum Alloys including Al-Li Alloys. 1. Waltham : Butterworth-Heinemann, 2016. ISBN 978-0-12-805368-3.
51. **Uday, M.B., Fauzi, M.N.A., Zuhailawati, H. and Ismail, A.B.** Advances in friction welding process: A review. Sci. Technol. Weld. Join. 2010, Vol. 15, 7, pp. 534-558.
52. **Threadgill, P.L., Leonard, A.J., Shercliff, H.R. and Withers, P.J.** Friction stir welding of aluminium alloys. Int. Mater. Rev. 2009, Vol. 54, 2, pp. 49-93.
53. **Kumar, N., Mishra, R. and Yuan, W.** Friction Stir Welding of Dissimilar Alloys and Materials. [ed.] Butterworth-Heinemann. 1. Waltham : s.n., 2015. ISBN 978-0-12-802418-8.
54. **DebRoy, T. and Bhadeshia, H.K.D.H.** Friction stir welding of dissimilar alloys: A perspective. Sci. Technol. Weld. Join. 2010, Vol. 15, 4, pp. 266-270.
55. **Murr, L.E.** A review of FSW research on dissimilar metal and alloy systems. J. Mater. Eng. Perform. 2010, Vol. 19, pp. 1071-1089.
56. **Chen, Y.C., Liu, H.J. and Feng, J.C.** Friction stir welding characteristics of different heat-treated-state 2219 aluminum alloy plates. Mater Sci Eng A. 2006, Vol. 420, 1-2, pp. 21-25.

57. **Liu, H.J., Fujii, H., Maeda, M. and Nogi, K.** Tensile properties and fracture locations of friction stir welded joints of 2017-T351 aluminum alloy. J Mater Process Technol. 2003, Vol. 142, 3, pp. 692-696.
58. **Meng, X.C., Xu, Z., Huang, Y., Xie, Y., Wang, Y., Wan, L., Lv, Z. and Cao, J.** Interface characteristic and tensile property of friction stir lap welding of dissimilar aircraft 2060-T8 and 2099-T83 Al-Li alloys. Int J Adv Manuf Technol. 2018, Vol. 94, pp. 1253-1261.
59. **Costa, M.I., Verdera, D., Leitão, C. and Rodrigues, D.M.** Dissimilar friction stir lap welding of AA 5754-H22/AA 6082-T6 aluminium alloys: influence of material properties and tool geometry on weld strength. Mater Des. 2015, Vol. 87, pp. 721-731.
60. **Kallee, S.W** Industrial applications of friction stir welding. [book auth.] D. Lohwasser and Z. (Eds.) Chen. Welding and Other Joining Technologies, Friction Stir Welding. s.l. : Woodhead Publishing, 2010, pp. 118-163.
61. **Ge, Z., Gao, S., Ji, S. and Yan, D.** Effect of pin length and welding speed on lap joint quality of friction stir welded dissimilar aluminum alloys. Int J Adv Manuf Technol. 2018, Vol. 98, pp. 1461-1469.
62. **Khan, N.Z., Khan, Z.A. and Siddiquee, A.N.** Effect of Shoulder Diameter to Pin Diameter (D/d) Ratio on Tensile Strength of Friction Stir Welded 6063 Aluminium Alloy. Materials Today: Proceedings. 2015, Vol. 2, 4-5, pp. 1450-1457.
63. **Vimalraj, C. and Kah, P.** Experimental Review on Friction Stir Welding of Aluminium Alloys with Nanoparticles. Metals. 2011, Vol. **11, p. 390.**
64. **Burek, R., Wydrzyński, D., Sęp, J. and Więckowski, W.** The effect of tool wear on the quality of lap joints between 7075 T6 aluminum alloy sheet metal created with the FSW method. Eksploatacja i Niezawodnosc – Maintenance and Reliability 2018; 20 (1): 100–106. 2018, Vol. 20, 1, pp. 100-106.
65. **Brown, B.M.** A comparison of AC and DC resistance welding of automotive steels. Welding Journal. 1987, Vol. 66, 1, pp. 18-23.
66. **Guo, H., Hu, J. and Tsai, H.L.** Three-Dimensional Modeling of Gas Metal Arc Welding of Aluminum Alloys. ASME. J. Manuf. Sci. Eng. 2010, Vol. 132, 2, p. 021011.
67. **Furukawa, K.** New CMT arc welding process – welding of steel to aluminium dissimilar metals and welding of super-thin aluminium sheets. Weld Int. 2006, Vol. 20, 6, pp. 440-445.
68. **Chinnasamy, Rajendran, Chelladurai, Samson Jerold Samuel and Sonar, Tushar**. Investigation on Microstructure and Tensile Properties of High-Strength AA2014 Aluminium Alloy Welds Joined by Pulsed CMT Welding Process. Advances in Materials Science and Engineering (Hindawi). 2021, p. 8163164.
69. **Pickin, C.G. and Young, K.** Evaluation of cold metal transfer (CMT) for welding aluminium alloy. Sci Technol Weld Join. 2006, Vol. 11, 5, pp. 583-585.
70. Pickin, C.G., Williams, S.W. and Lunt, M. Characterisation of the cold metal transfer (CMT) process and its application for low dilution cladding. J Mater Process Technol. 2011, Vol. 211, 3, pp. 496-502.
71. **Kah, P., Suoranta, R. and Martikainen, J.** Advanced gas metal arc welding processes. Int J Adv Manufacturing Technol. 2013, Vol. 67, pp. 655-674.
72. **Schierl, A.** The CMT-process - a revolution in welding technology. Weld World. 2005, Vol. 49, 9, p. 38.
73. **Gullino, A., Matteis, P. and D'Aiuto, F.** Review of Aluminum-To-Steel Welding Technologies for Car-Body Applications. Metals. 2019, Vol. 9, 3, p. 315.
74. **Dutra, J.C. and Goncalves e Silva, R.H., Marques, C**. Melting and welding power characteristics of MIG–CMT versus conventional MIG for aluminium 5183. Weld Int. 2015, Vol. 29, 3, pp. 181-186.
75. **Zhang, Y.** Investigation of magnetic pulse welding on lap joint of similar and dissimilar materials. PhD Thesis. s.l. : The Ohio State University, 2010.
76. Bellmann, J., Lueg-Althoff, J., Niessen, B., Böhme, M., Schumacher, E., Beyer, E., Leyens, C., Tekkaya, A.; Groche, P.; Wagner, F-X. and Böhm, S. Particle Ejection by Jetting and Related Effects in Impact Welding Processes. Metals. 2020, Vol. 10, 8, p. 1108.
77. Niessen, B., Schumacher, E., Lueg-Althoff, J., Bellmann, J., Böhme, M., Böhm, S., Tekkaya, A.E., Beyer, E., Leyens, C. and Wagner, M.F.-X. Interface Formation during Collision Welding of Aluminum. Metals 2020, Vol. 10, p. 1202.
78. **Wang, H. and Wang, Y.** High-Velocity Impact Welding Process: A Review. Metals. 2019, vol. 9, p. 144.
79. **Schumacher, E., Rebensdorf, A. and Böhm, S.** Influence of the jet velocity on the weld quality of magnetic pulse welded dissimilar sheet joints of aluminum and steel. Materialwiss. Werkstofftech. 2019, Vol. 50, pp. 965–973.
80. **Carpenter, S.H. and Wittman, R.H.** Explosion Welding. Ann. Rev. Mater. Sci. 1975, Vol. 5, pp. 177–199.
81. **Deribas, A.A. and Zakharenko, I.D.** Surface effects with oblique collisions between metallic plates. Combust. Explos. Shock Waves 1974, Vol. 10, pp. 358–367.
82. **Suman Patra, Kanwer Singh Arora, Mahadev Shome and Sandip Bysakh.** Interface characteristics and performance of magnetic pulse welded copper-Steel tubes. J Mater Process Technol. 2017, Vol. 245, pp. 278-286.

83. **Zhang, Y., Babu, S.S., Prothe, C., Blakely, M., Kwasegroch, J., LaHa, M. and Daehn, G.S.** Application of high velocity impact welding at varied different length scales 211 (2011). J Mater Process Technol. 2011, Vol. 211, 5, pp. 944-952.
84. **Kapil, A. and Sharma, A.** Magnetic pulse welding: An efficient and environmentally friendly multi-material joining technique. J. Clean. Prod. 2015, Vol. 100, pp. 35–58.
85. **Jassim, A.** Comparison of magnetic pulse welding with other welding methods. J. Energy Power Eng. 2011, Vol. 5, pp. 1173–1178.
86. **Aizawa, T., Kashani, M. and Okagawa, K.** Application of Magnetic Pulse Welding for Aluminum Alloys and SPCC Steel Sheet Joints. Welding Journal. 2007, Vol. 86, pp. 119-124.
87. **Qi, N., Wang, L., Zhao, Y., Tian, S. and Zhan, X.** The tensile properties of 2219 aluminum alloy plate butt joint welded by novel laser mirror welding. Optics & Laser Technology. 2022, Vol. 149, p. 107796.
88. **Theron, M., Burger, H.P., Van Rooyen, C. and Ivanchev, L.H.** Laser welding of A357 aluminium alloy. International Congress on Applications of Lasers & Electro-Optics. 2008, Vol. P112.
89. **Peterson, W., Pakalnins, E. and Carpenter, J.A.** Longlife electrodes for resistance spot welding of aluminium sheet alloys and coated high strength steel sheet. FY Progress Report. 2004, pp. 237-244.
90. **Boomer, D.R., Hunter, J.A. and Castle, D.R.** A new approach for robust high productivity resistance spot welding of aluminium. SAE Transactions. 2003, Vol. 112, pp. 280-292.
91. **Spinella, D.J., Brockenbrough, J.R. and Fridy, J.M.** Trends in aluminium resistance spot welding for the auto industry. Welding Journal. 2005, Vol. 84, 1, pp. 34-40.
92. **Bamberg, P., Seewald, R., Schiebahn, A., Reisgen, U., Precoma, N. and Epperlein, M.** Improvement of the resistance spot welding of Al-Mg-Si alloys by using cladding technology: An optical and mechanical characterization study. Journal of Advanced Joining Processes. 2022, Vol. 5, p. 100090.
93. **Indira Rani, M. and Marpu, R.N.** Effect of Pulsed Current TIG Welding Parameters on Mechanical Properties of J-Joint Strength of AA6351. The International Journal of Engineering and Science (IJES). 2012, Vol. 1, 1, pp. 1-5.
94. **Howard, R.D.** Industrial Heating. Aluminum Heat Treatment Processes, Applications and Equipment. [Online] 1 February 2007. https://www.industrialheating.com/articles/87310-aluminum-heat-treatment-processes-applications-and-equipment.
95. **Spira, N.** Aluminum in Cars: Aluminum Alloys for Car Bodies. Kloeckner Metals. [Online] 07 July 2021. https://www.kloecknermetals.com/blog/aluminum-in-cars.
96. EngineersEdge. Aluminium plate,Aluminium Cast and Wrough Engineering Specifications. [Online] 15 March 2023. https://www.engineersedge.com/aluminum_plate.htm.
97. **Davis, J.R.** Aluminum and Aluminum Alloys. Cleveland : ASM International, 1993.
98. **Bamberg, P., Gintrowski, G., Liang, Z., Schiebahn, A., Reisgen, U., Precoma, N. and Geffers, C.** Development of a new approach to resistance spot weld AW-7075 aluminum alloys for structural applications: an experimental study – Part 1, Journal of Materials Research and Technology 2021, Vol. 15, pp.: 5569-5581.
99. **Elrefaey, A.** Effectiveness of cold metal transfer process for welding 7075 aluminium alloys. Sci Technol Weld Join. 2015, Vol. 20, 4, pp. 280-285.
100. **Kumar, N.P., Vendan, S.A. and Shanmugam, N.S.** Investigations on the parametric effects of cold metal transfer process on the microstructural aspects in AA6061. J Alloys Compd. 2016, Vol. 658, pp. 255-264.
101. **Zhang, C., Li, G., Gao, M., Yan, J. and Zeng, X.Y.** Microstructure and process characterization of laser-cold metal transfer hybrid welding of AA6061 aluminum alloy. Int J Adv Manufacturing Technol. 2013, Vol. 68, 5, pp. 1253-1260.
102. **Ahmad, R. and Bakar, M.A.** Effect of a post-weld heat treatment on the mechanical and microstructure properties of AA6061 joints welded by the gas metal arc welding cold metal transfer method. Mater Design. 2011, Vol. 32, 10, pp. 5120-5126.
103. **Benoit, A., Paillard, P., Baudin, T., Klosek, V. and Mottin, J.-B.** Comparison of four arc welding processes used for aluminium alloy cladding. Sci Technol Weld Join. 2015, Vol. 20, 1, pp. 75-81.
104. **Cong, B., Ding, J. and Williams, S.** Effect of arc mode in cold metal transfer process on porosity of additively manufactured Al-6.3%Cu alloy. Int J Adv Manufacturing Technol. 2015, Vol. 76, pp. 1593-1606.
105. **Rajeev, G.P., Kamaraj, M. and Bakshi, S.R.** Al-Si-Mn alloy coating on aluminum substrate using cold metal transfer (CMT) welding technique. JOM: the journal of the Minerals, Metals & Materials Society. 2014, Vol. 66, 6, pp. 1061-1067.
106. **Luijendijk, T.** Welding of dissimilar aluminium alloys. Journal of Materials Processing Technology. 2000, Vol. 103, 1, pp. 29-35.
107. **Kaba, L., Djeghlal, M.E., Ouallam, S. and Kahla, S.** Dissimilar welding of aluminum alloys 2024 T3 and 7075 T6 by TIG process with double tungsten electrodes. Int J Adv Manuf Technol. 2022, Vol. 118, pp. 937-948.

108. **Jweeg, M.J., Resan, K.K., Abbod, E.A. and Al-Waily, M.** Dissimilar Aluminium Alloys Welding by Friction Stir Processing and Reverse Rotation Friction Stir Processing. IOP Conf. Ser.: Mater. Sci. Eng. . 2018, Vol. 454, p. 012059.
109. **P.A., Friedman and Kridli, G.T.** Microstructural and mechanical investigation of aluminum tailor-welded blanks. J. Mater. Eng. Performance. 2000, Vol. 9, 5, pp. 541-551.
110. Prediction of Strain Distribution in Aluminium Tailor Welded Blanks for Different Welding Techniques**. Buste, A., Lalbin, X. and Worswick, M.J. [ed.] M. Bouchard and A. (Eds.) Faucher.** Montreal : Canadian Institute of Mining, Metallurgy, and Petroleum, 1999. Proc. Int. Symp. on Light Metals . pp. 485-500.
111. **Davies, R.W., Grant, G.J., Khaleel, M.A., Smith, M.T. and Oliver, H.E.** Forming-limit diagrams of aluminum tailor-welded blank weld material. Metall. Mater. Trans. A,. 2001, Vol. 32, pp. 275-283.
112. **Pickering, E., Glagola, M., Ramage, R., and Taylor, G.** Production and Performance of High Speed GTA Welded Aluminum Tailored Blanks. SAE Technical Paper. 1995, p. 950722.
113. **Beytullah Gungor, Erdinc Kaluc, Emel Taban, Aydin SIK ŞŞ.** Mechanical and microstructural properties of robotic Cold Metal Transfer (CMT) welded 5083-H111 and 6082-T651 aluminum alloys. Materials & Design. 2014, Vol. 54, C, pp. 207-211.
114. **Totten, G.E. and Mackenzie, S.** Handbook of aluminum. vol 1. Physical metallurgy and processes. Marcel Dekker Inc. : s.n., 2003. pp. 66-73. Vol. 1.
115. **Mathers, G.** The welding of aluminium and its alloys . Cambridge : Woodhead Publishing Limited, 2002.
116. **Elrefaey, A. and Ross, N.G.** Microstructure and mechanical properties of cold metal transfer welding similar and dissimilar aluminum alloys. Acta Metall Sin Engl Lett. 2015, Vol. 28, 6, pp. 715-724.
117. **Boşneag, A., Constantin, M.A., Niţu, E. and Iordache, M.** Friction Stir Welding of three dissimilar aluminium alloy used in aeronautics industry. IOP Conf. Ser.: Mater. Sci. Eng. 2017, Vol. 252, p. 012041.
118. **Sharma, S. and Upadhyay, V.** Friction Stir Welding of Dissimilar Aluminum Alloys AA5086 and AA7039. J. Phys.: Conf. Ser. 2019, Vol. 1240, p. 012160.
119. **Pourabbas, M., Abdollah-zadeh, A., Sarvari, M., Pouranvari, M. and Miresmaeili, R.** Investigation of structural and mechanical properties of magnetic pulse welded dissimilar aluminum alloys. Journal of Manufacturing Processes. 2019, Vol. 37, pp. 292-304.
120. **Meng, Z., Wang, X., Guo, W., Hu, Z., Vivek, A., Hua, L. and Daehn, G.S.** Joining Performance and Microstructure of the 2024/7075 Aluminium Alloys Welded Joints by Vaporizing Foil Actuator Welding. J. Wuhan Univ. Technol.-Mat. Sci. Edit. 2019, Vol. 34, pp. 368-372.
121. **Kou, S.** The Partially Melted Zone. Welding Metallurgy. 2. New-Jersey : A John Wiley & Sons, Inc., Publication, 2002, 3, pp. 304-328.
122. **Huang, C. and Kou, S.** Liquation Mechanisms in Multi-Component Aluminum Alloys During Welding. Welding Journal. 2002, Vol. 81, 10, pp. 211s-222s.
123. **Huang, C. and Kou, S.** Liquation cracking in partial-penetration aluminum welds: Effect of penetration oscillation and backfilling. Welding Journal. 2003, Vol. 82, pp. 184s-194s.
124. **Huang, C. and Kou, S.** Liquation Cracking in Full-Penetration Al-Mg-Si Welds. Welding Journal. 2004, Vol. 83, pp. 111s-122s.
125. **Song, S.-W., Lee, S.-H., Kim, B.-C., Yoon, T.-J., Kim, N.-K., Kim, I.-B. and Kang, C.-Y.** Liquation Cracking of Dissimilar Aluminum Alloys during Friction Stir Welding. Mater. Trans. 2011, Vol. 52, 2, pp. 254-257.
126. **Cornacchia, G. and Cecchel, S.** Study and Characterization of EN AW 6181/6082-T6 and EN AC 42100-T6 Aluminum Alloy Welding of Structural Applications: Metal Inert Gas (MIG), Cold Metal Transfer (CMT), and Fiber Laser-MIG Hybrid Comparison. Metals. 2020, Vol. 10, 4, p. 441.
127. **Dalle Donne, C., Braun, R., Staniek, G., Jung, A. and Kaysser, W.A.** Mikrostrukturelle, mechanische und korrosive Eigenschaften reibrührgeschweißter Stumpfnähte in Aluminiumlegierungen. Materialwissenschaft und Werkstofftechnik./Materials Science & Engineering Technology. 1998, Vol. 29, 10, pp. 609-617.
128. **Hassan, K.A.A., Prangnell, P.B., Norman, A.F., Price, D.A. and Williams, S.W.** Effect of welding parameters on nugget zone microstructure and properties in high strength aluminium alloy friction stir welds. Science and Technology of Welding and Joining. 2003, Vol. 8, 4, pp. 257-268.
129. **Wang, P., Chen, K., Jiang, H., Chen, S. and Hu, G.** Microstructures and properties of TIG welded joint of 7003 aluminum alloy. Materials Science and Engineering of Powder Metallurgy. 2016, Vol. 2016, 6, pp. 832-839.
130. An Experimental Investigation of the Heat Affected Zone (HAZ) Properties of AA6060 and AA7046 Following Different Heat Treatment Schedules. **Alisibramulisi, A., Myhr, O., Lademo, O.-G. and Larsen, P.** Yokohama: The Japan Institute of Light Metals, 2010. Proceedings of the 12th International Conference on Aluminium Alloys, September 5-9, 2010, Yokohama, Japan. pp. 994-999.
131. **Haryadi, G.D. and Kim, S.J.** Influences of post weld heat treatment on fatigue crack growth behavior of TIG welding of 6013 T4 aluminum alloy joint (Part 1. Fatigue crack growth across the weld metal). Journal of Mechanical Science and Technology. 2011, Vol. 25, pp. 2161–2170.

132. **Hou, B., Zhao, Y., Zhou, C., Xie, M. and Hu, Z.** Research on Welding Properties of Al-Mg Alloy Welding Wire Containing In. Material Sciences. 2019, Vol. 9, 3, pp. 189-195.
133. Weldability of AA 5052 H32 aluminium alloy by TIG welding and FSW process – A comparative study**. Shanavas, S. and Raja Dhas,** J.E. 2017. IOP Conf. Ser.: Mater. Sci. Eng. Vol. 247, p. 012016.
134. **Vijay Mohan Shetty, V.M., Vattem, R.K. and Musku, S.** Optimization and Evaluation of Ageing Parameters on Mechanical Properties of AA 6061AND AA 5154 Welded Joints using Taguchi Method. International Journal of Engineering Sciences & Researches Technology. 2018, Vol. 7, 5, pp. 64-72.
135. **Zhu, G., Wang, S., Zhang, M., Yang, X., Liu, W. and Wang, G.** Application of laser cleaning in postwelding treatment of aluminum alloy. Appl Opt. 2020, Vol. 59, 34, pp. 10967-1097.
136. **Mossman, M.M. and Lippold, J.C.** Weldability Testing of Dissimilar Combinations of 5000- and 6000-Series Aluminum Alloys. Welding Journal. 2002, Vol. September, pp. 188s-194s.
137. European aluminium. Joining - Arc Welding, the Aluminium Automotive Manual. [Online] 2015. [Cited: 18 February 2020.] https://www.european-aluminium.eu/media/1518/3-arc-welding_2015_new.pdf.
138. **Peter, I. and Rosso, M.** Study of 7075 aluminium alloy joints. Sci. Bull. Valahia Univ. Mater. Mech. 2017, Vol. 15, 13, pp. 7-11.
139. **Kang, M. and Kim, C.** A Review of Joining Processes for High Strength 7xxx Series Aluminum Alloys. J. Weld. Join. 2017, Vol. 35, 6, pp. 79-88.
140. **Niu, L.-Q., Li, X.-Y., Zhang, L., Liang, X.-B. and Li, M.** Correlation Between Microstructure and Mechanical Properties of 2219-T8 Aluminum Alloy Joints by VPTIG Welding[J]. Acta Metallurgica Sinica (English Letters). 2017, Vol. 30, 5, pp. 438-446.
141. **Kwon, Y. and Weckman, D.C.** Analytical thermal model of conduction mode double sided arc welding. Sci. Technol Weld Joi. 2008, Vol. 13, 6, pp. 539-549.
142. Nyrkova, L.I., Labur, T.M., Shevtsov, E.I., Nazarenko, O.P., Dorofeev, A.V., Osadchuk, S., Yavorska, M.R., Poklyatsky, A.G. and Fedorchuk, V. Complex of properties of 2219 alloy weld joint in T62 state under modeling operating conditions. Space Sci. & Technol. 2022, Vol. 28, 2, pp. 14-29.
143. **Su, D., Zhang, J. and Wang, B.** The microstructure and weldability in welded joints for AA 5356 aluminum alloy after adding modified trace amounts of Sc and Zr. Journal of Manufacturing Processes. 2020, Vol. 57, 88, pp. 488-498.
144. **Palanivel, R., Laubscher, R.F., Dinaharan, I. and Murugan, N.** Developing a Friction-StirWeldingWindow for Joining the Dissimilar Aluminum Alloys AA6351 and AA5083. Mater. Technol. 2017, Vol. 51, 1, pp. 5-9.
145. **Kumar, A. and Sundarrajan, S.** Optimization of pulsed TIG welding process parameters on mechanical properties of AA 5456 Aluminum alloy weldments. Materials & Design 2009, Vol. 30, 4, pp. 1288-1297.
146. **Singh, A.K., Dey, V. and Rai, R.N.** Techniques to improve weld penetration in TIG welding (A review). Materials Today: Proceedings 2017, Vol. 4, 2, A, pp. 1252-1259].
147. **Chen, Q., Lin, S., Yang, C., Fan, C. and Ge, H**. Grain fragmentation in ultrasonic-assisted TIG weld of pure aluminum. Ultrasonics Sonochemistry 2017, Vol. 39, pp. 403-413.
148. **Gupta, Y., Tanwar, A. and Gupta, R.** Investigation of Microstructure and Mechanical Properties of TIG and MIG Welding Using Aluminium Alloy. IOSR Journal of Mechanical and Civil Engineering 2016, Vol. 13, 5, pp. 121-126.
149. **Zhang, Y.M., Pan, C. and Male, A.T.** Improved microstructure and properties of 6061 aluminum alloy weldments using a double-sided arc welding process. Metall. Mater Trans A. 2000, Vol. 31, 10, pp. 2537-2543.
150. **Squillace A., Fenzo A. D, Giorleo G. and Bellucci F.** A comparison between FSW and TIG welding techniques: modifications of microstructure and pitting corrosion resistance in AA 2024-T3 butt joints. Journal of Materials Processing Technology 2004, Vol. 152, 1, pp. 97-105.
151. **Wang, X., Wang, K., Shen, Y. and Hu, K.** Comparison of fatigue property between friction stir and TIG welds. Journal of University of Science and Technology Beijing, Mineral, Metallurgy, Material 2008, Vol. 15, pp. 280-284.
152. **Cabello M., Ruckert G., Huneau S. B. and Marya S.** Comparison of TIG welded and friction stir welded Al–4.5Mg–0.26Sc alloy, Journal of Materials Processing Technology 2008, Vol. 197, 1-3, pp. 337-343.
153. **Zhao J., Jiang F., Jian H., Wen K., Jiang L. and Chen X.** Comparative investigation of tungsten inert gas and friction stir welding characteristics of Al–Mg–Sc alloy plates. Materials & Design 2010, Vol. 31, 1, pp. 306-311.
154. **Malarvizhia S. and Balasubramanian V**. Effects of welding processes and post-weld aging treatment on fatigue behavior of AA2219 aluminium alloy joints. Journal of Materials Engineering and Performance 2011, Vol. 20, 3, pp. 359-367.
155. **Zhen H., Yong P., Zhi Y. and Xue L.** Comparison of FSW and TIG welded joints in Al-Mg-Mn-Sc-Zr alloy plates. Transactions of Nonferrous Metals Society of China 2011, Vol. 21, pp. 1685-1691.

156. **Anjaneya Prasad B. and Prasanna P.** Experimental Comparison of the MIG and Friction Stir Welding Processes for AA 6061(AlMgSiCu) Aluminium Alloy. International Journal of Mining, Metallurgy & Mechanical Engineering 2013, Vol. 1, pp. 137-140.
157. **Jannet, S., Mathews, P.K. and Raja, R.** Comparative investigation of Friction stir welding & Fusion welding of 6061T-6 & 5083-0 Aluminium Alloys based on mechanical properties & microstructure. Journal of Achievements in Materials & Manufacturing Engg. 2013, Vol. 61, pp. 181-186.
158. **Sasidharan, B., Narayanan, K.P. and Prakash. R.S**. Tensile & Microstructural characteristics of DCSP TIG welded & Friction stir welded AA2219 Aluminum Alloy. International Journal of Design & Manufacturing Technology 2014, Vol. 5, pp. 121-129.
159. **Ashwani Kumar, Shakti Singh Gautam and Alok Kumar.** Heat input & joint efficiency of three welding processes TIG, MIG & FSW using AA6061. International Journal of Mechanical Engg. & Robotic Research 2014, Vol. 1, pp. 89-94.
160. **Navyashree, S. and Sivaramakrishna, V.** Experimental Investigation of Friction Stir Welding and TIG Welding for Al-6082. International Journal of Innovative Research in Science, Engg. & Technology 2015, Vol. 4, pp. 5292-5298.
161. **Vimalraj, C., Kah, P., Mvola, B. and Martikainen, J.** Effect of nanomaterial addition using gmaw and gtaw processes. Rev. Adv. Mater. Sci. 2016, Vol. 44, pp. 370–382.
162. **Kumar, A. and Milton, M.S.** A Comparison of Welding Techniques of Aluminium Alloys. A Literature Review. International Journal of Scientific Research in Science, Engineering and Technology 2016, Vol. 2, 3, pp. 172-175.
163. **Sukhbir Singh, Vineet Kumar, Sudhir Kumar and Ajay Kumar.** Variant of MIG welding of similar and dissimilar metals: A review. Materials Today: Proceedings 2022, Vol. 56, 6, pp. 3550-3555.
164. **Nie, F., Dong, H., Chen, S., Li, P., Wang, L., Zhao, Z., Li, X., and Zhang, H.** Microstructure and Mechanical Properties of Pulse MIG Welded 6061/A356 Aluminum Alloy Dissimilar Butt Joints. Journal of Materials Science & Technology 2018, 34(3):551-560, https://doi.org/10.1016/j.jmst.2016.11.004.
165. **Eakkachai Warinsiriruk, Jukkapun Greebmalai and Montri Sangsuriyun.** Effect of Double Pulse MIG Welding on Porosity Formation on Aluminium 5083 Fillet Joint. MATEC Web of Conferences 2019, Vol. 269, p. 01002.
166. **Bai, Y., Gao, H.M. and Qiu, L.** Droplet transition for plasma-MIG welding on aluminium alloys. Transactions of Nonferrous Metals Society of China 2010, Vol. 20, 12, pp. 2234-2239.
167. **Liu, J., Zhu, H., Li, Z., Cui, W. and Shi, Y.** Effect of ultrasonic power on porosity, microstructure, mechanical properties of the aluminum alloy joint by ultrasonic assisted laser-MIG hybrid welding.
168. **Chen, C., Fan, C., Lin, S., Cai, X., Zhou, L., Ye, S., and Yang, C**. Effect of ultrasonic pattern on weld appearance and droplet transfer in ultrasonic assisted MIG welding process. Journal of Manufacturing Processes 2018, Vol. 35, pp. 368-372.
169. **Wojdat, T., Kustroń, P., Jaskiewicz, K., Zwierzchowski, M. and Margielewska, A**. Numerical modelling of welding of car body sheets made of selected aluminum alloys. Arch. Metall. Mater. 2019, Vol. 64, 4, pp. 1403-1409.
170. **Pfeifer, T. and Rykała, J.** Welding EN AW7075 Aluminium Alloy Sheets—Low-energy Versus Pulsed Current. Inst. Weld. Bull. Gliwice. 2014, Vol. 5, pp. 137-144.
171. The CMT process a revolution in welding technology. **Bruckner, J., Wagner, J. and Arenholz, E.** San Francisco : s.n., 2005. Proceedings of the International Light Metals Technology Conference 2005, San Francisco, CA, USA. pp. 275-284.
172. **Pfeifer, T. and Stano, S.** Modern methods of weldbrazing in the aspect of quality and properties of joints. Weld. Technol. Rev. 2016, Vol. 9, pp. 95-102.
173. **Talalaev, R., Veinthal, R., Laansoo, A. and Sarkans, M.** Cold metal transfer (CMT) welding of thin sheet metal products. Est J Eng. 2012, Vol. 18, 3, pp. 243-250.
174. **Feng, J., Zhang, H. and He, P.** The CMT short-circuiting metal transfer process and its use in thin aluminium sheets welding. Mater Design. 2009, Vol. 30, 5, pp. 1850-1852.
175. **Dutra, J.C., Gonçalves e Silva, R.H., Martinello Savi, B., Marques, C. and Alarcon, O.E.** Metallurgical characterization of the 5083H116 aluminum alloy welded with the cold metal transfer process and two different wire-electrodes (5183 and 5087). Weld world. 2015, Vol. 59, 6, pp. 797-807.
176. **Shu, F.Y., Tian, Z., Lu, Y.H., He, W.X., Lu, F.Y., Lin, J.J., Zhao, H.Y. and Xu, B.S.** Prediction of vulnerable zones based on residual stress and microstructure in cmt welded aluminium alloy joint. Trans Nonferrous Met. Soc China. 2015, Vol. 25, 8, pp. 2701-2707.
177. **Shu, F.Y., Lu, Y.H., Liu, Y.X., Xu, F.J., Sun, Z., He, P. and Xu, B.S.** FEM modeling of softened base metal in narrow-gap joint by CMT+Pmix welding procedure. Trans Nonferrous Met. Soc China. 2014, Vol. 24, 6, pp. 1830-1835.
178. **Kotsikos, G., Robinson, M., Zangani, D. and Roberts, J.** Investigation of the weld unzipping failure mode during collisions of welded aluminium rail vehicles. Proceedings of the Institution of Mechanical Engineers, Part F: Journal of Rail and Rapid Transit. 2008, Vol. 222, 1, pp. 59-68.

179. Improving the Crashworthiness of Aluminium Rail Vehicles**. Zangani, D., Robinson, M. and Kotsikos, G. [ed.] S., Rodopoulos, C. Pantelakis. s.l.** : Springer, Dordrecht, 2009. Engineering Against Fracture.
180. **Gay, R., Robinson, M. and Zangani, D.** Crashworthiness of Joints in Aluminium Rail Vehicles. [Online] 2022. https://trimis.ec.europa.eu/sites/default/files/project/documents/20091125_164508_79987_ALJOIN%20overview%20paper.pdf.
181. **Zhao, Y., Chen, F., Cao, S., Chen, C. and Xie, R.** Effect of CMT Welding Heat Input on Microstructure and Properties of 2A14 Aluminum Alloy Joint. Metals 2022, Vol. 12, p. 2100
182. **Hari Shanker and Reeta Wattal.** Comparative study of microstructural and mechanical properties of robotic CMT and GMAW welded 7475-T7351 aluminium alloy joints. Materials Today Communications 2023, Vol. 37, p. 106994
183. **Tian, Y., Shen, J., Hu, S. and Gou, J.** Macrostructure, microstructure and wear performance of Al alloy cladding fabricated by CMT technique. Eng. Res. Express 2020, Vol. 2, p. 015026
184. **Yang, G., Guan, K., Zou, L., Sun, Y. and Yang, X**. Weld Defect Detection of a CMT Arc-Welded Aluminum Alloy Sheet Based on Arc Sound Signal Processing. Appl. Sci. 2023, Vol. 13, p. 5152.
185. **Srinivasan, D., Sevvel, P., Solomon, I.J. and Tanushkumaar, P.** A review on Cold Metal Transfer (CMT) technology of welding. Materials Today: Proceedings 2022, Vol. 64, 1, pp. 108-115.
186. **Zhang, H., Feng, J., He, P., Zhang, B., Chen, J. and Wang, L.** The arc characteristics and metal transfer behaviour of cold metal transfer and its use in joining aluminium to zinc-coated steel. Mater. Sci. Eng. A 2007, Vol. 499, pp. 111–113.
187. **Shang, J., Wang, K., Zhou, Q., Zhang, D., Huang, J. and Li, G.** Microstructure characteristics and mechanical properties of cold metal transfer welding Mg/Al dissimilar metals. Mater. Des. 2012, Vol. 34, pp. 559–565.
188. **Cao, R., Wen, B., Chen, J. and Wang, P.-C.** Cold Metal Transfer joining of magnesium AZ31B-to-aluminum A6061-T6. Mater. Sci. Eng. A 2013, Vol. 560, pp. 256–266.
189. **Indra Jeet Singh, Qasim Murtaza and Paras Kumar.** A comprehensive review on effect of cold metal transfer welding parameters on dissimilar and similar metal welding. Journal of Engineering Research 2023, doi: 10.1016/j.jer.2023.12.009.
190. **Gierth, M., Henckell, P., Ali, Y., Scholl, J., and Bergmann, J**. Wire Arc Additive Manufacturing (WAAM) of aluminum alloy AlMg5Mn with energy-reduced Gas Metal Arc Welding (GMAW). Materials. 2020, Vol. 13, p. 2671.
191. **Bergmann, J.P., Bielenin, M. and T., Feustel.** Aluminum welding by combining a diode laser with a pulsed Nd:YAG laser. Welding in the World. 2015, Vol. 59, pp. 307-315.
192. **Park, Y.W. and Rhee, S.** Process modeling and parameter optimization using neural network and genetic algorithms for aluminum laser welding automation. Int J Adv Manuf Technol. 2008, Vol. 37, pp. 1014-1021.
193. Influence of Alloy and Solidification Parameters on Grain Refinement in Aluminum Weld Metal due to Inoculation. Schempp, **P., Tang, Z., Cross, C., Pittner, A., Seefeld, T. and Rethmeier, M**. Chicago : s.n., 2012. ASM Proceedings of the 9th International Conference: Trends in Welding Research June 4–8, 2012, Chicago, Illinois, USA. pp. 98-107.
194. **Zhao, H. and DebRoy, T.** Macroporosity free aluminum alloy weldments through numerical simulation of keyhole mode laser welding. J Appl Phys. 2003, Vol. 93, 12, pp. 10089-10096.
195. **Pastor, M., Zhao, H., Martukanitz, R.P. and Debroy, T.** Porosity, underfill and magnesium lose during continuous wave Nd: YAG laser welding of thin plates of aluminum alloys 5182 and 5754 78: 207-s. Welding Journal. 1999, Vol. 78, 6, pp. 207s-216s.
196. **Sheikhi, M, F.M., Ghaini and Assadi, H.** Prediction of solidification cracking in pulsed laser welding of 2024 aluminum alloy. Acta Mater. 2015, Vol. 82, pp. 491-502.
197. **Yi, H., Jian, H. and Pulin, N.** Microstructures and Textures of 6016 and 5182 Aluminum Laser Welded Joints. Chinese Journal of Lasers. 2019, Vol. 46, 4, p. 0402003.
198. **Sánchez-Amaya, J.M., Delgado, T., González-Rovira, L. and Botana, F.J.** Laser Welding of Aluminium Alloys 5083 and 6082 under Conduction Regime. Applied Surface Science. 2009, Vol. 255, 23, pp. 9512-9521.
199. Strengthening mechanism in laser-welded 2219 aluminium alloy under the cooperative effects of aging treatment and pulsed electromagnetic loadings. Mater. Sci. Eng. A 2018, Vol. 714, pp. 124–139.
200. **Wang, Z., Oliveira, J.P., Zeng, Z., Bu, X., Peng, B. and Shao, X**. Laser beam oscillating welding of 5A06 aluminum alloys: Microstructure, porosity and mechanical properties. Opt. Laser Technol. 2019, Vol. 111, pp. 58–65.
201. **Peng, G., Li, L., Wang, J., Xia, H., Meng, S. and Gong, J.** Effect of subatmospheric pressures on weld formation and mechanical properties during disk laser welding of 5A06 aluminium alloy. J. Mater. Process. Technol. 2020, Vol. 277, p. 116457.
202. **Braun, R.** Nd:YAG laser butt welding of AA6013 using silicon and magnesium containing filler powders. Mater. Sci. Eng. A 2006, Vol. 426, pp. 250-262.

203. **Zhang, L., Li, X., Nie, Z., Huang, H. and Sun, J.** Microstructure and mechanical properties of a new Al–Zn–Mg–Cu alloy joints welded by laser beam. Mater. Des. 2015, Vol. 83, pp. 451–458.
204. **Enz, J., Khomenko, V., Riekehr, S., Ventzke, V., Huber, N. and Kashaev, N.** Single-sided laser beam welding of a dissimilar AA2024–AA7050 T-joint. Mater. Des. 2015, Vol. 76, pp. 110-116.
205. **Viscusi, A., Leitão, C., Rodrigues, D.M., Scherillo, F., Squillace, A. and Carrino, L.** Laser beam welded joints of dissimilar heat treatable aluminium alloys. J. Mater. Process. Technol. 2016, Vol. 236, pp. 48-55.
206. **Enz, J., Kumar, M., Riekehr, S., Ventzke, V., Huber, N. and Kashaev, N.** Mechanical properties of laser beam welded similar and dissimilar aluminum alloys. J. Manuf. Process. 2017, Vol. 29, pp. 272–280.
207. **Bunaziv, I., Akselsen, O.M., Salminen, A. and Unt, A.** Fiber laser-MIG hybrid welding of 5mm 5083 aluminum alloy. Journal of Materials Processing Technology 2016, Vol. 233, pp. 107-114.
208. **Bunaziv, I., Akselsen, O.M., Ren, X., Nyhus, B. and Eriksson, M.** Laser Beam and Laser-Arc Hybrid Welding of Aluminium Alloys. Metals 2021, Vol. 11, 8, p. 8.
209. **Shibata, K., Sakamoto, H. and Iwase, T.** Laser-MIG Hybrid Welding of Aluminium Alloys. Weld World 2006, Vol. 50, pp. 28–34.
210. **Han, X., Yang, Z., Ma, Y., Shi, C. and Xin, Z.** Porosity distribution and mechanical response of laser-MIG hybrid butt welded 6082-T6 aluminum alloy joint. Optics & Laser Technology 2020, Vol. 132, p. 106511.
211. **Katayama, S., Uchiumi, S., Mizutani, M., Wang, J. and Fujii, K.** Penetration and porosity prevention mechanism in YAG laser-MIG hybrid welding, Welding International 2007, Vol. 21, 1, pp. 25–31.
212. **Yan, J., Zeng, X., Gao, M., Lai, J. and Lin, T**. Effect of welding wires on microstructure and mechanical properties of 2A12 aluminum alloy in CO2 laser-MIG hybrid welding. Appl. Surf. Sci. 2009, Vol. 255, pp. 7307–7313.
213. **Ahn, J., Chen, L., He, E., Davies, C.M. and Dear, J.P**. Effect of filler metal feed rate and composition on microstructure and mechanical properties of fibre laser welded AA 2024-T3. J. Manuf. Process. 2017, Vol. 25, pp. 26–36.
214. **Ahn, J., He, E., Chen, L., Dear, J. and Davies, C.** The effect of Ar and He shielding gas on fibre laser weld shape and microstructure in AA 2024-T3. J. Manuf. Process. 2017, Vol. 29, pp. 62–73.
215. **Ahn, J., Chen, L., He, E., Dear, J.P., and Davies, C.M.** Optimisation of process parameters and weld shape of high power Yb-fibre laser welded 2024-T3 aluminium alloy. J. Manuf. Process. 2018, Vol. 34, pp. 70–85.
216. **Yan, S., Nie, Y., Zhu, Z., Chen, H., Gou, G., Yu, J. and Wang, G.** Characteristics of microstructure and fatigue resistance of hybrid fiber laser-MIG welded Al–Mg alloy joints. Appl. Surf. Sci. 2014, Vol. 298, pp. 12–18.
217. **Huang, L., Wu, D., Hua, X., Liu, S., Jiang, Z., Li, F., Wang, H. and Shi, S**. Effect of the welding direction on the microstructural characterization in fiber laser-GMAW hybrid welding of 5083 aluminum alloy. J. Manuf. Process. 2018, Vol. 31, pp. 514–522.
218. **Leo, P., D'Ostuni, S. and Casalino, G.** Hybrid welding of AA5754 annealed alloy: Role of post weld heat treatment on microstructure and mechanical properties. Mater. Des. 2016, Vol. 90, pp. 777–786.
219. **Yan, S.H. Chen, H., Zhu, Z.T. and Gou, G.Q.** Hybrid laser-Metal Inert Gas welding of Al–Mg–Si alloy joints: Microstructure and mechanical properties. Mater. Design. 2014, Vol. 61, pp. 160-167.
220. **Zhang, C., Gao, M., Jiang, M. and Zeng, X.** Effect of weld characteristic on mechanical strength of laser-arc hybrid-welded Al-Mg-Si-Mn aluminum alloy. Metall. Mater. Trans. A 2016, Vol. 47, pp. 5438-5449.
221. **Yan, S., Xing, B., Zhou, H., Xiao, Y., Qin, Q.-H., and Chen, H**. Effect of filling materials on the microstructure and properties of hybrid laser welded Al-Mg-Si alloys joints. Mater. Charact. 2018, Vol. 144, pp. 205-218.
222. **Wang, H., Liu, X. and Liu, L.** Research on laser-TIG Hybrid welding of 6061-T6 aluminum alloys joint and post heat treatment. Metals 2020, 10, 130.
223. **Hu, B. and Richardson, I.M.** Microstructure and mechanical properties of AA7075(T6) hybrid laser/GMA welds. Mater. Sci. Eng. A 2007, Vol. 459, pp. 94-100.
224. **Ola, O.T. and Doern, F.E.** Fusion weldability studies in aerospace AA7075-T651 using high-power continuous wave laser beam techniques. Mater. Des. 2015, Vol. 77, pp. 50-58.
225. **Allen, C.M., Verhaeghe, G., Hilton, P.A., Heason, C.P. and Prangnell, P.B.** Laser and hybrid laser-MIG welding of 6.35 and 12.7 mm thick aluminium aerospace alloy. Mater. Sci. Forum 2006, Vol. 519–521, pp. 1139–1144.
226. **Korzhyk, V., Khaskin, V., Grinyuk, A.A., Shcheretskyi, V., Oleinychenko, T. and Babych, O.** Hybrid Laser-MIG Welding of Aluminum Alloys Al-Mg-Mn, Al-Cu-Mg and Al-Mg-Li Systems. Environment Technology Resources Proceedings of III International Scientific and Practical Conference Chicago, USA 1-3 September 2021, pp. 125-132 .
227. **Nathish, .P.V., Naveen Ram kumar M., Raghul Raaj, K. and Omprakasam, S.** Hybrid Laser Beam Welding of Aluminium Alloys. International Research Journal of Engineering and Technology 2017, Vol. 4, 11, pp. 520-524.
228. **Daehn, G.S. and Lippold, J.C.** Low-Temperature Spot Impact Welding Driven without Contact. U.S. Patent No. PCT/US09/36499, 27 December 2011.

229. **Zhao, Y.B., Lei, Z.L., Chen, Y.B. and Tao, W. A** comparative study of laser-arc double sided welding and double-sided arc welding of 6 mm 5A06 aluminium alloy. Mater. Design. 2011, Vol. 32, 4, pp. 2165-2171.
230. **Han, B., Chen, Y.B., Wang, T., Lei, Z.L., Li, H., Guo, S., and Li, P.** Nano-indentation investigation on the local softening of equiaxed zone in 2060–T8/2099-T83 aluminum-lithium alloys T-joints welded by double-sided laser beam welding. J. Alloy Compd. 2018, Vol. 756, pp. 145-162.
231. **Chen, X., Lei, Z., Chen, Y., Han, B., Jiang, M., Tian, Z., Bi, J. and Lin, S.** Nano-indentation and in-situ investigations of double-sided laser beam welded 2060–T8/2099-T83 Al-Li alloys T-joints. Mat. Sci Eng A-Struct. 2019, Vol. 756, pp. 291-301
232. **Sadeh, S., Gleason, G.H. Hatamleh, M.I., Sunny, S.F., Yu, H., Malik, A.S. and Qian, D**. Simulation and Experimental Comparison of Laser Impact Welding with a Plasma Pressure Model. Metals 2019, Vol. 9, p. 1196.
233. **Wang, X. and Gu, C.** Laser shock welding of aluminum/aluminum and aluminum/copper plates. Mater. Des. 2014, Vol. 56, pp. 26-30.
234. **Peyre, P., Berthe, L. and Fabbro, R.** Laser shock processing of materials: Basics mechanisms and applications. In Proceedings of the 65th Laser Materials Processing Conference, Tokyo, Japan, 2–5 December 2005; pp. 95–109.
235. **Wang, X. and Gu, Y.** An experimental and numerical study of laser impact spot welding. Mater. Des. 2015, Vol. 65, pp. 1143-1152].
236. **Çam, G., Ventzke, V., Dos Santos, J.F., Koçak, M., Jennequin, G. and Gonthier-Maurin, P.** Characterisation of electron beam welded aluminium alloys. Science and Technology of Welding and Joining. 1999, Vol. 4, 5, pp. 317-323.
237. **Fujii, H., Umakoshi, H., Aoki, Y. and Nogi, K.** Bubble formationin aluminium alloy during electron beam welding. Journal of Materials Processing Technology 2004, Vol. 155-156, 1-3, pp. 1252–1255.
238. **Elseddig, Z.A., Sobih, M., Almazy, Kh. and Sallam, M.** Experimental investigation of electron beam welding of AA1350aluminum alloy. in Proceedings of the in 14th International Conference on Applied Mechanics and Mechanical Engineering, Cairo, Egypt, 2010.
239. **Sobih, M., Elseddig, Z., Almazy, K., Youssef, A. and Sallam, M**. Optimization of EBW parameters for 2219 al-alloy using greyrelation method. Advanced Materials Research 2012, Vol. 591-593, pp. 507-514.
240. **Sobih, M., Elseddig, Z., Almazy, K. and Sallam, M.** Experimental Evaluation and Characterization of Electron Beam Welding of 2219 AL-Alloy. Indian Journal of Materials Science 2016, Vol. 5, pp. 1-6.
241. **Saha, D.C. and Park, Y.D.** A Review on Al-Al/Al-Steel Resistance Spot Welding Technologies for Light Weight Vehicles. Journal of KWJS. 2011, Vol. 29, 4, pp. 397-402.
242. **Auhl, J.R. and Patrick, E.P.** A fresh look at resistance spot welding of aluminium automotive components. SAE Technical Paper. 1994, p. 940160.
243. **Ronnhult, T., Rilby, U. and Olefjord, I.** The surface state and weldablity of aluminium alloys. Materials Science and Engineering. 1980, Vol. 42, pp. 329-336.
244. **Li, Z., Hao, C., ZHANG, J. and Zhang, H.** Effects of Sheet Surface Conditions on Electrode Life in Resistance Welding Aluminum. Welding journal. 2007, Vol. 86, 4, pp. 81s-89s.
245. **Newton, C., Thornton, M., Keay, B., Sheasby, P. and Boomer, D.** How to Weld Bond Aluminium with Structural Adhesives. SAE Technical Paper. 1997, p. 970018.
246. **Miller, W.S., Zhuang, L., Bottema, J., Wittebrood, A.J., De Smet, P., Haszler, A. and Vieregge, A.** Recent development in aluminium alloys for the automotive industry. Materials Science and Engineering. 2000, Vol. 280, 1, pp. 37-49.
247. **Shah, U. and Liu, X.** Effect of ultrasonic energy on the spot weldability of aluminum alloy AA6061. Mater. Des. 2020, Vol. 192, p. 108690.
248. **Qi, L., Zhang, Q., Ma, Y., Xu, Y., Han, X. and Li, Y.** A comparative study on mechanical performance of traditional and magnetically assisted resistance spot welds of A7N01 aluminum alloy. J. Manuf. Process. 2021, Vol. 66, pp. 133-144.
249. Metal Suppliers Online. Aluminum 7178 aluminum - material property data sheet. [Online] https://www.suppliersonline.com/propertypages/7178.asp.
250. **Davis, J.R.** Aluminum and Aluminum Alloys - Chapter. Alloying: Understanding the Basics. Materials Park, Ohio : ASM International, 2001, pp. 351-416.
251. **Fracchia, E., Gobber, F. and Rosso, M.** About weldability and welding of Al alloys: Case study and problem solving. Journal of Achievements in Materials and Manufacturing Engineering. 2017, Vol. 2, 85, pp. 67-74.
252. **Matokhnyuk, L.E., Byalonovich, A., Gopkalo, E., Vorob'ev, E., Karaush, D. and Malyshko, V.** Fatigue Resistance of 2219 Aluminum Alloy and its Welded Joints. Strength Mater. 2019, Vol. 51, pp. 860-867.
253. **Manladan, S.M., Yusof, F., Ramesh, S., Fadzil, M., Luo Z. and Ao, S. A** review on resistance spot welding of aluminum alloys. Int J Adv Manuf Technol 2017, Vol. 90, pp. 605-634.
254. Evaluation of Joint Performance of 5056 Aluminum Friction Welded Joints By Heat Input And Burn-Off Quantity. **Ochi, H., Sawai, T., Yamamoto, Y., Ogawa, K. and Suga, Y.** Seatle, Washington, USA : s.n., 2000.

Paper presented at the Tenth International Offshore and Polar Engineering Conference Seattle, Washington, USA, May 2000.

255. **Shambhu Kumar Manjhi, Ashish Das, and Shashi Bhushan Prasad.** Review on joining of aluminum alloy by solid-state welding technique. Materials Today: Proceedings 2020, Vol. 26, 2, pp. 1255-1261.
256. **Patel, V., Li, W., Wang, G., Wang, F., Vairis, A. and Niu, P.** Friction Stir Welding of Dissimilar Aluminum Alloy Combinations: State-of-the-Art. Metals. 9. 270. 10.3390/met9030270. 2019, Vol. 9, 3, p. 270.
257. **Barbini, A., Carstensen, J. and Dos Santos, J.** Influence of Alloys Position, Rolling and Welding Directions on Properties of AA2024/AA7050 Dissimilar ButtWeld Obtained by Friction Stir Welding. Metals. 2018, Vol. 8, 4, p. 202.
258. **Cavaliere, P., Santis, A., Panella, F. and Squillace, A.** Effect of welding parameters on mechanical and microstructural properties of dissimilar AA6082-AA2024 joints produced by friction stir welding. Mater. Des. 2009, 30, 609–616. Mater. Des. 2009, 30, 609–616. 2009, Vol. 30, 3, pp. 609-616.
259. Friction stir welding of dissimilar alloys for aircraft. Presented at the 5th International Symposium on Friction Stir Welding, Metz, France, 2004. **Gérard, H. and Ehrström, J.C.** 2004. Proceedings of International Friction Stirr Welding Symposium, Metz, France, 14–16 September 2004.
260. **Amancio-Filho, S.T., Sheikhi, S., dos Santos, J.F. and Bolfarini, C.** Preliminary study on the microstructure and mechanical properties of dissimilar friction stir welds in aircraft aluminium alloys 2024-T351 and 6056-T4. J Mater Process Technol. 2008, Vol. 206, 1-3, pp. 132-142.
261. **Lee, W.-B., Yeon, Y.-M. and Jung, S.-B.** The joint properties of dissimilar formed Al alloys by friction stir welding according to the fixed location of materials. Scr Mater. 2003, Vol. 49, 5, pp. 423-428.
262. **Niu, P., Li, W. and Chen, D.** Strain hardening behavior and mechanisms of friction stir welded dissimilar joints of aluminum alloys. Mater. Lett. 2018, 231, 68–71. 2018, Vol. 231, C, pp. 68-71.
263. **Niu, P., Li, W., Li, N., Xu, Y. and Chen, D.L.** Exfoliation corrosion of friction stir welded dissimilar 2024-to-7075 aluminum alloys. Mater. Charact. 2019, Vol. 147, pp. 93-100.
264. **Hasan, M.M., Ishak, M. and Rejab, M.R.M.** Effect of pin tool flute radius on the material flow and tensile properties of dissimilar friction stir welded aluminum alloys. Int J Adv Manuf Technol. 2018, Vol. 98, pp. 2747-2758.
265. **Kalemba-Rec, I., Kopyściański, M., Miara, D. and Krasnowski, K.** Effect of process parameters on mechanical properties of friction stir welded dissimilar 7075-T651 and 5083-H111 aluminum alloys. Int. J. Adv. Manuf. Technol. 2018, 97, 2767–2779. 2018, Vol. 97, pp. 2767-2779.
266. **Safarbali, B., Shamanian, M. and Eslami, A.** Effect of post-weld heat treatment on joint properties of dissimilar friction stir welded 2024-T4 and 7075-T6 aluminum alloys. Trans. Nonferrous Met. Soc. China. 2018, Vol. 28, 7, pp. 1287-1297.
267. **Palanivel, R., Laubscher, R., Vigneshwaran, S. and Dinaharan, I.** Prediction and optimization of the mechanical properties of dissimilar friction stir welding of aluminum alloys using design of experiments. Proceedings of the Institution of Mechanical Engineers, Part B: Journal of Engineering Manufacture. 2018, Vol. 232, 8, pp. 1384-1394.
268. **Hamilton, C., Dymek, S., Dryzek, E., Kopyscianski, M., Pietras, A., Węglowska, A. and Wrobel, M. Application** of positron lifetime annihilation spectroscopy for characterization of friction stir welded dissimilar aluminum alloys. Mater. Charact. 2017, Vol. 132, pp. 431-436.
269. Huang, B.W., Qin, Q.D., Zhang, D.H., Wu, Y.J., and Su, X.D. Microstructure and Mechanical Properties of Dissimilar Joints of Al-Mg2Si and 5052 Aluminum Alloy by Friction Stir Welding. J. Mater. Eng. Perform. 2018, 27, 1898–1907. 2018, Vol. 27, pp. 1898-1907.
270. **Moradi, M.M., Aval, H.J., Jamaati, R., Amirkhanlou, S. and Ji, S.** Microstructure and texture evolution of friction stir welded dissimilar aluminum alloys: AA2024 and AA6061. J. Manuf. Processes. 2018, Vol. 32, pp. 1-10.
271. **Prasanth, R.S.S. and Raj, K.H.** Determination of Optimal Process Parameters of Friction Stir Welding to Join Dissimilar Aluminum Alloys Using Artificial Bee Colony Algorithm. Trans. Indian Inst. Met. 2017, 71, 453–462. 2017, Vol. 71, pp. 453-462.
272. **Azeez, S. and Akinlabi, E.** Effect of processing parameters on microhardness and microstructure of a double-sided dissimilar friction stir welded aa6082-t6 and aa7075-t6 aluminum alloy. Mater. Today: Proc. 2018, Vol. 5, 9, pp. 18315-18324.
273. **Peng, G., Ma, Y., Hu, J., Jiang, W., Huan, Y., Chen, Z. and Zhang, T.** Nanoindentation Hardness Distribution and Strain Field and Fracture Evolution in Dissimilar Friction Stir-Welded AA 6061-AA 5A06 Aluminum Alloy Joints. Adv. Mater. Sci. Eng. 2018, p. 4873571.
274. **Das, U. and Toppo, V.** Effect of Tool Rotational Speed on Temperature and Impact Strength of Friction Stir Welded Joint of Two Dissimilar Aluminum Alloys. Mater. Today: Proc. 2018, Vol. 5, 2(1), pp. 6170-6175.
275. **Sarsılmaz, F.** Relationship between micro-structure and mechanical properties of dissimilar aluminum alloy plates by friction stir welding. J. Therm. Sci. 2018, 22, 55–66. 2018, Vol. 22, 1, pp. 55-66.
276. **No, K., Yoo, J.T., Yoon, J.H. and Lee, H.S.** Effect of Process Parameters on Friction Stir Welds on AA2219-AA2195 Dissimilar Aluminum Alloys. Korean J. Mater. Res. 2017, Vol. 27, 6, pp. 331-338.

277. **Kopyscianski, M., Dymek, S., Hamilton, C., Węglowska, A., Pietras, A., Szczepanek, M. and Wojnarowska, M.** Microstructure of Friction Stir Welded Dissimilar Wrought 2017A and Cast AlSi9Mg Aluminum Alloys. Acta Phys. Pol. A 2017, 131, 1390–1394. 2017, Vol. 130, 5, pp. 1390-1394.
278. **Ghaffarpour, M., Kazemi, M., Mohammadi Sefat, M.J., Aziz, A. and Dehghani, K.** Evaluation of dissimilar joints properties of 5083-H12 and 6061-T6 aluminum alloys produced by tungsten inert gas and friction stir welding. Proc. Inst. Mech. Eng. 2015, 231, 297–308. 2015, Vol. 231, 3, pp. 297-308.
279. **Bijanrostami, K., Barenji, R.V. and Hashemipour, M.** Effect of Traverse and Rotational Speeds on the Tensile Behavior of the Underwater Dissimilar Friction Stir Welded Aluminum Alloys. J. of Materi Eng and Perform. 2017, Vol. 26, pp. 909-920.
280. **Kasman, S., Kahraman, F. and Emiralioglu, A.** A Case Study for the Welding of Dissimilar EN AW 6082 and EN AW5083 Aluminum Alloys by Friction Stir Welding. Metals. 2016, Vol. 7, 1, p. 6.
281. **Doley, J.K. and Kore, S.D.** A Study on Friction Stir Welding of Dissimilar Thin Sheets of Aluminum Alloys AA 5052–AA 6061. J. Manuf. Sci. Eng. 2016, 138, 114502. 2016, Vol. 138, 11, p. 114502.
282. **Saravanan, V., Rajakumar, S., Nilotpal Banerjee and Amuthakkannan, R.** Effect of shoulder diameter to pin diameter ratio on microstructure and mechanical properties of dissimilar friction stir welded AA2024-T6 and AA7075-T6 aluminum alloy joints. Int. J. Adv. Manuf. Technol. 2016, Vol. 87, pp. 3637-3645.
283. **Yan, Z., Liu, X. and Fang, H.** Effect of Sheet Configuration on Microstructure and Mechanical Behaviors of Dissimilar Al–Mg–Si/Al–Zn–Mg Aluminum Alloys Friction Stir Welding Joints. J. Mater. Sci. Technol. 2016, 32, 1378–1385. 2016, Vol. 32, 12, pp. 1378-1385.
284. **Yan, Z.-J., Liu, X.-S. and Fang, H.-Y.** Fatigue Behavior of Dissimilar Al–Mg–Si/Al–Zn–Mg Aluminum Alloys Friction Stir Welding Joints. Acta Metall. Sinica 2016, 29, 1161–1168. 2016, Vol. 29, pp. 1161-1168.
285. **Zapata, J., Toro, M. and López, D.** Residual stresses in friction stir dissimilar welding of aluminum alloys. J. Mater. Process. Technol. 2016, Vol. 229, pp. 121-127.
286. **Sun, Y., Tsuji, N. and Fujii, H.** Microstructure and Mechanical Properties of Dissimilar Friction Stir Welding between Ultrafine Grained 1050 and 6061-T6 Aluminum Alloys. Metals. 2016, Vol. 6, 10, p. 249.
287. **Texier, D., Zedan, Y., Amoros, T., Feulvarch, E., Stinville, J.C. and Bocher, P.** Near-surface mechanical heterogeneities in a dissimilar aluminum alloys friction stir welded joint. Mater. Des. 2016, 108, 217–229. 2016, Vol. 108, pp. 217-229.
288. **Rodriguez, R.I., Jordon, J.B., Allison, P.G., Rushing, T. and Garcia, L.** Low-cycle fatigue of dissimilar friction stir welded aluminum alloys. Mater. Sci. Eng. A 2016, 654, 236–248. 2016, Vol. 654, pp. 236-248.
289. **Rodriguez, R.I., Jordon, J.B., Allison, P.G., Rushing, T. and Garcia, L.** Microstructure and mechanical properties of dissimilar friction stir welding of 6061-to-7050 aluminum alloys. Mater. Des. 2015, Vol. 83, pp. 60-65.
290. **Ilangovan, M., Boopathy, S.R. and Balasubramanian, V.** Effect of tool pin profile on microstructure and tensile properties of friction stir welded dissimilar AA 6061–AA 5086 aluminium alloy joints. Defence Technol. 2015, Vol. 11, 2, pp. 174-184.
291. **Reza-E-Rabby, M., Tang, W. and Reynolds, A.P.** Effect of tool pin features on process response variables during friction stir welding of dissimilar aluminum alloys. Sci. Technol. Weld. Joining. 2015, Vol. 20, 5, pp. 425-432.
292. **Donatus, U., Thompson, G.E. and Zhou, X.** Anodizing Behavior of Friction StirWelded Dissimilar Aluminum Alloys. J. Electrochem. Soc. 2015, 162, C657–C665. 2015, Vol. 162, 12, pp. C657-C665.
293. **Karam, A., Mahmoud, T.S., Zakaria, H.M. and Khalifa, T.A.** Friction Stir Welding of Dissimilar A319 and A413 Cast Aluminum Alloys. Arab J. Sci. Eng. 2014, 39, 6363–6373. 2014, Vol. 39, pp. 6363-6373.
294. **Ipekoglu, G. and Çam, G.** Effects of Initial Temper Condition and Postweld Heat Treatment on the Properties of Dissimilar Friction-Stir-Welded Joints between AA7075 and AA6061 Aluminum Alloys. Metall. Mater. Trans. A. 2014, Vol. 45, pp. 3074-3087.
295. **Cole, E.G., Fehrenbacher, A., Duffie, N.A., Zinn, M.R., Pfefferkorn, F.E. and Ferrier, N.J.** Weld temperature effects during friction stir welding of dissimilar aluminum alloys 6061-t6 and 7075-t6. Int. J. Adv. Manuf. Technol. 2013, Vol. 71, pp. 643-652.
296. **Song, Y., Yang, X., Cui, L., Hou, X., Shen, Z. and Xu, Y.** Defect features and mechanical properties of friction stir lap welded dissimilar AA2024–AA7075 aluminum alloy sheets. Mater. Des. 2014, Vol. 55, pp. 9-18.
297. **Jannet, S. and Mathews, P.K.** Effect of Welding Parameters on Mechanical and Microstructural Properties of Dissimilar Aluminum Alloy Joints Produced by Friction Stir Welding. Appl. Mech. Mater. 2014, 592, 250–254. 2014, Vols. 592-594, pp. 250-254.
298. **Palanivel, R., Koshy Mathews, P. Dinaharan, I. and Murugan, N.** Mechanical and metallurgical properties of dissimilar friction stir welded AA5083-H111 and AA6351-T6 aluminum alloys. Trans. Nonferrous Met. Soc. China 2014, 24, 58–65. 2014, Vol. 24, 1, pp. 58-65.
299. **Palanivel, R., Mathews, P.K. and Murugan, N.** Optimization of process parameters to maximize ultimate tensile strength of friction stir welded dissimilar aluminum alloys using response surface methodology. J. Cent. South Univ. 2013, Vol. 20, pp. 2929-2938.

300. **Jonckheere, C., de Meester, B., Denquin, A. and Simar, A.** Torque, temperature and hardening precipitation evolution in dissimilar friction stir welds between 6061-T6 and 2014-T6 aluminum alloys. J.Mater. Process. Technol. 2013, Vol. 213, 6, pp. 826-837.
301. **Jonckheere, C., de Meester, B., Denquin, A. and Simar, A.** Dissimilar friction stir welding of 2014 to 6061 aluminum alloys. Advanced Materials Research. 2012, Vol. 409, pp. 269-274.
302. **Ghosh, M., Husain, Md.M., Kumar, K. and Kailas, S.V.** Friction Stir-Welded Dissimilar Aluminum Alloys: Microstructure, Mechanical Properties, and Physical State. J. Mater. Eng. Perform. 2013, 22, 3890–3901. 2013, Vol. 22, pp. 3890-3901.
303. **Ghosh, M., Kumar, K., Kailas, S.V. and Ray, A.K.** Optimization of friction stir welding parameters for dissimilar aluminum alloys. Mater. Des. 2010, Vol. 31, 6, pp. 3033-3037.
304. **Koilraj, M., Sundareswaran, V., Vijayan, S., Koteswara Rao, Sajja.** Friction stir welding of dissimilar aluminum alloys AA2219 to AA5083 – Optimization of process parameters using Taguchi technique. Mater. Des. 2012, Vol. 42, pp. 1-7.
305. **Dinaharan, I., Kalaiselvan, K., Vijay, S.J. and Raja, P.** Effect of material location and tool rotational speed on microstructure and tensile strength of dissimilar friction stir welded aluminum alloys. Arch. Civ. Mech. Eng. 2012, 12, 446–454. 2012, Vol. 12, 4, pp. 446-454.
306. **Palanivel, R., Koshy Mathews, P., Murugan, N. and Dinaharan, I.** Effect of tool rotational speed and pin profile on microstructure and tensile strength of dissimilar friction stir welded AA5083-H111 and AA6351-T6 aluminum alloys. Mater. Des. 2012, 40, 7–16. 2012, Vol. 40, pp. 7-16.
307. **Kim, N.K., Kim, B.C., An, Y.G., Jung, B.H. Song, S.W. and Kang, C.Y.** The effect of material arrangement on mechanical properties in Friction Stir Welded dissimilar A5052/A5J32 aluminum alloys. Met. Mater. Int. 2009, Vol. 15, pp. 671-675.
308. **Prime, M.B., Gnäupel-Herold, T., Baumann, J.A., Lederich, R.J., Bowden, D.M. and Sebring, R.J.** Residual stress measurements in a thick, dissimilar aluminum alloy friction stir weld. Acta Mater. 2006, Vol. 54, 15, pp. 4013-4021.
309. **Liu, H.J., Fujii, H., Maeda M. and Nogi, K.** Mechanical properties of friction stir welded joints of 1050 – H24 aluminium alloy. Science and Technology of Welding and Joining. 2003, Vol. 8, 6, pp. 450-454.
310. **Mroczka, K.** Characteristics of AlSi9mg/2017A Aluminum Alloys Friction Stir Welded with Offset Welding Line and Root-Side Heating. Archives of Metallurgy and Materials. 2014, Vol. 59, 4, pp. 1293-1299.
311. **Mroczka, K., Dutkiewicz, J. and Pietras, A.** Microstructure of friction stir welded joints of 2017A aluminium alloy sheets. Journal of Microscopy, 237: 521-525. 2010, Vol. 237, 3, pp. 521-525.
312. **Yang, M., Li, C., Liu, S., Ye, L., Tang, J. and Liao, Z.** Effect of Artificial Aging on Microstructure and Mechanical Properties of Friction Stir Welded Joint of 7003/7046 Al-alloys. Chinese Journal of Materials Research. 2020, Vol. 34, 7, pp. 495-504.
313. **Kasman, S. and Ozan, S.** Effect of pin offset on the mechanical properties of friction stir welded AA 6013 aluminum alloy plates/Pin-Offset-Einfluss auf die mechanischen Eigenschaften beim Rührreibschweißen von Blechen aus der Aluminiumlegierung AA 6013. Materialwiss. Werkstofftech. 2019, Vol. 50, p. 1511.
314. **Zhao, Z., Liang, H., Zhao, Y. and Yan, K.** Effect of Exchanging Advancing and Retreating Side Materials on Mechanical Properties and Electrochemical Corrosion Resistance of Dissimilar 6013-T4 and 7003 Aluminum Alloys FSW Joints. J. of Materi Eng and Perform. 2018, Vol. 27, 10, pp. 1777-1783.
315. **Yoon, T.J., Jung, B.H. and Kang, C.Y**. The quantitative investigation of mechanical properties and characterization of fractured position for friction stir lap welded A6111/A5023. Mater. Des. 2015, Vol. 83, pp. 377-386.
316. **Verduzco-Juarez, J.C., Garcia-Hernandez, R., Dominguez-Almaraz, G.M. and Villalón-López, J.** Effect of Pre and Post Weld Heat Treatment on the Mechanical Properties of Friction Stir Welded AA6061-T6 Joint. International. Internatonal Journal of Automotive and Mechanical Engineering. 2020, Vol. 17, 2, pp. 7882-7889.
317. **Godhani, P.S., Patel, V.V., Vora, J.J., Chaudhary, N.D. and Banka, R.** Effect of Friction Stir Welding of Aluminum Alloys AA6061/AA7075: Temperature Measurement, Microstructure, and Mechanical Properties. [book auth.] D. Deb, V.E. Balas and R. (eds) Dey. In Innovations in Infrastructure. Proceedings of ICIIF 2018. s.l. : Springer, 2019, pp. 591-598.
318. **Chen, Y., Wang, H., Li, H., Wang, X., Ding, H., Zhao, J. and Zhang, F.** Investigation into the Dissimilar Friction Stir Welding of AA5052 and AA6061 Aluminum Alloys Using Pin-Eccentric Stir Tool. Metals 2019, Vol. 9, p. 718.
319. **Zhang, C., Huang, G., Yu, C., Zhu, Y. and Liu, Q.** On the microstructure and mechanical properties of similar and dissimilar AA7075 and AA2024 friction stir welding joints: Effect of rotational speed. Journal of Manufacturing Processes 2019, Vol. 37, pp. 470-487.
320. **Shiva Kumar, G.N. and Rajamurugan, G.** Friction stir welding of dissimilar alloy combinations - A Review. Proceedings of the Institution of Mechanical Engineers, Part C: Journal of Mechanical Engineering Science. 2022, Vol. 236, 12, pp. 6688-6705.

321. **Mastanaiah, P., Sharma, A. and Reddy, G.M.** Dissimilar Friction Stir Welds in AA2219-AA5083 Aluminium Alloys: Effect of Process Parameters on Material Inter-Mixing, Defect Formation, and Mechanical Properties. Trans. Indian Inst. Met. 2015, Vol. 69, 7, pp. 1397-1415.
322. **Kasman, S. and Yenier, Z.** Analyzing dissimilar friction stir welding of AA5754/AA7075. Int. J. Adv. Manuf. Technol. 2013, Vol. 70, pp. 145-156.
323. **Forcellese, A., Simoncini, M. and Casalino, G.** Influence of Process Parameters on the Vertical Forces Generated during Friction Stir Welding of AA6082-T6 and on the Mechanical Properties of the Joints. Metals. 2017, Vol. 7, 9, p. 350.
324. **Saeidi, M., Babak, M., Mohammad Kazem, B.G. and Ghader, F.** Mathematical modeling and optimization of friction stir welding process parameters in AA5083 and AA7075 aluminum alloy joints. Proc. Inst. Mech. Eng. Part B: J. Eng. Manuf. 2015, Vol. 230, pp. 1284-1294.
325. **Zhu, Z., Wang, M., Zhang, H., Zhang, X., Yu, T. and Wu, Z.** A Finite Element Model to Simulate Defect Formation during Friction Stir Welding. Metals. 2017, Vol. 7, 7, p. 256.
326. **Hamilton, C., Kopyściański, M., Węglowska, A., Dymek, S. and Pietras, A.** A Numerical Simulation for Dissimilar Aluminum Alloys Joined by Friction Stir Welding. Metall. Mater. Trans. A. 2016, Vol. 47, pp. 4519-4529.
327. **Gupta, S.K., Pandey, K. and Kumar, R.** Multi-objective optimization of friction stir welding process parameters for joining of dissimilar AA5083/AA6063 aluminium alloys using hybrid approach. Proceedings of the Institution of Mechanical Engineers, Part L: Journal of Materials: Design and Applications. 2016, Vol. 232, 4, pp. 343-353.
328. **Azeez, S., Akinlabi, E.T., Kailas, S.V. and Brandi, S.D.** Microstructural properties of a dissimilar friction stir welded thick aluminum aa6082-t6 and aa7075-t6 alloy. Mater. Today: Proc. 2018, Vol. 5, 9(3), pp. 18297-18306.
329. **Sun, Y., Liu, W., Li, Y., Gong, W. and Ju, C.** The Influence of Tool Shape on Plastic Metal Flow, Microstructure and Properties of Friction Stir Welded 2024 Aluminum Alloy Joints. Metals. 2022, Vol. 12, 3, p. 408.
330. Velotti, C., Astarita, A., & Squillace, A., Ciliberto, S., Villano, M., Giuliani, M., Prisco, U., Montuori, M., Giorleo, G. and Bellucci, F. On the critical technological issues of friction stir welding lap joints of dissimilar aluminum alloys. Surf. Interface Anal. 2013, Vol. 45, 10, pp. 1643-1648.
331. **Sivachidambaram, S., Rajamurugan, G. and Amirtharaj, D.** Optimizing the parameters for friction stir welding of dissimilar aluminium alloys AA5383/AA7075. ARPN J Eng Appl Sci. 2015, Vol. 10, pp. 5434–5437.
332. **Miles, M.P., Nelson, T.W. and Melton, D.W.** Formability of friction-stir-welded dissimilar-aluminum-alloy sheets. Metall. Mater. Trans. A 2005, 36, 3335–3342. 2005, Vol. 36, pp. 3335-3342.
333. **Ouyang, J.H. and Kovacevic, R.** Material flow and microstructure in the friction stir butt welds of the same and dissimilar aluminum alloys. Journal of Materials Engineering and Performance. 2002, Vol. 11, pp. 51-63.
334. Obtaining of aluminum alloys weld joints with specified strength properties by friction stir welding. Ivanov, A.N., Kalashnikova, T.A., Zhukov, L.L., Gurianov, D.A., Beloborodov, V.A., Kolubaev, E.A., Rubtsov, V.E., Tyurin, A.G., Bakshaev, V.A. and Nikitin, Y.V. 2022. AIP Conference Proceedings. Vol. 2467, p. 020058.
335. **Kumar, S.D. and Kumar, S.S.** Investigation of mechanical behavior of friction stir welded joints of AA6063 with AA5083 aluminum alloys. Mechanics and Mechanical Engineering. 2019, Vol. 23, 1, pp. 59-63.
336. Sasikala, G., Jothiprakash, V.M., Pant, B., Subalakshmi, R., Thirumal Azhagan, M., Arul, K., Alonazi, W.B., Karnan, M. and Kumar, S.P. Optimization of Process Parameters for Friction Stir Welding of Different Aluminum Alloys AA2618 to AA5086 by Taguchi Method. Advances in Materials Science and Engineering. SI: Application of Materials in Agricultural Engineering, 2022, p. 3808605.
337. **Aydin, H., Tutar, M., Durmuş, A., Bayram, A. and Sayaca, T.** Effect of Welding Parameters on Tensile Properties and Fatigue Behavior of Friction Stir Welded 2014-T6 Aluminum Alloy. Transactions of the Indian Institute of Metals. 2011, Vol. 65, 1, pp. 21-30.
338. **Aydin, H., Tutar, M., Yigit, K. and Bayram, A.** Mechanical Properties of Friction Stir Welded 3003 Aluminum Alloy in Different Welding Conditions. International Journal of Mechanical And Production Engineering. 2017, Vol. 5, 12, pp. 92-96.
339. **Aydin, H., Bayram, A., Yildirim, M.T. and Yigit, K.** Influence of Welding Parameters on the Fatigue Behaviours of Friction Stir Welds of 3003-O Aluminum Alloys. Materials Science (Medziagotyra). 2010, Vol. 16, 4, pp. 311-319.
340. **Weglowski, M.S., Pietras, A. and Weglowska, A.** Effect of welding parameters on mechanical and microstructural properties of AL 2024 joints produced by friction stir welding. Journal of KONES. 2009, Vol. 16, 1, pp. 523-532.
341. **Nejad, S.G., Yektapour, M. and Akbarifard, A.** Friction stir welding of 2024 aluminum alloy: Study of major parameters and threading feature on probe. J Mech Sci Technol. 2017, Vol. 31, pp. 5435-5445.

342. Mechanical behaviour of Al 2024 alloy welded by friction stir welding. **Milčić, M., Vuherer, T., Radisavljević, I., Milčić, D., Kramberger, J. and Andjelkovic, B.** Novi Sad, Serbia : s.n., 2018. IOP Conf. Ser.: Mater. Sci. Eng. The 10th International Symposium Machine and Industrial Design in Mechanical Engineering 6-8 June 2018. Vol. 393, p. 012107.
343. **Lin, S.B., Zhao, Y.H. and Wu, L.** Integral and layered mechanical properties of friction stir welded joints of 2014 aluminium alloy. Materials Science and Technology. 2006, Vol. 22, 8, pp. 995-998.
344. **Sinhmar, S. and Dwivedi, D.K.** Investigation of mechanical and corrosion behavior of friction stir weld joint of aluminium alloy. MaterialsToday: Proceedings. 2019, Vol. 18, 7, pp. 4542-4548.
345. **Ugender, S., Kumar, A. and Reddy, A.S.** Experimental Investigation of Tool Geometry on Mechanical Properties of Friction Stir Welding of AA 2014 Aluminium Alloy. Procedia Materials Science. 2014, Vol. 5, pp. 824-831.
346. **Mroczka, K., Dutkiewicz, J. and Pietras, A.** Structure and Properties of FSW Joints of 2017A Aluminum Alloy Welded at Different Pin-Tool Rate. ed. board Paweł Kurtyka et al., Insti. [ed.] P. Kurtyka. Problems of modern techniques in aspect of engineering and education. 2006, pp. 267-272.
347. **Takhakh, A.M. and Abdullah, A.M.** An Experimental Investigation on Fatigue Properties of AA3003-H14 Aluminum alloy Friction Stir Welds. Journal of Engineering. 17. 2012, Vol. 17, 6, pp. 1391-1401.
348. **Chekalil, I., Miloudi, A., Planche, M.P. and Ghazi, A.** Prediction of mechanical behavior of friction stir welded joints of AA3003 aluminum alloy. Frattura ed Integrità Strutturale. 2020, Vol. 54, 14, pp. 153-168.
349. **Kasman, S. and Ozan, S.** Characterization of friction stir welded AA 3003-H24 aluminum alloy plates. Sigma J Eng Nat Sci. 2022, Vol. 40, 3, pp. 620-629.
350. Properties of Friction Stir Welded 3003-H17 Aluminum Alloy at High Travel Speeds. **Xu, A**. Zhuhai, China : s.n., 2020. The 6th International Conference on Materials, Mechanical Engineering and Automation Technology 1-3 May 202. Vol. 1676, p. 012114.
351. **Goyal, A., Rohilla, P.K. and Kaushik, A.K.** Optimization of Friction Stir Welding Parameters for AA3003 Aluminum Alloy Joints Using Response Surface Methodology. International Journal of Mechanics and Solids. 2017, Vol. 12, 1, pp. 15-26.
352. **Janeczek, A., Tomkow, J. and Fydrych, D.** The Influence of Tool Shape and Process Parameters on the Mechanical Properties of AW-3004 Aluminium Alloy Friction Stir Welded Joints. Materials. 2021, Vol. 14, 12, p. 3244.
353. **Choi, W.H., Kwon, Y.J., Yoon, S., Kang, M.S., Lim, C.Y., Seo, J.D., Hong, S.T., Park, D.H. and Lee, K.H.** Influence of Welding Parameters on Macrostructure and Mechanical Properties of Friction-Stir-Spot-Welded 5454-O Aluminum Alloy Sheets. Journal of Welding and Joining. 2011, Vol. 29, 6, pp. 56-64.
354. **Selvarajan, R. and Balasubramanian, V.** Multi-Response Optimization of Friction-Stir-Welded AA1100 Aluminum Alloy Joints. Journal of Materials Engineering and Performance. 2011, Vol. 21, 6, pp. 1-14.
355. **Dong, J., Zhang, D., Zhang, W., Zhang, W. and Qiu, C.** Microstructure and properties of underwater friction stir-welded 7003-T4/6060-T4 aluminum alloys. Journal of Materials Science. 2019, Vol. 54, 1-2, pp. 11254–11262.
356. **Sheikhi, S. and dos Santos, J.** Effect of process parameter on mechanical properties of friction stir welded tailored blanks from aluminium alloy 6181-T4. Science and Technology of Welding and Joining. 2007, Vol. 12, 4, pp. 370-375.
357. **Zhou, Y., Chen, S., Wang, J., Wang, P. and Xia, J.** Influences of Pin Shape on a High Rotation Speed Friction Stir Welding Joint of a 6061-T6 Aluminum Alloy Sheet. Metals. 2018, Vol. 8, 12, p. 987.
358. **Aval, H.J., Serajzadeh, S., Kokabi, A.H. and Loureiro, A.** Effect of tool geometry on mechanical and microstructural behaviours in dissimilar friction stir welding of AA 5086 – AA 6061. Sci Technol Weld Join. 2011, Vol. 16, 7, pp. 597-604.
359. **Xu, W., Liu, J. and Zhu, H.** Analysis of residual stresses in thick aluminum friction stir welded butt joints. Materials & Design. 2011, Vol. 32, pp. 2000-2005.
360. **Goel, P., Siddiquee, A.N., Khan, N.Z., Hussain, M.A., Khan, Z.A., Abidi, M.H. and Al-Ahmari, A.** Investigation on the Effect of Tool Pin Profiles on Mechanical and Microstructural Properties of Friction Stir Butt and Scarf Welded Aluminium Alloy 6063. Metals. 2018, Vol. 8, 1, p. 74.
361. **Patel, V.V., Badheka, V. and Kumar, A.** Friction Stir Processing as a Novel Technique to Achieve Superplasticity in Aluminum Alloys: Process Variables, Variants, and Applications. Metallogr. Microstruct. Anal. 2016, 5, 278–293. 2016, Vol. 5, pp. 278-293.
362. **Patel, V.V., Badheka, V. and Kumar, A.** Effect of polygonal pin profiles on friction stir processed superplasticity of AA7075 alloy. J. Mater. Process. Technol. 2017, Vol. 240, pp. 68-76.
363. **Patel, V.V., Badheka, V.J. and Kumar, A.** Influence of Pin Profile on the Tool Plunge Stage in Friction Stir Processing of Al–Zn–Mg–Cu Alloy. Trans. Indian Inst. Met. 2016, Vol. 70, 4, pp. 1151-1158.
364. **Patel, V.V., Li, W., Vairis, A. and Badheka, V.** Recent Development in Friction Stir Processing as a Solid-State Grain Refinement Technique: Microstructural Evolution and Property Enhancement. Critical Reviews in Solid State and Materials Sciences. 2019, Vol. 44, 5, pp. 378-426.

365. **Burek, R., Wydrzyński, D. and Sęp, J. Więckowski, W.** The effect of tool wear on the quality of lap joints between 7075 T6 aluminium alloy sheet metal created with the FSW method. Eksploatacja i Niezawodnosc/Maintenance and Reliability. 2018, Vol. 20, 1, pp. 100-106.
366. **Khan, N.Z., Siddiquee, A.N., Khan, Z.A. and Shihab, S.K.** Investigations on tunneling and kissing bond defects in FSW joints for dissimilar aluminum alloys. J Alloys Compd. 2015, Vol. 648, pp. 360-367.
367. **Dialami, N., Cervera, M. and Chiumenti, M.** Numerical Modelling of Microstructure Evolution in Friction Stir Welding (FSW). Metals 2018, 8, 183. 2018, Vol. 8, 3, p. 183.
368. **Nakamura, T., Obikawa, T., Nishizaki, I., Enomoto, M. and Fang, Z.** Friction Stir Welding of Non-Heat-Treatable High-Strength Alloy 5083-O. Metals 2018, 8, 208. 2018, Vol. 8, 4, p. 208.
369. **Patel, V.V., Badheka, V. and Kumar, A.** Influence of Friction Stir Processed Parameters on Superplasticity of Al-Zn-Mg-Cu Alloy. Mater. Manuf. Process. 2015, Vol. 31, 12, pp. 1-10.
370. **Fadaeifard, F., Matori, K.A., Abd Aziz, S., Zolkarnain, L. and Abdul Rahim, M.A.Z.B.** Effect of the Welding Speed on the Macrostructure, Microstructure and Mechanical Properties of AA6061-T6 Friction Stir Butt Welds. Metals. 2017, Vol. 7, 2, p. 48.
371. **Niu, P., Li, W.Y., Vairis, A. and Chen, D.L.** Cyclic deformation behavior of friction-stir-welded dissimilar AA5083-to-AA2024 joints: Effect of microstructure and loading history. Mater. Sci. Eng. A. 2019, Vol. 744, pp. 145-153.
372. **Ji, S.D., Xing, J., Yue, Y., Ma, Y., Zhang, L. and Gao, S.** Design of friction stir welding tool for avoiding root flaws. Materials. 2013, Vol. 6, 12, pp. 5870-5877.
373. **Wan, L., Guo, W., Lv, S. and Feng, J.** Mechanical properties and microstructure of 6082-T6 aluminum alloy joints by self-support friction stir welding. J Mater Sci Technol. 2014, Vol. 30, 12, pp. 1243-1250.
374. **Liu, L., Yang, K. and Yan, D.** Refill Friction Stir SpotWelding of Dissimilar 6061/7075 Aluminum Alloy. High Temp. Mater. Process. 2019, Vol. 39, pp. 69-75.
375. **Tra, H.M., Okazaki, M. and Suzuki, K.** Fatigue crack propagation behavior in friction stir welding of AA6063-T5: roles of residual stress and microstructure. Int. J. Fatigue. 2012, Vol. 43, pp. 23-29.
376. Mechanical Properties of 6013-T6 Aluminium Alloy Friction Stir Welded Plate. **Kafali, H. and ay, Nuran**. Cairo, Egypt : s.n., 2009. 13th International Conference on Aerospace Sciences & Aviation Technology, ASAT- 13, May 26 – 28, 2009. pp. ASAT-13-MS-14.
377. **Saleh, A.A.** Joining of AA2014 and AA5059 dissimilar aluminium alloys by Friction Stir Welding. Journal of Achievements in Materials and Manufacturing Engineering. 2019, Vol. 91, 1, pp. 15-20.
378. Analysing the Friction Stir Welded Joints of AA2219 Al-Cu Alloy in Different Heat-Treated-State. **Venkateswarlu, D., Cheepu, M., Kranthi kumar, B. and Mahapatra, M.M.** Hyderabad, India : s.n., 2018. International Conference on Recent Advances in Materials, Mechanical and Civil Engineering 1–2 June 2017. Vol. 330, p. 012074.
379. A Study on the Corrosion Behaviour of Aluminium Alloy 2014 T-651 Friction Stir Welds Using Stress Corrosion Cracking. **Kollapuri, T., Monoharan, M., Sadayan, R. and Sajja, R.** Houston, Texas, USA : s.n., 2015. ASME 2015 International Mechanical Engineering Congress and Exposition November 13–19, 2015. Vol. 14: Emerging Technologies; Safety Engineering and Risk Analysis; Materials: Genetics to Structures, p. V014T11A004.
380. **Tan, Y.B., Wang, X.M., Ma, M., Zhang, J.X., Liu, W.C., Fu, R. and Xiang, S.** A study on microstructure and mechanical properties of AA 3003 aluminum alloy joints by underwater friction stir welding. Materials Characterization. 2017, Vol. 127, pp. 41-52.
381. **Deng, Y.L., Deng, S.H., Ye, L.Y., Lin, S., Sun, L. and Ji, H.** Effects of post-weld heat treatment on microstructures and mechanical properties of AA7204-T4 aluminum alloy FSW joint[J]. Journal of Materials Engineering. 2020, Vol. 48, 4, pp. 131-138.
382. **Unfried-Silgado, J., Rodriguez, J., Torres, A. and Carrasco, J.** Effects of shoulder geometry of tool on microstructure and mechanical properties of friction stir welded joints of AA1100 aluminum alloy. DYNA. 2017, Vol. 84, 200, pp. 202-208.
383. **Chen Y, Wang H, Li H, et al.** Investigation into the dissimilar friction stir welding of AA5052 and AA6061 aluminum 6702 Proc IMechE Part C: J Mechanical Engineering Science 236(12) alloys using pin-eccentric stir tool. Metals (Basel). 2019;9(7):1-12.
384. **Guo, J.F., Chen, H.C., Sun, C.N., Bi, G., Sun, Z. and Wei, J**. Friction stir welding of dissimilar materials between AA6061 and AA7075 Al alloys effects of process parameters, Materials & Design 2014, Vol. 56, pp. 185-192.
385. **Sato, Y.S., Kurihara, Y. and Kokawa, H.** Microstructural characteristics of dissimilar butt friction stir welds of AA7075 and AA2024. Proc. 6th Int. FSW Symp., Saint-Sauveur, Que., Canada, October (2006) TWI, CD-ROM.
386. **da Silva, A.A.M., Arruti, E., Janeiro, G., Aldanondo, E., Alvarez, P. and Echeverria, A.** Material flow and mechanical behaviour of dissimilar AA2024-T3 and AA7075-T6 aluminium alloys friction stir welds. J. Materials and Design 2011, Vol. 32, pp. 2021-2027.

 doi:10.20944/preprints202403.1458.v1

387. **Dewangan, S.K., Tripathi, M.K. and Manoj, M.K.** Effect of WSs on microstructure and mechanical properties of dissimilar friction stir welding of AA7075 and AA5083 alloy. Mater Today Proc. 2019, vol. 27, pp. 2713-2717.
388. **Khan, N.Z., Siddiquee, A.N., Zahid A. Khan, Z.A. and Mukhopadhyay, A.K.** Mechanical and microstructural behavior of friction stir welded similar and dissimilar sheets of AA2219 and AA7475 aluminium alloys. Journal of Alloys and Compounds 2017, Vol. 695, pp. 2902-2908.
389. **Abidi, M.H., Ali, N., Ibrahimi, H., Anjum, S., Bajaj, D., Siddiquee, A.N., Alkahtani, M. and Rehman, A.U.** T-FSW of Dissimilar Aerospace Grade Aluminium Alloys: Influence of Second Pass on Weld Defects. Metals 2020, Vol. 10, p. 525.
390. **Morikawa, K., Kawai, G., Ochi, H., Yamamoto, Y. and Suga, Y.** Strength of 2017 aluminium alloy stud joints by friction welding. Welding International. 2013, Vol. 27, 1, pp. 18-23.
391. **Dixit, S.** Hardness Testing of Friction Stir Welded AA 1200 Aluminium Alloy. IJMSE. 2017, Vol. 8, 1, pp. 17-21.
392. **Attah, B.I., Lawal, S.A., Akinlabi, E.T. and Bala, K.C**. Evaluation of mechanical properties of dissimilar aluminium alloys during friction stir welding using tapered tool. Cogent Engineering. 2021, Vol. 8, p. 1909520.
393. **Jassim, A.K. and Al-Subar, R.K.** Studying the Possibility to Weld AA1100 Aluminum Alloy by Friction Stir Spot Welding. World Academy of Science, Engineering and Technology International Journal of Materials and Metallurgical Engineering. 2017, Vol. 11, 9, p. 10008041.
394. **Senapati, N.P. and Bhoi, R.K.** Improving the Strength of Friction-Stir-Welded Joints of AA1100 Alloy. J. of Materi Eng and Perform. 2021, Vol. 30, pp. 510-521.
395. **Joseph, M.G., Shaji, J., Francis, M.J., Raghavan, A. and Shunmugesh, K.** Measurement of Tensile Properties and Hardness of Friction Stir Welded Aluminium Alloy AA1200. Materials Today: Proceedings. 2020, Vol. 24, 3, pp. 1987-1993.
396. **Sato, Y.S., Kurihara, Y., Park, S.H.C., Kokawa, H. and Tsuji, N.** Friction stir welding of ultrafine grained Al alloy 1100 produced by accumulative roll-bonding. Scripta Materialia. 2004, Vol. 50, 1, pp. 57-60.
397. **Jannet, S., Mathews, K. and Raja, R.** Comparative investigation of friction stir welding and fusion welding of 6061 T6-5083 O aluminum alloy based on mechanical properties and microstructure. Bull. Pol. Acad. Sci. Tech. Sci. 2014, Vol. 62, pp. 791-795.
398. **Dolatkhah, A., Golbabaei, P., Besharati Givi, M.K. and Molaiekiya, F.** Investigating effects of process parameters on microstructural and mechanical properties of Al5052/SiC metal matrix composite fabricated via friction stir processing. Mater. Des. 2012, Vol. 37, pp. 458-464.
399. **Bahrami, M., Dehghani, K. and Givi, M.K.B.** A novel approach to develop aluminum matrix nano-composite employing friction stir welding technique. Mater. Des. 2014, Vol. 53, pp. 217–225.
400. **Pantelis, D.I., Karakizis, P.N., Daniolos, N.M., Charitidis, C.A., Koumoulos, E.P. and Dragatogiannis, D.A.** Microstructural study and mechanical properties of dissimilar friction stir welded AA5083-H111 and AA6082-T6 reinforced with SiC nanoparticles. Mater. Manuf. Process. 2016, Vol. 31, pp. 264-274.
401. **Dragatogiannis, D.A., Koumoulos, E.P., Kartsonakis, I.A., Pantelis, D.I., Karakizis, P.N. and Charitidis, C.A.** Dissimilar Friction Stir Welding Between 5083 and 6082 Al Alloys Reinforced With TiC Nanoparticles. Mater. Manuf. Process. 2016, Vol. 31, pp. 2101-2114.
402. **Scudino, S., Liu, G., Prashanth, K.G., Bartusch, B., Surreddi, K.B., Murty, B.S. and Eckert, J.** Mechanical properties of Al-based metal matrix composites reinforced with Zr-based glassy particles produced by powder metallurgy. Acta Mater. 2009, Vol. 57, pp. 2029-2039
403. **Vimalraj, C. and Kah, P.** Experimental Review on Friction Stir Welding of Aluminium Alloys with Nanoparticles. Metals (Basel) 2021, Vol. 11, 3, pp. 1-26.
404. **Moradi, M.M., Jamshidi, A.H. and Jamaati, R.** Effect of tool pin geometry and weld pass number on microstructural, natural aging and mechanical behaviour of SiC-incorporated dissimilar friction-stir-welded aluminium alloys. Sadhana - Acad Proc Eng Sci 2019, Vol. 44, pp. 1-9.
405. **Kulekci, M.K., Esme, U., Er, O. and Kazançoğlu, Y.** Modeling and prediction of weld shear strength in friction stir spot welding using design of experiments and neural network. Materialwissenschaft und Werkstofftechnik. 42. 10.1002/mawe.201100781. 2011, Vol. 42, 11, pp. 990-995.
406. **Scotchmer, N. and Chan, K.** What's New for Welding Aluminum in the Auto Industry. Welding Journal. 2012, Vol. 91, 1, pp. 34-37.
407. **Kulekci, M.K.** Effects of Process Parameters on Tensile Shear Strength of Friction Stir Spot Welded Aluminium Alloy (EN AW 5005). Archives of Metalurgy and Materials. 2014, Vol. 59, 1, pp. 221-224.
408. Friction stir welding for the 21st century automotive industry. **Hinrichs, J.F., Smith, C.B., Orsini, B.F., DeGeorge, R.J., Smale, B.J. and Ruehl, PC.** Metz, France : The Welding Institute, 2004. Proceedings of the 5th International Symposium on Friction Stir Welding, 14-16 September 2004.
409. **Praveen, P. and Yarlagadda, P.K.D.V.** Meeting challenges in welding of aluminum alloys through pulse gas metal arc welding. Journal of Materials Processing Technology. 2005, Vols. 164-165, pp. 1106-1112.

410. **Lewise, K.A.S., Dhas, J.E.R. and Pandiyarajan, R.** Optimising aluminium 2024/7075 friction stir welded joints. Advances in Materials and Processing Technologies. 2022, Vol. 8, 4, pp. 4579-4597.
411. **Borah, M.J., Rajbongshi, S.K., Saha, N. and Buddhi, D.** Friction stir spot welding process: an innovative approach for transforming from engineering design to production. Int J Interact Des Manuf. 2022.
412. **Suresh, S., Elango, N., Venkatesan, K., Lim, W.H., Palanikumar, K. and Rajesh, S.** Sustainable friction stir spot welding of 6061-T6 aluminium alloy using improved non-dominated sorting teaching learning algorithm. Journal of Materials Research and Technology. 2020, Vol. 9, 5, pp. 11650-11674.
413. **Zhu, Z., Li, Y., Zhang, M. and Hui, C.** Effects of stress concentration on the fatigue strength of 7003-T5 aluminum alloy butt joints with weld reinforcement. International Journal of Modern Physics B. 2015, Vol. 29, 10-11, p. 1540023.
414. **Sangduang, W., Wattanathum, P. and Eidhed, K.** The Study on welding Effect and Porosity Distribution of 5154 Aluminum Alloys by Gas Metal Arc Welding (GMAW). Thai Industrial Engineering Network Journal, 6(2), 59–67. 2020, Vol. 6, 2, pp. 59-67.
415. **Ramaswamy, A., Malarvizhi, S. and Balasubramanian, V.** Effect of variants of gas metal arc welding process on tensile properties of AA6061-T6 aluminium alloy joints. Int J Adv Manuf Technol. 2020, Vol. 108, pp. 2967-2983.
416. **Mercan, E., Ayan, Y. and Kahraman, N.** Microstructure and Mechanical Properties of Aluminum Alloys AA5754 and AA6013 Joined by GMAW (Gas Metal Arc Welding) Method. Pamukkale Univ. Journal of Engineering Sciences. 2020, Vol. 26, 1, pp. 82-87.
417. **Kaushal, C. and Sharma, L.** To Determine Effects of Gas Metal Arc Welding (GMAW) Parameters on Mechanical Properties of Aluminium Alloys. International Journal of Innovative Research in Science, Engineering and Technology. 2015, Vol. 4, 6, pp. 4564-4572.
418. **Çevik, B.** Gas tungsten arc welding of 7075 aluminum alloy: microstructure properties, impact strength, and weld defects. Mater. Res. Express. 2018, Vol. 5, 6, p. 066540.
419. **Jin, L., Yang, Y., Yao, P., Chen, W., Qian, Z. and Xue, J.** Investigation of the Difference in the Pulse Current in the Double Pulsed Gas Metal Arc Welding of Aluminum Alloys. Materials. 2022, Vol. 15, 7, p. 2513.
420. **Huang, L.; Hua, X.; Wu, D.; Jiang, Z.; Li, F.; Wang, H.; Shi, S.** Microstructural characterization of 5083 aluminum alloy thick plates welded with GMAW and twin wire GMAW processes. Int. J. Adv. Manuf. Technol. 2017, 93, 1809–1817.
421. **Kim, C.; Ahn, Y.; Lee, K.-B.; Kim, D.** High-deposition-rate position welding of Al 5083 alloy for spherical-type liquefied natural gas tank. Proc. Inst. Mech. Eng. Part B J. Eng. Manuf. 2015, 230, 818–824.
422. **Yu, H., Tong, Y.** Magnetic pulse welding of aluminum to steel using uniform pressure electromagnetic actuator. Int J Adv Manuf Technol. 2017, Vol. 91, pp. 2257-2265.
423. **Drehmann, R., Scheffler, C., Winter, S., Psyk, V., Kräusel, V. and Lampke, T.** Experimental and Numerical Investigations into Magnetic Pulse Welding of Aluminum Alloy 6016 to Hardened Steel 22MnB5. J. Manuf. Mater. Process. 2021, Vol. 5, 3, p. 66.
424. **Khalil, C., Marya, S. and Racineux, G.** Magnetic Pulse Welding and Spot Welding with Improved Coil Efficiency - Application for Dissimilar Welding of Automotive Metal Alloys. J. Manuf. Mater. Process. 2020, Vol. 4, 3, p. 69.
425. **Yan, Z., Xiao, A., Cui, X., Guo, Y., Lin, Y., Zhang, L. and Zhao, P.** Magnetic pulse welding of aluminum to steel tubes using a field-shaper with multiple seams. Journal of Manufacturing Processes. 2021, Vol. 65, 1-4, pp. 214-227.
426. **Chen, S., Han, Y., Gong, W., Yuan, Y. and Jiang, X.** Mechanical properties and joining mechanism of magnetic pulse welding of aluminum and titanium. Int J Adv Manuf Technol. 2022, Vol. 120, pp. 7115-7126.
427. Magnetic Pulse Welding (MPW) Method for Dissimilar Sheet Metal Joints. **Aizawa, T. and Kashani, M.** Osaka, Japan : s.n., 2004. 57th Ann. Assembly of the Int. Institute of Welding (IIW) Osaka, 2004.
428. **Zhang, Y., Babu, S.S., Zhang, P., Kenik, E.A. and Daehn, G.S.** Microstructure characterisation of magnetic pulse welded AA6061-T6 by electron backscattered diffraction. Science and Technology of Welding and Joining. 2008, Vol. 13, 5, pp. 467-471.
429. **Pereira, D., Oliveira, J.P., Pardal, T., Miranda, R.M. and Santos, T.G.** Magnetic pulse welding: machine optimisation for aluminium tubular joints production. Science and Technology of Welding and Joining. 2018, Vol. 23, 2, pp. 172-179.
430. **Okagawa, K.; Aizawa, T.** Impact seam welding with magnetic pressure for aluminum sheets. Mater. Sci. Forum 2004, 465, 231–236.
431. **Raoelison, R.N.; Sapanathan, T**. Interfacial kinematics and governing mechanisms under the influence of high strain rate impact conditions: Numerical computations of experimental observations. J. Mech. Phys. Solids 2016, 96, 147–161.
432. **Liu, B., Vivek, A., Daehn, G.S.** Use of Vaporizing Foil Actuator for Impact Welding of Aluminum Alloy Sheets with Steel and Magnesium Alloys. [ed.] M. (eds) Hyland. Light Metals. s.l. : Springer, Cham., 2015.
433. **Vivek, A.** Vaporizing foil actuator: A tool for collision welding. Journal of Materials Processing Technology. 2013, Vol. 213, 12, pp. 2304-2311.

434. **Hahn, M., Weddeling, C., Taber, G., Vivek, A., Daehn, G.S. and Tekkaya, E.A.** Vaporizing foil actuator welding as a competing technology to magnetic pulse welding. Journal of Materials Processing Technology. 2016, Vol. 230, pp. 8-20.
435. **Kapil, A.** Aspects of Vaporizing Foil Actuator Welding for Practical Automotive Applications. PhD Thesis. Ohio : The Ohio State University, 2020.
436. **Kapil, A., Lee, T., Vivek, A., Bockbrader, J., Abke, T. and Daehn, G**. Benchmarking strength and fatigue properties of spot impact welds. Journal of Materials Processing Technology. 2018, Vol. 255, pp. 219-233.
437. **Nassiri, A. and Kinsey, B.** Numerical studies on high-velocity impact welding: Smoothed particle hydrodynamics (SPH) and arbitrary Lagrangian–Eulerian (ALE). J. Manuf. Process. 2016, Vol. 24, pp. 376–381.
438. **Groche, P. and Becker, M.** Process window acquisition for impact welding processes. Mater. Des. 2017, Vol. 118, pp. 286–293.
439. **Hansen, S.R., Vivek, A. and Daehn, G.S.** Impact Welding of Aluminum Alloys 6061 and 5052 by Vaporizing Foil Actuators: Heat-Affected Zone Size and Peel Strength. Journal of Manufacturing Science and Engineering 2015, Vol. 137, p. 051013.
440. **Hansen, S.R., Vivek, A. and Daehn, G.S.** Control of Velocity, Driving Pressure, and Planarity During Flyer Launch with Vaporizing Foil Actuator. 6th International Conference on High Speed Forming - 2014, 325-334.
441. **Meng, Z., Su, S., Mao, Y., Vivek, A., Huang, S.Y., Hua, L., Chen, S., Daehn, G.S.** Welding of 2024-7075 Aluminum Alloys and 5A06 Aluminum to Stainless Steel 321 by Vaporizing Foil Actuator. International Conference on High Speed Forming 14th May to 16th May 2018 at the Ohio State University in Columbus, USA.
442. Current Research and Challenges in Innovative Technology of Joining Dissimilar Materials for Electric Vehicles. **Li, H., Liu, X., Zhang, Y., Ma, M., Li, G.Y. and Senkara, J.**. Proceedings of the 4th International Conference on Advanced High Strength Steel and Press Hardening (ICHSU2018), February 2019.
443. **Li, D., Slater, C., Cai, H., Hou, X., Li, Y. and Wang, Q.** Joining Technologies for Aluminium Castings - A Review. Coatings 2023, Vol. 13, 5, p. 958.
444. 442**Cavaliere P. et al.** Effect of welding parameters on mechanical and microstructural properties of dissimilar AA6082–AA2024 joints produced by friction stir welding. Mater. Des. (2009).
445. **Khodir S.A. et al.** Friction stir welding of dissimilar AA2024 and AA7075 aluminum alloys. Mater. Sci. Eng. B (2008).
446. **Song Y. et al.** Defect features and mechanical properties of friction stir lap welded dissimilar AA2024–AA7075 aluminum alloy sheets. Mater. Des. (2014).
447. **Dragatogiannis, D.A., Kollaros, D., Karakizis, P., Pantelis, D., Lin, J. and Charitidis, C.** Friction Stir Welding between 6082 and 7075 Aluminum Alloys Thermal Treated for Automotive Applications. Materials Performance and Characterization 2019, Vol. 8, 4, pp. 571–589.
448. Venkateswarlu, D. Nageswararao, P., Mahapatra, M.M., Harsha, S.P. and Mandal, N. R. Venkateswarlu, D., Nageswararao, P., Mahapatra, M.M. and Mandal N.R. Processing and Optimization of Dissimilar Friction Stir Welding of AA 2219 and AA 7039 Alloys. J. of Materi Eng and Perform 2015, Vol. 24, pp. 4809–4824.
449. **Pouranvari, M. and Marashi, S.P.H.** Critical review of automotive steels spot welding: process, structure and properties. Science and Technology of Welding and Joining. 2013, Vol. 18, 5, pp. 361-403.
450. **Armao, F**. Aluminum Workshop: Adding weld strength with aging [Online] 20 November 2014. https://www.thefabricator.com/thewelder/article/aluminumwelding/aluminum-workshop-adding-weld-strength-with-aging.
451. **Lumley, R.N., Morton, A.J., O'Donnell, R.G. and Polmear, I.J.** New heat treatments for age-hardenable aluminum alloys. Heat Treating Progress. 2005, Vol. 5, 2, pp. 23-29.
452. **Fujita, T., Hasegawa, K., Mitao, S., Niikura, M., Koike, T., Funakawa, M., Yoshihara, N. and Ohori, K**. A new paint-bake-hardenable aluminum alloy for auto body sheet applications. SAE Transactions. 1995, Vol. 104, 5, pp. 667-672.
453. **Engler, O. and Myhr, O.R.** Effect of Natural Ageing on Strength and Anisotropy in Aluminium Alloy AA 6005C. Materials Science Forum. 2017, Vol. 877, pp. 688-694.